RESPONSIVE NANOSTRUCTURE MORPHOLOGIES THROUGH DYNAMIC ASSEMBLY OF BRANCHED FUNCTIONAL POLYMERS

A Dissertation
Presented to
The Academic Faculty

by

Hansol Lee

In Partial Fulfillment
of the Requirements for the Degree
Doctor of Philosophy in the
School of Materials Science and Engineering

Georgia Institute of Technology
August 2021

RESPONSIVE NANOSTRUCTURE MORPHOLOGIES THROUGH DYNAMIC ASSEMBLY OF BRANCHED FUNCTIONAL POLYMERS

Approved by:

Dr. Vladimir V. Tsukruk, Advisor
School of Materials Science and Engineering
Georgia Institute of Technology

Dr. Blair Brettmann
School of Chemical and Biomolecular Engineering
School of Materials Science and Engineering
Georgia Institute of Technology

Dr. Valeria Milam
School of Materials Science and Engineering
Georgia Institute of Technology

Dr. Andrei Fedorov
George W. Woodruff School of Mechanical Engineering
Georgia Institute of Technology

Dr. Zhiqun Lin
School of Materials Science and Engineering
Georgia Institute of Technology

Date Approved: July 13, 2021

Dedicated to my loving family and friends.

ACKNOWLEDGEMENTS

I would like to thank everyone who has helped me throughout my journey through this dissertation process. First of all, I would like to express my greatest gratitude to my advisor, Prof. Vladimir V. Tsukruk for his constant guidance, motivation and support. His attitudes towards research and life have helped me grow as a researcher who has strong confidence and an open-minded and positive attitude. I also thank all other Ph.D. committee members, Prof. Zhiqun Lin, Prof. Valeria Milam, Prof. Andrei Fedorov and Prof. Blair K. Brettmann for their kind willingness to take part on my committee, providing critical feedback and insight to this project.

I would like to thank all our collaborators in this project: Prof. Valery V. Shevchenko (National Academy of Science of Ukraine, Ukraine) for providing us novel polymer materials, Prof. Yaroslava G. Yingling (North Carolina State University) for help and insights on simulation studies, and Prof. Alexei P. Sokolov (Oak Ridge National Lab, University of Tennessee) for assisting ion transport measurements. Thanks also go to researchers and students in the collaborators' groups. It is a great honor to have the chance to work with them and do exceptional collaborations.

I would also like to acknowledge all the past and current SEMA Lab members for creating a friendly work environment and providing me encouragements in order to finish up my Ph.D. studies. In particular, I extend special thanks to Dr. Volodymyr F. Korolovych for helping me with transition to this project, Dr. Andrew Erwin for providing valuable discussion, and Dr. Minkyu Kim for his helpful instruction, discussion and insights and technical assistance. Financial support of this work is acknowledged by the National Science Foundation, DMR 1505234 and 2001968.

Finally, I am deeply grateful to my parents, family and fiancé, Seoungwon Ryu, for the boundless support and love I receive from them, without which, none of my accomplishments was possible.

TABLE OF CONTENTS

LIST OF TABLES

LIST OF FIGURES

LIST OF SYMBOLS AND ABBREVIATIONS

a_0	Equilibrium Area of Hydrophilic Surface Group
A_l	Surface Area per Molecule in Liquid Phase
A_s	Surface Area per Molecule in Solid Phase
A_{domain}	Area Coverage of Domains
A_{under}	Area Coverage of Underlying Sublayer
χ_{12}	Interaction Parameter
δ	Solubility Parameter
ε	Porosity
$\varepsilon_{monolayer}$	Permittivity of Monolayer
E	Elastic Modulus
G'	Storage Modulus
G''	Loss Modulus
l_c	Maximum Effective Chain Length Per Amphiphilic Molecule
$\mu_{monolayer}$	Net Dipole Moment of Monolayer
ρ_B	Bulk Density
ρ_S	Substance Density
p	Packing Parameter
σ_{dc}	DC Conductivity
σ'	Real Part of Complex Conductivity
σ_y	Yield Strength
$\sigma_{75\%}$	Maximum Strength at 75% Strain
T_g	Glass Transition Temperature
$t_{effective}$	Effective Thickness
t_{domain}	Height of Domains

t_{under}	Thickness of Underlying Sublayer
v	Volume Fraction of Hydrophobic Segment
$V_{monolayer}$	Surface Potential of Monolayer
V_{SiO2}	Surface Potential of SiO_2 Region
AFM	Atomic Force Microscopy
ATR-FTIR	Attenuated Total Reflectance Fourier Transform Infrared Spectroscopy
BC	Bacterial Cellulose
BDS	Broadband Dielectric Spectroscopy
CD	Circular Dichroism
CNC	Cellulose Nanocrystal
DAB	Debye-Andersen-Brumberger
DLS	Dynamic Light Scattering
DMA	Dynamic Mechanical Analysis
DSC	Dynamic Scanning Calorimetry
EDS	Energy-Dispersive X-ray Spectroscopy
EMIM	1-Ethyl-3-Methylimidazolium
FDC	Force-Distance Curve
FTIR	Fourier Transform Infrared Spectroscopy
HBP-24Oct8[COO]$^-$ [PNIPAM]$^+$	Thermo-responsive Hyperbranched Polyelectrolytes with 24 *N*-octadecylurethane Arms and 8 PNIPAM Macrocations
HBPE	Hyperbranched Polyelectrolytes
HBP-OH	Hyperbranched Polyester Polyol
HEX	Hexagonal Cylinder
^{1}H NMR	Proton Nuclear Magnetic Resonance
IL	Ionic Liquid
LB	Langmuir-Blodgett

LBL	Layer-by-Layer
LCST	Lower Critical Solution Temperature
L-PIL	Linear Poly(ionic liquid) with Imidazolium Counterions
MIM	N-methylimidazole
MMA	Mean Molecular Area
MOF	Mean Molecular Area
MW	Metal-Organic Framework
OEG	Oligo(ethylene glycol)
OIL	Oligomeric Ionic Liquid
OSS	Octahedral Silsesquioxane
OSS(N+OH)	Octahedral Silsesquioxane with Tertiary Amino Group
OSS($C_3N^+Br^-$)	OSS-based Ionic Liquid with Ammonium Terminal Group and Short Alkyl Substitute (C_3)
OSS($C_{10}N^+Br^-$)	OSS-based Ionic Liquid with Ammonium Terminal Group and Long Alkyl Substitute (C_{10})
P2VP	Poly(2-vinyl-pyridine)
PAA	Poly(acrylic acid)
PA-K	Hyperbranched Polymeric Sulfonic Acid with Potassium Salt
PAMAM	Poly(amidoamine)
PBDT	Poly(2,2′-disulfonyl-4,4′-benzidine terephthalamide)
PDMAEA	Poly(2-(dimethylamino)ethyl methacrylate)
PE	Polyelectrolyte
PF-KPFM	Peak-Force Kelvin Probe Force Microscopy
PIL	Poly(ionic liquid)
PMMA	Poly(methyl methacrylate)
PNIPAM	Poly(N-isopropylacrylamide)
POSS	Polyhedral Oligomeric Silsequioxanes

PS	Polystyrene
PSS	Poly(styrene sulfonate)
PSSNa	Poly(sodium styrenesulfonate)
QNM	Quantitative Nanomechanical Mapping
S8P8	Hyperbranched Polyelectrolytes with 8 Sulfonate Groups, 8 PNIPAM Macrocations and 24 N-octadecylurethane Arms
S16P16	Hyperbranched Polyelectrolytes with 16 Sulfonate Groups, 16 PNIPAM Macrocations and 16 N-octadecylurethane Arms
SANS	Small-Angle Neutron Scattering
SEM	Scanning Electron Microscopy
TEM	Transmission Electron Microscopy
TF2N or TFSI	Bis(trifluoromethane sulfonyl)imide
TGA	Thermogravimetric Analysis
UV-Vis	Ultraviolet-Visible
VDW	Van Der Waals
XPS	X-ray Photoelectron Spectroscopy
XRD	X-ray Diffraction

SUMMARY

Responsive polymeric materials and structures have received considerable attention due to their abilities to change their morphologies and properties by responding to external stimuli, and potential applications in drug delivery, bio-sensing, bio-imaging, self-healing coatings, and soft robotics. Polymers containing ionic groups, such as polyelectrolytes and poly(ionic liquid)s, are promising candidates for designing unique responsive polymeric nanostructures with diverse morphologies and functionalities. However, it is challenging to program the formation of complex morphologies with adaptive and switchable properties by using polyelectrolytes and poly(ionic liquid)s with simplistic linear architecture and amorphous organization. This research addresses this issue by considering variable macromolecular architecture, well beyond simple linear chains, functionality, and environmental conditions into the assembly of polyelectrolytes and poly(ionic liquid)s.

The ultimate goal of the research is to establish fundamental routes for generating nanostructures with pre-programmed and responsive morphology and properties by controlling the assembly of novel branched polyelectrolytes at solid and liquid interfaces. Accordingly, in the first place, the role of chain architecture and chemical composition on the assembly, interfacial behavior, and complex interfacial morphologies of branched polyelectrolytes is examined. We studied the responsive properties of amphiphilic hyperbranched polyelectrolytes with variable peripheral chemical composition at air-water interface and in Langmuir-Blodgett monolayer at air-solid interfaces. We found that thermo-responsive hyperbranched polyelectrolytes with asymmetric chemical composition and different terminal ionic groups showed unusual morphological transformation from disk to ridge-like structures upon surface compression, which is different from that of traditional amphiphilic block copolymers. Not only morphology and but also mechanical response of their monolayers can be tuned by changing temperature and surface pressure. Secondly, we studied the effect of highly mobile thermo-responsive macro-cations, ionically linked to terminal ionic groups on dynamic assembly of hyperbranched polyelectrolytes. The macrocations can hop between neighboring terminal ionic groups, generating mobile coronas which can contribute to obtaining diverse morphological variation under changing assembling condition. In solution, vesicle or planar structures were formed and changed into chains of spherical structures with increasing temperature or large aggregates with increasing solvent ionic strength. Temperature-induced morphological transition from well-defined disk domains to heterogenous morphologies was also observed in the monolayers at air-solid interfaces. Thirdly, the assembly of star-shaped oligomeric ionic liquids containing inorganic cores and organic shells with alkyl substituents of variable lengths is investigated. The length of hydrophobic alkyl substitutes significantly affects the self-organization in aqueous media and on a solid surface. Surface morphology of the films of the oligomeric ionic liquids was transformed from spherical to

cylinder micelles with decrease in surface adhesion by increasing the length of the alkyl substituents. Finally, we utilized hyperbranched poly(ionic liquid)s as a binding functional component to fabricate functional composite materials. Multiple functionalities of hyperbranched poly(ionic liquid)s enable the generation of multiple physical interactions with 1D cellulose nanocrystals in the network-formed composite materials. The resulting composite ionogel materials show both enhanced mechanical and ion transport properties, which exceed those of traditional electrolyte materials. Thus, the ionogel materials developed in this study can provide a breakthrough to resolve mechanical stability vs ionic conductivity dilemma for developing high-performance electrolyte materials.

Overall, this work provides novel approaches to preparing finely tuned polymer nanostructures with responsive morphology and properties by modulating the assembly of branched polyelectrolytes. This work also offers promising potential of branched polyelectrolytes in the development of novel composite materials with tunable morphologies and unique smart functions, potentially discovering next-generation materials in advanced applications, such as self-healable and self-charged devices, targeted drug delivery, multi-stimuli responsive soft actuators, and switchable optics.

CHAPTER 1. INTRODUCTION

The development of responsive nanostructures with controlled and tunable morphology and properties is critical for demanding applications, including biomaterials, drug delivery, catalysis, sensing and optics.[1,2] Polyelectrolytes (PEs) with ionizable groups in backbone or side chain have shown promise as building block materials to fabricate responsive nanostructures with tailored capabilities. The ionization degree and hence the charge density of PEs can be tuned in a wide range via the solution pH or ionic strength, which enables PEs to form a variety of responsive morphologies. Poly(ionic liquid)s (PILs), a subclass of PEs with ionic liquid moieties, have received increasing attention since the amphiphilic nature of PILs with countless combinations of ionic liquid pairs can help to achieve precise control over structural complexity and ordering in polymers, creating non-traditional morphologies with distinct interior domains. Variation of chain architectures of PEs offers greater control over the conformations, interactions, organization, and final morphologies. There have been invested efforts on synthesizing branched PEs with diverse architectures, such as star, miktoarm star, hyperbranched, and dendritic PEs as well as understanding their self-assembly behavior into complex morphologies in bulk and solution. Unlike linear counterparts, branched PEs can have functionalized branched cores and terminal groups and exhibit pronounced steric repulsions and heterogenous core-shell morphology, all of which can be used to control molecular organization, phase separation and resulting morphologies and properties.

1.1 Assembly of Polyelectrolytes and Poly(ionic liquid)s

1.1.1 Introduction to PEs and PILs and Their Phase Behavior

Polyelectrolytes (PEs) are polymers that are composed of ionizable groups in backbone or side chains. Depending on the type of the ionizable group, PEs can be classified into three groups: cationic, anionic and zwitterionic polyelectrolytes that carry both cationic and anionic groups. PEs can be also divided into strong and weak polyelectrolytes. Strong polyelectrolytes are fully charged over a wide range of pH, and their charge density is

relatively insensitive to pH. On the other hand, weak polyelectrolytes are charged in a smaller pH window, showing pH-dependent charge density (Figure 1.1).[3]

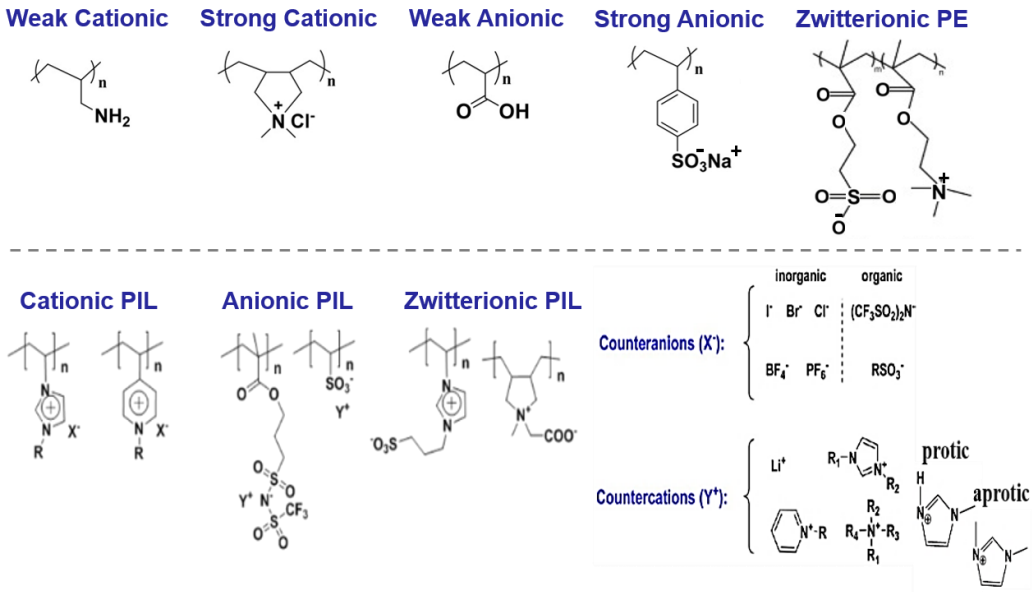

Figure 1.1. Chemical structures of common polyelectrolytes and poly(ionic liquid)s.

Polyelectrolytes can dissociate in a polar solvent and leave a charged chain and counterions in solution. They show peculiar phase behavior compared to neutral polymers due to intra- and intermolecular electrostatic interactions, such as extended chain conformations, a significantly lower critical concentration, and a higher osmotic pressure in solution.[4,5] End-group modification of neutral amphiphilic block copolymers with ionic groups significantly alters intermolecular interactions such as hydrogen bonding and/or dipolar interactions, enhancing the segregation strength between polymer blocks.[6] Therefore, the self-assembly behavior can be modulated by introducing ionic end groups of block copolymers.[7,8] For example, the attachment of one ionic group to the end of poly(ethylene oxide) (PEO) block in amphiphilic block copolymers comprising polystyrene (PS) and PEO resulted in the morphological transition from disordered to ordered morphologies, such as lamellae, cylinders or gyroid (Figure 1.2a).[7] Not only electrostatic interactions but also counterion entropy and local solubility play an important role in phase behavior of polyelectrolytes. For PE-based block copolymers, counterion entropy suppresses phase separation due to the penalty of counterion condensation in the vicinity of the PE block,

and counterion solubility can lead to either suppression or enhancement of phase separation depending on the polarization of surrounding medium.[9,10,11] Thus, the phase diagrams of PE-based block copolymers are shifted compared to those of neutral block copolymers, showing a diverse range of ordered and disordered morphologies, including some of which are normally inaccessible to traditional neutral block copolymers (Figure 1.2b).[12,13]

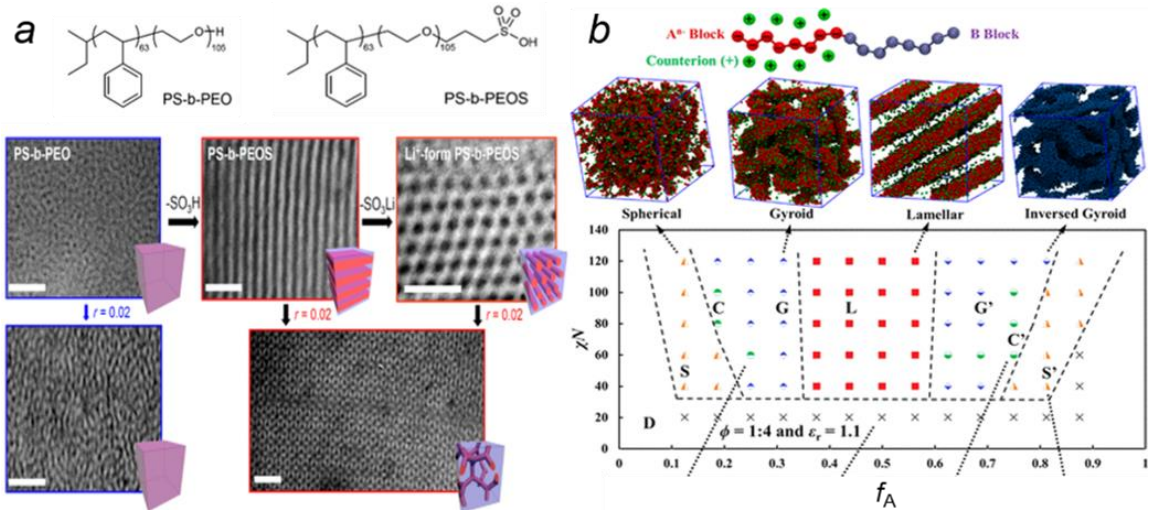

Figure 1.2. Major phases and transitions of diblock polymers without and with sulfonate terminal group (*a*)[7] and a diblock polyelectrolyte aqueous system (*b*).[13]

Poly(ionic liquid)s (PILs) are a subclass of polyelectrolytes where ionic liquid (IL) species are polymerized or incorporated as counterions (Figure 1.1). Ionic liquids are an interesting class of materials due to their unique properties, such as negligible vapor pressure, high chemical/thermal stability and ionic conductivity, wide electrochemical stability widow and non-flammability.[14,15,16,17] The inclusion of IL groups can alter intra- and intermolecular interactions depending on the type of ionic liquids. PILs typically have counterions of hydrophobic character. In case of cationic PILs, common counter-anions are hydrophobic anions such as tetrafluoroborate (BF_4^-), hexafluorophosphate (PF_6^-) or fluorinated amides ($(CF_3CF_2SO_2)_2N^-$ and $(CF_3SO_2)_2N^-$), while halide anions (Cl^-, Br^- and I^-) are commonly used as counter-anions for conventional cationic PEs.[18] It was reported that the doping of acid-tethered block copolymers with ionic liquids composed of imidazoles and hydrophobic $(CF_3SO_2)_2N^-$counter-anions enhanced the thermodynamic incompatibility with the ionophobic polymer block, resulting in the formation of ordered

morphologies. However, as the content of hydrophobic counter-anions increased, repulsive interactions between the anions and polymer chains became predominant and disrupted the ordered morphologies.[19] When the IL with aromatic character is employed, π-type interactions are involved in self-assembly of PIL-containing polymers, forming novel π-stacked structures.[20,21] In fact, various organized morphologies have been generated from PIL-containing polymers due to their peculiar intra- and intermolecular interactions in solution and bulk.[22,23,24,25,26] Non-traditional morphologies with distinct interior domains such as cubosomes and pyramids were obtained via self-assembly of PIL-based copolymers in solution (Figure 1.3a).[27,28,29] Morphological transition from lamellar to a coexistence of lamellar and 3D networks was also found in strongly microphase-separated states of PIL block copolymers (Figure 1.3b).[30]

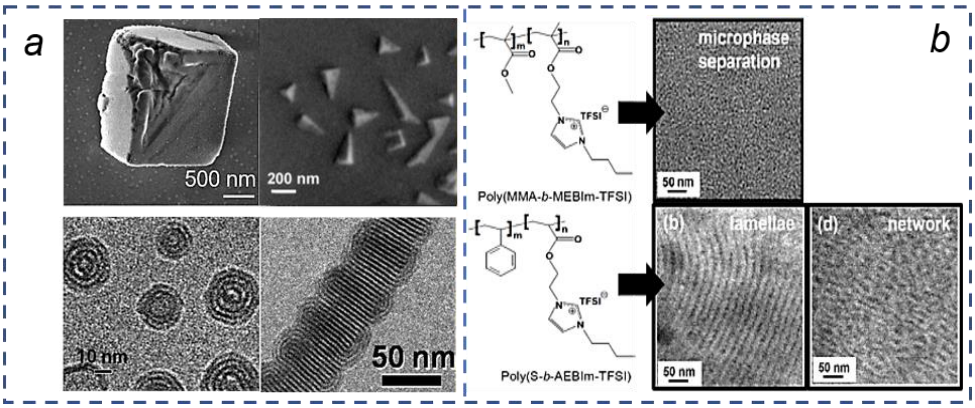

Figure 1.3. (a) self-assembled structures of PILs: cubosomes, pyramids, multilamellar particles, and nanoworms.[27,28,29] (b) chemical structure (left) and TEM images (right) of PIL block copolymers with weak (top) and strong (bottom) microphase separation.[30]

1.1.2 Stimuli-responsive Assembly of PEs and PILs

The presence of ionizable groups and counterions of polyelectrolytes enables them to create responsive nanostructures that can deform their shapes and sizes in respond to variation of external stimuli, such as solvent pH, and ionic strength.[4,31,32] For weak polyelectrolytes, pH is a key parameter to tun their self-assembly behavior and morphology. When the solvent pH is changed, the ionizable groups of weak polyelectrolytes can either accept or donate protons, resulting in ionic/non-ionic transition Such transition influences the hydrophobicity of the polyelectrolyte chains, leading to a change in their

conformation.[33,34] For example, the variation of pH strongly affected the self-assembly and resulting morphology of amphiphilic block copolymers consisting of poly(2-(dimethylamino)ethyl methacrylate) (PDMAEA). At pH 3, tertiary amine groups of PDMAEA are protonated, resulting in the formation of spherical nanoparticles. At pH 7 where the amine groups are partially protonated, diverse morphologies were generated, including spherical nanoparticles, multicomponent vesicles and larger vesicles. At pH 10 where the amine groups are fully deprotonated, a unique vesicle morphology was formed, having a well-structured membrane, which encloses small spherical particles and surrounds an inner vesicle, which either encloses small spherical particles or vesicles in their interior.[35] In addition, increasing the solvent ionic strength (e.g. adding salts) typically induces conformational change of polyelectrolyte chains from extended to collapsed state.[36,37] It has been demonstrated that the salt addition results in a significant decrease in the size of micelles formed from amphiphilic block copolymers containing polyelectrolyte block. This is due to the electrostatic shielding of salt ions on the charged groups, leading to the shrinkage of the micellar corona. [38,39] A rich variety of responsive morphologies have been reported from polyelectrolyte block copolymers, such as spherical, star-like/hairy, crew-cut, and cylindrical micelles, vesicles, lamellar mesophases, and micellar aggregates, at different solvent conditions (Figure 1.4).[40,41,42,43,44,45]

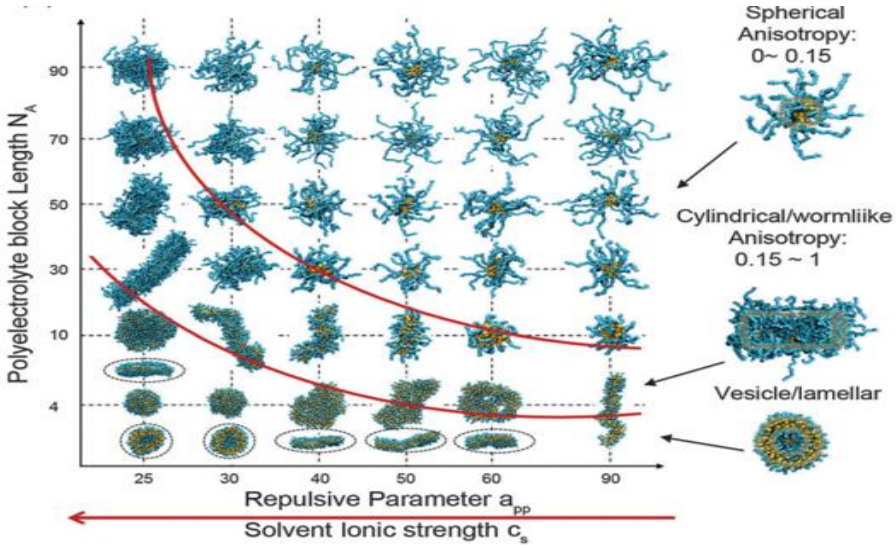

Figure 1.4. Phase diagrams of typical assemblies of polyelectrolyte block copolymers in aqueous media as a function of ionic strength.[43]

1.2 Assembly of Branched Polyelectrolytes and Poly(ionic liquid)s

Branched PEs with various architectures, such as brushes,[46,47] star copolymers,[48,49,50] and hyperbranched molecules,[51,52] have been reported to show distinct phase behavior due to their spatial confinement and complex intra- and intermolecular interactions.[53,54,55] For instance, branched polymers exhibit properties intermediate of those of tenuous chains and soft deformable nanoparticles.[56,57,58,59] Readily controlled diverse functionalities in separate blocks within cores, branches, grafts, and terminal groups of branched polyelectrolytes can facilitate the formation of complex morphologies with multifunctional responsive behavior.[56,60,61,62]

1.2.1 Assembly of Star PEs and PILs

Star PEs are intriguing since they can possess a well-defined composition and dimensionality of arms, promoting the formation of novel colloidal soft nanoparticles with core-shell morphologies.[63,64] Star PEs can form various nanostructures which can dynamically change via external stimuli, such as solution pH, ionic strength or temperature. It was reported that star terpolymers bearing hydrophobic polystyrene (PS) arms and amphoteric poly(2-vinyl-pyridine)-b-poly(acrylic acid) (P2VP-b-PAA) arms exhibited pH-dependent conformations in aqueous media and formed various self-assemblies at different pH conditions. At low pH, inner P2VP segment is protonated and adopts an extended conformation, while outer PAA segment takes a collapsed conformation. The star terpolymers can self-assemble into core−shell unimolecular micelles, worm-like micelles, and multicore large compound micelles (Figure 1.5a). At high pH, deprotonated inner P2VP chains take a collapsed conformation, while outer PAA chains are extended. Multistar aggregates, network-like large assemblies, and finally patchy compartmentalized micelles were formed (Figure 1.5b).[65]

Assembly of miktoarm star PEs bearing chemically distinct arms can result in the formation of nanostructure of increased complexity. The interplay of unlike polymer–polymer interaction parameters and solvents being selective for one or two segments enables the preparation of core-shell-corona structures or core- and corona-compartmentalized aggregates.[66,67,68] For example, miktoarm star PEs consisting of polybutadiene, poly(2-

vinylpyridine) and poly(*tert*-butyl methacrylate) constructed spherical micelles in dioxane, while a mixture of inverted micelles and elongated barrel-like "woodlouse" aggregates were formed in water. The assembly behavior of these PEs can be controlled by the nature of counterion. The addition of iodine increased the ratio of triiodide versus iodide counterions, resulting inf the transformation from spherical micelles to worm-like micelles, their superstructures and woodlouse aggregates with a periodic, multilayered structure (Figure 1.5c).[50]

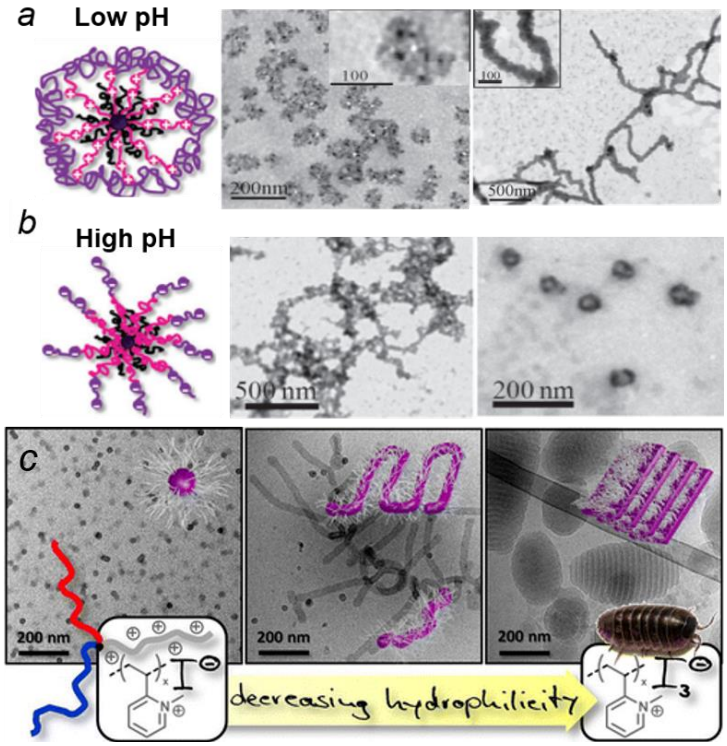

Figure 1.5. Schematic and TEM images of star terpolymers bearing hydrophobic arms and diblock copolymer amphoteric arms (a) below and (b) above isoelectric point in aqueous media.[65] (c) Counterion-mediated morphological transformation of miktoarm star polyelectrolytes.[50]

The incorporation of star-shaped inorganic core with functional groups is an alternative approach to synthesize star PEs. Hybrid inorganic-organic star PEs have advantages over conventional organic star PEs since the introduction of an inorganic core increases thermal, chemical, and mechanical stability of materials.[69, 70, 71] Polyhedral oligomeric silsesquioxanes (POSS) is a common inorganic core used for star PEs. POSS has well-

defined nanometer-sized cage structures with eight reaction sites and can be easily functionalized with various groups, which can react with polymers, resulting in the preparation of star-shaped polymers with well-controlled arm length.[72,73,74,75] The synthesis and assembly of POSS-cored star PEs with stimuli-responsive properties have been reported.[60,76,77,78] For example, star PEs consisting of POSS core and poly[2-(dimethylamino)ethyl methacrylate] arms self-assembled into micelles with a core-shell morphology since the POSS provided a driving force for the self-assembly where the POSS cages formed the crystalline core while the PDMAEMA chains formed the corona. Upon changing solution condition (pH, ionic strength and temperature), complex "micelle-on-micelle" structures were also observed.

Compared to star-shaped PEs, star-shaped PILs have been less explored with a few studies reported [79,80,81,82,83,84] It has been reported that the assembly behavior of star PILs strongly depends on the macromolecular architecture and counterions. For example, layer-by-layer (LBL) films of star PILs containing hydrophobic bis(trifluoromethylsulfonyl)imide (Tf_2N^-) counterions with anionic poly(styrene sulfonate) (PSS) showed unique porous morphology with interconnected networks, which is contrast to the LBL film of linear counterparts with uniform morphology. During the PIL-PSS deposition, as an aqueous solution of PSS is added, the PIL segments immediately contract as controlled by hydrophobic counterions, resulting in the formation of granular and porous morphology.[81]

1.2.2 Assembly of Hyperbranched PEs and PILs.

Hyperbranched PEs are branched macromolecules with randomly branched polyelectrolytes chains.[85] The presence of multiple functional groups of hyperbranched PEs allows for formation of complex morphologies with multifunctional responsive behavior.[86,87,88] For example, hyperbranched PEs bearing a pH-sensitive hyperbranched core and thermoresponsive blocks exhibited morphological variation under changing pH and temperature, forming uni- and multi-micellar aggregates and their fusion.[88] Change in the ionization degree of terminal ionic groups results in the formation of diverse morphologies including worm-like, branched, and curved sheet-like micelles.[89]

In addition, introducing large counterions of different nature can alter the functionality of outer shells, affect hydrophilic/hydrophobic balance, and induce stimuli-sensitive behavior.[90,91,92,93,94,95] For example, the assembly of hyperbranched PEs with fatty acid as macro-counterions significantly depends on the content of fatty acid. With increasing the content of fatty acid, the transformation from micelles to lamellae and to nanospheres occurred.[95] Hyperbranched PEs ionically bound with thermo-responsive poly(N-isopropylacrylamide) (PNIPAM) macrocations also showed morphological transformation from spherical micellar aggregates to vesicles under changing temperature due to low critical solution temperature (LCST) transition of PNIPAM (Figure 1.6a).[96]

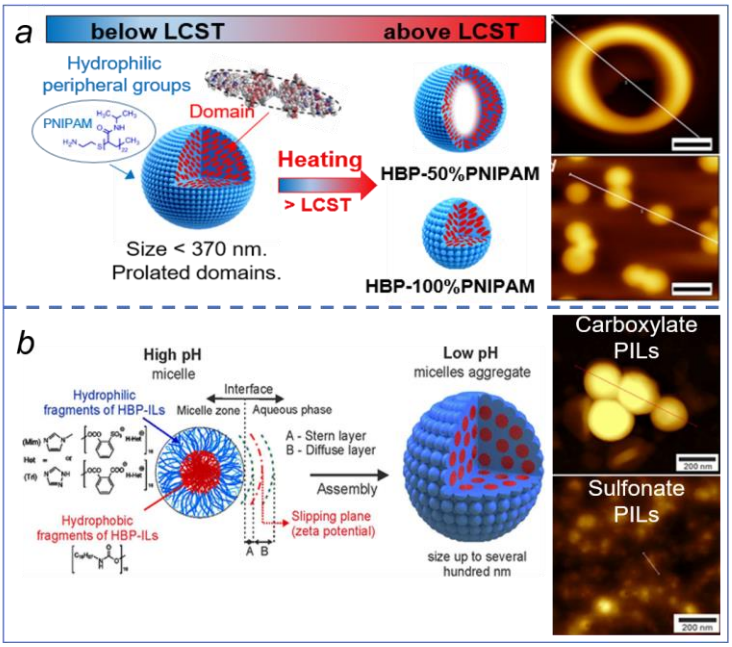

Figure 1.6. Schematic of the assembly of (a) hyperbranched PEs with PNIPAM macrocations below and above LCST and (b) hyperbranched PILs with different terminal ionic groups and counterions (left). AFM topography images of their self-assemblies (right).[96,105]

Hyperbranched PILs have been synthesized with focus on studying their structure-property relationship.[97,98,99,100,101,102,103] Three generations of hyperbranched PILs with 24, 32, and 56 imidazolium terminal groups were synthesized with hexafluorophosphate as counterions. Among these three PILs, the hyperbranched PILs with 56 imidazolium groups exhibited the highest ionic conductivity of 2.4 x 10^{-4} S cm^{-1} at 30 ^{o}C, indicating that the

ionic transport properties of hyperbranched PILs can be tuned by varying their ionic liquid terminal groups.[104] Amphiphilic hyperbranched PILs were synthesized with different terminal ionic groups (carboxylate vs sulfonate) and counterions (imidazolium vs triazolium). These amphiphilic hyperbranched PILs formed core-corona micelles with the size of 12-16 nm at pH 11.6. On the other hands, the assembly of the hyperbranched PILs at pH 5.2 depends on the type of terminal ionic groups due to higher degree of ionization of sulfonate groups. The hyperbranched PILs with carboxylate groups formed large micellar aggregates with the size of 150-200 nm, while the hyperbranched PILs with sulfonate groups constructed micelles with the size of 25-40 nm (Figure 1.6b).[105]

1.2.3 Assembly of other branched PEs and PILs

Other than hyperbranched and star architectures, there are many additional architectures introduced to polyelectrolytes. For one, polyelectrolytes with brush structures, called as bottlebrush polyelectrolytes, have been synthesized with a large number of short grafted chains which are ionizable. The bottlebrush polyelectrolytes are of particular interest in the field of the polymer assembly since the response of their short ionizable chains to environmental conditions can cause a significant structural change. In a good solvent without salt, the ionizable chains extend away from the grafting surface much more strongly than neutral chains, while the addition of salts results in the substantial shrinkage of the chains.[106,107] Numerous studies have reported conformational and morphological transformation of bottlebrush polyelectrolytes induced by external conditions, such as salt addition and change in solvent pH.[108,109,110, 111,112,113,114,115] For example, the combination of bottlebrush poly(sodium styrenesulfonate) (PSSNa) with tetravalent counterions resulted in the formation of polyelectrolyte/counterion complexes. The morphological transition from worm-like to curled structures was observed with increasing the concentration of counterions (Figure 1.7a).[110] Similarly, it was reported that the morphology interpolyelectrolyte complexes formed by PSSNa with linear anionic polyelectrolytes can be tuned by adjusting the charge ration between two polyelectrolytes. With increasing the content of PSSNa, brush-like structures were transformed to intermediate, pearl-necklace structures and then to fully collapsed spheres.[111]

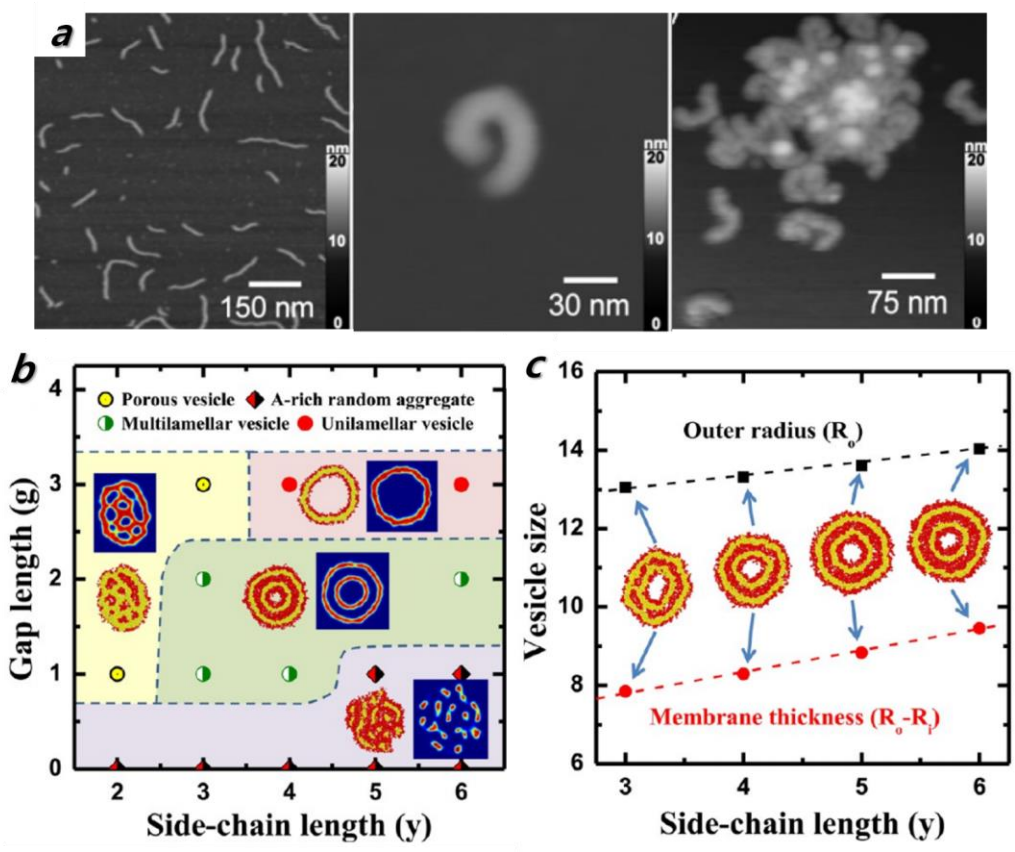

Figure 1.7. (a) AFM images of PSSNa bottlebrush polyelectrolytes showing morphological variation.[110] (b) Morphological phase diagram and characteristic snapshots of assemblies formed by amphiphilic bottlebrush polyelectrolytes as function of side chain length and gap length (reciprocal to side chain density) and (c) Variation of the vesicle size as function of side chain length.[113]

In addition to external conditions, the length and density of side chains play a critical role in determining the morphology of bottlebrush polyelectrolytes.[113,116] The computational study for bottlebrush polyelectrolyte composed of hydrophobic backbone and hydrophilic, polyelectrolyte side chains revealed that various morphologies can be obtained by varying the length and density of side chains, such as random aggregates, unilamellar vesicles, multilamellar vesicles and porous vesicles (Figure 1.7b). Further control on the size and overall membrane thickness of multilamellar vesicles can be also achieved by adjusting the side chain length, attributed to the change of hydrophilic side-chain beads between two hydrophobic layers of the membrane (Figure 1.7c).[113]

Moreover, polyelectrolyte dendrimers have attracted great attention due to the presence of multiple functional groups easily accessible and located on the surface of the macromolecules. They can interact with oppositely charged molecules or polymers, forming diverse morphologies.[117,118,119,120,121] For example, the self-assembling features of 2nd-generation poly(amidoamine) (PAMAM) dendrimers ionically functionalized with hydrophobic fatty acids as counterions can be modulated by changing the content of fatty acids. Spherical micelles was formed with low fatty acid content and merged to form lamellae and then nanospheres with a lamellar structures (Figure 1.8a).[119] It was also reported that association of PAMA dendrimers with anionic organic dyes can create diverse morphologies, including micelles, ellipsoids, cylinders, and flexible cylinders, depending on the type of organic dyes as well as the generation of PAMA dendrimer (Figure 1.8b).[120]

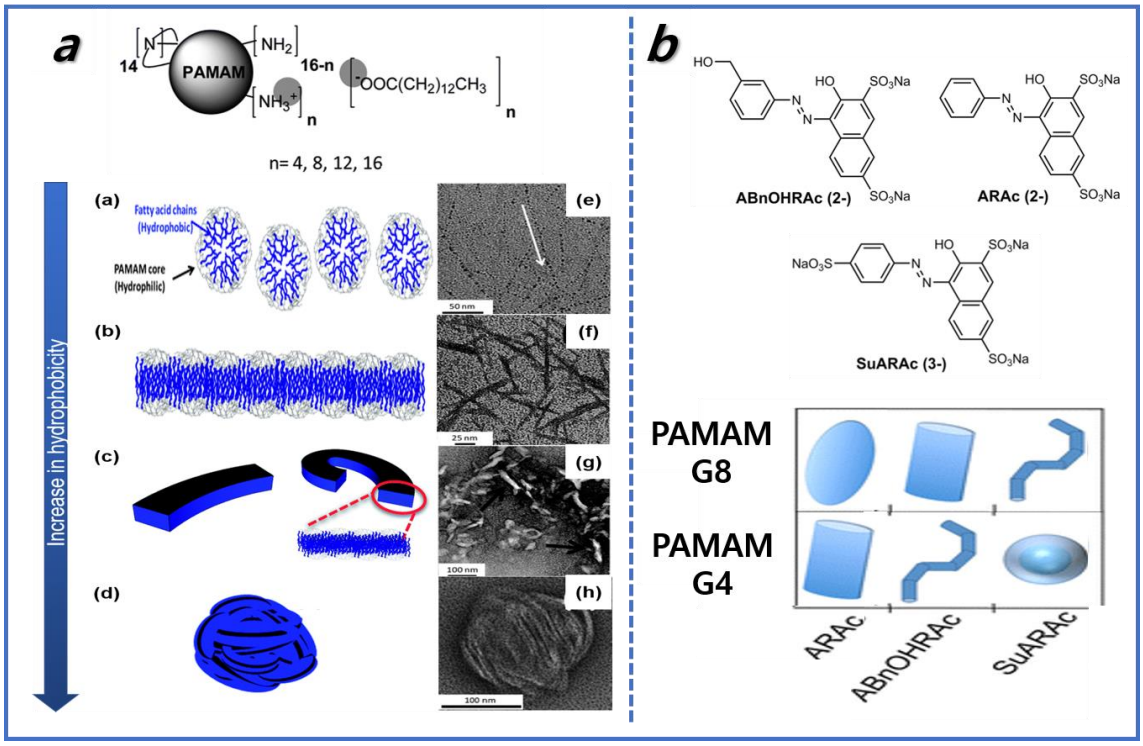

Figure 1.8. (a) Morphology transition of PAMAM dendrimers with increasing the content of hydrophobic fatty acids.[119] (b) Morphological variation of PAMAM dendrimers combined with anionic organic dyes.[120]

In comparison to dendritic polyelectrolytes, the synthesis and assembly of dendritic poly(ionic liquid)s have been rarely explored.[122,123,124] Among very few studies, it was

reported that highly fibrous spheres with a size of ~300 nm were formed by dendritic poly(ionic liquid)s immobilized on nanosilica combined with ruthenium(II) dimer. These spheres exhibited corrugated radial anatomy which creates open conical holes, facilitating the chemical transport and reaction.[125]

1.3 Assembly of Polyelectrolytes and Poly(ionic liquid)s in Ionic Liquids

The assembly of polymers in ionic liquids (ILs) is reported to be distinct from that in conventional solvents since incorporating ionic liquid moieties introduces additional interactions such as Coulombic forces. Many studies have investigated the effect of ionic liquids on morphology of block copolymers.[126,127,128,129] Ionic liquids are selectively soluble with a more polar block. This selective partitioning of ILs increases the swelling and polarity of the resident block and enhances the segregation strength between dissimilar blocks, which decreases the minimum achievable long period and hence domain size.[130] For example, addition of bis(trifluoromethane sulfonyl)imide (Tf_2N)-based ILs into polystyrene-b-poly(methyl methacrylate) (PS-b-PMMA) induced disorder-to-order transition, creating domains with sub-10 nm size (Figure 1.9a).[131,132]

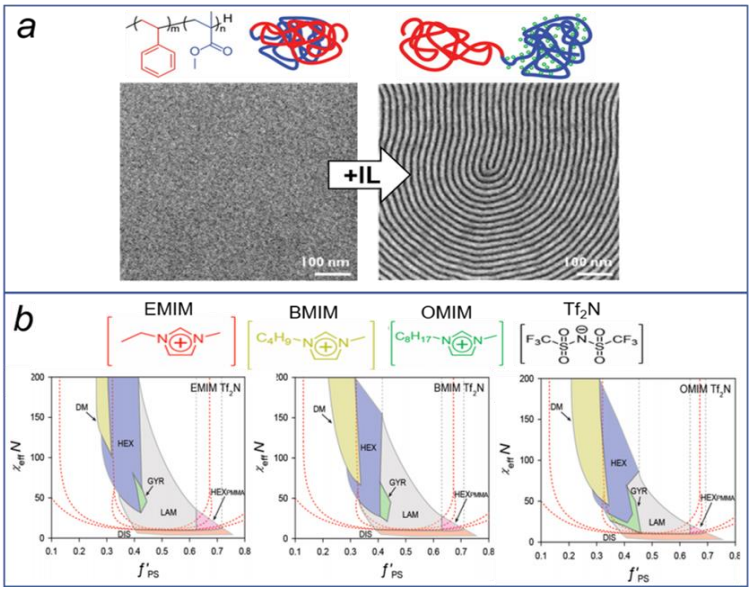

Figure 1.9. (a) Disorder-to-order transition of PS-b-PMMA upon addition of ionic liquids.[132] (b) Phase diagrams of PS-b-PMMA in ionic liquids. The red dotted lines show the mean-field theory phase boundaries for diblock copolymer melts.[133]

The phase diagrams of PS-b-PMMA in ILs showed shifted phase boundaries with a gyroid phase, which is difficult to access in neat PS-b-PMMA. The phase boundaries shifted toward lower values of the effective PS volume fraction by increasing the length of alkyl groups of IL cations (Figure 1.9b). This shift is attributed to the increase in van der Waals interactions, which reduces relative contribution of Columbic interactions and thus decreases the degree of swelling of the PMMA domains.[133]

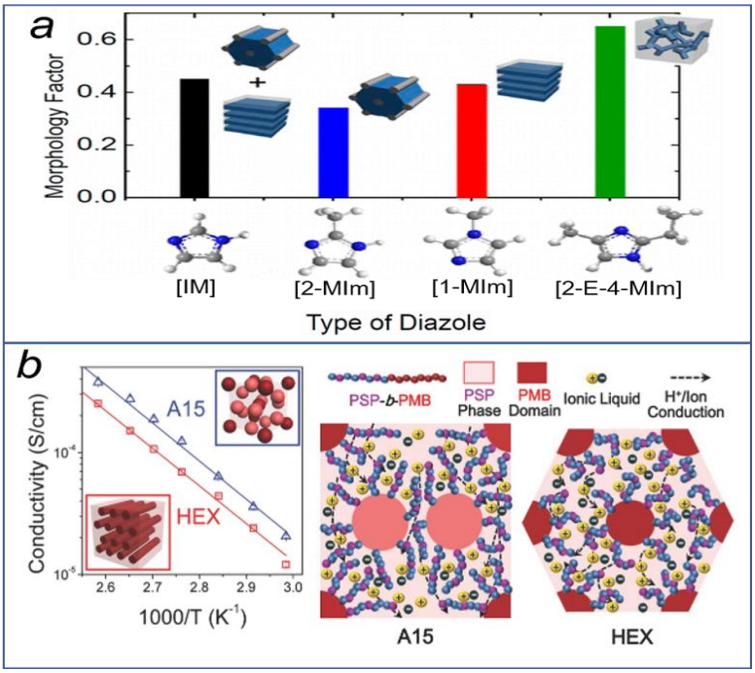

Figure 1.10. (a) Morphology of poly(styrenesulfonate-b-methylbutylene) with different ILs.[141] (b) Morphology and ionic conductivity of IL-incorporated poly(styrenephosphonate-b-methylbutylene) (left) and schematic illustration of ion-conduction pathways (right).[140]

The assembly of polyelectrolyte block copolymers in the presence of ionic liquids have been studied with focus on morphology-transport relationships in polymer/IL composites.[134,135,136] Ionic liquids exclusively reside in the PE block and increase the segregation strength between blocks, thus modifying the assembly behavior of PE block copolymers.[137,138,139,140] For example, the addition of different ILs into poly(styrenesulfonate-b-methylbutylene) copolymers resulted in various ordered morphologies, such as lamellar, hexagonal cylinder, and gyroid, attributed to the dissimilar

strength of ionic interactions between ILs and sulfonate groups, depending on the type of ILs (Figure 1.10a).[141] In addition, ionization level of polyelectrolytes significantly affects the assembly and resulting morphology of PE block copolymers by controlling the amount of the absorbed IL on PE block.[139] For instance, IL-incorporated poly(styrenephosphonate-b-methylbutylene) copolymers formed a series of ordered morphologies, such as lamellae, gyroid, hexagonal cylinder (HEX), body-centered cubic, and A15 lattice, in the absence and presence of ionic liquids. Small change in phosphonation level from 30% to 38% led to morphological transition from HEX to A15 lattice while enhancing ionic conductivity owing to a well-defined 3D symmetry of A15 lattice (Figure 1.10b).[140]

1.3.1 Ionogels

The development of solid and quasi-solid polymer/ionic liquid composite materials is a real breakthrough in the field of energy storage/conversion applications since reformulating liquid-state electrolytes into the solid form is a key to circumvent potential safety concerns due to viscous fluidic nature of the liquid-state electrolytes. The solid and quasi-solid composites can be formed by swelling polymer in an ionic liquid or mixing the polymer and ionic liquid together with a co-solvent which is subsequently removed. This special class of materials is referred to as "ionogels".[142] Ionogels combines the desired properties of IL and solid-state matrices, such as high ionic conductivity and mechanical stability. A majority of ionogels reported to date have been prepared by using traditional neutral polymers, such as poly(ethylene oxide) and poly(vinylidene fluoride-co-hexafluoropropylene), in relation to their ability to solvate ionic liquids.[143] Even for the polymers which have complete miscibility with ionic liquids, there is a grand challenging associated with the plasticizing effect of ionic liquids which results in the loss of mechanical stability on increasing the IL loading.[144] Therefore, the development of ionogels with both high ionic conductivity and mechanical resistance is a key to expand the range of potential application of ILs, such as solid-state electrolytes for electrochemical applications and novel functional materials in the fields of sensors, display devices, catalysts, and separation.[145]

Since there is an inverse relationship between ionic conductivity and mechanical strength, highly conductive ionogels have been obtained only at the expense of mechanical strength.[146147] One approach to prepare ionogels with enhanced mechanical and ion transport properties is the utilization of block copolymers consisting of an ion-conducting block and a rigid block. However, most ionogels prepared from block copolymers show insufficient ionic conductivity and low mechanical strength which cannot satisfy the requirements for solid batteries, restricting the practical use of the ionogels.[148,149,150,151] As an alternative, ionic polymers have been explored to produce a supporting matrix for ionogels.[152,153,154] For example, the ionogels formed by zwitterionic copolymers exhibited remarkable room-temperature ionic conductivities above 1 mS cm^{-1} and compressive elastic moduli in the MPa range (Figure 1.11a-b).[154]

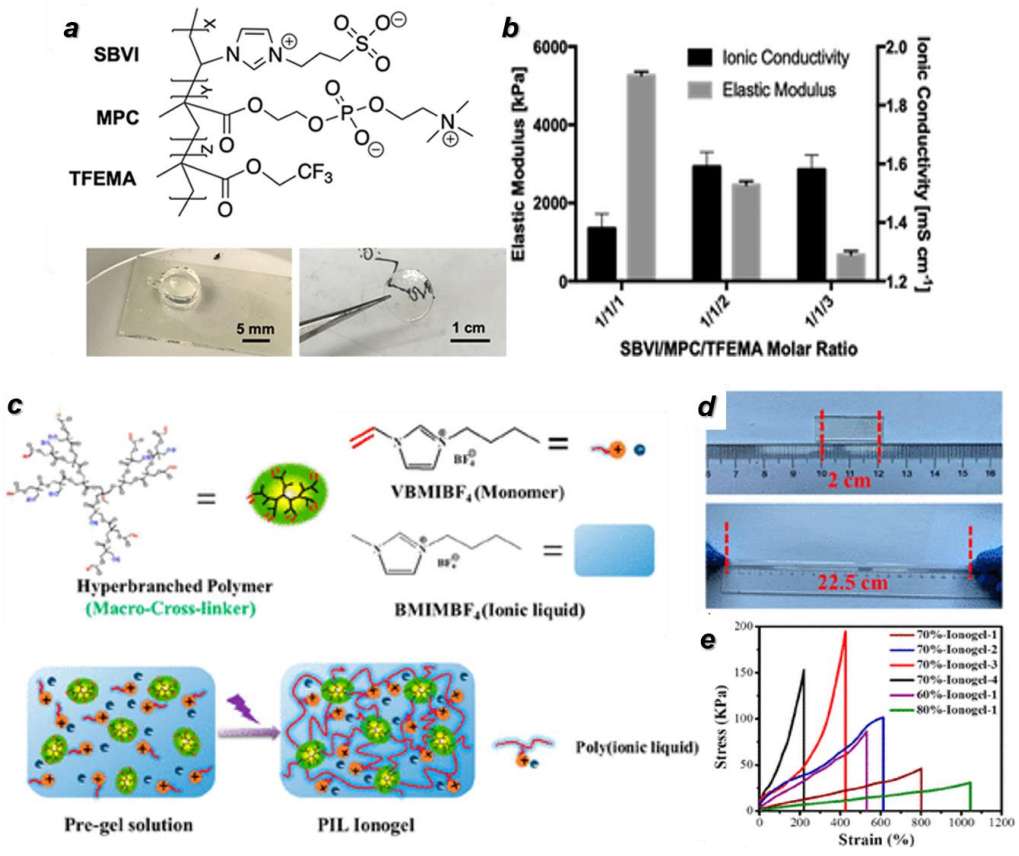

Figure 1.11. (a) zwitterion polymer-based ionogels and (b) their ionic conductivity and elastic modulus.[154] (c) poly(ionic liquid)-based ionogels, (d) a photo of the ionogel showing superior mechanical flexibility and (e) stress-strain curves of the ionogels.[158]

While branched polyelectrolyte with multiple functionalities have numerous opportunities to generate network morphologies which can be used as a supporting matrix for ionogels and create interactions with ionic liquids, the use of branched polyelectrolytes for ionogels has been rarely discussed to date with few studies reported on ionogels prepared with linear poly(ionic liquid)s.[155,156,157] A recent study demonstrated the fabrication of stretchable ionogels consisting of cross-linking network based on linear poly(ionic liquid) with hyperbranched polymers as macro-cross-linkers (Figure 1.11c). The resulting ionogels possess outstanding mechanical flexibility (>1000%) and high room-temperature ionic conductivity up to 5.8 mS cm^{-1}, making them attractive as high-performance strain sensors (Figure 1.11d-e).[158]

1.3.2 Ionogels Reinforced with Nanofillers

High ionic liquid loading is critical to produce highly conductive ionogels but reduces mechanical stability of the ionogels due to plasticizing effects of ILs. The inclusion of nanofillers in the ionogels permits the improvement of the mechanical resistance arising from numerous intermolecular interactions including hydrogen bonding, van der Waals and electrostatic interactions between the polymer, nanofillers and ionic liquid. Polymer ionogels reinforced with inorganic nanofillers (carbon, metal, metal oxide and silica nanofillers) have been widely fabricated and shown enhanced mechanical strength without lowering ionic conductivity.[159,160,161,162] For example, the incorporation of TiO_2 nanoparticles as nanofillers enhanced the mechanical properties of the ionogel since TiO_2 nanoparticles provided cross-linking sites. Indeed, as the content of TiO_2 nanoparticles increases from 0.2 wt% to 1 wt%, compressive modulus of the ionogel increased.[161] Various biopolymers such as cellulose and chitosan have been also utilized as reinforcement in ionogels to improve mechanical strength.[163,164] For example, it was reported that the addition of a small amount of chitosan (3 wt%) increased compressive strength of the ionogels five times since hydrogen bonding interactions of chitosan reinforced the three-dimensional network of the ionogel.[165]

1.3.3 Cellulose Nanocrystals-based Ionogels

In addition to reinforcement, nanocellulose can be used as supporting scaffolds for ionogels.[166] Typical preparation of cellulose-based ionogels involves dissolution and reconstitution of cellulose in Ionic liquids.[160,167,168] However, this method results in loss of inherent structural integrity, yielding fragile and thermosensitive gels with lack of sturdiness. Cellulose-based ionogels can be also formed by entrapping ionic liquids into readily formed cellulose network structure without dissolving cellulose. For example, bacterial cellulose (BC) ionogels were prepared using a solvent exchange method where water in BC hydrogels is exchanged to volatile organic solvent (e.g., ethanol) which is subsequently evaporated and eventually to ionic liquids. BC ionogels had high mechanical strength and flexibility since the web-like structure and high crystallinity of the host BC were preserved within the ionogels.[169]

Moreover, cellulose nanocrystals (CNCs) can provide a mechanically robust host matrix for ionogels due to their capability of forming a nanoscale network structure and their inherent, high mechanical properties.[170,171] The presence of surface hydroxyl and sulfate groups of CNCs enable them to form physically cross-linked networks by mixing with additives and polymers.[172,173] While multifunctional CNC ionogels can be formed by integrating CNCs with functional substances, current available studies have focused on CNC hydrogels with little attention paid on CNC ionogels. For example, integration of CNCs and thermo-responsive polyelectrolyte terpolymer, poly(di(ethylene glycol) methyl ether methacrylate)-*rnd*-poly(oligo(ethylene glycol) methyl ether methacrylate)-*rnd*-poly(2-aminoethyl methacrylate) resulted in the formation of hydrogels with LCST behavior.[174] CO_2-switchable CNC hydrogels were also prepared from the CNC suspension with imidazole added where the reversible transformation of the imidazole to imidazolium ion occurred in presence and absence of CO_2.[175]

It was reported that CNCs grafted with PILs self-assembled a three-dimensional interpenetrating network in ionic liquids, which served as a supporting scaffold for ionogels. The mechanically strong CNC skeletons enhanced the mechanical properties of the ionogels. The grafted PILs associated with IL formed a continuous ion conduction domain to facilitate effective ion transport (Figure 1.12a-c). Therefore, the resulting ionogels exhibited exceptional ionic conductivity and low activation energies, close to those of

PIL/IL ionogels which had lower mechanical stability (Figure 1.12d).[171] In total, there are a wide range of opportunities to form ionogels with enhanced mechanical and ionic transport properties as well as responsive behavior by employing CNCs as mechanically robust scaffolds and polyelectrolytes as ion-associating and functional domain building block materials.

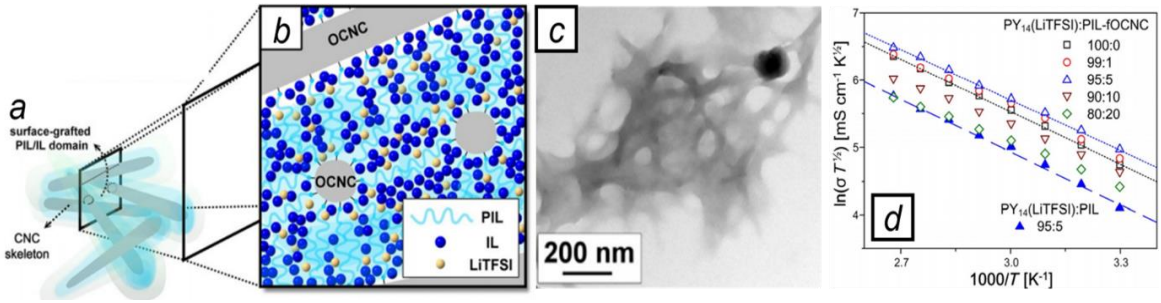

Figure 1.12. (a,b) Schematic illustration of self-assembly of PIL-functionalized CNCs (PIL-fOCNC) in an ionic liquid. (c) TEM image of PIL-fOCNC. (d) Ionic conductivity vs temperature of IL/PIL-fOCNC and IL/PIL composites.[171]

CHAPTER 2. RESEARCH GOALS, TECHNICAL OBJECTIVES AND DISSERTATION OVERVIEW

Although significant efforts have made on the synthesis and assembly of branched polyelectrolytes, there are still several critical issues to be addressed to generate responsive nanostructures with pre-programmed complex morphologies and multifunctional properties from branched PEs.

First, comprehensive understanding of **the role of branched architecture and interplay of core-arm functionality on the assembly of branched polyelectrolytes** is not achieved yet due to the complexity of interactions and conformations of branched PEs. It is important to note that going beyond simple linear architecture makes polymer assembly complicated and difficult to predict given very challenging and complex component-structure relationships in macromolecular structures bearing variable cores, arms, and terminal groups with virtually unlimited compositional combinations.

Second**, the presence of macrocation and anions as well as labile chain grafting are critical for modifying structure-morphology relationship in polyelectrolytes** which remain largely unexplored to date. Instead, there have been many studies for developing an understanding toward unveiling the effect of traditional small counterions on the assembly of polyelectrolytes with less attention paid on the role of macroions that can drive hierarchical assembly arising from the balanced electrostatic interactions of ionic polymers with oppositely charged macroions and the resulting multiplex formation.

Third, as the assembly of branched polyelectrolytes is affected by environmental conditions such as solvent natures and temperature, not only elaborate design of polymer architecture and functionalities but also **careful control of environmental conditions are challenging requirements for realizing dynamic assembly of branched PEs** where their self-assembly behaviors are controllably initiated and terminated via external conditions.

Lastly, **the potential of exploiting branched polyelectrolytes for producing novel functional composites** has been explored only occasionally. Although branched PEs are

capable of assembling into well-defined, compartmentalized structures with multifunctional responsive behavior, which are very attractive in emerging applications such as drug delivery, controlled transport, and self-healing, the majority of studies reported to date have focused on integrating linear polyelectrolytes with functional substances to form novel composite materials with little attention paid on employing branched PEs, which can unlock the next-generation composite materials by offering novel properties and functions.

2.1 Research Goals

The primary goal of this work is to establish fundamental predictable routes for generating nanostructures of complex morphologies with multifunctional responsive behavior and tunable physical properties by controlling the assembly of branched polyelectrolytes on different solid-liquid and liquid-air interfaces, under different assembling conditions, and in multi-phase states.

This work aims to elucidate the role of polymer architectures, functionalities, and environments (stimuli, additives, solvents, and substrates) on the assembly of branched polyelectrolytes, which all afford control over functional and amphiphilic balance (Figure 2.1). The *main hypothesis of the proposed research* is that branched macromolecular architecture with multiple terminal functionalities can be leveraged to mediate the organization of polyelectrolytes and poly(ionic liquid)s and guide their assembly into a variety of domain morphologies, some of which that are distinct from the discrete nanostructures encountered from linear counterparts. The complex organized morphologies of branched PEs are evaluated in connection to their physical properties, including phase state, mechanical and viscoelastic behavior, and ion transport.

This research goal is divided into the following research tasks with specific objectives:

Objective 1. Unveil **the role of chain architecture and chemical composition on the assembly, interfacial behavior, and resulting morphologies** of novel branched polyelectrolytes and poly(ionic liquid)s.

Branched polyelectrolytes with different ratios of hydrophobic and hydrophilic arms and types of cores, ionic terminal groups and counterions are explored to control phase separation and resulting morphologies. In particular, the role of **asymmetric composition** of branched PEs is investigated to facilitate the formation of non-spherical morphologies. The **variation of terminal ionic groups, counterions and macroions** is employed in this research as a tool for modifying functional and amphiphilic balance and thus obtaining prospective pre-programmed complex morphologies beyond symmetric/spherical organization.

Objective 2. Exploit the branched polyelectrolytes with stimuli-responsive macroions as active building blocks for generating **multifunctional, responsive polymer nanostructures via dynamic self-assembly with on-demand molecular organization transformation.**

The assembly and morphology of branched polyelectrolytes containing **stimuli-responsive macroions** are investigated with the corresponding phase transition at different interfaces. Understanding the reorganization of intermolecular interactions and micellar shapes/orientation/separation caused by intramolecular transformation under external stimuli is critical for establishing fundamental mechanisms of dynamic self-assembly of branched PEs where their self-assembly can be manipulated via external conditions, resulting in forming diverse, **responsive interfacial morphologies**.

Objective 3. Exploit the mechanisms of organization of branched polyelectrolytes to **develop PE-nanocellulose ionogels with novel mechanical and ion transport properties.**

The assembly behavior of branched polyelectrolytes with cellulose nanocrystals is studied to produce mechanically robust and ion conducting supporting matrices for ionogels. The relationships between morphology, microstructure, and interfacial interactions of the ionogels to their physical properties are examined in order to unlock novel mechanical and

ion transport performance and expand the potential applications of novel functional multi-phase materials with inclusion of branched PEs.

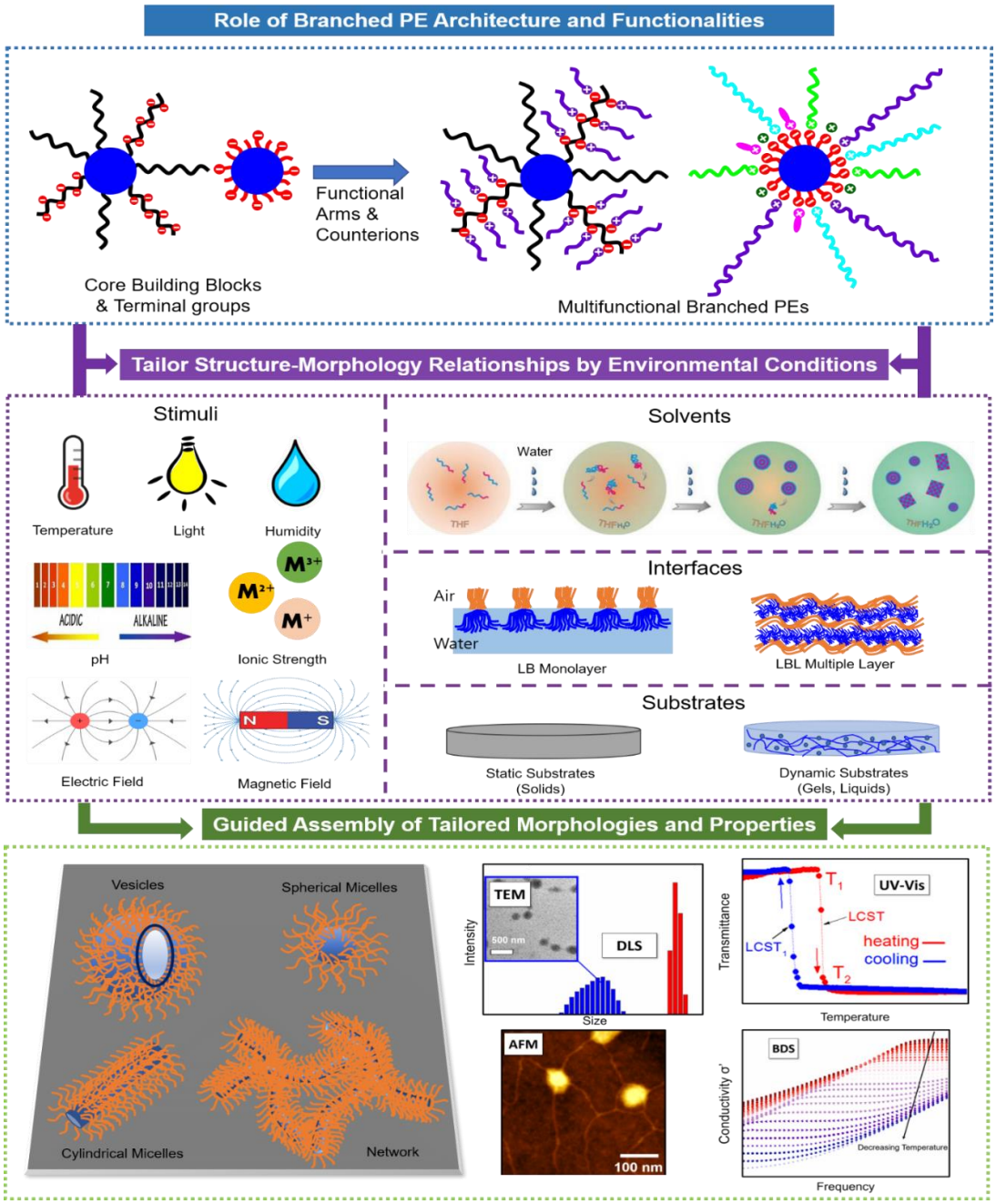

Figure 2.1. Outline of research tasks. The structure-morphology-property relationships of branched polyelectrolytes to be addressed: molecular architecture and functionality (top), environmental conditions (middle), and diverse morphologies and functional properties (bottom).

2.2 Technical Objectives

This research is conducted with prospective molecular architectures, functionalities, and conditions in a step-by-step approach for responsive nanostructures with tunable morphologies and properties and for forming multifunctional nanocomposites with novel mechanical and ion transport properties.

Task 1. Understanding the role of chain architecture and chemical composition on the assembly, interfacial behavior, and complex interfacial morphologies of branched polyelectrolytes.

Branched polyelectrolytes bearing diverse functionalities are synthesized by varying type of cores and terminal groups and ratios of hydrophilic and hydrophobic arms and introducing stimuli-responsive macroions (Figure 2.2). For the synthesis of hyperbranched polyelectrolytes, 3rd generation hyperbranched polyester polyol with 32 hydroxyl groups is selected as an initial core, which allows for wide compositional widow for terminal and pendant groups by exploring different branches. *N*-octadecylurethane and PNIPAM are exploited as hydrophobic arms and hydrophilic macrocations, respectively. On the other hands, polyhedral oligomeric silsesquioxanes (POSS) is chosen for synthesizing star-shaped oligomeric ionic liquids. Aliphatic tertiary ammonium groups with variable lengths of alkyl substitutent is introducted in an organic shell, providing various peripheral hydrophilic-hydrophobic balance.

The selection of chemical composition is based upon the analysis of the differences in solubility parameter, δ which reflects the dominating enthalpic contribution to the interaction parameter, χ_{12}. The solubility parameter of 3rd generation hyperbranched polyester polyol core is 14.9 MPa$^{1/2}$, while POSS has a higher solubility parameter of 20.6 MPa $^{1/2}$.[176, 177] The solubility parameter for the aliphatic and PNIPAM chains is ~17 MPa$^{1/2}$ and ~23 MPa$^{1/2}$, respectively. [178 , 179] Therefore, it is expected that hyperbranched polyelectrolytes containing hydrophobic octadecylurethane arms and hydrophilic PNIPAM macrocations promote weak and strong segregated states. Variation of ratios of hydrophilic and hydrophobic peripheral composition would create hierarchical complexity in segregated states, tailoring morphologies in a wide range from poorly organized

morphologies in weak segregated state to discrete ordered morphologies in strong segregated state.

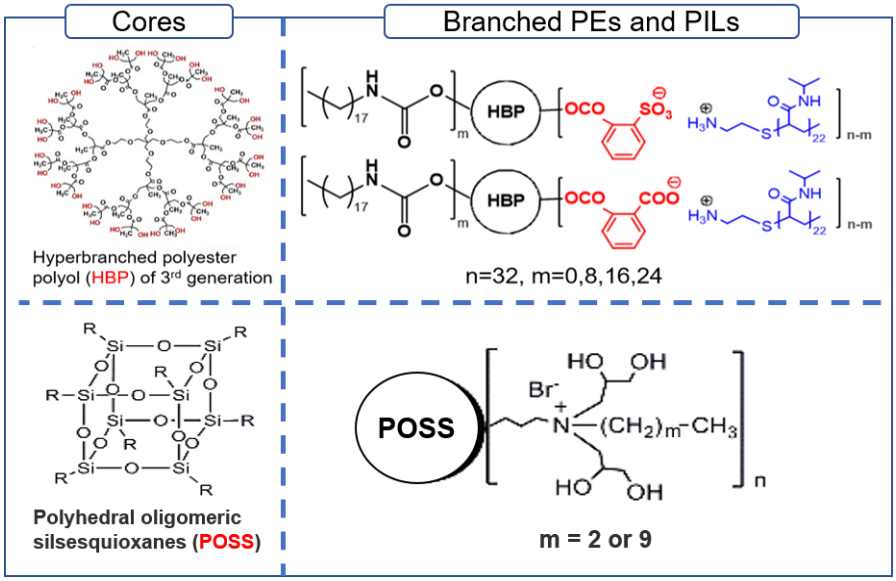

Figure 2.2. Chemical structures of the initial core and branched polyelectrolytes studied in this research.

Task 2. Elucidating the role of highly mobile thermo-responsive macrocations on the dynamic assembly of branched polyelectrolytes.

The presence of thermo-responsive PNIPAM macrocations permits fine control over the hyperbranched polyelectrolyte assemblies. Firstly, due to the LCST transition of PNIPAM, the assembly behavior of the hyperbranched polyelectrolytes can be controlled by adjusting temperature.[96] In addition, mobile ionic bonding of the macrocations brings an intriguing possibility of having tailored dynamic assembly behavior in different environmental conditions, unlike static covalent bonding (e.g. dynamic association and disassociation of macrocations under changing ionic strength and pH), which offers the potential for forming diverse responsive morphologies.

Task 3. Developing ionogels with novel mechanical and ion transport properties by using composites of branched PILs and cellulose nanocrystals as a supporting matrix.

Branched poly(ionic liquid)s are complexed with cellulose nanocrystals (CNCs) to produce mechanically strong and ion-conducting matrix for entrapping a large amount of ionic liquids. The selection of CNCs is based on the high mechanical properties and nanoscale network forming capability of CNCs and the presence of surface functional groups (hydroxyl and sulfate groups) that enable CNCs to make strong interactions with ionic liquids and PILs, all which improve mechanical stability of the ionogels (Figure 2.3).[180,181,182,183,184] The robust percolating CNC/PIL networks can serve as the supporting matrix with continuous ionophilic channels.

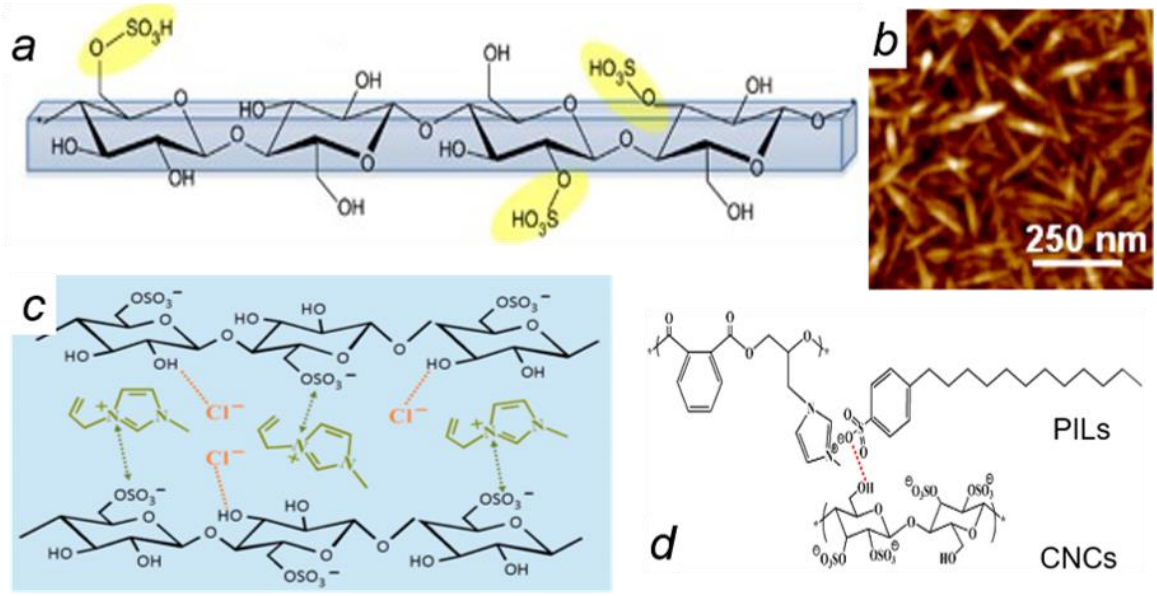

Figure 2.3. (a) Chemical structure of CNCs prepared via sulfuric acid hydrolysis. [182] (b) AFM topography images of CNCs.[183] Schematic illustration of interactions with CNCs and ionic liquids (c)[183] and poly(ionic liquid)s (d)[184].

In summary, this study focuses on understanding the assembly behavior of functional branched polyelectrolytes to establish predictable routes for generating nanostructures with tunable morphologies and physical properties. This research task addresses significant fundamental questions of how polymer architecture and chemical composition affect the assembly behavior of branched polyelectrolytes in solutions, at different interfaces and in condensed state and responsive properties of their assembled structures.

In addition, exploiting these functional branched polyelectrolytes as emerging building blocks provides a new approach for developing multifunctional composites with enhanced properties. In this regard, we elucidate the principles of organization for branched polyelectrolytes and poly(ionic liquid)s with cellulose nanocrystals for fabrication of shape-persistent gel electrolyte materials with a combination of both enhanced mechanical stability and high ionic conductivity, promising for energy harvesting and storage, gas separation, and ion-exchange membranes, and so on.

2.3 Organization and Composition of Dissertation

Chapter 1 is a critical review of the structure of polyelectrolytes with linear and branched architectures, their assembly as well as functional composites generated via ionic interactions, which defines the state-of-art in relevant research field.

Chapter 2 outlines the goals and objectives of this dissertation. It also contains an overview of the organization of the dissertation, and brief description of each chapter.

Chapter 3 describes the major experimental techniques used throughout the work of this dissertation, which includes polymer synthesis, film deposition and comprehensive materials characterization. In several subsequent chapters, the experimental techniques are supplemented with specific protocols used for the particular studies presented.

Chapter 4 is the study on the interfacial properties and assembly of thermally responsive hyperbranched polyelectrolytes with carboxylate terminal groups at air/water interface. It also describes temperature-induced transformation of morphology and mechanical property distribution of the monolayers of the PEs.

Chapter 5 is the study on the assembly of thermally responsive, sulfonate hyperbranched polyelectrolytes with variable peripheral composition in aqueous media and at air/water interface, which provides a significant insight into the detailed conformational changes mediated by ionically tethered macrocations with high mobility.

Chapter 6 is the study on the synthesis and assembly of star-shaped oligomeric ionic liquids containing inorganic cores with variable alkyl substituents in their organic shells,

which can make conclusions on how the variation of core-shell composition affect the morphology as well as mechanical properties of polyelectrolyte films.

Chapter 7 is about the assembly of hyperbranched poly(ionic liquid)s with cellulose nanocrystals, resulting in the formation of PIL/CNC composites used as mechanically strong, ion-conducting supporting matrices for ionogels. The PIL/CNC ionogels have both high elastic modulus and high ionic conductivity simultaneously.

Chapter 8 provides general conclusions for the overall work in the dissertation with a focus on broad impact and prospective future research directions.

CHAPTER 3. EXPERIMENTAL TECHNIQUES AND MATERIALS

3.1 Materials: Composition and Chemistry

Materials used during the course of this study are acquired from our collaborators. Branched polyelectrolytes and poly(ionic liquid)s are supplied by Dr. Aleksandr Stryutsky in Prof. Valery Shevchenko's group (Macromolecular Chemistry, Ukraine National Academy of Sciences) in the course of ongoing collaboration. Cellulose nanocrystals are provided via collaboration with Dr. Minkyu Kim in Prof. V. V. Tsukruk's group at Georgia Tech.

3.1.1 Hyperbranched Polyelectrolytes

Hyperbranched polyelectrolytes with different terminal groups and counterions are obtained in course of collaboration with Prof. Prof. Valery Shevchenko (Macromolecular Chemistry, Ukraine National Academy of Sciences, Ukraine). Hyperbranched polyester polyol (HBP-OH; Boltorn H30, Perstorp, Sweden) containing 32 terminal OH groups with weight-average molecular weight of 3500 g/mol was used as an initial component for synthesis of hyperbranched polyelectrolytes in this study. Amphiphilic hyperbranched polymer with variable contents of hydrophobic *N*-octadecylurethane arms and hydrophilic terminal ionic (carboxylate or sulfonate) groups were synthesized by reaction of HBP-OH with *N*-octadecylisocyanate, followed by reaction with phthalic anhydride or 2-sulfobenzonic acid cyclic anhydride for carboxylate or sulfonate-containing hyperbranched PEs, respectively.[105] These amphiphilic HBPEs were then neutralized with PNIPAM (Mn = 2500 g/mol) to prepare thermally responsive HBPEs with PNIPAM macrocations (Figure 3.1).

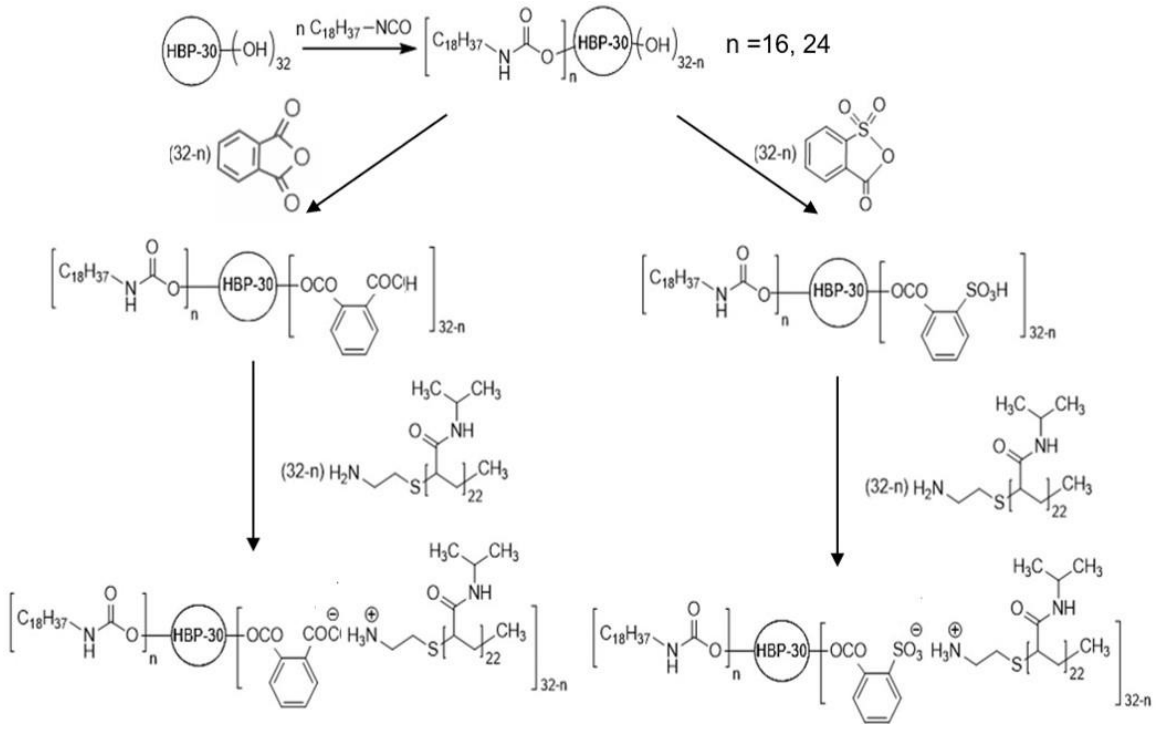

Figure 3.1. Scheme for the synthesis of thermally responsive hyperbranched polyelectrolytes.

3.1.2 Star Oligomeric Ionic Liquids

Star-shaped oligomeric ionic liquids (OILs) containing tertiary ammonium groups with alkyl substituent of different lengths as an organic shell and a mixture of octahedral silsesquioxane (OSS) with cage and open-chain structures as an inorganic core are synthesized in course of collaboration with Prof. Valery Shevchenko (Macromolecular Chemistry, Ukraine National Academy of Sciences). The initial compound, OSS with hydroxyl and tertiary amino groups (OSSN+OH) was synthesized according to a well-established method by hydrolytic condensation of the product of interaction of 3-aminopropyl triethoxysilane with excess of glycidol.[185,186] OSS(N+OH) was reacted with 1-bromopropane or 1-bromodecane by quaternization of tertiary amine groups, resulting in the synthesis of star oligomeric ionic liquids with the OSS core (OSS-OILs) containing alkyl substitutes with variable lengths (OSS($C_3N^+Br^-$) or OSS($C_{10}N^+Br^-$), respectively.) (Figure 3.2).

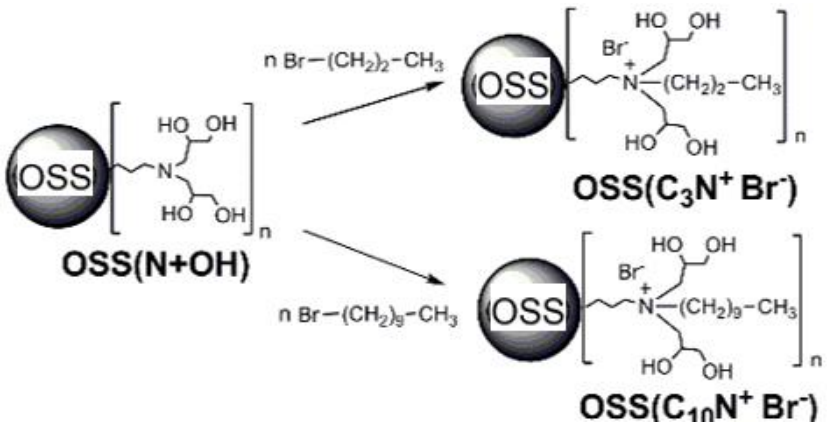

Figure 3.2. Scheme for the synthesis of star oligomeric ionic liquid with inorganic OSS cores.

3.1.3 Preparation of Cellulose Nanocrystal Suspension

Cellulose nanocrystals (CNCs) were prepared using the common sulfuric acid hydrolysis method.[187,188] Firstly, pre-cleaned and dried wood pulp was hydrolyzed by treating with 64% w/w sulfuric acid at 45 ^{o}C under vigorous stirring for 60 min. The hydrolysis was quenched by diluting the solution 10 times with Nanopure water (18.2 MΩ cm; Synergy UV-R, EMD Millipore). The solution was allowed to settle overnight, during which the hydrolyzed wood pulp separated from water. The water was discarded, and the cloudy sediment was collected and centrifuged at 6,000 rpm for 5 min twice to remove excess acid. The aqueous phase (supernatant) was discarded, and the hydrolyzed wood pulp (sediment) was collected and dialyzed against deionized water using regenerated cellulose dialysis tubing (12 000 – 14 000 MWCO, Thermal Scientific) until the pH value of the water became constant. After dialysis, the solution was centrifuged at 11,000 rpm for 20 min twice in order to obtain CNC dispersion with a narrow size distribution. The supernatant was cooled down to 13.5 ^{o}C and then exposed to sonication for 4.5 min using on/off pulse regime (5s/5s) and 40% amplitude (Q700 model with 1.2 cm diameter probe, Qsonica). CNC aqueous suspension was concentrated to a described concentration by evaporating water at 32.5 ^{o}C.

3.2 Film Deposition

3.2.1 Substrate Preparation

For film deposition on a silicon substrate, highly polished [100] silicon substrates (University Wafer) were cleaned with Piranha solution (2:1 concentrated sulfuric acid to hydrogen peroxide mixture, caution: strong oxidizer!) according to the common procedure.[31] The substrates were thoroughly rinsed with ultrapure water and then dried with dry nitrogen before film deposition.

3.2.2 Drop casting and Spin casting

Drop-casting and spin-casting were used to produce films of PEs and PILs under static and shear conditions, respectively. Drop-cast films of the hyperbranched polyelectrolytes were prepared by placing a drop of hyperbranched PE aqueous solutions, followed by drying at ambient condition. Spin-cast film of the hyperbranched PEs and star OILs were also prepared using a spin-coater (Laurell Technologies) at desired spin speeds and time.

3.2.3 Langmuir Monolayers and Langmuir-Blodgett Deposition

The pressure-area (Langmuir) isotherms and monolayer films of the hyperbranched PEs were obtained below and above LCST temperature using a KSV 2000 minithrough equipped with water temperature control. Ultrapure water was used as the subphase. The PE solutions were prepared at a concentration of 0.2 mg/mL in chloroform and spread uniformly onto the water surface in a dropwise manner. For experiments elevated temperature, water subphase in the through was heated to a target temperature before spreading the PE solutions. Langmuir monolayer at the air-water interface was left undisturbed for 30 min to allow for equilibration and solvent evaporation. Afterward, the Langmuir isotherms were recorded under compression at a rate of 5 mm/min to the target pressure. Compression−decompression isotherms were also recorded by compressing the monolayers to the maximum pressure and then expanding to maximum trough area. Monolayer films of the hyperbranched PEs were prepared by Langmuir-Blodgett (LB) deposition (Figure 3.3). The LB monolayers were transferred onto the pre-cleaned silicon substrates via vertical dipping at a rate of 1 mm/min.[61]

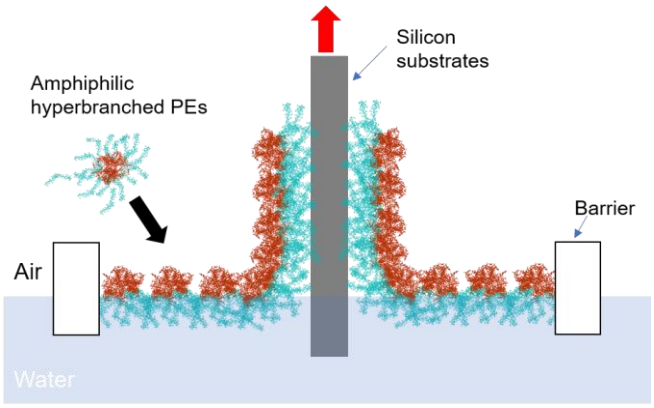

Figure 3.3. Scheme of Langmuir-Blodgett deposition of the hyperbranched polyelectrolytes.

3.3 Characterization

3.3.1 Attenuated Total Reflectance Fourier Transform Infrared Spectroscopy (ATR-FTIR)

ATR-FTIR was conducted to monitor the chemical composition of the PEs and PILs and molecular interactions in composite materials using a Bruker Vertex 70 system with resolution of 4 cm^{-1} and the number of scans of 100. For each sample, 200 background scans on a silicon ATR crystal without sample were collected before sample deposition. Samples for FTIR were prepared as pellets mixed with KBr.

3.3.2 Proton Nuclear Magnetic Resonance (^1H NMR)

^1H NMRspectra were recorded with a Varian VXR-400 MHz spectrometer using DMSO-d_6 (Cambridge Isotope Laboratories, Inc.) as a solvent to investigate the chemical composition of the synthesized PEs and PILs.

3.3.3 LCST temperature measurements

LCST behavior of the thermally responsive hyperbranched PEs was investigated by observing transmittance at 500 nm with heating/cooling rate of 0.5 °C/min (Chirascan-plus, Applied Photophysics) in temperature range of 25-50 ^oC.

3.3.4 Dynamic Light Scattering (DLS)/ Zeta-potential Measurements

DLS/Zeta-potential measurements were conducted with Zetasizer Nano ZS (Malvern) with Non-Invasive Back-Scatter (NIBS) technology (HeNe gas laser operating at a wavelength of 633 nm, scattering angle is 173°) to study the assembly behavior of the PEs and PILs in aqueous media and determine the size and surface charge of the PE and PIL assemblies. Each value of the size and zeta-potential was obtained at ambient conditions by averaging three independent measurements of 35 sub-runs each.

3.3.5 Atomic Force Microscopy (AFM)

AFM imaging was carried out to observe the surface morphology of samples using an ICON Dimension microscope (Bruker) in tapping mode. AFM probes purchased from Mikro-masch, (Hi'Res-C15/Cr-Au and HQ:XSC11/AL BS) were used with a desired spring constant depending on the stiffness of samples. The scanning rate varies in the range of 0.1−1.0 Hz, based on scan size. The resolution of AFM images was either 512x512 pixels or 1024x1024 pixels. All AFM images were processed and analyzed using Nanoscope Analysis software (Bruker).

3.3.6 Quantitative Nanomechanical Mapping (QNM)

Quantitative Nanomechanics (QNM)) was conducted with the ICON AFM (Bruker) to map and investigate the nanomechanical properties of samples. For QNM mode, AFM probes (Mikro-masch, HQ:XSC11/AL BS) were used with a tip radius of ~8 nm. Prior to each new sample measurement, tip characterization was performed. Deflection sensitivity was determined from force-distance curves (FDCs) on a sapphire crystal and the spring constant was calculated using the thermal calibration method. These measurements provide simultaneous contrast variation for regions with difference in stiffness and adhesion. For the quantitative mechanical measurements, FDCs were collected from the selected regions and analyzed using a micromechanical analysis software or Nanoscope Analysis software (Bruker).

3.3.7 Scanning Electron Microscopy (SEM)

SEM imaging of samples was performed on a Hitachi 8230 field emission SEM with a resolution of 1 nm. Prior to imaging, samples were dried and sputter-coated with gold/platinum.

3.3.8 Ellipsometry

The effective thickness of the hyperbranched PE monolayers was determined using an M-2000U spectroscopic ellipsometer with WVASE32 analysis software at three incident angles of 65°, 70°, and 75°. At least three separate locations on the sample were measured to determine the average thickness.

3.3.9 Thermogravimetric Analysis (TGA) and Dynamic Scanning Calorimetry (DSC)

TGA was performed on TGAQ50 (TA Instruments) for CNC/PIL ionogels. DSC was conducted on STARe system DSC 3 (Mettler Toledo) for the PEs, PILs and CNC/PIL ionogels. All samples were dried under vacuum at 70 ^{o}C for 24 hours before TGA and DSC measurements. For TGA, 6-10 mg of dried samples were used and heated from room temperature to 600-700 ^{o}C at heating rate of 10 ^{o}C/min under nitrogen gas (40 or 80 mL/min). For DSC, 6-10 mg of dried samples were placed and sealed into a standard Mettler aluminium crucible. DSC measurements were conducted with the temperature range under nitrogen gas (80 mL/min). The heating/cooling cycle was repeated three times at the heating/cooling rate of 10 ^{o}C/min. While the first heating/cooling run erased the previous thermal history of the samples, the second heating curves were used for determining the glass transition temperature, melting temperature and cold crystallization temperature.[189]

CHAPTER 4. TRANSFORMATIONS OF THERMO-SENSITIVE HYPERBRANCHED POLYELECTROLYTE MONOLAYERS

4.1 Introduction

The assembly of functional polymers provides exciting possibilities for the design and development of materials with novel morphologies and properties for a variety of applications, such as biomedical, sensing, energy storage and electrochemical applications.[190,191,192] In this regard, polyelectrolytes (PEs) are promising as they can exhibit hierarchical assembly, forming various organized morphologies, such as micelles, vesicles, and cubosomes.[27,28,29] PEs are polymers composed of ionizable groups in their backbone or side chains, which can dissociate into charged polymer chains and small counterions in polar solvents.[193] The presence of ionizable groups can diversify intra- and intermolecular interactions of PEs, providing multidimensional driving forces for the assembly of molecules. Compared to conventional neutral polymers, PEs show different phase behavior due to dramatic asymmetry in charge, mass and size between the polyelectrolyte backbone and the counterions, co-ions and solvent molecules. For example, PEs have a higher osmotic pressure and more extended chain conformations in solution.[4,5]

Various star and branched polymer architectures have been introduced to PEs.[194] The presence of multiple terminal groups can provide pathways to control the assembly of polymers in solutions, at surfaces and interfaces as well as their stimuli-responsive behavior.[195, 196] The assembly of hyperbranched PEs (HBPEs) can be controlled by changing the type of terminal ionic groups[105] and the ratio of terminal hydrophilic/hydrophobic segments.[197] In addition, various morphologies can be achieved by introducing terminal stimuli-responsive segments which respond to external stimuli, such as temperature, pH and light.[198 , 199 , 200 , 201 , 202 , 203] Poly(N-isopropylacrylamide) (PNIPAM) blocks with low critical solution temperature (LCST) behavior have been explored for this purpose as PNIPAM graft[202,203,204] and macrocations.[96] For example, bottlebrush copolymers composed of PEs with grafted PNIPAM formed disassociated nanoscale discoidal assemblies below LCST, while thicker circular discs above LCST.[204] For the HBPEs containing PNIPAM macrocations, micellar assemblies were formed with

diverse morphologies depending on temperature.[96] Temperature-induced transition in mechanical properties has been also observed for the polymer surface grafted with PNIPAM brushes. The collapse of PNIPAM chains above LCST causes the increase in adhesion and elastic modulus as a result of the combination of dehydration and chain entanglement.[96,205,206,207] Moreover, the incorporation of asymmetric composition of functional terminal groups can produce interesting morphologies by shifting the phase boundaries.[208,209,210,211,212] For example, hyperbranched polyethers possessing homogenous peripheral chemical composition did not self-organize into ordered structures, while hyperbranched polyethers partially terminated with benzoyl groups formed macroscopic aggregates.[213] However, to date, the majority of HBPE studies focused on the synthesis and morphologies of HBPEs composed of symmetric chemical composition[99,104,214] with less attention paid to the assembly of HBPEs at interfaces.[197] It has been shown that amphiphilic branched polymers at the air-water interface exhibit interesting morphological transition upon lateral compression.[195,215,216,217,218,219] For example, poly(styrene)-block-poly(acrylic acid) (PS-b-PAA) dendrimer-like copolymers underwent 'pancake-to-brush' transition under compression.[216] Peculiar rod-to-globule and pancake-to-island transitions were also observed from brush block copolymers.[218,219]

Here, we report the synthesis and assembly of novel thermo-responsive amphiphilic hyperbranched polyelectrolytes with asymmetric peripheral chemical composition. These HBPEs are composed of hydrophobic polyester cores with 24 hydrophobic n-octadecylurethane groups and 8 hydrophilic PNIPAM macrocations as peripheral components with LCST transition (Figure 4.1a). Their assembly at the air-water interface is investigated at different temperatures and surface pressures. The morphology and mechanical property distribution of their monolayer films at the air-solid interfaces are also examine in dry and wet conditions. These amphiphilic HBPEs showed domain and coalescent morphology due to the persistence of their shape afforded by the asymmetric composition with branched architecture. Thermally triggered phase reorganization resulted in alternating heterogeneous surface mechanical and adhesion distribution due to the transformation of the beneath PNIPAM phase.

4.2 Experimental Section

4.2.1 Materials

Poly(N-isopropylacrylamide) amine terminated (PNIPAM, M_n= 2500 g/mol) was obtained from Aldrich and used as received. Hyperbranched aliphatic oligoether polyol Boltorn H30 (Perstorp, Sweden) with weight average molecular weight (M_w) of 3500 g/mol (comprising 32 terminal OH groups in outer shell) was purified by precipitation of dimethylformamide (DMF) solution in diethyl ether followed by vacuum drying at 25-30 °C for 6 h (an equivalent M_w measured by hydroxyl groups via acetylation technique is equal to 117 gram/equivalent).[220] Phthalic anhydride was purified by sublimation. DMF, ethanol, diethyl ether, acetone, acetonitrile, were dried and distilled before use. The ultrapure water used in all experiments was prepared in a three-stage Millipore Milli-Q Plus 185 purification system (resistivity ≥18.2 MΩ·cm) (see more detail in Supporting Information).

4.2.2 Langmuir Monolayers and Deposition

The pressure−area (Langmuir) isotherms at the air-water interface and Langmuir-Blodgett (LB) deposition onto a silicon substrate were obtained below and above LCST (23 °C and 37 °C) (as described earlier). The monolayer films of the HBPE were prepared via LB deposition at different pressures (0.3, 20, and 49 mN/m).

4.2.3 Characterization

Fourier transform infrared (FTIR) spectra in 200-4500 cm^{-1} range and Proton nuclear magnetic resonance (^{1}H NMR) spectra of synthesized HBPEs were collected as described earlier.

The surface morphology of HBPE monolayers was investigated with an atomic force microscope (AFM) in the "light" tapping mode according to the usual procedure.[221] High-resolution AFM probes (MikroMasch, Hi'Res-C15/Cr-Au) were used with a spring constant of 40 N/m. The scanning rate was kept in the range of 0.2−0.5 Hz, and the resolution was either 512 X 512 pixels or 1024 X 1024 pixels. The effective thickness of HBPE monolayers was determined using the ellipsometer (as mentioned earlier in Chapter

3). AFM scratch test was also conducted to measure the monolayer thickness. The monolayer samples were scratched with a sharp needle. After the scratched area was scanned over 10 X 10 μm^2 area, the thickness of the HBPE monolayers was obtained by subtracting the average height of the bare silicon region from the average height of the region where HBPEs were deposited using a height histogram distribution with NanoScope Analysis v1.4 software (Bruker, USA).

Force-tapping mode (Bruker's Quantitative Nanomechanics (QNM)) was conducted to map the nanomechanical properties of HBPE monolayers as described earlier. The HBPE monolayers were scanned in QNM mode at scan rate of 0.5 Hz using the resolution of 512 X 512 pixels. QNM measurements were conducted in air as well as in water below and above LCST. For the measurements above LCST, the samples were placed on a Peltier heating/cooling stage. Water was injected into the system by taking advantage of capillary forces between the AFM tip and sample. After adding water, the samples were allowed to equilibrate for 2 h. Water temperature was monitored to be maintained above LCST. For the quantitative mechanical measurements, FDCs were collected from the selected regions with a ramp size of 200 nm and analyzed using a micromechanical analysis software (see Supporting Information).[222]

4.3 Results and Discussion

4.3.1 Synthesis of Hyperbranched Polyelectrolytes

We synthesized amphiphilic HBPEs consisting of 24 hydrophobic n-octadecylurethane groups and 8 hydrophilic carboxylate anions and PNIPAM macrocations as peripheral components (abbreviated as HBP-24Oct8$[COO]^-[PNIPAM]^+$) (Figure 4.1).[96] Boltorn®H30 of 3rd generation (HBP-OH) containing 32 terminal primary hydroxyl groups was used as an initial compound. The hydrophobicity of the hyperbranched oligoester core was enhanced by the incorporation of hydrophobic octadecyl urethane fragments (Figure 4.1). The change in the ratio of the hydrophobic octadecyl urethane fragments to hydrophilic PNIPAM macrocations allows control over the hydrophilic-hydrophobic balance.

The synthesis of HBP-24Oct8[COO]$^-$[PNIPAM]$^+$ was based on the partial blocking of the terminal hydroxyl groups of the initial HBP-OH with n-octadecylisocyanate (OH : NCO = 4 : 3) followed by acylation of the residual hydroxyl groups of the reaction product with phthalic anhydride (OH: $(CO)_2O$ = 1 : 1) and neutralization of carboxyl groups by a primary amino groups of the PNIPAM (Figure S4.1).

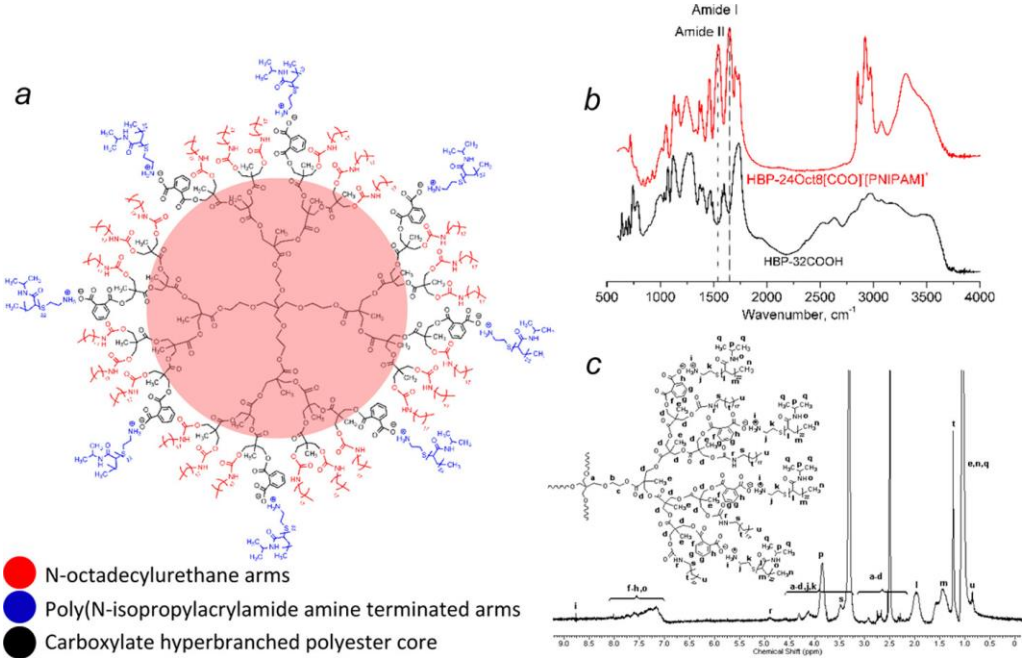

Figure 4.1. Amphiphilic HBPE with 24 hydrophobic n-octadecylurethane arms and hydrophilic 8 poly(N-isopropylacrylamide) amine terminated macrocations (a). Red circle indicates the polyester core. Representative FTIR spectra of oligomeric hyperbranched polycarboxylic acid, HBP-32COOH and HBPE, HBP-24Oct8[COO]$^-$[PNIPAM]$^+$ (b). ^{1}H NMR spectrum of HBP-24Oct8[COO]$^-$[PNIPAM]$^+$ (c).

The chemical structure of the synthesized HBPE compound was confirmed by FT-IR and ^{1}H NMR spectroscopies (Figure 4.1b,c). The FT-IR spectrum of the HBPE compound contains absorption bands of aliphatic fragments (ν C-H of CH_2 (2874, 2922, 2972 cm^{-1}), ν C-H of CH_3 (1087-1312 cm^{-1}), δ C-H of CH_2 and δ as C-H of CH_3 (1460 cm^{-1}), δ sy C-H of CH_3 (1367, 1387 cm^{-1})) of hyperbranched core, octadecyl urethane fragments and PNIPAM macrocations, bands of ν C-O-C bonds of ester fragments which overlap ν C-H of CH_3 (1000-1312 cm^{-1}), bands of ν C=O bonds of ester and carboxylate groups (1703-1735 cm^{-1}), bands of the characteristic amide groups of PNIPAM (ν C=O amide I at 1649

cm^{-1} and δ N-H amide II at 1543 cm^{-1}), bands of aromatic rings (ν C-H at 3075 cm^{-1}), ammonium cations, amide and urethane groups (ν N-H at 3130-3700 cm^{-1}) (Figure 4.1b). The characteristic peaks of HBP-24Oct8$[COO]^-[PNIPAM]^+$ and its distinctive feature from the initial oligomeric acid are signals from the carbonyl groups of PNIPAM (Amide I and Amide II) and a significant increase in the intensity of the alkyl signals (2800-3030 cm^{-1}) (Figure 4.1b).

^{1}H NMR spectrum of the HBPE compound shows signals of methyl (0.76-1.14 ppm) and methylene (1.24, 1.46, 2.25-4.30 ppm) groups of hyperbranched core, PNIPAM fragments and octadecyl tails, signals of protons from tertiary carbon atoms of PNIPAM fragments (1.99, 3.85 ppm), urethane groups (4.80 ppm) of octadecyl tails, aromatic rings, amide groups (7.83-7.90 ppm) and ammonium cations (8.77 ppm) (Figure 4.1c). The chemical structure of the HBPE is confirmed by positions of characteristic peaks and ratios of integral areas of these signals (See Figure 4.1c and SI).

The degree of branching (DB) of the initial HBP-OH which is a ratio of sum of branched units and those containing terminal groups to sum of all units including linear ones was determined based on the ^{13}C NMR spectra as described by our previous study[223] (see SI). The obtained DB values are 38-39% (Mean value is 38.7%, Table 4.1), corresponding to the literature data for DB of the HBP-OH Boltorn H40 (36-43%)[224] which has a similar chemical structure but with a different number of terminal hydroxyl groups (64 hydroxyl groups). The DB values are valid for both an intermediate product, oligomeric hyperbranched polycarboxylic acid (HBP-24Oct8COOH, see SI) and a final HBPE, HBP-24Oct8$[COO]^-[PNIPAM]^+$ since these compounds were obtained by successive polymer-analogous transformations of the initial cores without changing the total number of terminal functional groups (see SI). The molecular weight (MW) for the HBPE was determined as 32,857 g/mol based on the MW of oligomeric hyperbranched polycarboxylic acid (from acid-base titration technique) and MW of terminal groups of PNIPAM and constitutes (Table 4.1). This value is close to the theoretical value (33,204 g/mol).

Table 4.1. MW and DB values for HBP-OH, HBP-24Oct8COOH and HBP-24Oct8$[COO]^-$ $[PNIPAM]^+$

Sample	MW g/mol		Mean DB %
	Calculated	Found	
HBP-OH	3564	3744	38.7
HBP-24Oct8COOH	13204	12857	
HBP-24Oct8$[COO]^-$ $[PNIPAM]^+$	33204	32857	

4.3.2 Langmuir Monolayers

The HBP-24Oct8$[COO]^-[PNIPAM]^+$ compounds formed stable Langmuir monolayers transferable to solid surfaces due to their well-balanced hydrophilic-hydrophobic character. They have hydrophobic segments (core and octadecyl arms) sufficiently enough to overcome the hydrophilicity of PNIPAM segments and thus irreversible dissolution in water subphase.[225] At the same time, their PNIPAM macrocations are sufficiently hydrophilic to prevent the desorption and aggregation of HBPEs on top of water surface. To investigate the thermally responsive behavior of Langmuir monolayers, the pressure-area isotherms were recorded below and above LCST (at 23 ^oC and 37 ^oC) (Figure 4.2a,b and Table 4.2).

First of all, to determine the LCST of HBPEs, the transmittance of HBPE aqueous solution (0.5 mg/mL) was measured at different temperatures in range of 25-50 ^oC (Figure S4.3). The transmittance slightly and gradually decreased to 15% from the initial transmittance at around 35 ^oC and dramatically dropped from 35 to 38 ^oC, which corresponds to the LCST range (see SI).[226,227] LCST can be defined as the temperature where the transmittance

decreases to 10% from the initial transmittance when a sharp LCST transition occurs.[228,229] According to this definition with a slight modification, we defined LCST as the temperature where the transmittance decreases to 10% from the transmittance at the onset transition temperature (34.9±0.1°C) instead of from the initial transmittance. LCST was defined at 35.8±0.1°C. Therefore, we chose 23 °C and 37 °C as below and above LCST, respectively. We also observed that the contact angle of water on the HBPE monolayer films deposited in a liquid phase increased from 58° to 85° with increasing water subphase temperature from 23 °C to 37 °C (Figure S4.4). This result supports our choice of 37 °C as above LCST, confirming that HBPEs underwent temperature-induced phase transition with PNIPAMs being less hydrophilic at 37 °C.

Table 4.2. The dimensions of the HBPE domains and the surface area per molecule at different surface pressures and temperatures.

Temperature (°C)	**23**		**37**		
Surface area per molecule in liquid phase, A_l (nm^2)	56.4		81.2		
Surface area per molecule in solid phase, A_s (nm^2)	10.3		9.6		
Surface Pressure (mN/m)	20	49	20	49	
Domain Shape	Disk	Ridge	Disk	Ridge	Island
Domain height (nm)	2.1±0.5	1.1±0.2	2.1±0.5	1.3±0.3	4.3±0.6
Domain diameter/width (nm)	86.1±44.2	8.6±1.0	90.0±19.0	10.5±1.1	58.1±31.3
Domain surface coverage (%)	39.6±5.2	11.3±2.2	40.6±0.7	6.6±1.1	4.9±1.8

The pressure-area isotherms for both temperatures showed a steady increase in surface pressure upon compression, indicating the formation of stable Langmuir monolayers.[223] The isotherms were shifted toward larger surface area above LCST due to the increased hydrophobicity arising from LCST transition of PNIPAMs, which indicates the enhanced stability of monolayers.[225] The surface pressure started to rise below 80 nm^2 at 23 °C and below 100 nm^2 at 37 °C (Figure 4.2). For the isotherm at 23 °C, a significant pseudoplateau region appeared for the surface area below 30 nm^2, while the isotherm recorded at 37 °C showed a relatively small pseudoplateau region for the surface area below 20 nm^2. When the surface area was below 10 nm^2, the surface pressure abruptly increased for both temperatures, indicating the formation of the solid monolayers. For the isotherm at 37 °C, a small shoulder appeared when the surface area reached 8 nm^2.

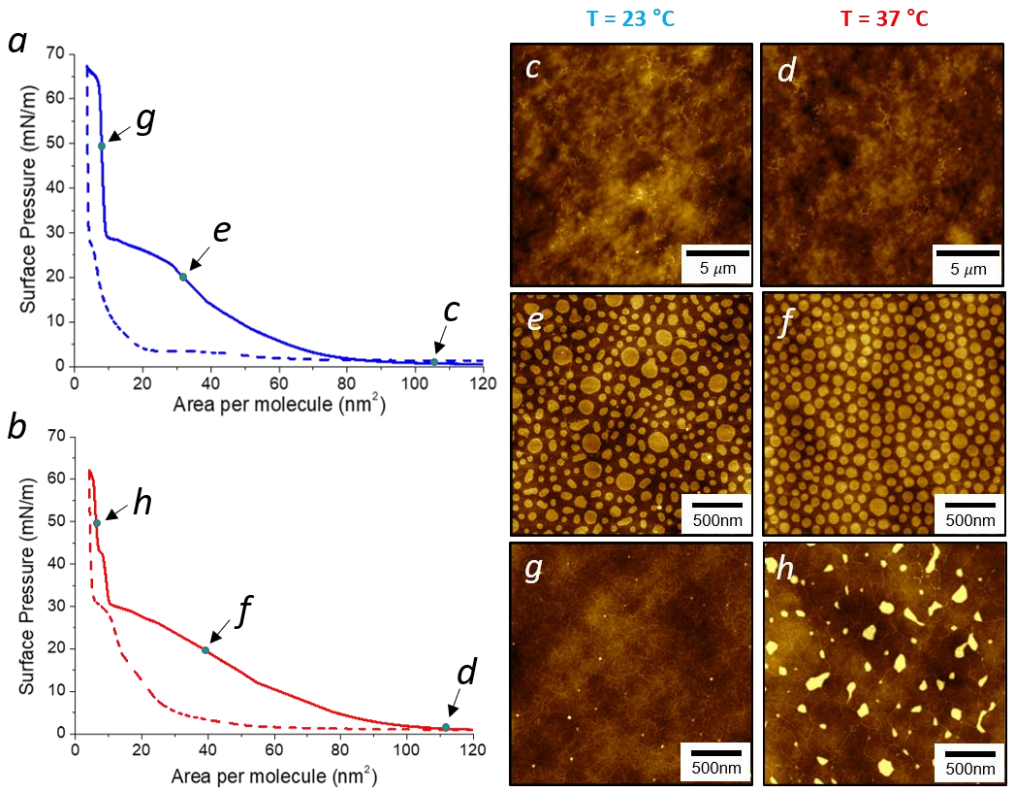

Figure 4.2. Langmuir isotherms of HBPEs (left) at 23 °C (*a*) and 37 °C (*b*). The solid and dashed lines are collected during compression and expansion, respectively. AFM height images (right) of HBPE monolayers deposited at 0.3 mN/m (*c*,*d*), 20 mN/m (*e*,*f*) and 49 mN/m (*g*,*h*) at 23 °C (*c*,*e*,*g*) and 37 °C (*d*,*f*,*h*). Z scale is 11 nm for (c,d) and 7 nm for (e-h).

The surface area occupied per molecules in liquid and solid phases, A_l and A_s, were calculated by extrapolating the steepest segment of the linear portion of the liquid and solid phases down to the zero surface pressure, respectively (Figure S4.5 and Table 4.2).[81,230] The value of A_l is much larger at 37 °C, indicating that the HBPE molecules above LCST occupy a larger surface area since the hydrophobized PNIPAM segments are desorbed from water subphase to the air-water interface and act as barriers which limit compact packaging between the molecules.[195,231,232,233,234] The value of A_s was around 10 nm^2 for both temperatures (Figure S4.4 and Table 4.2). The theoretical area occupied per molecule in a solid phase can be calculated by considering 0.2 nm^2 as the known surface area occupied per alkyl tail in a densely packed phase.[223] The total projected surface area per molecule occupied by 24 hydrophobic alkyl chains is theoretically estimated to be 4.8 nm^2, suggesting that not only hydrophobic octadecyl tails but also hyperbranched core govern the limiting surface molecular area of HBPE monolayers in a solid phase.

The sharp drop in surface pressure upon expansion indicates that the reconstruction of the condensed monolayer to the initial state is rather kinetically hindered at decompression (Figure 4.2).[235,236,237] Then, the second compression results in the shift of Langmuir isotherms toward lower surface due to the presence of the nuclei after first expansion as well as the formation of continuous domains during second compression (Figure S4.6-7).[225,238]

4.3.3 Monolayer Morphology

AFM images show a featureless, uniform morphology in a gas phase, a well-defined disk-like domains in a liquid phase, and eventually, a network of ridge-like morphology in a solid phase (Figures 4.2c-g and S4.8-10). First of all, the disk-like domains observed at the surface pressure of 20 mN/m have the similar average diameters (86±44 nm and 90±19 nm at 23 °C and 37 °C, respectively) and height of 2.1±0.5 nm for both temperatures (Figure 4.3-4, Table 4.2). The size distribution of the disk-like domains is broader below LCST than above LCST. Below LCST, about 16% of the disk-like domains have a diameter larger than 150 nm, while very few (less than 1%) of the domains have a diameter larger than 150 nm above LCST (Figure 4.4). It should be noted that the disk-like domains

exhibit a contrast between the outer region of about 10 nm and center area of disk-like domains in AFM phase images (Figure 4.5a,b), having a concave shape with elevated rims, observed from height profiles of AFM images as well as three-dimensional images (Figures 4.3a,b and 4.6a,b).

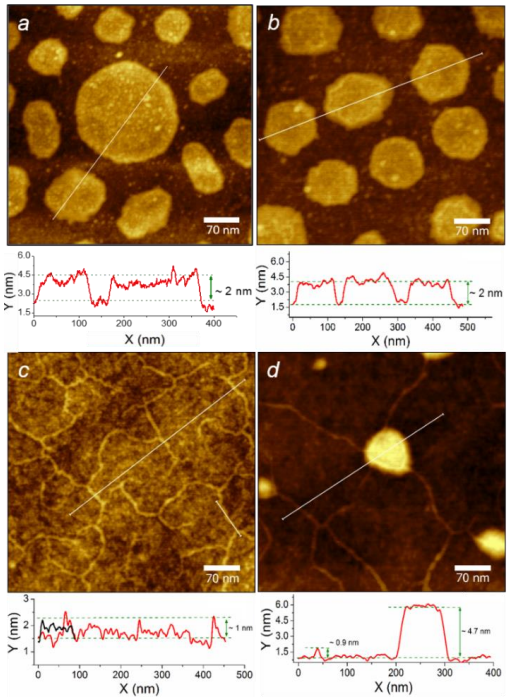

Figure 4.3. High resolution AFM images and height profiles of HBPE monolayers at different surface pressures; 20 mN/m (a,b), 49 mN/m (c,d) and at different temperatures; 23 °C (a,c) and 37 °C (b,d). Z scale are 3 nm (c) and 6 nm (a,*b*,*d*).

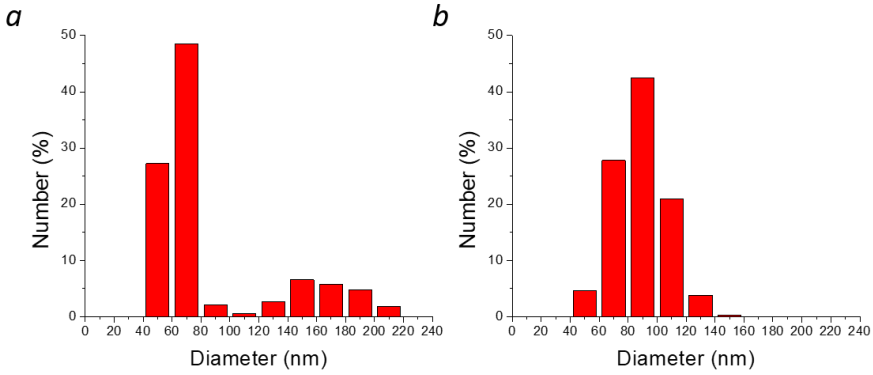

Figure 4.4. Size distribution of disk-like domains in HBPE monolayers at 20mN/m and different temperatures; 23°C (a) and 37°C (b).

Further compression induces a morphological transition where the disk-like structures are transformed into the network of ridges for both temperatures (Figure 4.3c). The average height of the elevated ridges is 1.1±0.2 nm and 1.3±0.3 nm at 23 °C and 37 °C, respectively (see profiles in Figure 4.3 and Table 4.2). Larger islands with height of 4.3±0.6 nm connected by the network of ridge-like domains are observed only at 37 °C (Figure 4.3d). AFM phase and three-dimensional height images also show the morphological transition induced by temperature and surface pressure (Figures 4.5-6).

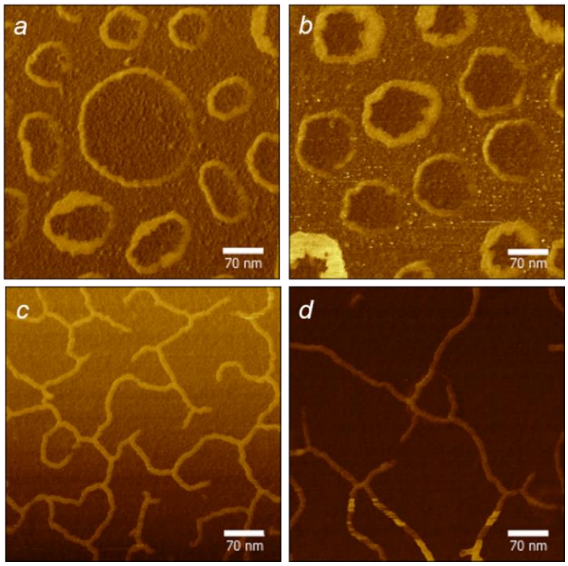

Figure 4.5. High resolution AFM phase images of HBPE monolayers at different surface pressures; 20 mN/m (a,b), 49 mN/m (c,d) and at different temperatures; 23 °C (a,c) and 37 °C (b,d). Z scale is 8^{o} for all images.

At the first glance, the Langmuir isotherms and monolayer morphology resemble those commonly observed for linear amphiphilic block copolymers.[239,240] As known, 'pancake-to-brush' or 'carpet-to-brush' transitions take place for neutral or ionic amphiphilic block copolymers, respectively, upon compression at the air-water interface as the hydrophilic blocks desorbed from the water surface and submerged into the subphase.[216,240,241,242,243] In this case, the domain height should largely increase as surface pressure increases.[233,244] However, the height of the ridge-like domains formed by HBPEs is close to 1 nm, which is lower than that of the disk-like domains at lower pressure (Table 4.2). Therefore, the

interfacial behavior of HBPEs upon compression cannot be explained by the common pancake-brush transition.

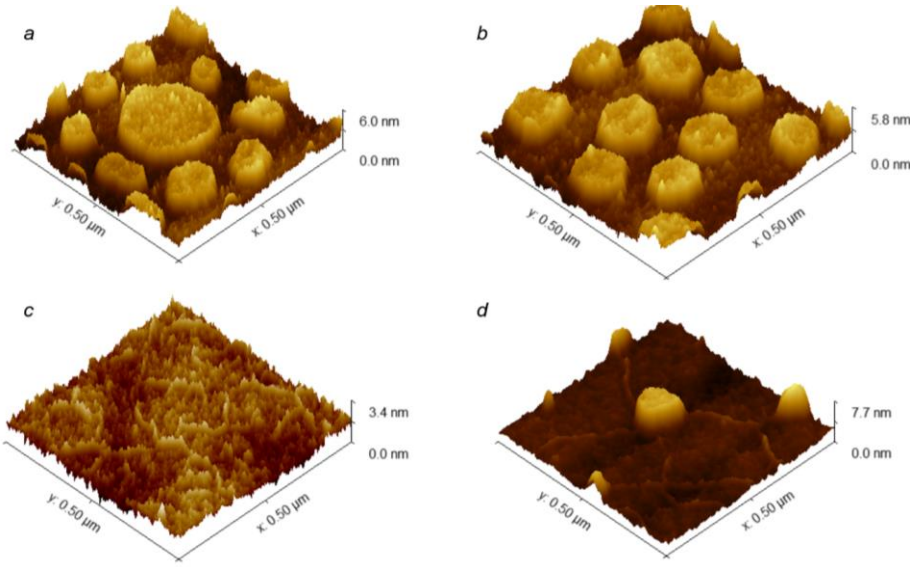

Figure 4.6. Three-dimensional AFM images of HBPE monolayers at different surface pressures; 20 mN/m (a,b) and 49 mN/m (c,d) and at different temperatures: 23 ^{o}C (a,c) and 37 ^{o}C (b,d).

4.3.4 Monolayer Formation

Considering that AFM monitors only the surface morphology, we also analyzed the data on heights and effective thickness of the monolayers under different conditions as measured by ellipsometry and AFM scratch test (Figure 4.7). As we observe, the effective thickness of the monolayers in a liquid phase is 1.5-1.6 nm below and above LCST. In a solid phase, the average effective thickness increases to 2.4-3.3 nm at 23 °C and 4.1-4.4 nm at 37 °C. The larger effective thickness above LCST is associated with the presence of the islands with height over 4 nm.

The effective thickness of the monolayers, $t_{effective}$ is calculated as $A_{domain}(t_{domain}+t_{under})+A_{under}(t_{under})$, where A_{domain} and A_{under} are the area coverage of the domains and underlying layer, respectively, in percentage ($A_{domain}+A_{under}$ = 100%), t_{domain} is the height of the domains, and t_{under} is the thickness of the underlying sub-layer.[215] From this equation, the thickness of the underlying layer was calculated to be 0.6-0.8 nm for the monolayers in a liquid phase both below and above LCST.

Therefore, a model for the monolayer organization in liquid and solid states that fulfills these morphological observations is suggested in Figure 8. In this model, below LCST, the disk-like domains are formed in a liquid phase since hydrophobic segments of HBPEs tend to combine across the air-water interface to avoid unfavorable interaction with water, while the hydrophilic carboxylate terminal groups are anchored at the interface, ionically linked with PNIPAM macrocations that submerge in the water subphase. The hydrophobic-hydrophobic interactions of terminal alkyl chains of HBPEs facilitate large disk-like domain formation.

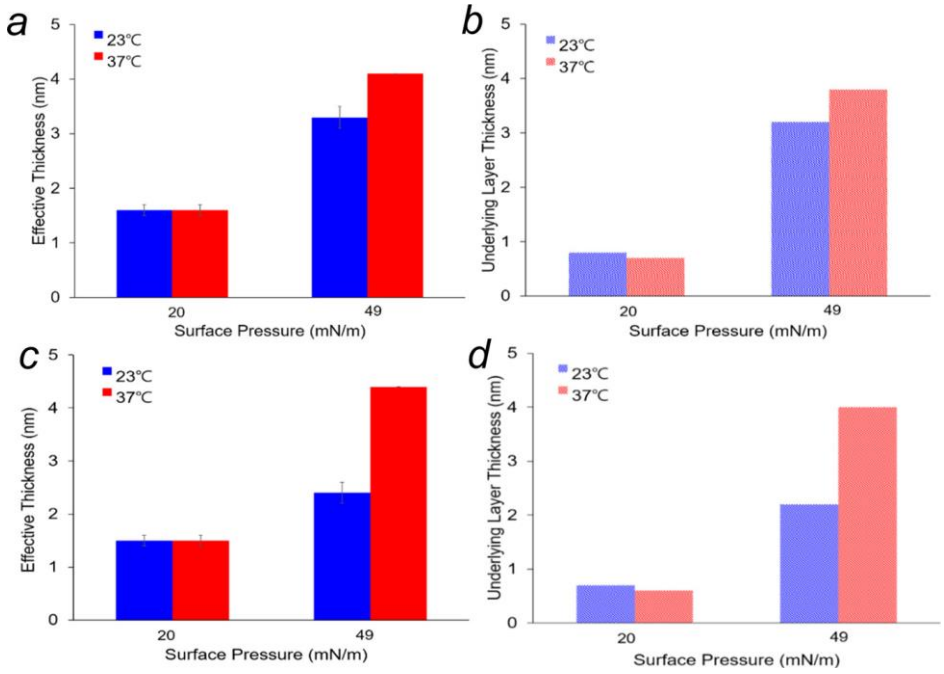

Figure 4.7. Effective thickness (a,c) and underlying layer thickness (b,d) of HBPE monolayer films measured by ellipsometry (a,b) and AFM scratch test (c,d).

It is also worth mentioning that the height of disk-like domains is around 2 nm, and this value is slightly larger than the height of the hyperbranched core being flattened to a pancake shape (1.5-1.9 nm) [245] and smaller than the estimated length of fully extended octadecyl chain (2.4 nm, see Figure S4.11). Therefore, we suggest that the disk-like domains are formed by the molecules with flattened hyperbranched core and randomly oriented alkyl tails. Regarding thin underlying sub-layer, we suggest that it is formed by hydrophilic PNIPAM macrocations, which spread between hydrophobic segments and hydrophilic silicon oxide surface (Figure 4.8).

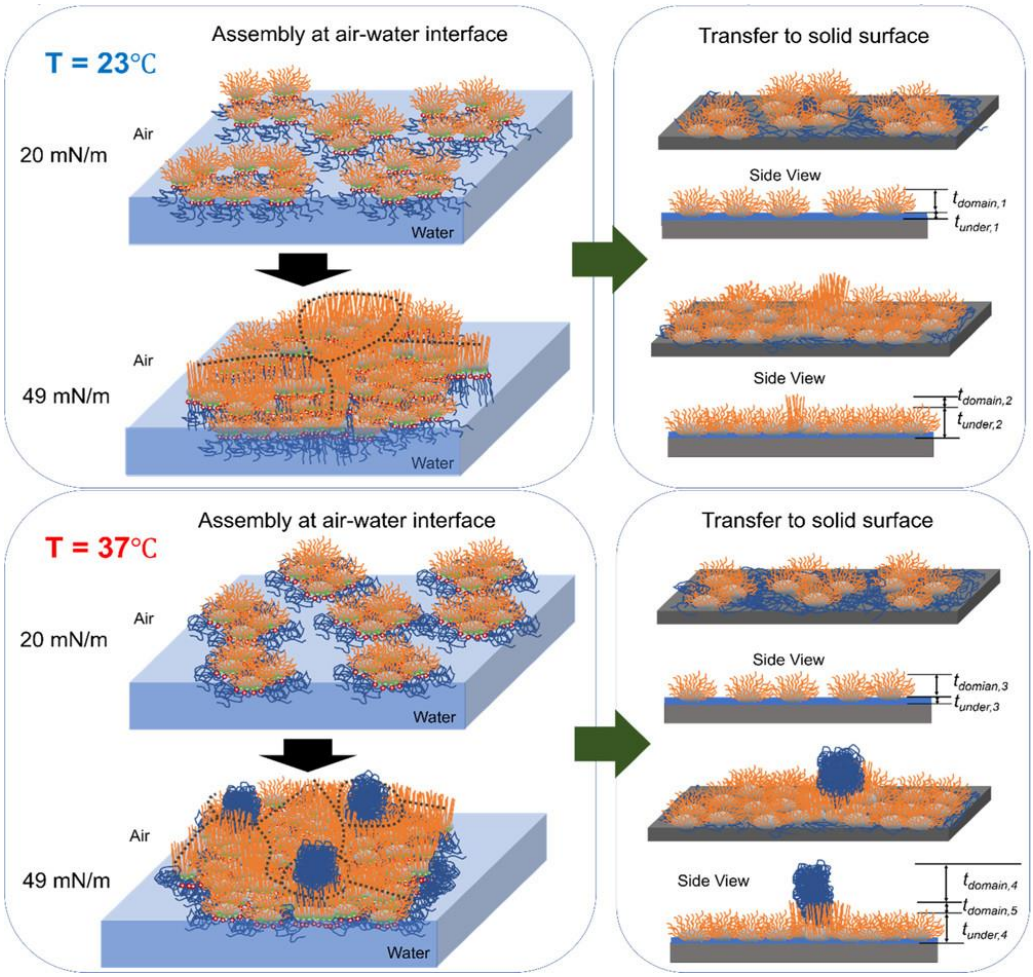

Figure 4.8. Models of HBPE monolayer at the air-water interface at 23 °C (top) and at 37 °C (bottom) at different surface pressures (20 and 49 mN/m) (left) and molecular packing of monolayers at solid substrate (right). Dashed line shows the ridge-like domains formed by the molecules with alkyl tails in an up-right orientation.

The formation of the ridge-like network morphology in the solid state can be attributed by the high stability of disk-like domains under compression caused by branched architecture and asymmetric chemical composition of HBPEs (Figures 4.3 and 4.6). We suggest that the branched architecture and asymmetry in chemical composition of HBPEs favor the formation of the disk-like domains that have a concave shape with elevated rims, making the pancake-to-brush or carpet-to-brush transition less likely to occur and allowing the disk-like domains to preserve their shape under high lateral compression. Meanwhile, the steric and electrostatic repulsions induced by the PNIPAM macrocations may not be strong

enough to convert their structure from flat carpet-like to brush-like structure even at high surface pressure; thus, initial disk-like domains are preserved in the merged structures with interdomain boundaries formed by peripheral rims at the original contact lines (Figure 4.8).

Moreover, the thickness of the underlying layer in a solid phase is close to the sum of the initial height of disk-like domains (2.1 nm) and the thickness of the underlying PNIPAM layer in a liquid phase (0.6-0.8 nm) (Figure 4.7). This result suggests that the underlying layer of the monolayers in a solid phase is formed by the integration of the disk-like domains, and the ridge-like network is produced as the alkyl tails of HBPE molecules are vertically oriented when trapped and compressed at the interdomain boundaries. This is further supported by the large contact angle of water over 90° (Figure S4.4), indicating that hydrophobic components constitute the surface of the monolayers. Indeed, our previous study found that alkyl tails of hyperbranched polyesters can be vertically oriented at high surface pressure, forming aggregate domains with height of 0.6-0.8 nm above the beneath sub-layer.[223]

Increasing temperature above LCST does not change the overall shape and dimension of the domains but affects their size distribution in a liquid phase (Figures 4.3-4). Above LCST, the disk-like domains have diameters mostly within 120 nm, showing more uniform size distribution, compared to below LCST. This can be explained by the effect of the collapsed PNIPAM macrocations on limiting the domain combination. Above LCST, PNIPAM macrocations collapse and become partially hydrophobic, thus promoting PNIPAM desorption from water subphase and anchoring at the air-water interface. This anchoring results in the formation of a thicker outer region of disk-like domains and causes increased steric repulsion between HBPE molecules, preventing full merge of the initial domains (Figure 4.5).

4.3.5 Nanomechanical Mapping

QNM surface mapping was further performed to reveal the surface properties (apparent elastic modulus and adhesion distribution) below and above LCST (Figures 4.9 and S4.12). For both temperatures, under dry conditions, the disk-like domains possess slightly higher elastic modulus and adhesion compared to the interdomain region (Figure 4.9a). Further

analysis of force-distance curves (FDC) was performed to obtain quantitative values of elastic modulus and adhesion (Figures S4.14-15). The FDC analysis shows the similarity of the average elastic modulus of 2.5-3.5 GPa within experimental deviation (Figure 4.10a). These values are characteristics of ordered alkyl chain surfaces, in range of 1-5 GPa.[246,247] This observation suggests that the topmost surface of the HBPE monolayer might be covered by terminal octadecyl tails, which supports the proposed model (Figure 4.8). In addition, the adhesive forces for the domains and interdomain region are similar within experimental deviation with a modest temperature dependence (Figure 4.10b). The uniformity of surface adhesion distribution also supports our model that the topmost surface does not consist of dissimilar components, and hydrophobic components are located at the surface with beneath hydrophilic sublayer.

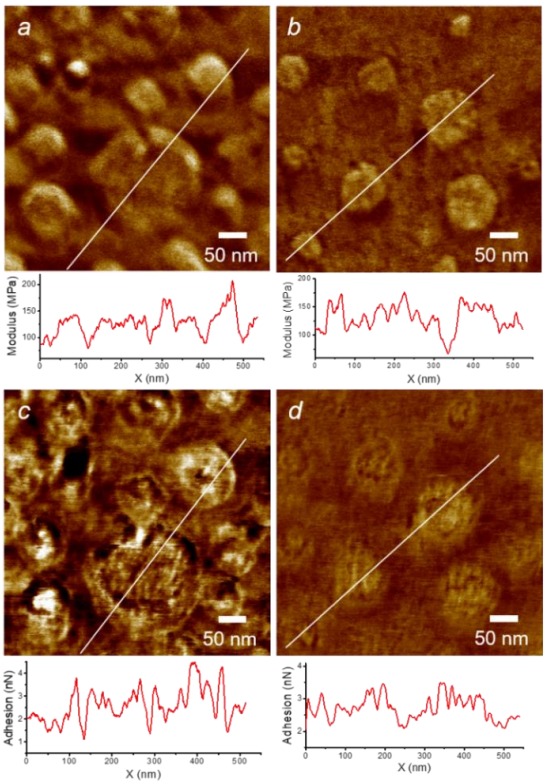

Figure 4.9. Elastic modulus (a,b) and adhesion (c,d) distribution of HBPE monolayers at surface pressure 20 mN/m and at 23℃ (a,c) and 37℃ (b,d). Z scale is 250 MPa and 5 nN for the modulus and adhesion images, respectively.

QNM mapping and FDC analysis were also conducted for HBPE monolayers deposited in a solid phase (Figures S4.13 and S4.16-18). QNM mapping for those deposited at 23 °C

shows that the ridge-like domains have a higher elastic modulus and lower adhesion than the interdomain region, supporting the suggestion that the ridge-like network is formed by vertically oriented alkyl chains (Figure S4.13a,c). The vertically oriented alkyl chains are more likely crystallized and thus expected to have higher elastic modulus and lower adhesion compared to randomly oriented alkyl chains.[248,249] On the other hand, the FDC analysis shows that the ridges and interdomain region have similar average values of elastic modulus (around 2.5 GPa) and adhesion (around 4 nN) (Figure S4.18). This similarity further supports that the monolayers have the topmost layer composed of hydrophobic and stiff octadecyl tails with the underlying sub-layer formed by hydrophilic terminal arms.

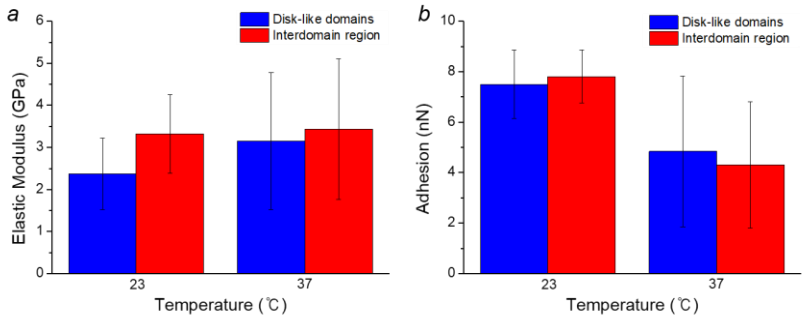

Figure 4.10. Elastic modulus (a) and adhesion (b) of the domain and interdomain region of HBPE monolayers at surface pressure 20 mN/m. All measurements were performed in a dry state.

For the monolayers deposited at 37 °C, the elastic modulus distribution does not show a significant contrast between domains and interdomain region, but adhesion mapping shows a remarkable difference between domains and inter-domain region with much lower adhesion within the island domains (Figure S4.13b,d). This observation suggests that the surface components for the islands are dissimilar from those for ridges and interdomain region, supporting the proposed model that the islands are formed by the integration of hydrophobized PNIPAM arms. The FDC analysis also shows the similarity in elastic modulus and adhesion between the ridges and interdomain region. Notably, island domains possess a lower elastic modulus of 1.4 ± 0.4 GPa suggesting that the island domains are formed by PNIPAM macrocations, which are much softer than the other composition of the HBPEs, hyperbranched core and octadecyl tails.[246,247,250,251,252] It should be noted that all measurements discussed above were conducted in an ambient air,

which is a bad solvent for all compositions of the HBPEs and for all temperatures. Therefore, with all molecular components collapsing in air, the topmost surface of the monolayers can show a relative uniformity of elastic properties irrespective of constituents.

In contrast to dry conditions, a clear heterogeneity of mechanical properties was observed by QNM measurements in water below and above LCST (Figure 4.11). Firstly, the individual domains show a lower elastic modulus than the interdomain region below LCST (Figure 4.11a), which is also confirmed by the FDC analysis (Figure 4.12a). The surface adhesion distribution displays that the individual domains possess a higher adhesion than the interdomain region (Figure 4.11c), and the average adhesive force for the domains is four-fold higher than that for the interdomain region (1.1 nN and 0.3 nN, respectively) according to the FDC analysis (Figure 4.12a).

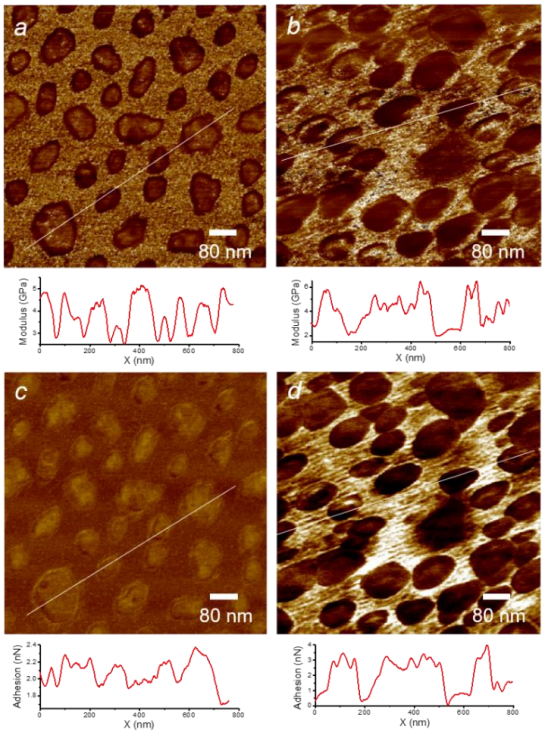

Figure 4.11. Elastic modulus (a,b) and adhesion (c,d) distribution of HBPE monolayers deposited at surface pressure 20 mN/m at different temperatures: 23℃ (a,c) and 37℃ (b,d). The images were collected in water at temperature below (a,c) and above LCST (b,d). Z scale is 250 MPa and 5 nN for the modulus and adhesion images, respectively.

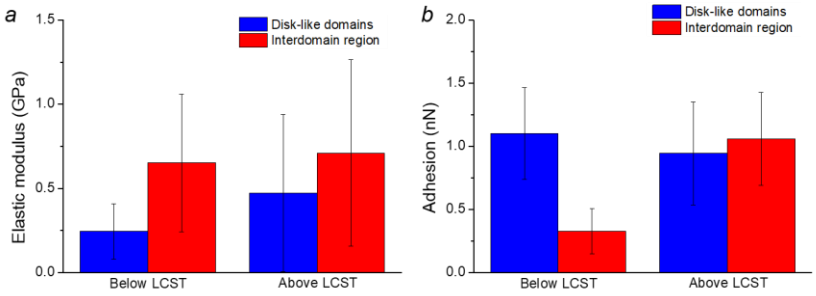

Figure 4.12. Elastic modulus (a) and adhesion (b) of the domain and spreading areas of HBPE monolayers at surface pressure 20 mN/m. All measurements were performed in water below and above PNIPAM LCST temperature.

These results suggest that the topmost surface of the domains is composed of softer and more hydrophilic components than the interdomain region.[253] In addition, such heterogeneity of mechanical response is in stark contrast to that under dry conditions, indicating that the molecular reorganization occurs in water below LCST with PNIPAM chains saturating the water-domain interface. When exposed to water, hydrophilic and soft segments, such as terminal ionic groups and PNIPAM macrocations, beneath hydrophobic and stiff components of the dried films swell and emerge to the surface, while the hydrophobic segments collapse in water, which is a bad solvent for these terminal groups.[254,255]

Above LCST, the modulus distribution changed to rather uniform across all domains and interdomain region (Figure 4.11b). The FDC analysis also shows the reduced difference in the average elastic modulus between the domains and interdomain region. The average elastic modulus for the domains increases from 250 MPa below LCST to 470 MPa above LCST, while for the interdomain region, the average values of elastic modulus are about 700 MPa for both temperatures. In addition, the adhesion distribution shows a higher adhesion for the interdomain region, which is in contrast to that observed below LCST (Figure 4.11d). However, the FDC analysis shows that the adhesive forces for the domains and interdomain region are similar above LCST (0.9 nN and 1.1 nN, respectively) (Figure 4.12b). These changes in mechanical contrast distribution suggest additional reorganization of HBPE molecules due to the hydrophilic-hydrophobic transformation of PNIPAM chains. PNIPAM fragments are transited from swollen to collapsed state

preferably in the domains with their subsequent aggregation accompanied by orientation of hydrophilic ionic ammonium and carboxylate groups on the surface of the aggregates formed. This reorganization might enable the hyperbranched core to be exposed to the surface, leading to the increased elastic modulus above LCST, and the ionic groups oriented onto the surface could predominate the adhesive forces across the entire area of the monolayers.

It should be also added that the increase in elastic modulus of PNIPAM fragments above LCST can contribute to the increased elastic modulus due to water repulsion from collapsed shells. It has been reported that the elastic modulus of PNIPAM films increases by two orders of magnitude from around 10-100 kPa in highly swollen state below LCST to several MPa in collapsed state above LCST.[250,256,257] In addition, the temperature-induced change in mechanical response confirms that the PNIPAM fragments provide thermally responsive surface behavior, supporting the proposed model that they have a critical role in the formation of HBPE monolayers with temperature-dependent morphology.

4.4 Conclusion

In this paper, we report the synthesis and assembly behavior of novel amphiphilic hyperbranched polyelectrolytes at the air-water interface. The HBPEs studied here consist of asymmetrical peripheral composition of hydrophobic octadecyl tails and hydrophilic PNIPAM macrocations, which provides HBPEs with amphiphilicity as well as thermo-responsive behavior. Stable HBPE monolayers were successfully formed with diverse morphologies at the interface. The disk-like domains were formed in a liquid phase and transformed into almost uniform with the network of ridge-like domains representing interdomain boundary in a solid phase due to the high stability of disk-like morphology. In a solid phase, islands connected by the network of ridge-like domains were only observed above LCST due to the integration of hydrophobized PNIPAM macrocations into monolayers.

Moreover, we observed the transition in mechanical response of HBPE monolayers from homogenous distribution in a dry state to heterogeneous distribution in a wet state, suggesting the surface reconstruction under wet conditions, which further supports that the

as-assembled HBPE monolayers are composed of hydrophobic surface and hydrophilic underlying sub-layer. Further change in the mechanical response was observed when water temperature increased above LCST, which confirms the important role of thermo-responsive PNIPAM macrocations in the monolayer formation. The distribution of mechanical properties changed from highly contrasted two-phase distribution below LCST to near uniform distribution above LCST due to the molecular reorganization associated with the hydrophilic-hydrophobic transformation of PNIPAM macrocations above LCST. Therefore, the thermo-responsive HBPEs synthesized in this study enable the design of multifunctional, smart nanofilms with tunable morphologies and mechanical response.

Chapter 4 Appendix: Supporting Information

Materials

SI4-1. Materials.

N-octadecylisocyanate (Aldrich, 98%) and poly(N-isopropylacrylamide) (PNIPAM) amine terminated ("Aldrich", Mn = 2500 g/mol) were used as received. Hyperbranched aliphatic oligoether polyol (HBP-OH) Boltorn H30 (Perstorp, Sweden) with weight average molecular weight (MW) of 3500 g/mol (comprising 32 terminal OH groups in outer shell) was purified by precipitation of dimethylformamide (DMF) solution in diethyl ether followed by vacuum drying at 25-30 °C for 6 h (an equivalent MW measured by hydroxyl groups via acetylation technique is equal to 117 gram/equivalent). Phthalic anhydride was purified by sublimation. DMF, diethyl ether, acetone, isopropyl alcohol, acetonitrile, chloroform were dried and distilled before use. The content of acidic groups in the composition of synthesized hyperbranched carboxyl and sulfone derivatives at intermediate stage were determined by reverse acid-base titration.[258] The ultrapure water used in all experiments was prepared in a three-stage Millipore Milli-Q Plus 185 purification system (resistivity ≥18.2 MΩ·cm). All PILs were dissolved in a tetrahydrofuran (BDH, CAS No 109-99-9) for 16 h at room temperature. The resulting solution was added dropwise to water under stirring in Laminar Airflow unit at room temperature. The tetrahydrofuran (THF) was evaporated by thorough stirring for 20 h. The final concentration of PEs was 5 mg/mL.

SI4-2. Synthesis of hyperbranched polyelectrolytes.

Synthesis of initial hyperbranched polycarboxylic acid (abbr. HBP-24Oct8COOH) with octadecyl tails.

HBP-24Oct8COOH was obtained as we described earlier.[105] 5.894 (0.0200 g-equivalent) of n-octadecylisocyanate was added to 3.124 g (0.0267 g-equivalent) of HBP-OH in 16 ml of DMF at 80 °C and reaction was held under stirring for 12 h until the isocyanate groups were completely consumed (according to FT-IR spectroscopy) (see Figure S4-1). Further

0.981 g (0.0067 g-equivalent) of phthalic anhydride was added to the resultant solution followed by reaction for 20 h at 80 °C being stirred. The solvent was partially evaporated under reduced pressure and the remaining product was re-precipitated from acetone to hexane and dried at 40-50 °C. Yield 6.24 g (62.4%). COOH group content: 2.8% (calculated 3.0%). The product is a clear light brown liquid, readily soluble in hexane, alcohols, chloroform, and DMF and insoluble in acetone, water, and diethyl ether.

Synthesis of hyperbranched thermally responsive HBPE (Abbr. HBP-24Oct8[COO]$^-$ [PNIPAM]$^+$).

The HBPE was synthesized by neutralisation of 1.956 g (0.0012 g-equivalent) of hyperbranched oligoester polycarboxylic acid C8 with 3.043 g (0.0012 g-equivalent) PNIPAM in 5 ml of isopropyl alcohol followed by precipitation of resultant product to diethyl ether. The synthesized compound was purified by reprecipitation from alcohol to diethyl ether. Yield 4.83 g (96.6%). The compound C8P8 is a light brownish solid soluble in isopropyl alcohol, chloroform and THF, soluble under heating in DMF and DMSO, partially in water and insoluble in hexane and diethyl ether.

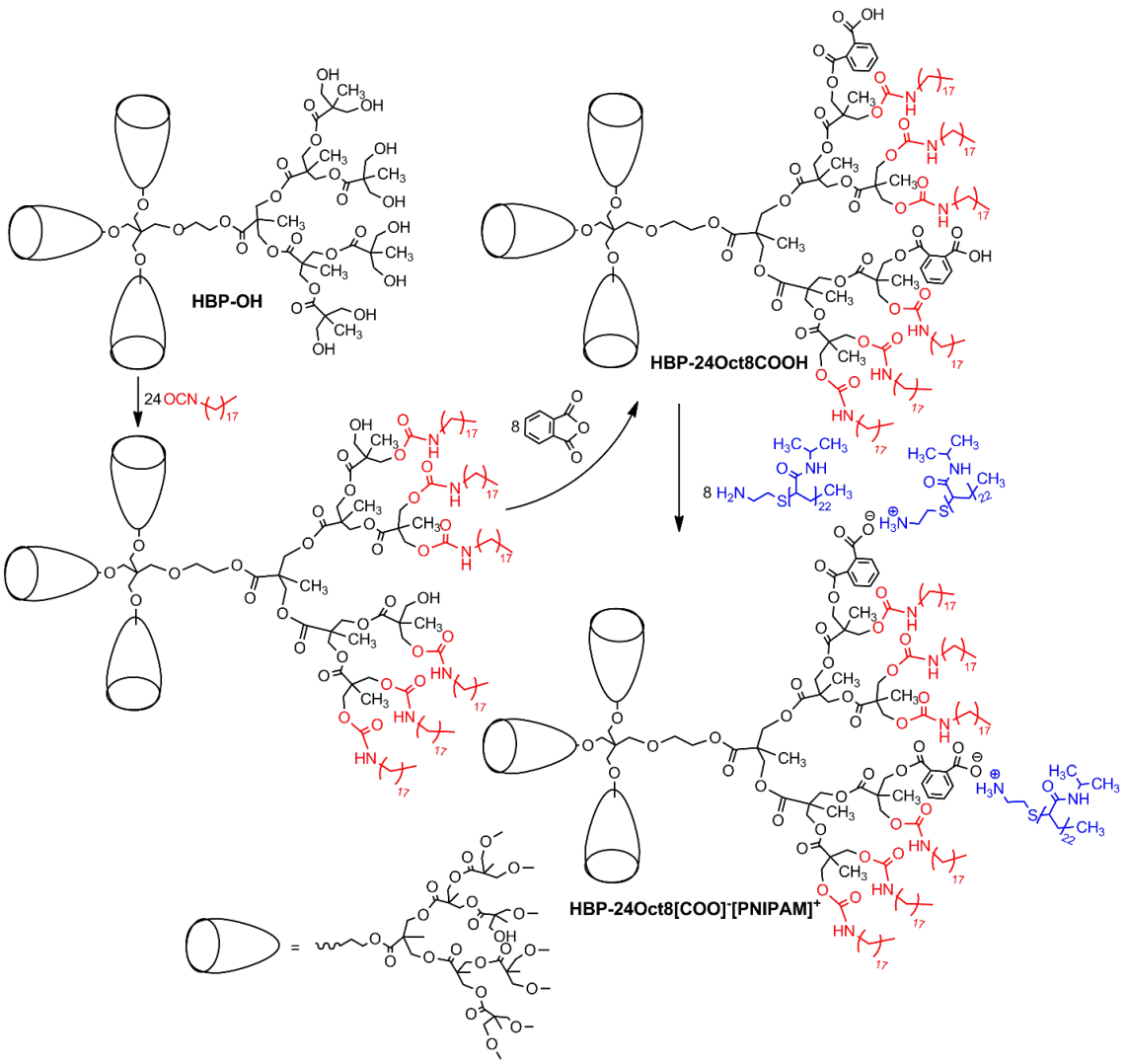

Figure S4.1. Synthesis of hyperbranched thermally responsive protic anionic HBPE, HBP-24Oct8[COO]$^{-}$[PNIPAM]$^{+}$

FT-IR: ν C=O amide I (1649 cm^{-1}), ν NHC=O, δ N-H amide II (1543 cm^{-1}), ν C=O of ester and carboxylate groups (1703-1735 cm^{-1}), δ C-H of CH_2, δ as C-H of CH_3 (1460 cm^{-1}), δ sy C-H of CH_3 (1367, 1387 cm^{-1}), γ C-H of CH_3 (1087-1312 cm^{-1}), ν C-H of CH_2 (2874, 2922, 2972 cm^{-1}), ν ar C-H (3075 cm^{-1}), ν N-H of ammonium, amide and urethane groups (3130-3700 cm^{-1}).

^{1}H NMR (DMSO-d$_6$): 0.76-1.14 (CH(C**H**$_3$)$_2$, CH_2C**H**$_3$, C(CH_2CO(O))C**H**$_3$, 313H), 1.24 (CH_2C**H**$_2$$CH_2$, 198H), 1.46 (CH(C(O)NH)C**H**$_2$, 86H), 1.99 (C**H**(C(O)NH)CH_2, 44H), 2.25-4.30 (C**H**$_2$ of HBP core, C**H**$_2$S, NH_3^+C**H**$_2$, 126H), 3.48 (OC(O)NHC**H**$_2$, 12H), 3.85

(C**H**$(CH_3)_2$, 42H), 4.80 ($CH_2OC(O)N$**H**CH_2, 6H), 6.83-7.90 (Ar, CH(C(O)N**H**)CH_2, 48H), 8.77 (N**H**$_3^+$, 2H).

Degree of branching (DB)

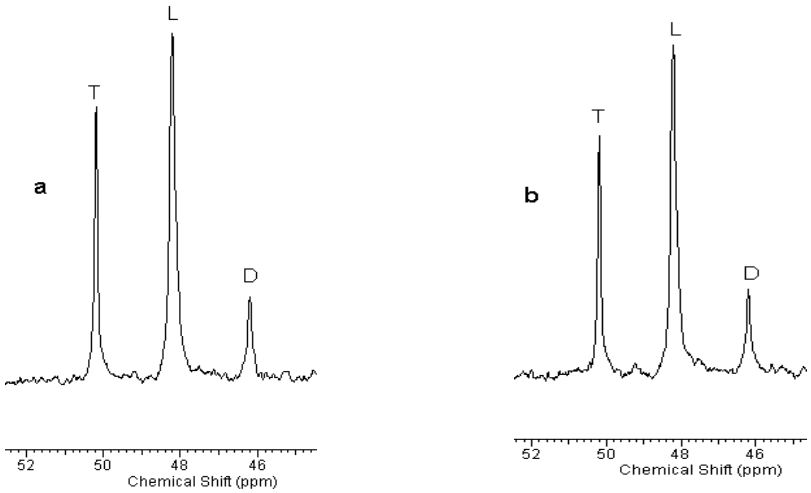

Figure S4.2. ^{13}C NMR spectra of initial HBP-OH with decoupling during relaxation (a) and without decoupling (b)

The degree of branching (DB) of the initial HBP-OH was determined based on the ^{13}C NMR (Fig S4.2) spectra according to Ref.223 The spectra was recorded with signal accumulation (200 scans) both with (Fig S4.2(a)) and without (Fig S4.2(b)) decoupling. DB was calculated in accordance with Ref.223 as the ratio of the sum of the integrals corresponding to the signals of a quaternary carbon atom in branched (D) units and those containing terminal functional groups (T) to their sum with integral corresponding to quaternary carbon atom in linear units (L) (Fig. S4.2). Chemical shifts and integrals values for the Fig. S4.2 are summarized in Table S4.1. DB values obtained on the basis of the ^{13}C NMR spectra recorded both with and without decoupling are almost the same and constitute respectively 38,9% and 38,4%.

Table S4.1. Chemical shifts and integral values for ^{13}C NMR spectra (Fig. S2) of initial HBP-OH with and without decoupling

Unit	Chemical shift, ppm		Integration, relative units	
	with decoupling	without decoupling	with decoupling	without decoupling
D	46.20	46.20	12.73	17.94
L	48.20	48.21	67.53	31.92
T	50.19	50.19	30.26	80.00

MW characteristics

Table S4.2. MW values for the initial HBP-OH, oligomeric polycarboxylic acid HBP-24Oct8COOH and HBPE, HBP-24Oct8$[COO]^-[PNIPAM]^+$

Sample	MW g/mol	
	Calculated	Found
HBP-OH	3564	3744
HBP-24Oct8COOH	13204	12857
HBP-24Oct8$[COO]^-[PNIPAM]^+$	33204	32857

The MW values for the initial HBP-OH, polycarboxylic acid HBP-24Oct8COOH and HBP-PIL HBP-24Oct8$[COO]^-[PNIPAM]^+$ were calculated based on their ideal structures (Figure S4.1). The real (found) MW value for HBP-OH was established with use of acetylation technique (see "SI4-1. Materials"). The real (found) MW value for the oligomeric acid HBP-24Oct8COOH was established via acid-base titration technique (see "SI4-1"). The real (found) MW value for HBPE, HBP-24Oct8$[COO]^-[PNIPAM]^+$ was

calculated based on the MW value for the oligomeric acid HBP-24Oct8COOH and PNIPAM.

SI4-3. Thermoresponsive phase behavior of HBPILs

Measurement of Transmittance vs Temperature

To investigate temperature-induced phase behavior of HBPEs, the transmittance of HBPIL aqueous solution vs temperature was observed at 500 nm using Chirascan-plus spectrometer (Applied Photophysics) in the temperature range of 25-50 °C.

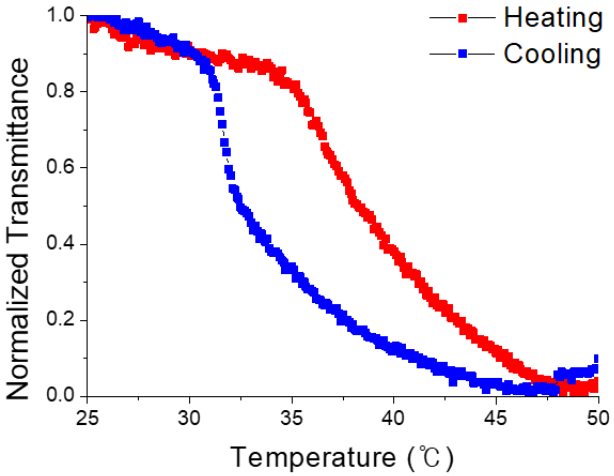

Figure S4.3. Transmittance of HBPEs aqueous solution (0.5 mg/mL) vs temperature during heating and cooling (Heating and cooling rate was 0.5 °C/min).

Measurement of Contact Angle

The contact angle of water on the HBPE monolayer films was measured using a KSV CAM101 measuring system within 10 s of application of the water drop and at least three separate locations on the sample.

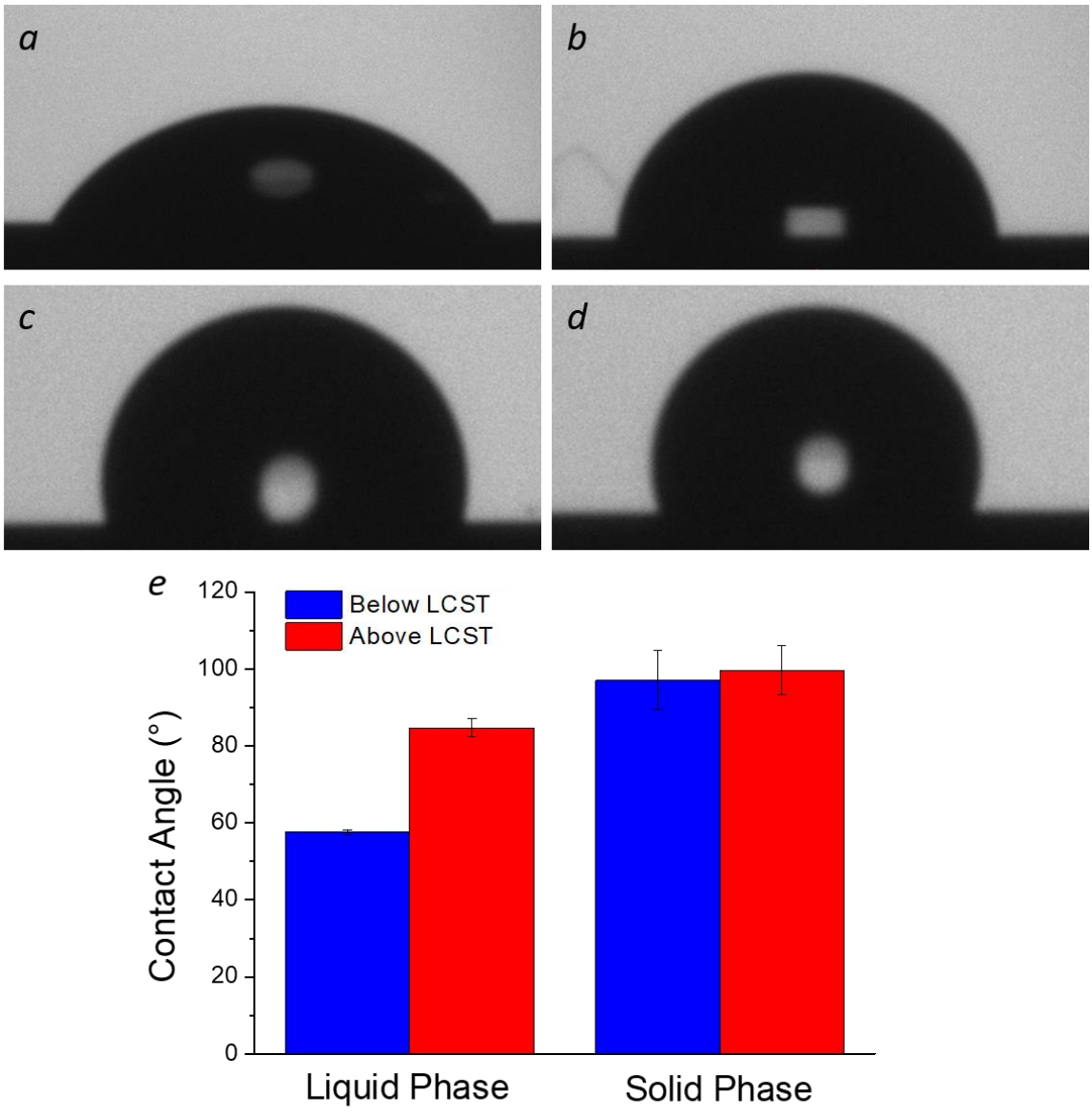

Figure S4.4. Water contact angle on HBPE monolayer films deposited in a liquid phase (a,b) and in a solid phase (c,d) and at different temperatures; 23 °C (a,c) and 37 °C (b,d). Corresponding contact angle measurements (e).

SI4-4. Langmuir isotherms of HBPE monolayers

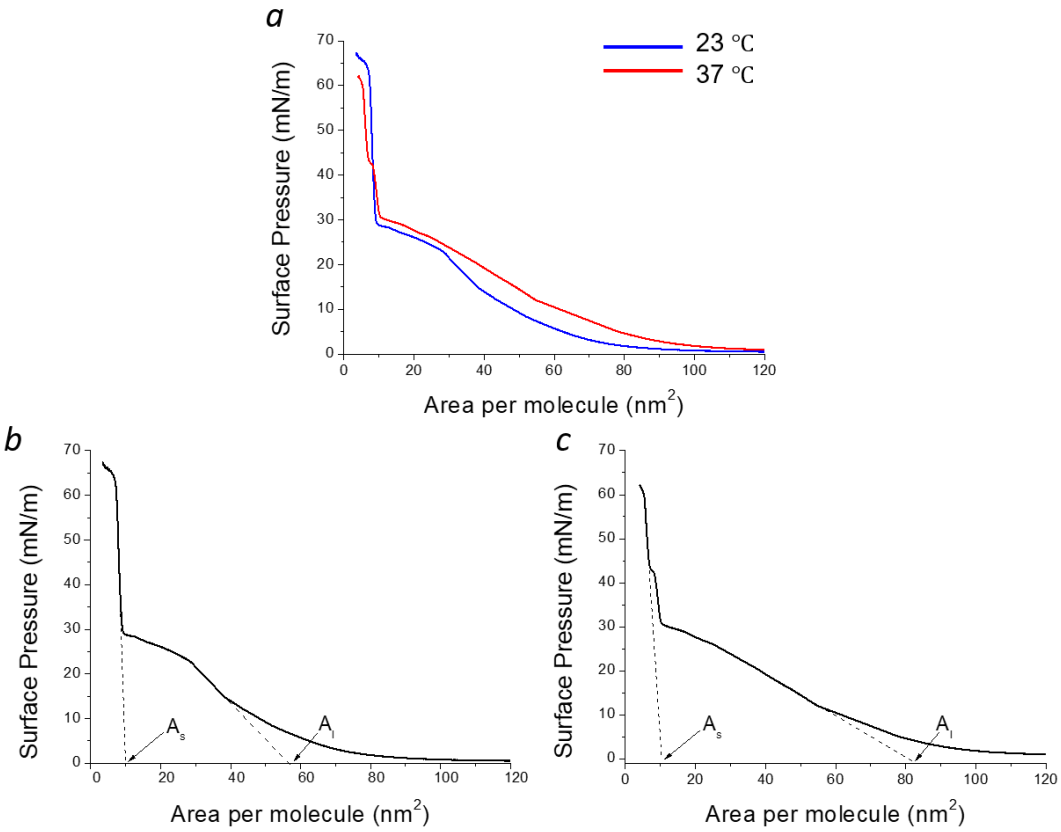

Figure S4.5. Langmuir isotherms of HBPEs during first compression at different temperatures (a). Langmuir isotherm recorded at 23 °C (b) and 37 °C (c), showing the limiting area per molecule in solid and liquid phases (A_s and A_l, respectively).

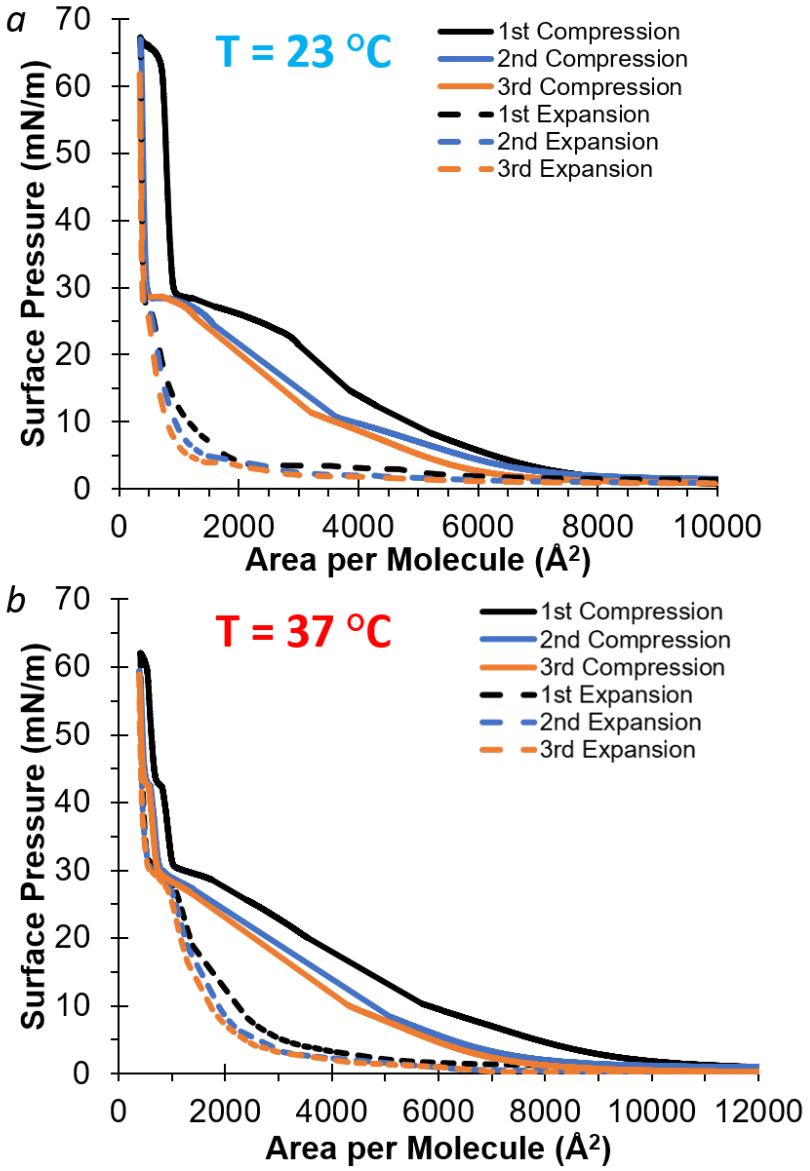

Figure S4.6. Langmuir isotherms of HBPEs at 23 °C (a) and 37 °C (b) recorded during multiple compression-expansion cycles.

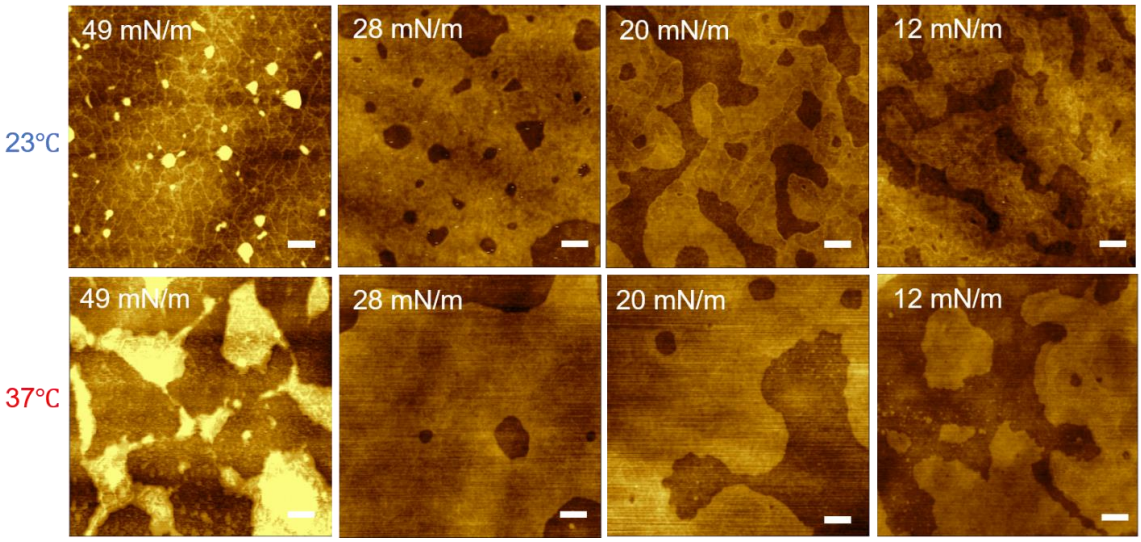

Figure S4.7. AFM height images of HBPE monolayers deposited at 23 °C (top) and 37 °C (bottom) at different surface pressures during second compression. Scale bar is 200 nm and Z scale is 10 nm for all images.

***SI4-5*. Morphology of HBP monolayers Deposited from Air-Water Interface.**

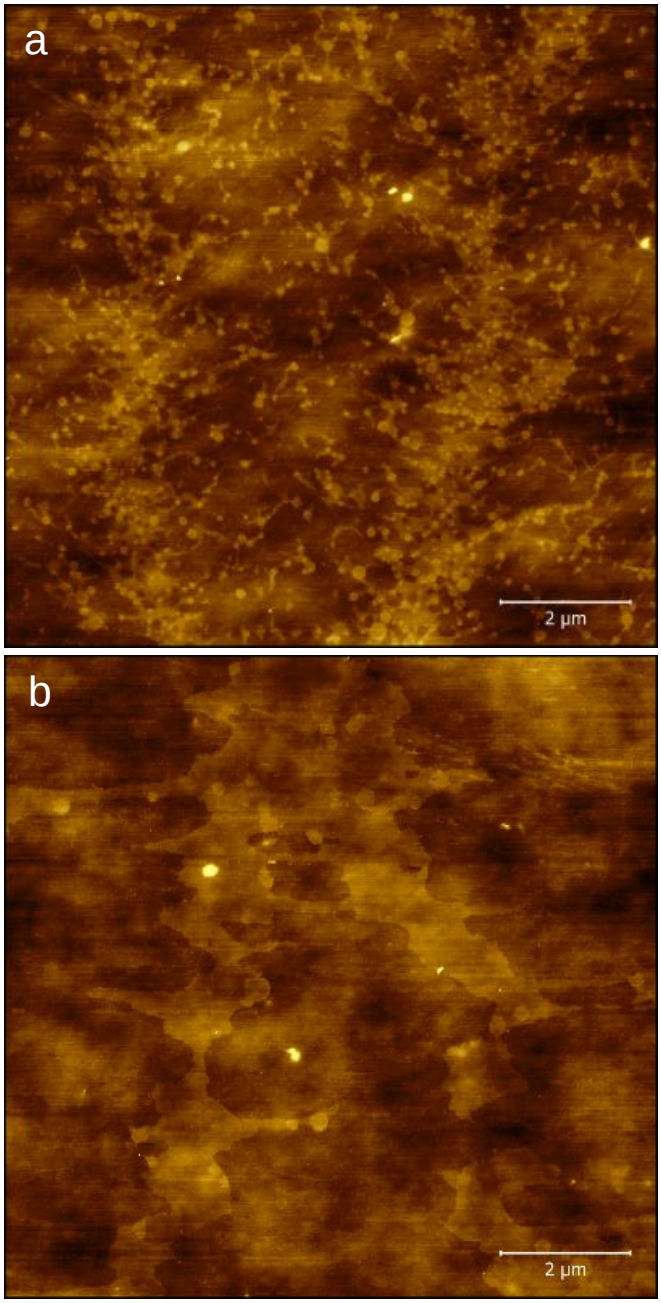

Figure S4.8. AFM image of HBPE monolayers at 0.3 mN/m at 23℃ (a) and 37℃ (b). Z scale is 11 nm for both images.

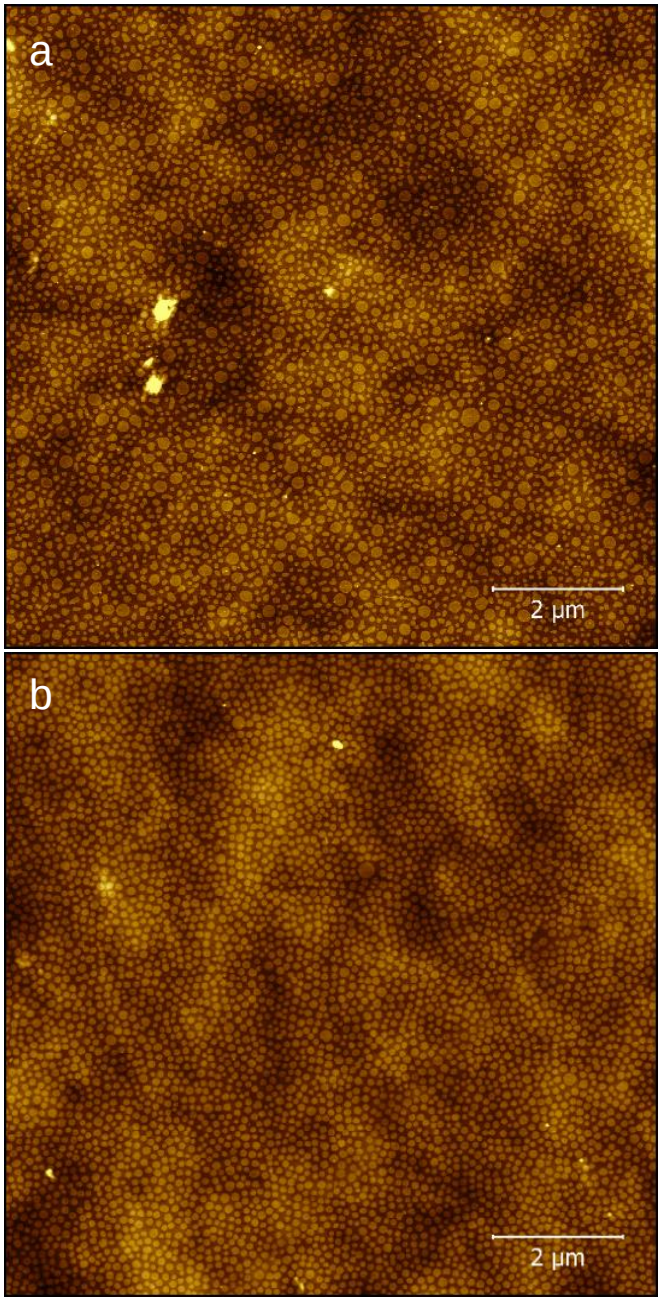

Figure S4.9. AFM image of HBPE monolayers at 20 mN/m at 23℃ (a) and 37℃ (b). Z scale is 7 nm for both images.

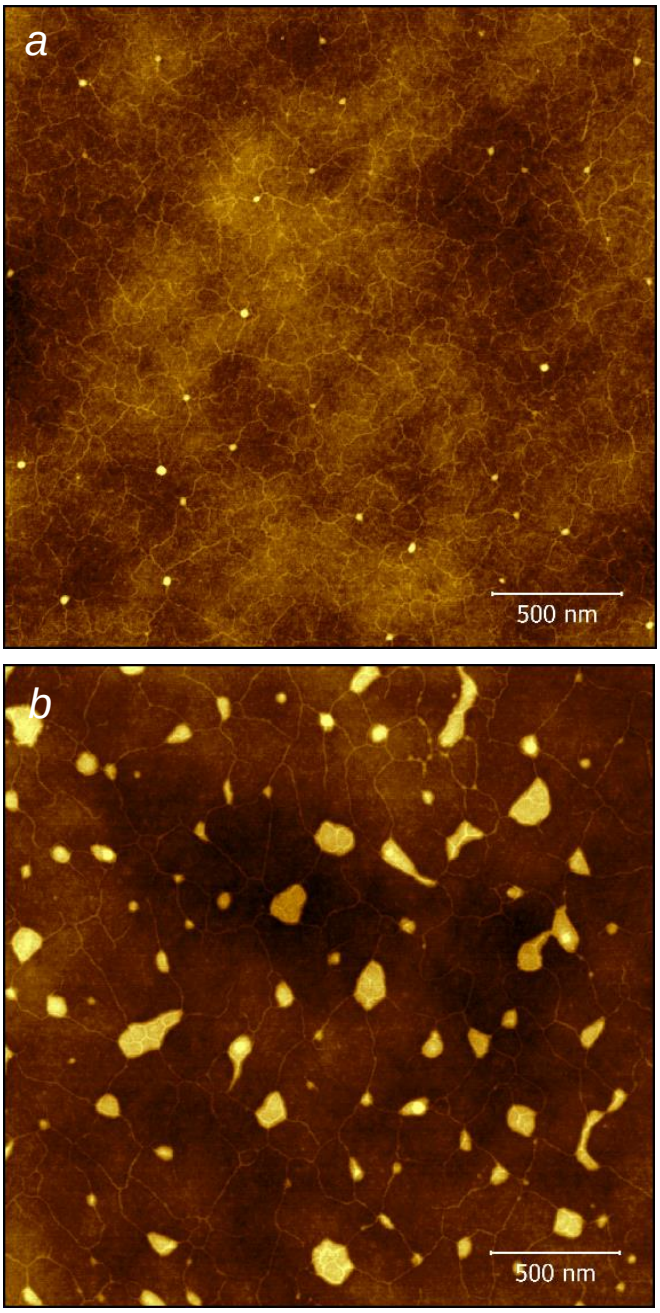

Figure S4.10. AFM image of HBPE monolayers at 49 mN/m at 23℃ (a) and 37℃ (b). Z scales are 6 nm (*a*) and 9 nm (b).

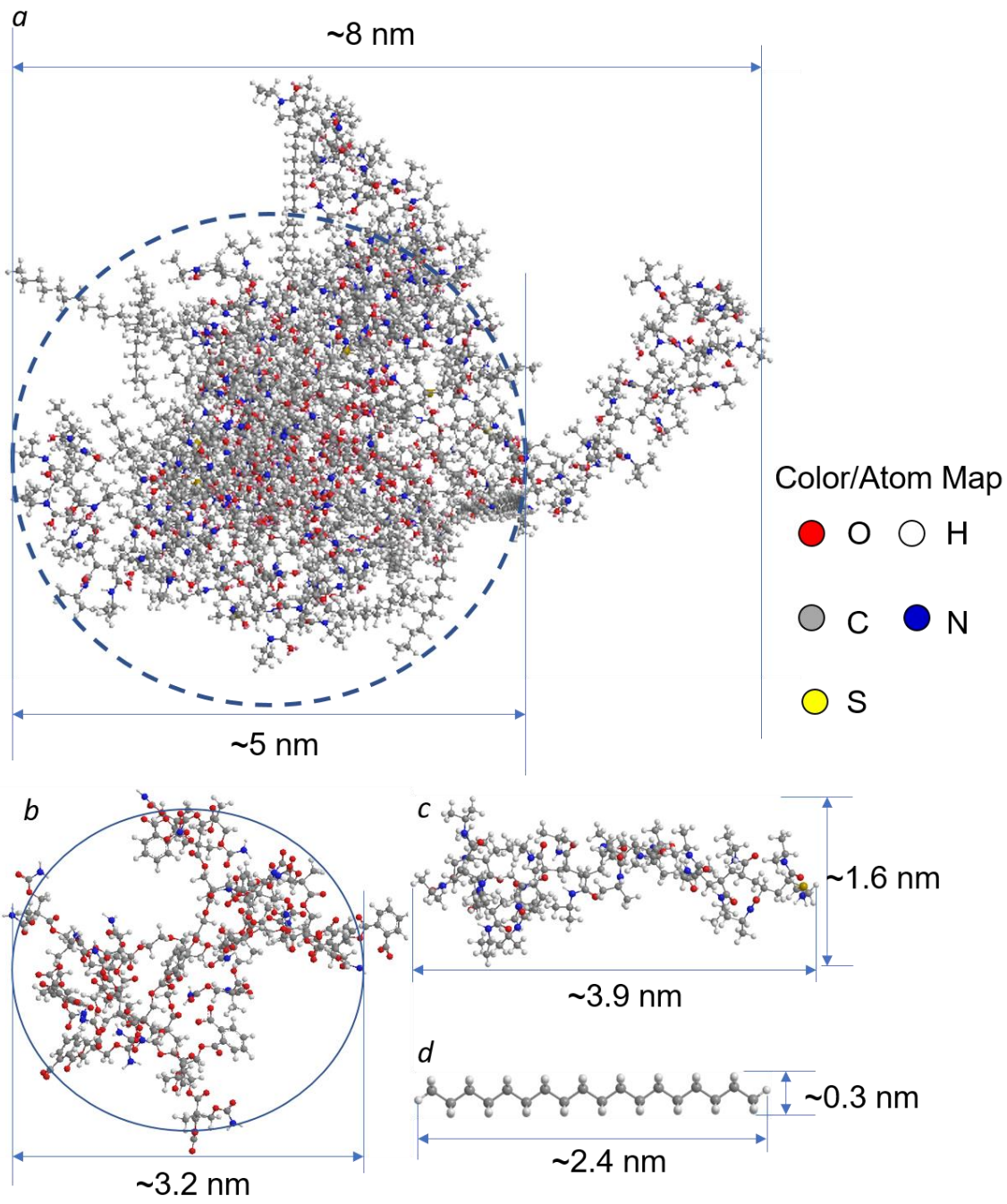

Figure S4.11. Molecular modeling of HBPEs (a), hyperbranched polyester core (b), PNIPAM macrocation (c), and octadecyl chain (d).

SI4-6. **Molecular modeling of hyperbranched polyelectrolytes**

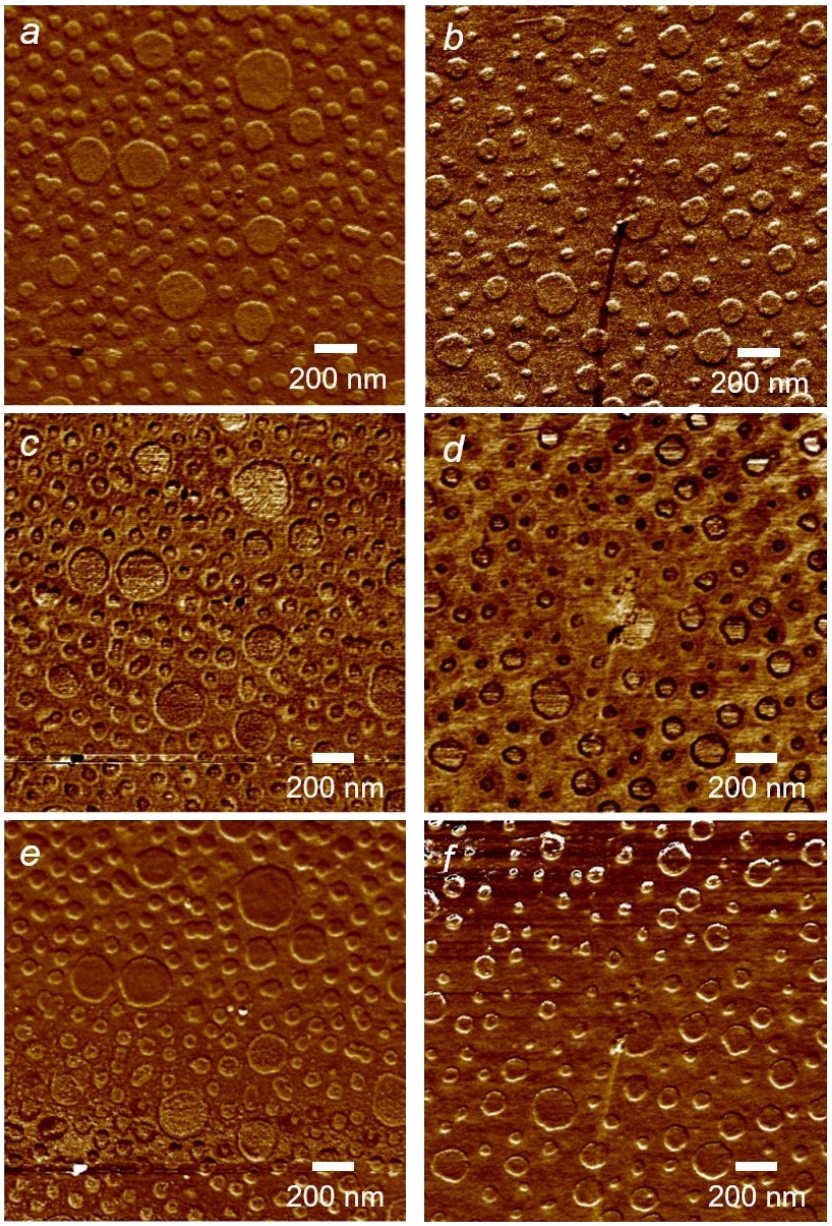

Figure S4.12. Elastic modulus (a,b), adhesion (c,d) and deformation (e,f) images of HBPE monolayers at 20 mN/m at different water subphase temperatures: 23 °C (left) and 37 °C (right) Z scale for DMT modulus image is 600 MPa for (a) and 1,200 MPa for (b). Z scale for adhesion images (c,d) is 4 nN and for deformation images (e.f) is 3 nm. The images were collected in a dry state.

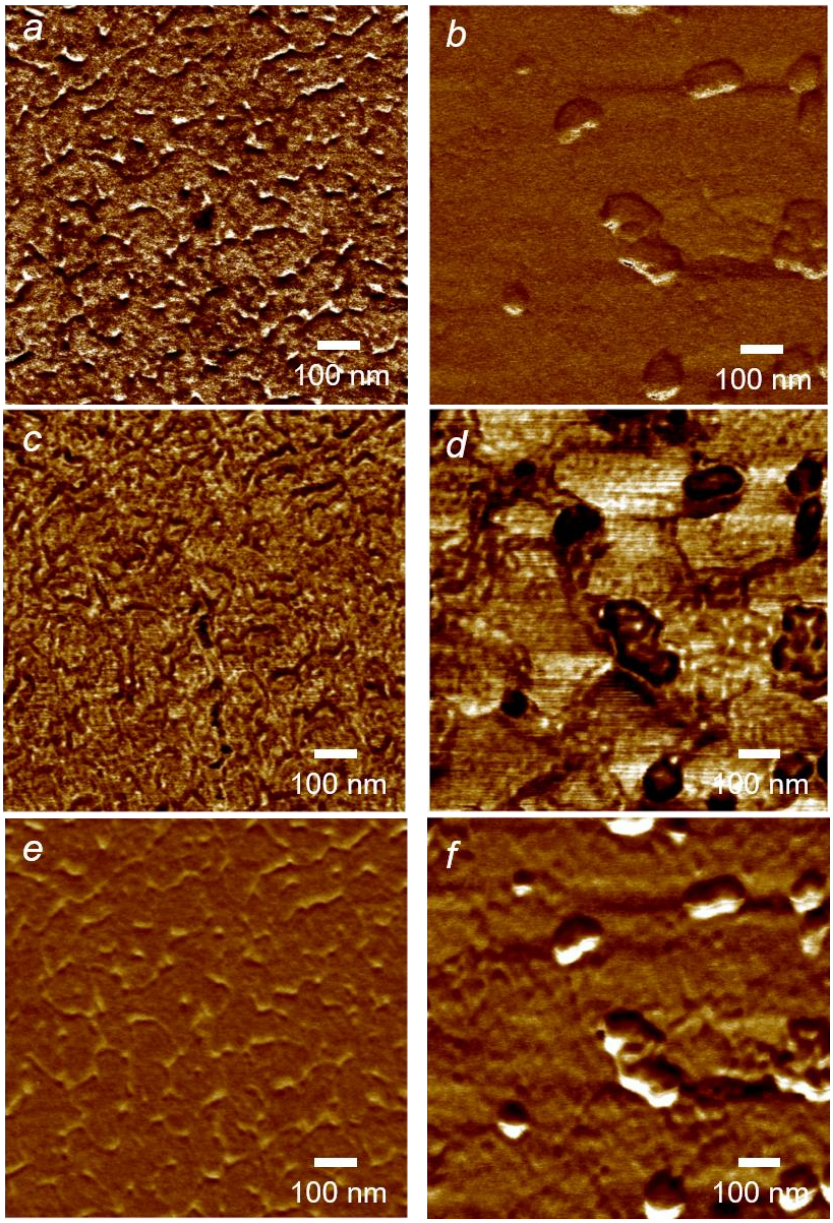

Figure S4.13. Elastic modulus (a,b), adhesion (c,d) and deformation (e,f) distributions of HBPE monolayers at 49 mN/m and at 23 °C (left) and 37 °C (right). Z scale for elastic modulus image is 4 GPa and 2 GPa for (a) and (b), respectively. Z scale for adhesion images is 2nN and 4 nN for (c) and (d), respectively. Z scale for deformation images is 3 nm and 6 nm for (e) and (f), respectively. The images were collected in a dry state.

SI4-8. Force-distance curve analysis of HBPIL monolayers

Force-distance curve (FDC) analysis.

FDC data were analyzed using a micromechanical analysis software where Sneddon's model is employed as described in detail elsewhere.[222] Briefly, in the nanomechanical test, the data is analyzed in terms of the continuous penetration of the AFM tip into the material as induced by the near-normal load (so-called loading curves). These loading curves are derived from experimental FDCs in which cantilever deflection *d* and position *z* are directly measured while the tip moves toward (approaching curve) or away from (retracting curve) the surface. The penetration, δ is determined as a difference between the piezoelement displacement (Δz) and the cantilever deflection (Δd), $\delta = \Delta z - \Delta d$, and it accounts for the amount of the local deformation of the surface. Assuming purely elastic cantilever behavior with a spring constant *k*, the force exerted by the AFM tip on the surface, *F*, can be calculated from the cantilever deflection as $F = k\Delta d$.

Considering the indenter is much harder than the studied material, Sneddon's model is used to solve the problem of the indentation of an axisymmetric hard punch into an elastic half space with Young's modulus *E*. According to this model, the following equation is used for an axisymmetric tip with a parabolic cross-section:

$$F = \frac{4}{3}\sqrt{R}E'\delta^{3/2} \qquad (1)$$

where *R* is the radius of curvature of the apex of paraboloid, and $E' = E/(1 - \nu^2)$ is the reduced modulus of the material with Poisson's ratio ν. Poisson's ratio $\nu = 0.3$ was used in this study with the assumption that the surface of HBPIL monolayers is composed of alkyl tails which have an elastic modulus over 1 GPa.[259] Fitting of the $\delta^{3/2}$ penetration data versus force data with Eq. (1) allows for the calculation of the elastic modulus of the material. Only the approaching curves were used for fitting in this study to avoid large hysteresis in retracting curves as a result of adhesive contributions and piezoelement creep.

In the case where a remarkable adhesion is present, the adhesive forces may change the behavior of tip-sample contact interaction, producing negative cantilever deflection jump, particularly during the retraction of the FDC. Two models of adhesive contact interactions, Derjaguin-Muller-Toporov [260] and Johnson-Kendall-Roberts [261] models, were used to account the adhesive forces in elastic property calculation. In addition, the adhesive forces were determined from the minimum point of cantilever deflection in the retracting curve.

Force-distance curves and loading curves of HBPE monolayers in air

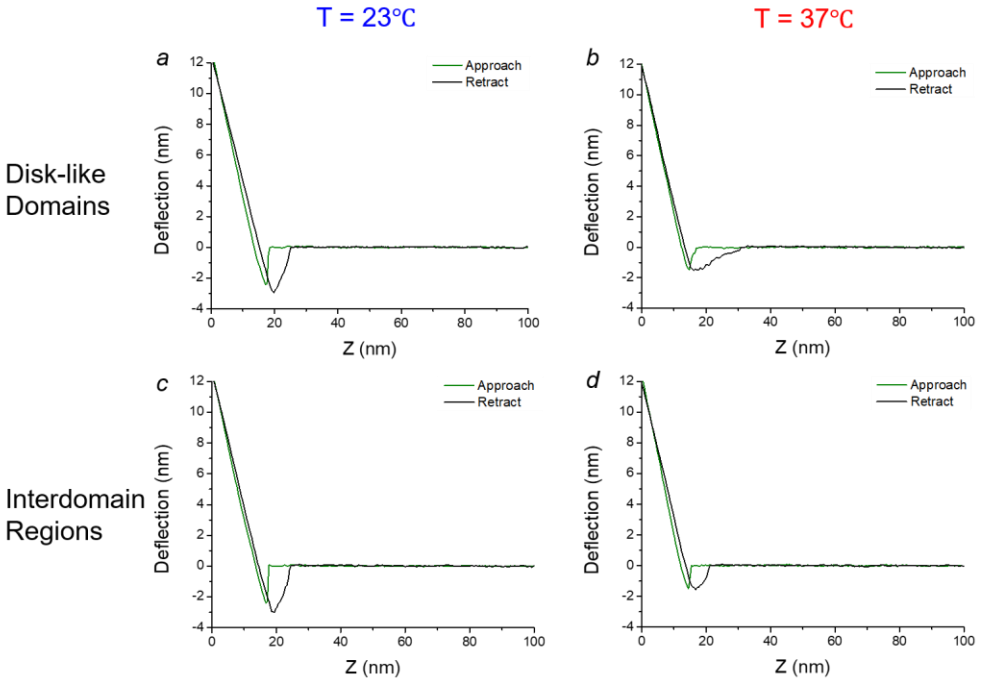

Figure S4.14. Representative tip deflection-displacement (Z) curves for (a,b) disk-like domains and (c,d) interdomain regions of HBPE monolayers deposited in a liquid phase at different water temperatures: (a,c) 23℃ and (b,d) 37℃. The experiments were conducted in a dry state.

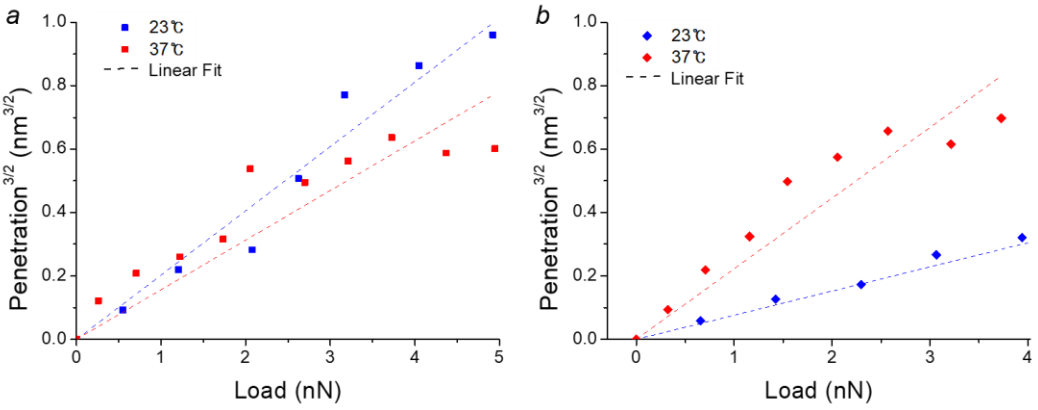

Figure S4.15. Representative loading curves ($\delta^{3/2}$ vs force) for (a) disk-like domains and (b) interdomain regions of HBPE monolayers deposited in a liquid phase at different water temperatures: (a) 23℃ and (b) 37℃. The experiments were conducted in a dry state.

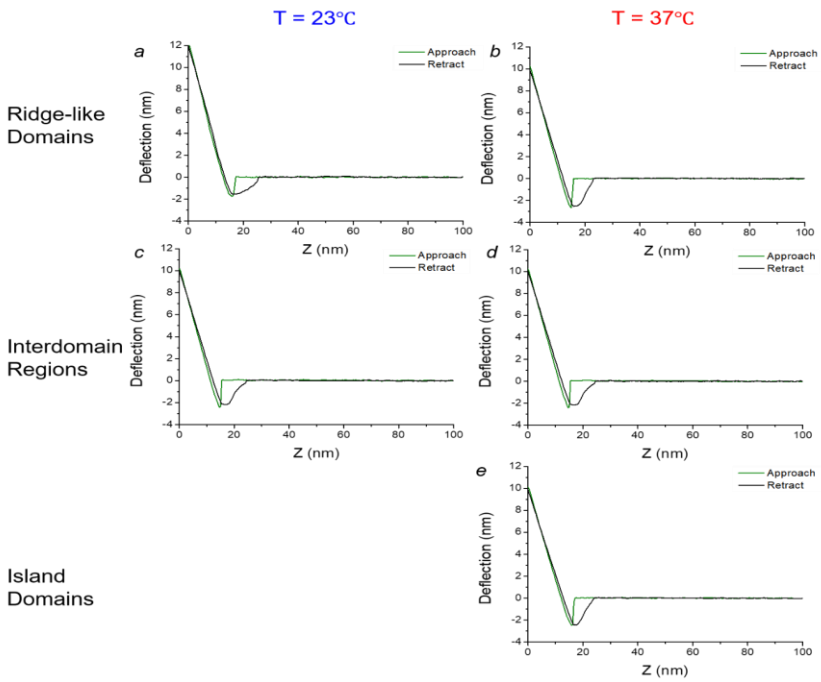

Figure S4.16. Representative tip deflection-displacement (Z) curves for (a,b) ridge-like domains, (c,d) interdomain regions and (e) island domains of HBPE monolayers deposited in a solid phase at different water temperatures: (a,c) 23 ℃ and (b,d,e) 37 ℃. The experiments were conducted in a dry state.

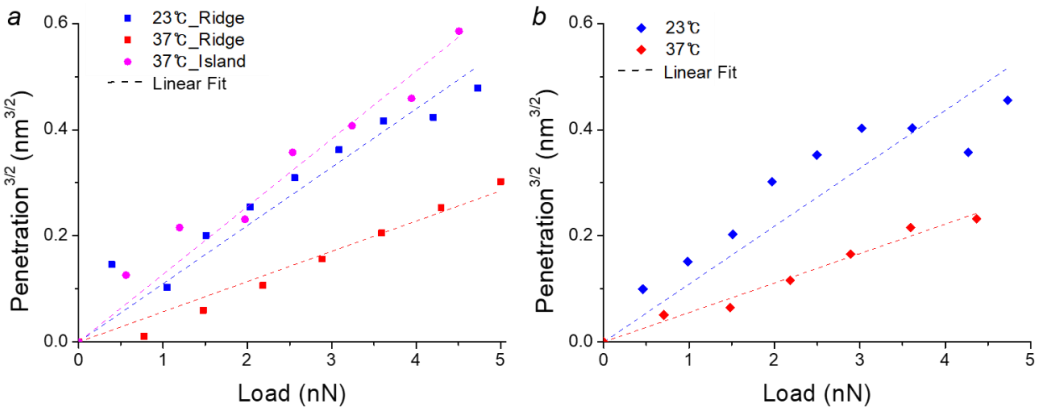

Figure S4.17. Representative loading curves ($\boldsymbol{\delta}^{3/2}$ vs force) for (a) ridge-like and island domains and (b) interdomain regions of HBPE monolayers deposited in a solid phase at different water temperatures: (a) 23℃ and (b) 37℃. The experiments were conducted in a dry state.

Elastic modulus and adhesion for HBPE monolayers in a solid phase

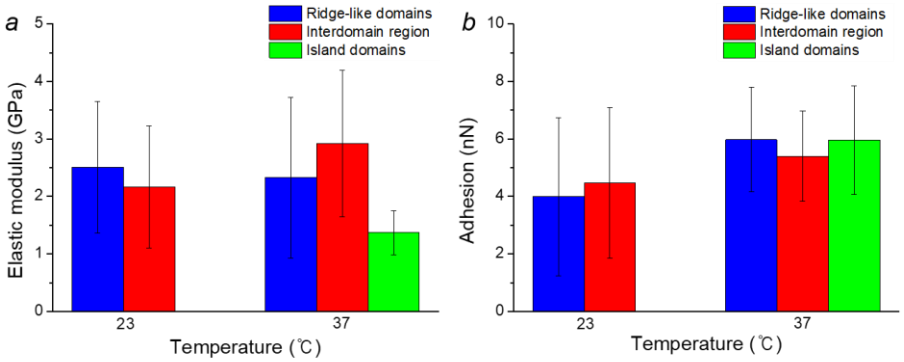

Figure S4.18. Elastic modulus of the domains and interdomain region of HBPE monolayers deposited at 49 mN/m at different water subphase temperatures: 23 °C and 37 °C. The measurements were performed in a dry state.

Force-distance curves and loading curves of HBPE monolayers in water

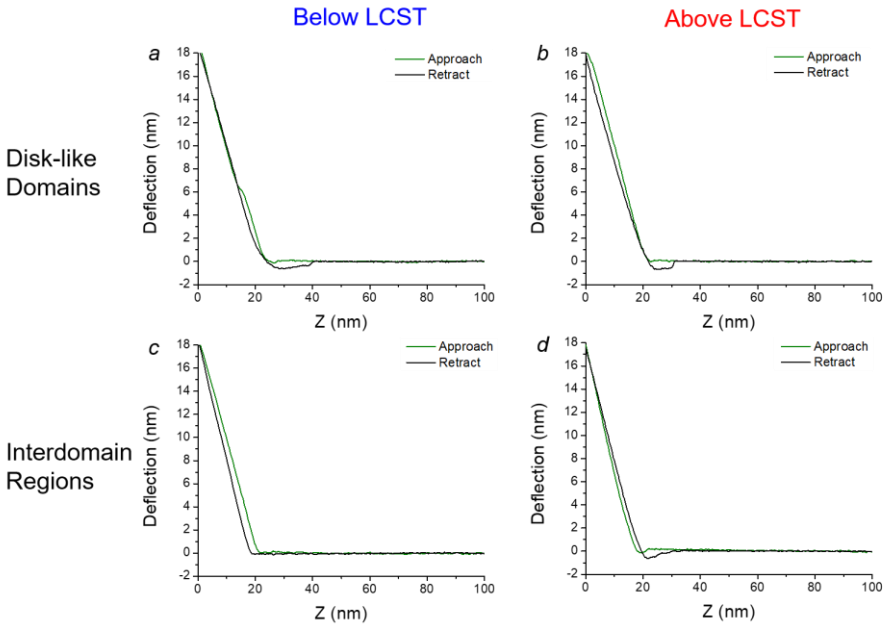

Figure S4.19. Representative tip deflection-displacement (Z) curves for (a,b) disk-like domains and (c,d) interdomain regions of HBPE monolayers deposited in a liquid phase at different water temperatures: (a,c) 23 ℃ and (b,d) 37℃. The experiments were conducted in water below and above LCST (34 ℃).

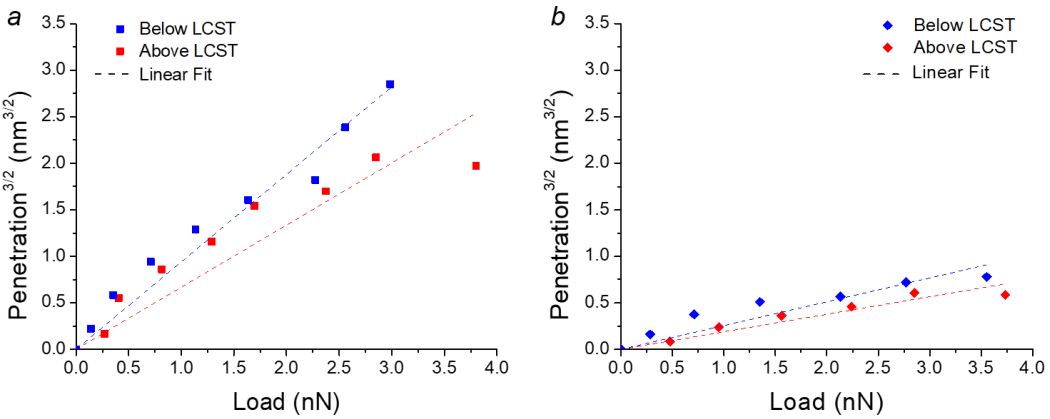

Figure S4.20. Representative loading curves ($\boldsymbol{\delta}^{3/2}$ vs force) for (a) disk-like domains and (d) interdomain regions of HBPE monolayers deposited in a liquid phase at different water temperatures: (a,c) 23 ℃ and (b,d) 37 ℃. The experiments were conducted in water below and above LCST (34 ℃).

CHAPTER 5. ASSEMBLY OF WEAKLY IONICALLY BOUND THERMO-SENSITIVE HYPERBRANCHED POLYELECTROLYTES

5.1 Introduction

Incorporating ionizable groups into macromolecular backbones is a known strategy for generating nanostructures that can change morphologies in response to variations in pH or ionic strength. In a polar solvent, the ionizable groups dissociate and leave behind a system of charged chains and counterions that can be either bound or mobile. The association/dissociation of counterions can thus be tuned in a wide range.[4,32] In particular, amphiphilic polyelectrolytes (PEs) bearing ionizable groups as repeating units can dynamically respond to external stimuli, forming various morphologies, such as spherical, star-like/hairy, crew-cut, and cylindrical micelles, vesicles, lamellar mesophases, and micellar aggregates.[40,41,42,43,262] In addition to stimuli-responsive behavior, the interplay of electrostatic interactions with counterion entropy and local solubility contributes to creating a diverse range of order/disordered morphologies, which are normally inaccessible to traditional non-ionic polymers, by shifting traditional phase boundaries.[12,68,263,264,265] For instance, phase diagrams for linear polyelectrolyte block copolymers show gyroid or cylindrical phases with long-range continuity governed by ionic interactions.[13,266]

Branched polymers with multiple functionalities are promising candidates to realize polymer materials with pre-programmed complex morphologies and multifunctional properties. Branched polyelectrolytes with various architectures, such as brushes[46,47], star copolymers[48,49], and hyperbranched molecules[51,52] were reported to show rich phase behavior and responsive micellar organization.[54,55,196,208,267] In contrast to linear PEs, branched counterparts possess readily controlled diverse functionalities in cores, inner arms, and outer shells which can promote the formation of complex morphologies with multifunctional responsive behavior.[56,60,61,62] For example, star PEs composed of hydrophobic polystyrene (PS) arms and amphoteric poly(2-vinyl-pyridine)-b-poly(acrylic acid) (P2VP-b-PAA) arms formed various morphologies, such as unimolecular micelles, worm-like micelles and network-like large assemblies. Their morphologies were determined by the location and pH-dependent conformations of P2VP segment (inner) and

PAA segment (outer).[65] Introducing large counterions of a different nature can alter the functionality of outer shells, affect hydrophilic/hydrophobic balance, and induce stimuli-sensitive behavior. [90,91,92,95,96] For example, ionic dendrimers functionalized with hydrophobic fatty acids as counterions self-assembled into micelles, lamellae or nanospheres with a lamellar structure depending on the number of fatty acids linked to the dendrimer core.[119] In our recent study, we found that hyperbranched polymers (HBPs) with thermo-responsive poly(N-isopropylacrylamide) (PNIPAM) macrocations showed temperature-induced phase transformation controlled by low critical solution transition (LCST) of PNIPAM macrocations.[96] Moreover, it has been demonstrated that the deposition of polyelectrolytes changes the surface charge of films and manipulates the film properties, such as water content and mobility, electrochemical charge transport, and electrocatalytic properties.[268,269,270,271,272,273,274] Although a plenty of studies have been reported on the control over surface properties using linear polyelectrolytes, branched polyelectrolytes have been relatively unexplored to date.[275,276]

In this work, we report the synthesis and assembling behavior of novel hyperbranched polyelectrolytes (HBPEs) functionalized with weakly ionically bound thermo-responsive chains as macro-counterions. The macromolecules synthesized here are composed of hydrophobic polyester cores with variable peripheral chemical composition. Hydrophobic n-octadecylurethane arms and weakly-tethered ionically bound hydrophilic macrocations are employed as peripheral components. The presence of mobile macrocations provides the HBPEs with dynamic response characteristics, allowing for tuning the morphology of HBPE assemblies by changing temperature and adding salts. In addition, strong vertical amphiphilicity-driven segregation at the air-water interface restricts PNIPAM macrocations in water, resulting in the formation of Langmuir monolayers of HBPEs with diverse surface morphologies. Not only the surface morphology but also surface mechanical and surface charge distribution of the monolayers can be tuned by adjusting deposition condition (e.g., temperature and surface pressure) and peripheral chemical composition.

5.2 Experimental Section

5.2.1 Synthesis of Materials

N-octadecylisocyanate, 2-sulfobenzoic acid cyclic anhydride, and poly(N-isopropylacrylamide) amine terminated (M_n = 2500 g/mol) were purchased from Aldrich and used as received. Hyperbranched aliphatic polyester polyol Boltorn H30 (Perstorp) with molecular weight M_w = 3500 g/mol comprising 32 terminal OH groups in outer shell was purified by precipitation of dimethylformamide (DMF) solution in diethyl ether followed by vacuum drying at 25-30 °C for 6 hours (an equivalent molecular weight measured by hydroxyl groups via acetylation technique is equal to 117 g/equivalent).[220] Phthalic anhydride was purified by sublimation and all solvents were dried and distilled before use. The ultrapure water was obtained with a three-stage Millipore Milli-Q Plus 185 purification system (resistivity ≥18.2 MΩ·cm) (see more detail in Supporting Information).

5.2.2 Assembly of Hyperbranched Polyelectrolytes in Aqueous Media

The aqueous assembly was carried out using the solvent-addition method.[105, 277] Hyperbranched polyelectrolytes were dissolved in tetrahydrofuran (THF) at 50 mg/mL under stirring for 24 hours at room temperature and then added to water dropwise at 1 mL/min. THF was evaporated under stirring for 24 hours at room temperature and the final concentration was 1 mg/mL.

A drop (5 μL) of hyperbranched polyelectrolyte solution was placed onto the pre-cleaned silicon substrate and air-dried to prepare drop-cast films. For preparing samples above LCST, the HBPE solution and silicon substrates were heated at 50 ^{o}C before deposition.

5.2.3 Langmuir Monolayers and Deposition

The pressure−area (Langmuir) isotherms and Langmuir-Blodgett (LB) monolayers on the silicon substrates were acquired as described in Chapter 3. The LB monolayer films of the HBPEs were obtained at two different pressures (20 and 50 mN/m) and temperatures (23 and 38 ^{o}C).

5.2.4 Characterization

Fourier transform infrared (FTIR) spectra in the 600−4500 cm^{-1} range and proton nuclear magnetic resonance (^{1}H NMR) spectra were recorded as described in Chapter 3. LCST behavior was investigated based on change in transmittance of HBPE solutions (as described earlier). Zeta-potential and size of HBPE assemblies in aqueous media were also measured at different temperatures (described earlier). Samples for light transmittance, zeta potential and size measurements all were aqueous solutions at 1 mg/mL concentration.

Morphology was observed using atomic force microscopy (AFM) on an ICON microscope (Bruker) in the soft tapping mode according to the established procedure.[221] The scan rate was between 0.1 and 0.7 Hz, and the resolution was 512x512 or 1024x1024 pixels. For LB monolayers, the microroughness was determined from the root-mean-square average of the height deviation taken from the 1 x 1 μm^2 areas with at least three independent locations scanned. The film thickness was also obtained using the ellipsometer (described earlier).

Surface mechanical and electrical properties of the monolayers were mapped using Peak-Force Kelvin probe force microscopy (PF-KPFM) (Bruker). We used silicon probes with a metallic back contact layer with a spring constant of 0.8 N/m and a tip radius of 5 nm (PFQNE-AL, Bruker), which are designed for PF-KPFM. Prior to each new sample measurement, tip characterization was performed. Deflection sensitivity and spring constant of the tips were determined from force−distance curves (FDCs) on a sapphire crystal. The monolayers were scanned in the PF-KPFM mode at a scan rate of 0.5 Hz and a resolution of 512x512 pixels. PF-KPFM measurements were conducted at a lift height of 100 nm. All images were analyzed using Nanoscope Analysis 2.0 (Bruker).

5.3 Results and Discussion

5.3.1 Synthesis of Thermo-sensitive Hyperbranched Polyelectrolytes

We synthesized amphiphilic hyperbranched polyelectrolytes bearing sulfonate terminal groups ionically functionalized with thermo-responsive linear PNIPAM chains as macro-counter-cations tethered to the ionized thermal groups of HBPE cores via ionic interactions (Figures 5.1 and S5.1-4). The synthesized polymers belong to a special class of branched polymers with end ionized groups, which is not a traditional class of polyelectrolytes with a substantial portion of the constitutional units containing ionic or ionizable groups.[278] However, since the synthesized polymers are composed of branches with ionic sulfonate terminal groups as repeating units, these polymers generally belong to polyelectrolytes or ionomers depending upon molar content.

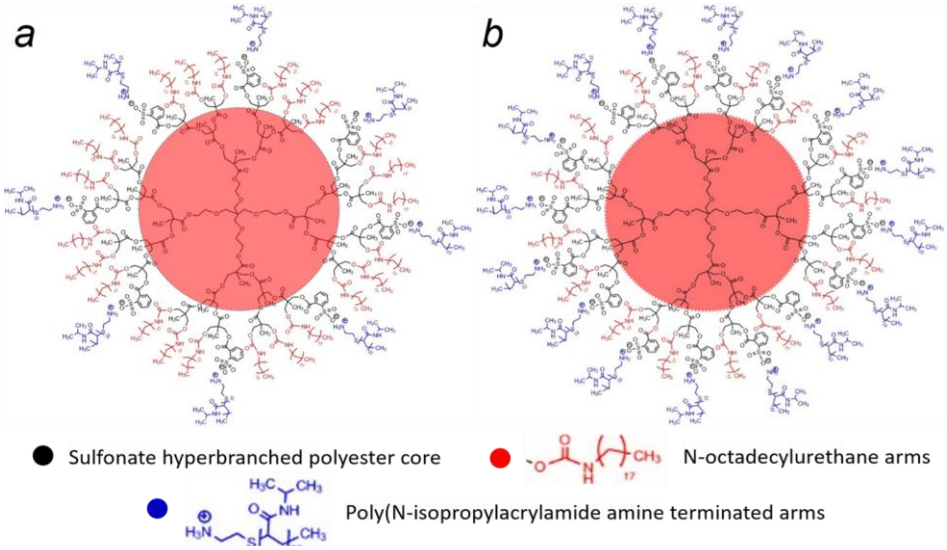

Figure 5.1. Chemical structure of ionically bound thermo-sensitive HBPEs: (a) S8P8 HBPE and (b) S16P16 HBPE.

In fact, the molar content of ionizable groups for the HBPEs (calculated to be around 1/2000 and 1/1200 $(g/mol)^{-1}$ for S8P8 and S16P16, respectively) approaches common border between polyelectrolytes and ionomers (between 1/500 to 1/5000 $(g/mol)^{-1}$) for common polystyrene sulfonate copolymers).[279, 280, 281, 282, 283] Indeed, hyperbranched polymers with cationic or anionic terminal groups have been referred as hyperbranched polyelectrolytes.[97, 284, 285, 286] The hyperbranched polyelectrolytes of asymmetric type (abbreviated as S8P8) were synthesized, containing 24 hydrophobic n-octadecylurethane arms and 8 hydrophilic PNIPAM macrocations (Figure 5.1a). The hyperbranched

polyelectrolytes of symmetric type (abbreviated as S16P16) were also produced, which contained 16 n-octadecylurethane and 16 PNIPAM macrocations (Figure 5.1b).

Scheme 5.1 shows a synthesis pathway of the hyperbranched polyelectrolytes. The synthesis was based on partial blocking of terminal hydroxyl groups of the hyperbranched polyester polyol of pseudo 3rd generation by n-octadecylisocyanate followed by acylation of residual hydroxyl groups of the reaction product with 2-sulfobenzoic acid cyclic anhydride (see SI for detailed information).

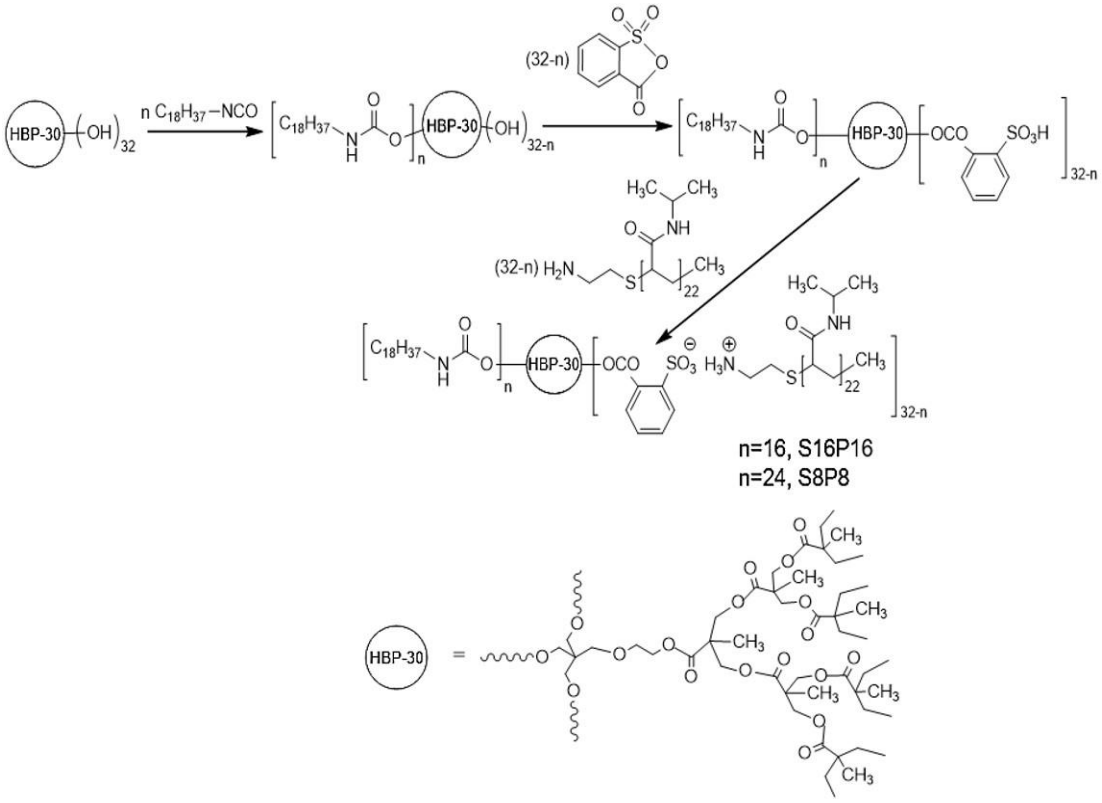

Scheme 5.1. Synthesis pathway for ionically bound thermo-sensitive HBPEs.

The chemical structure of the synthesized HBPEs is confirmed by FTIR (Figure S5.2) and ^{1}H NMR (Figures S5.3-4). The FTIR spectra of S8P8 and S16P16 show characteristic absorption bands that confirm targeted chemical compositions. The FTIR spectra exhibit the absorption bands for aliphatic fragments: ν C-H of CH_2 in the range of 2850-2980 cm^{-1}, ν C-H of CH_3 (1090-1309 cm^{-1}), δ C-H of CH_2, δ as C-H of CH_3 (1458 or 1460 cm^{-1}), and δ sy C-H of CH_3 (1367, 1387 cm^{-1}). The band at 1000-1090 cm^{-1} represents ν S=O bonds of sulfonate anions which overlap ν C-H of CH_3. The bands at 1650 cm^{-1} and 1543

cm^{-1} are assigned to ν C=O amide I and δ N-H amide II, respectively, which are the characteristic bands of carbonyl groups of PNIPAM. The band at 3074 cm^{-1} represents aromatic rings (ν C-H), and the bands at 3130-3700 cm^{-1} suggest ammonium cations, amide and urethane groups (ν N-H) (Figure S5.2).

Table 5.1. Molecular Weights, Volume Ratios of *N*-Octadecylurethane Arms to PNIPAM Chains, T_g Values, and Mean DBs for the HBPEs.

Sample	**Abbreviation**	**MW (g/mol)**		**V_{Oct}/V_{PNIPAM}**	**T_g (°C)**	**Mean DB %[91]**
		Calculated	Found			
HBP-24Oct8$[SO_3]^-$ $[PNIPAM]^+$	S8P8	32320	32960	0.44	81.3	38.7
HBP-16Oct16$[SO_3]^-$ $[PNIPAM]^+$	S16P16	50848	52000	0.15	89.2	

The ^{1}H NMR spectra show the characteristic signals for methyl and methylene groups of the hyperbranched core, PNIPAM fragments, and n-octadecylurethane arms in range of 0.74-4.30 ppm. The ^{1}H NMR spectra also exhibit the peaks of protons from tertiary carbon atoms of PNIPAM fragments (1.99/1.98, 3.85 ppm). The signals for aromatic rings and amide groups appear in range of 7.00-7.90 ppm, and the signal at 8.78/8.76 ppm is for ammonium cations of PNIPAM. The neutralization degree of the obtained HBPEs is evidenced by both positions of protons corresponding to characteristic groups and rations of the signal areas (Figure S5.3-4).

Molecular weight (MW) values of the HBPEs were determined based on MW of the intermediate hyperbranched polysulfonic acids (from acid-base titration technique, see SI) and MW of PNIPAM macrocations, and the determined MW values are close to theoretical values (Table 5.1). The volume fraction of n-octadecylurethane arms to PNIPAM chains (V_{Oct}/V_{PNIPAM}) was calculated from their molecular weights and densities. The values of V_{Oct}/V_{PNIPAM} decreased from 0.44 to 0.15 with increasing PNIPAM content. According to

the results of our previous studies based on ^{13}C NMR, the starting polyester polyol HBP-OH has a degree of branching (DB) of 38.7%[91] in good agreement with the literature data which gives DB values of 36-43% for the HBP-OH (Boltorn H40) which has a similar chemical structure to the starting HBP-OH in this study but with more terminal hydroxyl groups (64).[224] The determined DB values are valid for both intermediate hyperbranched polysulfonic acids and final HBPEs (Table 5.1).

5.3.2 Thermal Behavior of Thermo-sensitive Hyperbranched Polyelectrolytes.

Dynamic scanning calorimetry (DSC) curves of S8P8 and S16P16 show one glass transition temperature (T_g) of 81 ^oC and 89 ^oC, respectively, indicating an amorphous state without signs of crystallization (DSC methodology and curves in SI, Figure S5). The T_g values for these compounds are significantly lower than that of regular high-molecular-weight PNIPAM materials (within 110-140 ^oC).[287,288,289] This depression is due to the low T_g of the hyperbranched polyester core with T_g values of similar branched polyester polyols reported within 25-40 °C.[290,291,292] The hyperbranched polyesters with terminal alkyl fragments obtained in our previous study have a T_g value of -30 °C and melting points of 40-60 °C attributed to the crystalline phase formed by the alkyl component.[223] The absence of melting peaks for S8P8 and S16P16 can be related to the suppression of crystallization of the alkyl branched components by adjacent PNIPAM macrocations.[292]

In aqueous solutions, S8P8 and S16P16 showed a broad LCST transition with modest hysteresis (4-6 ^oC) (Figure 2a,d). This is in contrast to a sharp LCST transition of traditional linear PNIPAM homopolymers around 32 ^oC.[293] The PNIPAM macrocations with highly polar ammonium end groups and their mobile tethering cause broadening and LCST shift toward higher temperature in comparison with common linear PNIPAMs.[294,295] S8P8 have a higher LCST around 36.5 ^oC, compared to that of S16P16 around 35 ^oC (defined as the temperature where the transmittance decreases by 10% from the initial transmittance during heating).[226,227] This result is in contrast to those found for PNIPAM-containing copolymers where increasing hydrophobicity causes a decrease in LCST.[296,297] A possible explanation for the opposite LCST trend is that the number of ionically-tethered PNIPAM macrocations for S8P8 is too small to create strong intermolecular interactions

between PNIPAM which induce coil-to-globule transition of PNIPAM at lower temperatures despite the increased hydrophobicity. In other words, the lower density of PNIPAM terminal chains for S8P8 makes PNIPAM chain aggregation less likely to occur, increasing the overall entropy of the system through aggregation between PNIPAM chains and thus resulting to a higher LCST temperatures. Similar observation was reported for PINPAM-grafted copolymers with different graft lengths: for longer PNIPAM grafts, chain aggregation was limited due to fewer chain ends in the grafts, resulting in a greater entropy contribution and a higher LCST.[298] It was also reported that the LCST transition of end grafted PNIPAM with a low chain grafting density was very subtle due to weak attractive interactions between PNIPAM chains.[299,300]

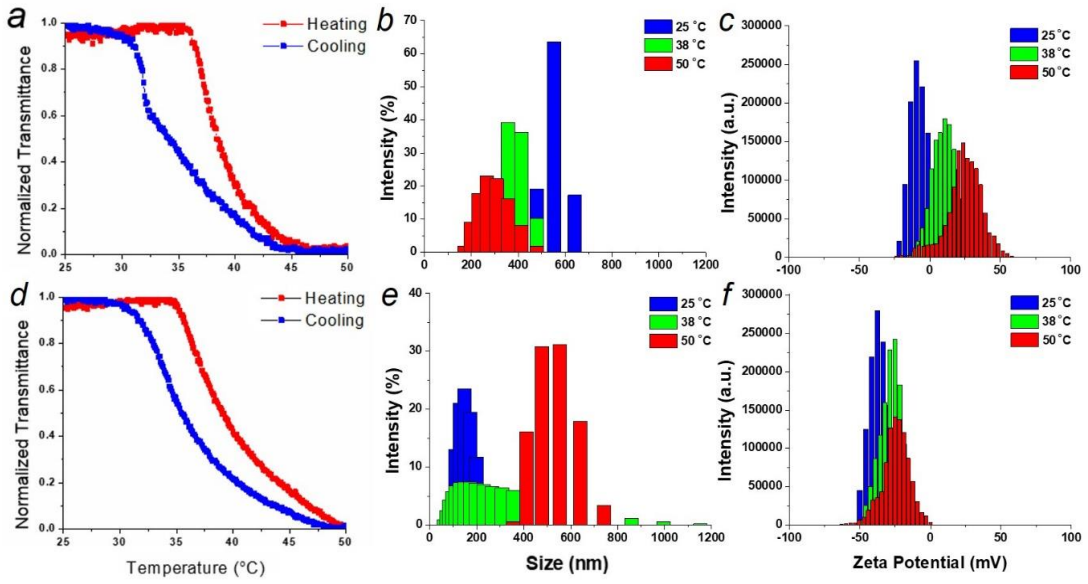

Figure 5.2. Transmittance (*a*,*d*), size (*b*,*e*) and ζ-potential (*c*,*f*) and of S8P8 (*a*,*b*,*c*) and S16P16 (*d*,*e*,*f*) HBPEs vs temperature (heating and cooling rates are 0.5 ^{o}C min^{-1} for transmittance measurements).

In addition, S8P8 and S16P16 HBPEs showed temperature-induced size change, reflecting LCST transition of PNIPAM (Figure 5.2b,e). Interestingly, S8P8 and S16P16 HBPEs exhibited opposite trend in size change upon heating. S8P8 HBPEs had the average size of 554 ± 45 nm at 25 ^{o}C and gradually decreased to 320 ± 60 nm and 287 ± 4 nm at 38 ^{o}C and 50 ^{o}C, respectively. For S16P16 HBPEs, the average size was 306 ± 69 nm at 25 ^{o}C. This value is comparable to that of spherical assemblies (e.g. vesicles) formed by

amphiphilic hyperbranched copolymers composed of an initial core that is the same as with S16P16.[101,301] When temperature increased to 38 °C, S16P16 HBPEs showed a broad size distribution with an increased average size of 383 ± 42 nm. Further heating to 50 °C led to the size increase to 568 ± 52 nm. These results indicate that a significant molecular reorganization of S8P8 and S16P16 HBPEs take place with increasing temperature.

The zeta-potential values of S8P8 and S16P16 also changed in response to temperature (Figure 5.2c,f). S8P8 and S16P16 had the average zeta-potential value of -9 ± 2 mV and -39 ± 2 mV, respectively, at 25 °C. The lower zeta-potential for S8P8 is due to a lower density of ionic terminal groups. The zeta-potential of S16P16 is comparable to that of hyperbranched polyelectrolytes bearing 50% sulfonate terminal groups reported in literature (Figure 5.2f). [302] Indeed, sulfonate-terminated HBPEs have shown negative zeta potentials from -60 mV to -20 mV, depending on the density of terminal ionic groups and the type of counterions.[105,302] S16P16 exhibited a lower negative zeta-potential compared to the HBPEs with the same chemical structure as S16P16 but small counterions (around -60 mV).[105] This indicates that large PNIPAM macrocations partially screen the core sulfonate anions.[96]

The zeta-potential value increased from -9 mV to 11 mV for S8P8 and from -39 mV to -28 mV for S16P16 upon heating to 38 °C. The values further increased to 24 mV and -24 mV for S8P8 and S16P16, respectively, as temperature increased to 50 °C. This result indicates that collapsed PNIPAM macrocations above LCST screen the sulfonate terminal groups of the core with ammonium end groups of PNIPAM macrocations being exposed to the surface of the HBPE micelles and molecules. Similar change in surface charge upon heating was observed for other classes of polyelectrolytes with PNIPAM macrocations[96] and PNIPAM-polycation block copolymers.[303, 304]

5.3.3 Assembly of Thermo-sensitive Hyperbranched Polyelectrolytes

5.3.3.1 Morphology of drop-cast films

First, solutions of S8P8 and S16P16 were drop-cast on silicon substrates and allowed to dry. The morphology of the dried films depended on peripheral chemical composition of

the HBPEs. S8P8 HBPEs formed planar network-like structure whereas S16P16 HBPEs formed vesicles with size of 432± 168 nm (Figure S5.6). This morphological change can be explained by the increased hydrophilicity with increasing the number of PNIPAM macrocations. It has been demonstrated that hydrophilic/hydrophobic balance is critical for determining the morphology of amphiphilic block copolymers in aqueous media and increasing the volume fraction of hydrophobic blocks can lead to the morphological transition from vesicles to lamellar structure.[305,306,307]

Above LCST (50 ^{o}C), S8P8 and S16P16 HBPEs formed chains of spherical structures with different heights of ~200 nm and ~800 nm, respectively (Figure S5.7). This temperature-induced morphological transition can be understood by the increased hydrophobicity arising from LCST transition of PNIPAM. We suggest that although PNIPAM macrocations become hydrophobic above LCST, sulfonate and ammonium groups of the HBPEs are capable of bonding to water molecules. Therefore, the HBPEs preserve an amphiphilic character with reduced hydrophilicity even above LCST, allowing them to self-assemble into the spherical features. In addition, it should be noted that the dimension of S8P8 assemblies was smaller than that of S16P16 assemblies as observed by DLS (Figures 5.2b,e and S5.7). Such size difference is due to the difference in the number of charged terminal groups. We suggest that the greater number of charged terminal groups of S16P16 HBPEs provides peripheral hydrophilicity strong enough to stabilize the formation of the large spherical features. On the other hands, the peripheral hydrophilicity of S8P8 HBPEs created by fewer charged terminal groups results in the formation of relatively small spherical morphologies (Figure S5.8). Similarly, a morphological transition from spheres, through vesicles to large spherical micelles was reported for linear amphiphilic block copolymers, PS-*b*-PAA, as the volume fraction of the hydrophilic PAA block decreased.[308]

To understand the role of weakly ionically tethered macrocations on the overall assembly of the HBPEs, we investigated the HBPE solutions with salt-added media. Firstly, the addition of salts caused a significant increase in the size of S8P8 and S16P16 HBPE assemblies. With 0.1M NaCl, the average sizes of S8P8 and S16P16 assemblies at 25 ^{o}C were 1.3 $\pm$ 0.1 μm and 517 $\pm$ 49 nm, respectively, which were about twice larger than

those without salts (Figure S5.9a,b). Upon salt addition, the zeta-potential value increased from -9 mV to -3 mV and from -39 mV to -10 mV for S8P8 and S16P16 HBPEs, respectively, (Figure S9c,d). This increase in zeta potential value is attributed to the screening of the charged surface of the HBPEs, which leads to the presence of less ions in the diffuse layer and then to a lower absolute value of zeta-potential. Similar reduction in zeta-potential was reported for hyperbranched polyelectrolytes with increasing ionic strength due to decreasing the ionization degree of terminal ionic groups.[105,309] AFM images of the drop-cast films of S8P8 and S16P16 salt-added solutions also showed the formation of large, irregular aggregates, confirming that the salt addition caused the aggregation of the HBPEs facilitated by the decreased ionization degree (Figure S5.10). Thus, we can conclude that the presence of mobile macrocations provides the HBPEs enables control of the HBPE assemblies, which is not accessible for traditional neutral polymers. Next, we consider dynamic of terminal chain assembly with molecular dynamics simulations in the following section.

5.3.3.2 Molecular Dynamics Simulations

Figure 5.3 shows the time evolution of two representative S16P16 HBPE molecules on a SiO_2 surface. We did not observe significant aggregation between the S16P16 HBPEs within the simulation trajectory, primarily due to the competition between HBPE-HBPE and HBPE-surface interactions (Figures 5.3 and S5.11, Movie S5.1-2). Within the first 10 ns, the terminal dimethyl acetamide groups of the PNIPAM macrocations form weak van der Waals (VDW) interactions with the hyperbranched core and macrocations of the neighboring HBPEs. At the same time, the terminal dimethyl acetamide groups within the vicinity of the surface form strong interactions with the silanol surface groups (Figure 5.3). As a result, the surface bonding is largely dominated by VDW interactions between the silanol surface groups and the terminal dimethylacetamide groups of the PNIPAM macrocations. Overall, the HBPE-surface interactions are two orders of magnitude stronger than the intermolecular interactions, indicating strong surface bonding of absorbed molecules (Figure S5.12).

The macrocations farther away from the surface did not deposit on the surface even after 100 ns of simulation (Figure 5.3). The cores of the HBPE molecules also do not interact favorably with the surface, mainly due to steric restrictions associated with the preferential macrocation-surface bonding. However, a hydrophobically-driven clustering within macrocations is evident from the reduced radius of gyration of the molecules which occurs due to increased intramolecular hydrogen bonding after the first 20 ns. As the radius of gyration decreased, the interaction between the neighboring HBPEs was no longer noticeable after 50 ns (Figure S5.14).

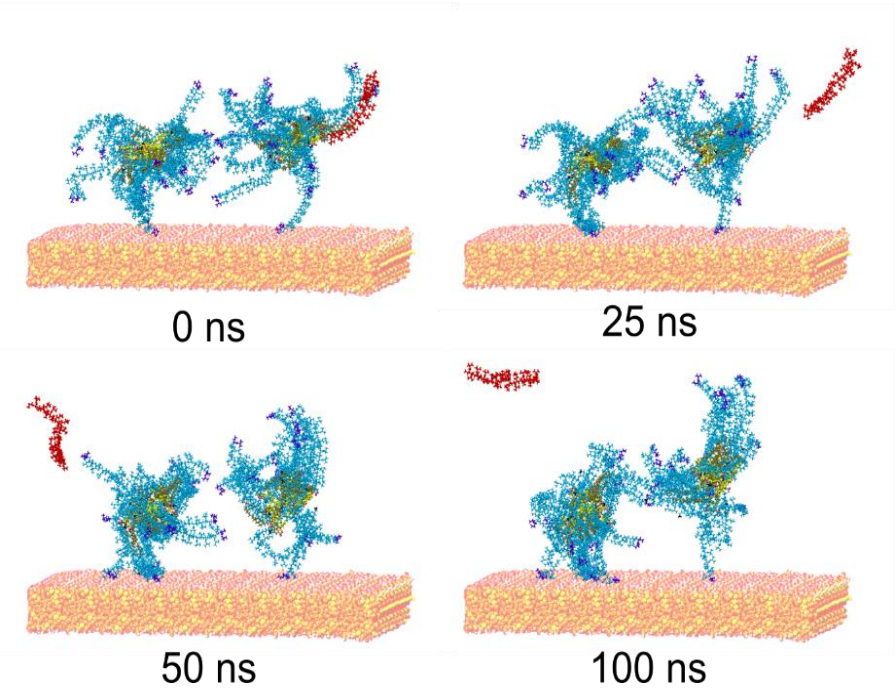

Figure 5.3. Molecular dynamics simulations of the assembly behavior of S16P16 HBPEs on a silicon substrate that show detaching and hopping of PNIPAM macrocations (cyan) between SO_3- anions (orange) of the hyperbranched cores (tan). The dimethyl acetamide groups are shown in violet and water molecules are hidden for clarity.

It is critical to note that the outer PNIPAM macrocations in this study are highly mobile in contrast to traditional covalently-tethered arms.[61,62] In our case, the macrocations are non-covalently attached to the core via Coulombic-controlled bonding between the terminal NH_3^+ and SO_3^- groups of terminal chains and core branches (Figure 5.1). Such weak bonding allows to hop between SO_3^- sites and/or completely dissociate from the core. Our

simulations show that a single macrocation (out of 80 in total) was completely dissociated from the HBPE core and became solvated (Figure 5.3). The rest of the macrocations hopped between the nearby SO_3^- sites of their respective cores, forming highly mobile coronas. In total, during simulation cycle, about 45% of the macrocations (36 out of 80) left the original sulfonate site and did not return. The rest of the macrocations hopped between the neighboring SO_3^- with a high frequency (Figure S5.13). Only a small fraction of macrocations (10%) remained tethered to their original sulfonate site for more than 80 ns (Figure S5.13). Thus, overall, about 90% of the PNIPAM macrocations are dynamically hopping between the SO_3^- terminal sites to balance interactions between NH_3^+ and SO_3^- ions. These detached and hopping can lead to large mobile coronas surrounding a hydrophobic cluster, which can contribute to obtaining diverse morphological variation of HBPEs under changing assembling condition (Movie S5.3).

5.3.4 Hyperbranched Polyelectrolytes at the Air-Water Interface

To further investigate the role of the weakly tethered PNIPAM macrocations, we studied their interfacial assembly behavior at the air-water interface with strong vertical amphiphilicity-driven segregation trend caused by the interface between water sub-phase and air as a poor solvent for these molecules.

5.3.4.1 Langmuir Monolayers

The pressure-area isotherms of Langmuir monolayers from S8P8 and S16P16 HBPEs show the formation of stable monolayers with characteristic gas, liquid expanded and condensed phases, and solid phase, confirmed by steady increase in surface pressure upon compression (Figure 5.4).[204] The isotherms for S8P8 HBPEs were shifted toward smaller surface area compared that those for S16P16 HBEPs, indicating more compact state. This isotherm shift can be explained by stronger interactions of alkyl arms with increasing the number of alkyl arms. As the interactions of the alkyl arms increase, the alkyl arms straighten out, align parallel to each other and arrange perpendicular to the water surface, making hyperbranched polyelectrolyte molecules adapt compact conformation and thus reducing the surface area occupied by the HBPE molecule.[310] Correspondingly, the limiting mean molecular area (MMA) in a liquid phase for S8P8 HBPEs (71.9 nm^2) was

also smaller than that for S16P16 HBPEs (90.7 nm^2) (Figures S5.15-16). Moreover, increasing the water subphase temperature above LCST does not change the overall character with a slightly smoother pressure increase (Figure 5.4 and S5.15-16).

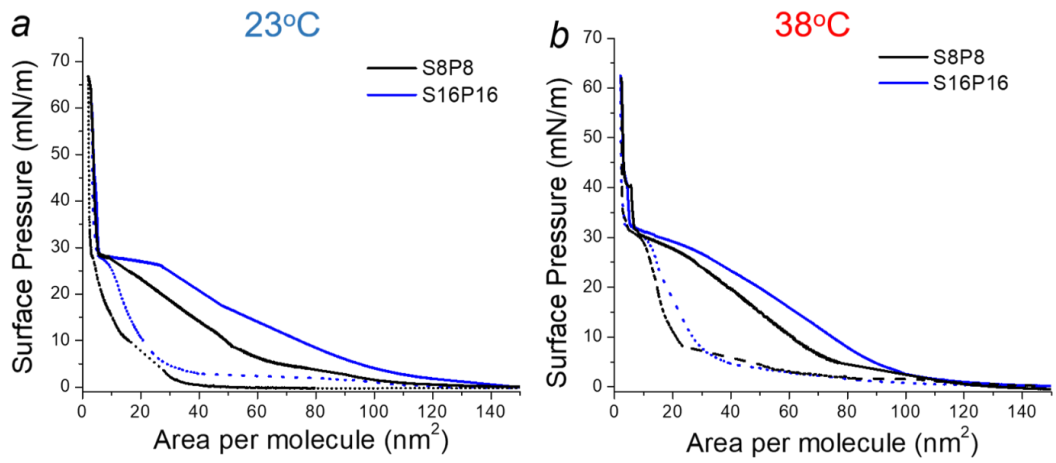

Figure 5.4. Langmuir pressure-area isotherms of S8P8 and S16P16 HBPEs at ambient temperature (*a*) and 38 ^{o}C (*b*).

5.3.4.2 LB Monolayer Morphology

AFM images of LB monolayers show that circular domains were formed in a liquid phase (at 20 mN/m) and transformed into coalescent domain morphologies in a solid phase (at 50 mN/m) (Figures S5.18-19). These morphologies are different from those of the drop-cast films, suggesting that the organization of hyperbranched polyelectrolytes in 3D environment (in aqueous media) is distinct from that in 2D confined environment (at the air-water interface). In the aqueous media, PNIPAM macrocations are highly mobile, while the lateral compression within monolayers promotes strong segregation where attached macrocations submerged into the water subphase.

High resolution AFM images show that S8P8 and S16P16 HPBEs formed circular domains with height of 2-3 nm in the liquid phase for both temperatures (Figure 5.5). The diameter of the circular domains depends on peripheral chemical composition as well as water subphase temperature. At ambient temperature, the circular domains formed by S8P8 HBPEs have an average diameter of 2.8 ± 0.8 μm and height of 3.1 ± 1.0 nm (Figure 5.5a).

The domain diameter decreases to 532 ± 266 nm upon heating above LCST with an average height of 2.9 ± 0.6 nm (Figure 5.5b). In addition, S16P16 HBPEs formed circular domains with much smaller diameters. At ambient temperature, the circular domains have an average diameter of 60 ± 3 nm and height of 2.3 ± 0.3 nm whereas the circular domains at 38 ^{o}C have a larger average diameter of 110 ± 58 nm and height of 3.2 ± 0.3 nm (Figure 5.5c,d).

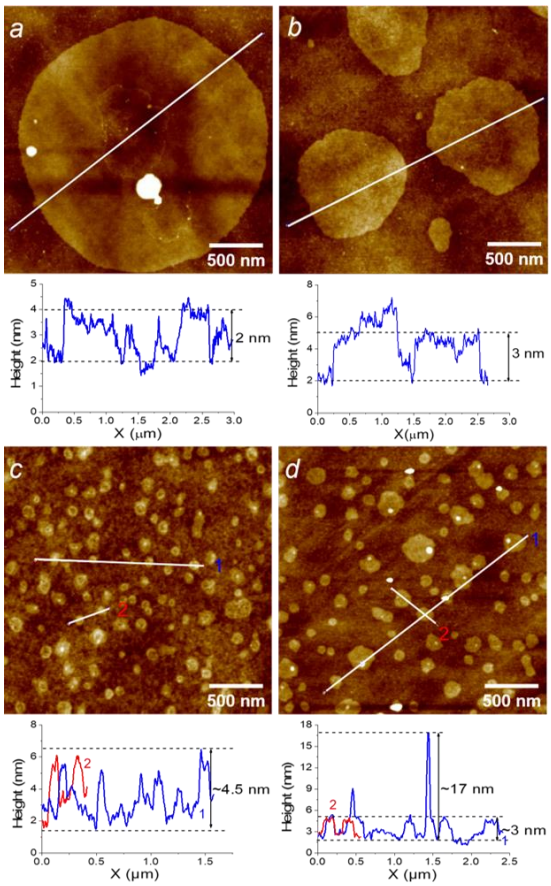

Figure 5.5. AFM topography images and height profiles of S8P8 (*a*,*b*) and S16P16 (*c*,*d*) monolayers at 20 mN/m and at different temperatures; ambient temperature (*a*,*c*) and 38 ^{o}C (*b*,*d*). Z scales are 10 nm for all images.

Upon compression, morphological transition occurred where the circular domains became porous for both temperatures for S8P8 monolayers (Figure 5.6). The S8P8 monolayer at ambient temperature showed elevated structures connected each other and surrounding hole-like regions. The elevated network-like structures have an average height of 6.3 ± 0.9

nm. Pillars with an average height of 17.7 ± 5.5 nm were also observed occasionally in the monolayer (Figures 5.6a). Above LCST, the monolayer showed elevated but wide structures of 8.0 ± 1.2 nm height with a few towering pillars of 26.5 ± 6.6 nm height (Figure 5.6b). On the other hand, S16P16 monolayers in the solid phase exhibited a relatively continuous morphology. At ambient temperature, protruding islands were formed with an average height of 7.7 ± 1.3 nm (Figure 5.6c). Upon heating to 38 ^{o}C, the monolayer contained flat domains with pillar-like and ring-like features formed. The average height of the flat domains and elevated pillars are 2.4 ± 0.6 nm and 13.1 ± 3.5 nm, respectively (Figure 5.6d). The morphological variation depending on peripherical composition and deposition condition can be also seen in AFM three-dimensional images and phase images (Figures S5.20-S23).

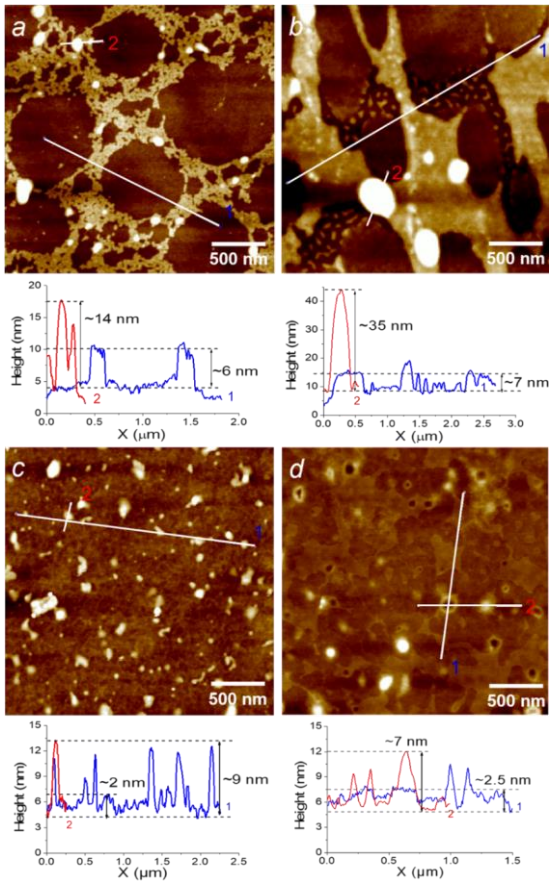

Figure 5.6. High resolution AFM topography images and height profiles of S8P8 (*a*,*b*) and S16P16 (*c*,*d*) monolayers at 50 mN/m and at different temperatures; ambient temperature (*a*,*c*) and 38 ^{o}C (*b*,*d*). Z scales are 15 nm for all images.

5.3.4.3 Monolayer Formation

Considering that AFM provides only the surface morphology, we analyzed the data on heights and area fraction of the domains obtained from the profile analysis of AFM topography images and effective thickness of the monolayers measured by ellipsometry (Table 5.2-3). The effective thickness of the monolayers in the liquid phase was measured to be 0.8-1.4 nm (Figure S5.24). The effective thickness, $t_{effective}$ is calculated as $A_{domain,1}(h_{domain,1} + t_{under}) + A_{domain,2}(h_{domain,2} + t_{under}) + \cdots + A_{domain,n}(h_{domain,n} + t_{under}) + A_{under}(t_{under})$ where $A_{domain,1}$, $A_{domain,2}$, $\cdots$, $A_{domain,n}$ and A_{under} are the area fraction of n different domains and underlying sub-layer, respectively, $h_{domain,1}$, $h_{domain,2}$, $\cdots$, $h_{domain,n}$ are the height of the domains, and t_{under} is the thickness of the underlying sub-layer.[215] From this equation, the thickness of the underlying sub-layer was calculated to be 0.1 and 0.6 nm for the S8P8 monolayers in the liquid phase at ambient temperature and 38 ^{o}C, respectively. For the S16P16 monolayers in the liquid phase, the calculated thickness of the underlying sub-layer was 0.3-0.5 nm for both temperatures.

The analysis on the heights and effective thickness was also performed for the monolayers in the solid phase. The effective thickness of the S8P8 monolayers in the solid phase was measured to be 4.7 nm and 6.3 nm for ambient temperature and 38 ^{o}C, respectively (Figure S5.24). The thickness of the underlying sub-layer was calculated to be 2.1 nm and 3.6 nm for ambient temperature and 38 ^{o}C, respectively, implying that the circular regions which look like holes are not perforated. For the S16P16 monolayers, the effective thickness was 3.5 nm and 6.3 nm, and the calculated thickness of the underlying sub-layer was 3.0 nm and 5.1 nm, for ambient temperature and 38 ^{o}C, respectively.

Above LCST, hydrophobized PNIPAM chains preferentially absorb at the water surface. For S8P8 HBPEs, as a large number of molecules combine together, the PNIAPM chains anchored at the water surface act as barriers and prevent additional aggregation of the molecules. Therefore, the domain diameter above LCST is smaller than below LCST. In contrast, since the domains of S16P16 HPBEs consist of fewer molecules, the barrier effect of the hydrophobized PNIPAM chains seems modest. For S16P16 HBPEs, circular domains with increased effective volume were formed above LCST.

Table 5.2. Parameters Analyzed for Estimating Underlying Sublayer Thickness for S8P8 Monolayers.

Temperature (°C)	23			38		
Surface Pressure (mN/m)	20	50		20	50	
Domain Shape	Disk	Network	Pillar	Disk	Network	Pillar
Domain Height (nm)	3.1 ± 1.0	6.3 ± 0.9	17.7 ± 5.5	2.9 ± 0.6	8.0 ± 1.2	26.5 ± 6.6
Domain Surface Coverage (%)	25.6 ± 3.9	36.7 ± 1.5	1.4 ± 0.5	27.4 ± 2.6	20.6 ± 1.4	3.9 ± 1.1
Film Thickness (nm)	0.9 ± 0.0	4.7 ± 0.1		1.4 ± 0.0	6.3± 0.4	
Estimated Underlying Sub-layer Thickness (nm)	0.1	2.1		0.6	3.6	

Upon compression to the solid phase, the hyperbranched polyelectrolyte molecules are closely packed while adapting compact conformation with alkyl arms and PNIPAM chains being vertically oriented, resulting in the formation of coalescent morphologies. At the first glance, the S8P8 monolayers displayed porous morphology whereas S16P16 HBPEs formed condensed monolayers. Based on the analysis on height and effective thickness, the hole-like regions are not open space. We suggest that these hole-like regions in the S8P8 monolayers are formed since part of initial circular domains are preserved to high pressures (Figure 5.7a). This is supported by the fact that the thickness of the sub-layer (2.1-3.6 nm) is close to the sum of the initial height of circular domains (2-3 nm) and the thickness of the underlying sub-layer in the liquid phase (0.1-0.6 nm).

Table 5.3. Parameters Analyzed for Estimating Underlying Sublayer Thickness for S16P816 Monolayers.

Temperature (ºC)	23		50		
Surface Pressure (mN/m)	20	50	20	50	
Domain Shape	Disk	Island	Disk	Flat	Pillar
Domain Height (nm)	2.3 ± 0.3	7.7 ± 1.3	3.2 ± 0.3	2.4 ± 0.6	13.1 ± 3.5
Domain Surface Coverage (%)	13.5 ± 1.1	7.0 ± 1.1	16.2 ± 1.4	38.8 ± 3.4	1.9 ± 0.7
Film Thickness (nm)	0.8 ± 0.0	3.5 ± 0.0	0.9 ± 0.1	6.3 ± 0.1	
Estimated Underlying Sub-layer Thickness (nm)	0.5	3.0	0.3	5.1	

The high stability of the circular domains is attributed to the branched architecture and asymmetric chemical composition of S8P8 HBPEs. It has been demonstrated that branched copolymers of asymmetric chemical composition with higher content of hydrophobic arms form stable circular domains at the air-water interface, which are preserved to high pressures.[174,195] Crowding of multiple hydrophobic arms tethered to a single joint point would favor the stabilization of highly curved interfaces, remaining the polymer morphology buried in circular shape territory far from the border between spherical and cylindrical morphologies.[174] For S16P16 HBPEs with symmetric peripheral chemical composition, segregation of hydrophobic arms would lead to the formation of less curved interface, making circular domains more vulnerable to pressure which causes

morphological transition to a continuous monolayer during compression in the S16P16 monolayers (Figure 5.7b).[174,311] Above LCST, the hydrophilic-to-hydrophobic transition of terminal PNIPAM chains promotes rearrangement of the whole HBPE molecules. The hydrophobic PNIPAM chains in this state are absorbed at the water surface contributing the formation of surface morphology with additional features (Figure 5.7).

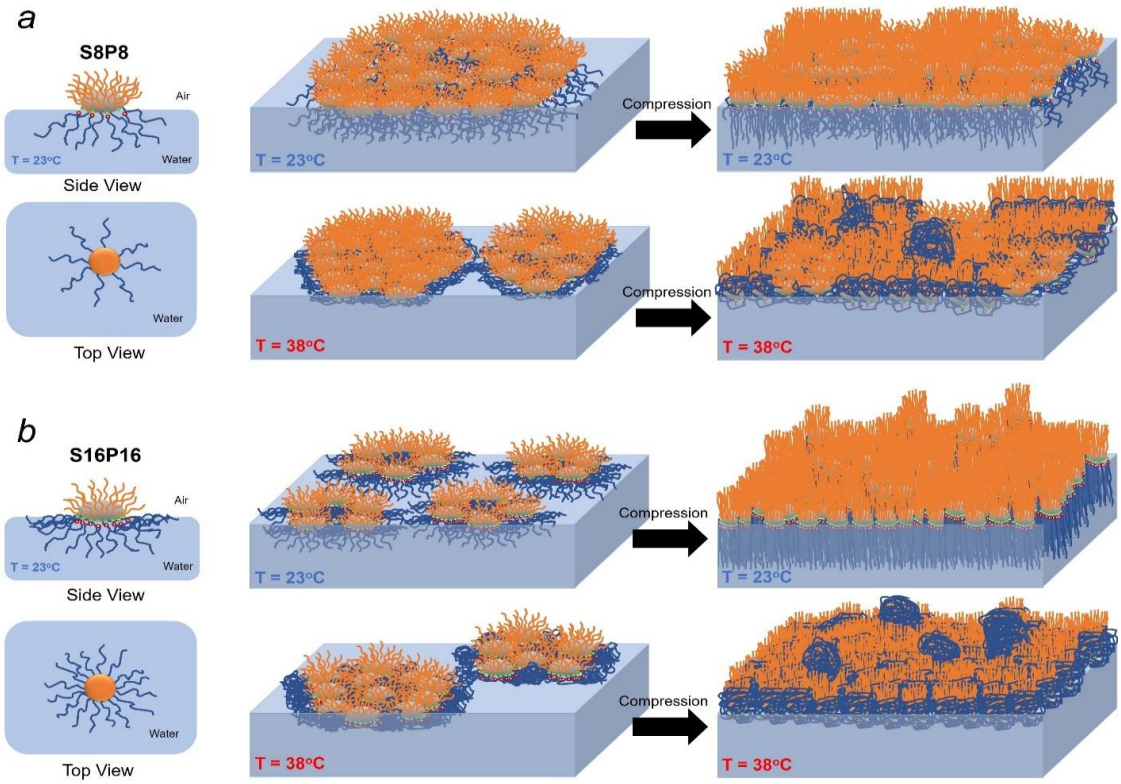

Figure 5.7. Schematic of the molecular conformation of S8P8 (*a*) and S16P16 (*b*) HBPEs at the air-water interface (left); suggesting monolayer formations at different surface pressures and temperatures; (right).

5.3.5 Surface Mechanical and Electrical Properties of Monolayers

Not only surface morphology but also surface mechanical and electrostatic charges distribution of the monolayers can be tuned by adjusting peripheral chemical compositions as discussed in this section. Peak-Force Kelvin probe force microscopy (PF-KPFM) was performed to map the surface properties of the HBPE monolayers. Firstly, the circular domains showed a lower surface potential than the interdomain region although the surface potential contrasts in S16P16 monolayers were less apparent compared to those in S8P8

monolayers, probably owing to the existence of fewer molecules in the circular domains of S16P16 (Figures S5.25-28). The lower surface potential of the domains originates from the presence of negatively charged, covalently bound sulfonated terminal groups of the hyperbranched polyelectrolytes. It is expected that a dipole layer was formed in the domains with negative charges residing at the substrate/monolayer interface and positive charges at the monolayer/air interface, thus resulting in the lower surface potential than that of the interdomain region. Indeed, deposition of anionic polyelectrolytes causes a decrease in surface potential whereas an increased surface potential was observed for cationic polyelectrolyte domains.[312,313]

In the solid phase, the monolayers at ambient temperature showed rather uniform modulus and adhesion distribution, supporting the suggested model in which the topmost surface of the monolayers does not consist of dissimilar components. With reorganization of HBPE molecules under high compression of Langmuir monolayers, hydrophobic core-arm segments are located at the topmost surface with the beneath hydrophilic segments (Figures 5.8b-c and S5.29b-c). Meanwhile, surface potential images exhibited a remarkable contrast (Figures 5.8d and S5.29d). Above LCST, the modulus and adhesion distribution of the monolayers became heterogeneous, supporting that the topmost surface of the monolayers is composed of dissimilar components, including hydrophobized PNIPAM chains and hydrophobic core segments as suggested in Figure 5.7 (see Figures 5.9b-c and S5.30b-c). A significant contrast in surface potential was observed for all states (Figures 5.9d and S5.30d). The surface potential contrasts in the solid phase arise from the difference in net dipole distribution. Although the topmost layer of all monolayers in the solid phase is mostly composed of alkyl tails, the alkyl arms are vertically aligned or inclined to some extent associated with the presence of adjacent alkyl arms or PNIPAM chains as suggested in the monolayer formation model (Figure 5.7). The difference in the orientation of alkyl arms between surface features causes the distinction in net dipole moment, resulting in the surface potential contrast. It was reported that molecule orientation affected the true dipole

moment, and thus experimentally measured surface potential of molecule-covered region differed from theoretical results calculated for vertically aligned molecules.[314]

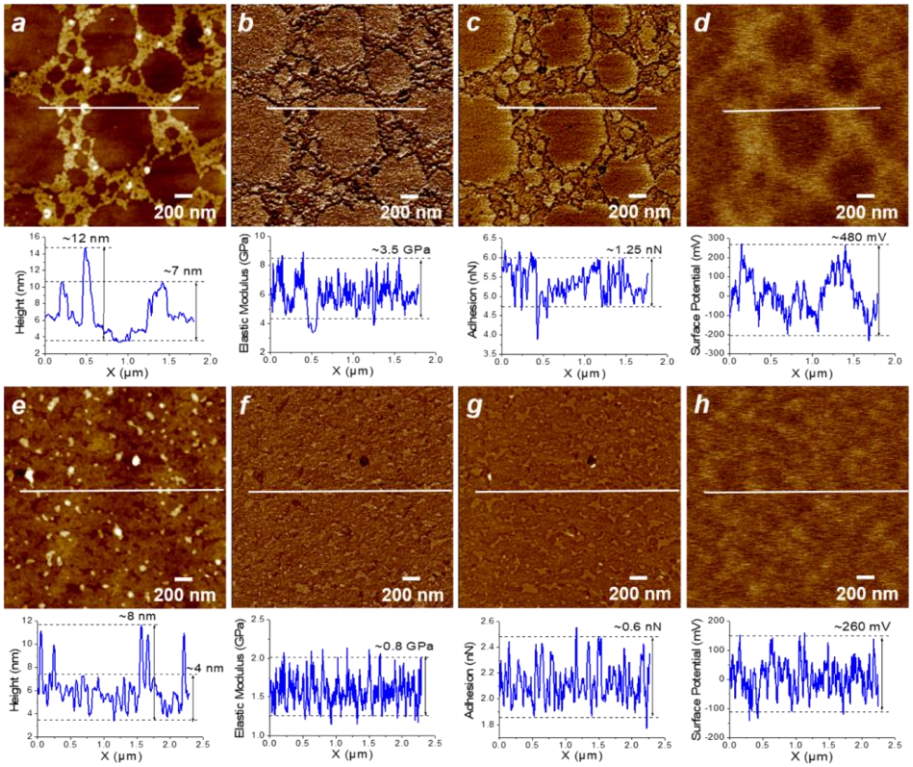

Figure 5.8. AFM topography (*a*,*e*), elastic modulus (*b*,*f*), adhesion (*c*,*g*) and surface potential (*d*,*h*), images and corresponding profiles of S8P8 (*a*-*d*) and S16P16 (e-h) monolayers at 50 mN/m and ambient temperature. Z scales are 15 nm for (*a*,*e*), 5 GPa for (*b*), 2.5 GPa for (*f*), 3 nN for (*c*,*g*) and 1 V for (*d*,*h*).

To further elucidate the origin of surface potential contrast, we performed PK-KPFM to compare surface potential between SiO_2-exposed region and monolayer region. We scratched the monolayer films with a sharp needle to expose the silicon substrate covered with a SiO_2 layer of ~2 nm. For all monolayers, the surface potential of the bare SiO_2-exposed region was higher than that of the HBPE monolayer regions (Figures 5.10 and S5.31).

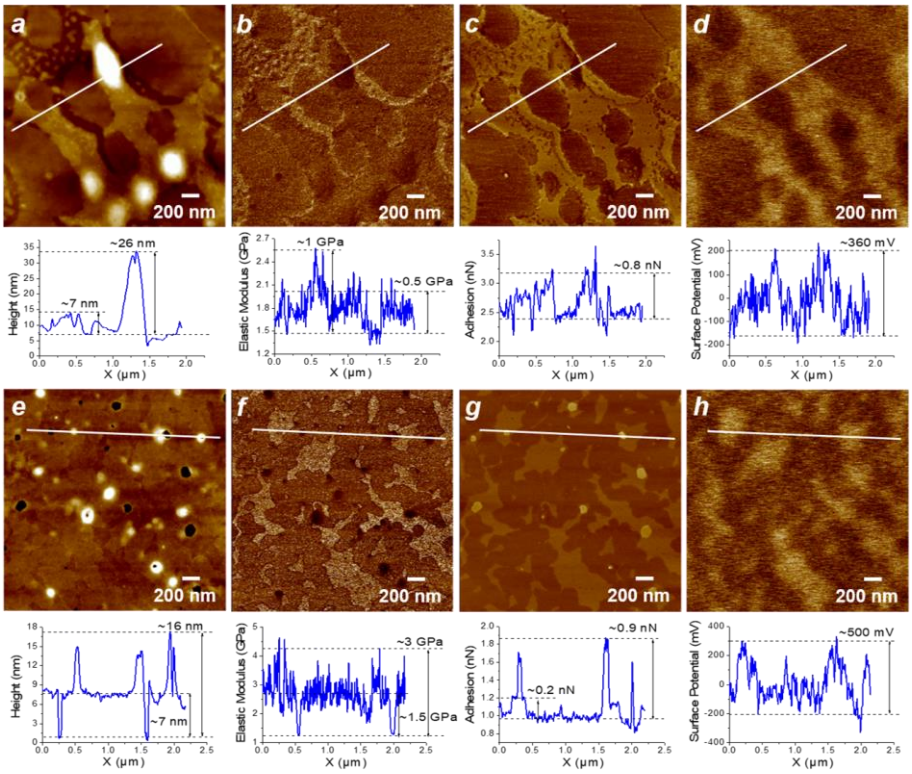

Figure 5.9. AFM topography (*a*,*e*), elastic modulus (*b*,*f*), adhesion (*c*,*g*) and surface potential (*d*,*h*) images and corresponding profiles of S8P8 (*a-d*) and S16P16 (*e-h)* monolayers at 50 mN/m and 38 ^{o}C. Z scales are 15 nm for (*a*), 30 nm for (*e*), 2.5 GPa for (*b*), 5 GPa for (*f*) and 3 nN for (*c*,*g*) and 1 V for (*d*,*h*).

This result suggests that the surface potential contrasts in the monolayers is attributed to the net dipole distribution caused by the difference in molecular composition and orientation, rather than the substrate effect associated with the thickness difference between the domains. As known, the surface potential difference between the monolayers and SiO_2-exposed region is described by $V_{monolayer} - V_{Sio2} = \frac{\mu_{monolayer}}{A_{monolayer}\varepsilon_{monolayer}\varepsilon_0}$, where $V_{monolayer}$ and V_{SiO2} are the surface potential of the monolayer and SiO_2-exposed region, respectively, $\mu_{monolayer}$ is the net dipole moment of the monolayer directed normally to the substrate surface, $A_{monolayer}$ is the area occupied by each molecule, and $\varepsilon_{monolayer}$ and ε_0 the permitivities of the monolayer and free space, respectively.[314] This relationship suggests that the surface potential contrasts in the monolayers can be governed by the

dipole moments formed by the presence of negatively charged sulfonate groups residing at the substrate/monolayer interface and affected by molecular orientations.

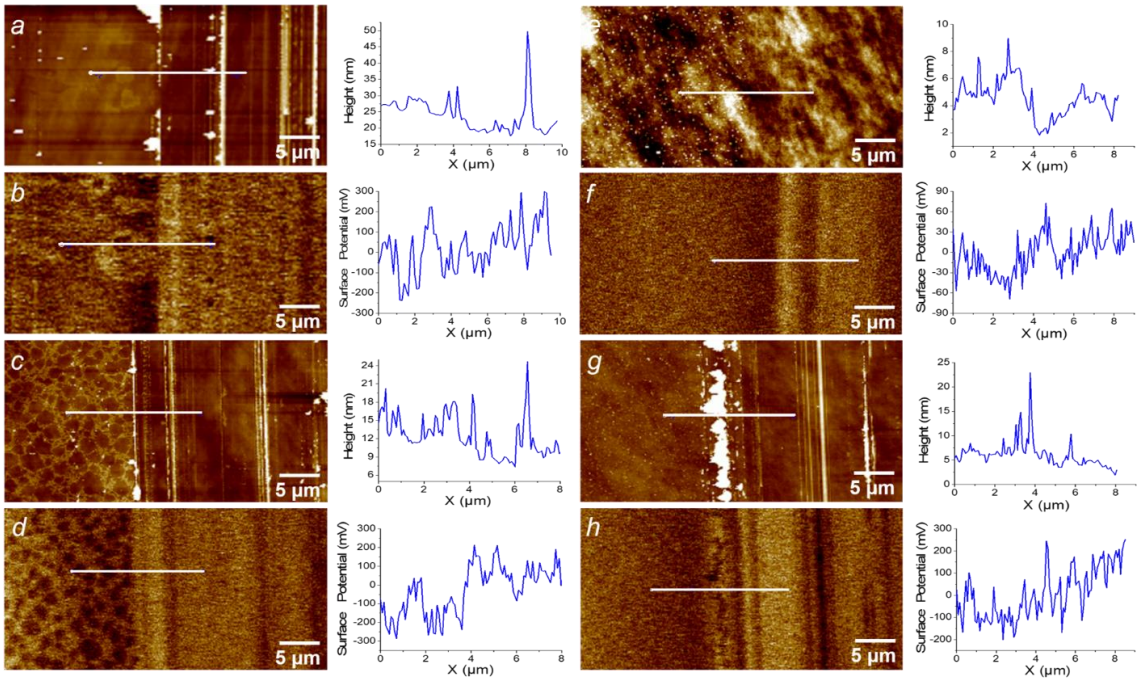

Figure 5.10. AFM topography (*a*,*c*,*e*,*g*), and surface potential (*b*,*d*,*f*,*h*) images and corresponding profiles of S8P8 (*a*-*d*) and S16P16 (*e*-*h*) monolayers with SiO_2-exposed region at ambient temperature at different surface pressures: 20 mN/m (a,b,e,f) and 50 mN/m (*c*,*d*,*g*,*h*). Z scales are 50 nm for (*a*,*g*), 30 nm for (*c*), 7 nm for *(e*), 1 V for (*b*,*d*,*h*) and 0.3 V for (*f*).

5.4 Conclusions

In conclusion, we report the assembly behavior of novel amphiphilic hyperbranched polyelectrolytes weakly, ionically bound with terminal PNIPAM macrocations of variable contents. Terminal, mobile PNIPAM chains provide HBPEs with dynamic response due to not only their thermo-responsive behavior but also labile ionic bonding, which is inaccessible to traditional covalently tethered polymer arms. Indeed, the hyperbranched polyelectrolytes with PNIPAM macrocations showed morphological transition under changing temperature and ionic strength. Molecular dynamic simulation also probes the dynamic nature of PNIPAM macrocations with about 90% of the PNIPAM macrocations hopping between terminal sulfonate groups.

In addition, the HBPEs at the air-water interface underwent amphiphilicity-driven vertical segregation where PNIPAM macrocations were confined in water subphase. Such segregation resulted in the formation of HBPE monolayers with various distinct surface morphologies. Overall, circular domains were formed at modest compression and transformed into condensed morphologies at high compression. The surface morphology strongly depends on peripheral chemical composition since the variation of peripheral composition changes molecular conformation, organization and resulting morphology. S8P8 HBPEs with 24 alkyl arms and 8 PNIPAM macrocations take more compact molecular conformation and organize into a more curved but stable interface compared to S16P16 HBPEs with 16 alkyl arms and 16 macrocations. Therefore, S8P8 HBPEs formed much larger circular domains, and these domains were partially preserved even at very high pressure. Increasing temperature above LCST also causes morphological transition to more complex morphologies since hydrophobized PNIPAM chains are involved in surface morphology formation. Moreover, the surface mechanical and electrical response was governed by changing assembling condition. In particular, the presence of negatively charged sulfonate groups at the substrate/monolayer interface induces the formation of a dipole layer, promoting surface potential contrast caused by the difference in dipole distribution between domains. Changes in assembling condition causes rearrangement of HBPE molecules facilitated by LCST behavior of PNIPAM macrocations which makes them hydrophobic above LCST, resulting in redistribution of net dipole moments and thus surface potential contrast as measured with KPFM. Consequently, the hyperbranched polyelectrolytes with weakly bound terminal PNIPAM macrocations provide opportunities for concurrent control over morphology, mechanical and electrical response by adjusting peripheral composition or changing assembling conditions, which are difficult to achieve by using traditional polymers with covalently bound arms. The tunable morphology and properties of HBPEs hold promising potential for a wide range of applications where responsive nanostructures are required.

Chapter 5 Appendix: Supporting Information

Materials

n-octadecylisocyanate (Aldrich, 98%), 2-sulfobenzoic acid cyclic anhydride (Aldrich, ≥95%), poly(N-isopropylacrylamide) (PNIPAM) amine terminated (Aldrich, M_n = 2500 g/mol), were used as received. Hyperbranched aliphatic polyester polyol (HBP-OH) Boltorn H30 (Perstorp, Sweden, hereinafter referred to as HBP-OH) with weight average molecular weight (M_W) of 3500 g/mol (comprising 32 terminal OH groups in outer shell) was purified by precipitation of dimethylformamide (DMF) solution in diethyl ether followed by vacuum drying at 25-30 °C for 6 h (an equivalent MW measured by hydroxyl groups via acylation technique is equal to 117 g/equiv). DMF, ethanol, isopropyl alcohol, ether, acetonitrile, and chloroform were dried and distilled before use. The content of acidic groups in the composition of synthesized hyperbranched sulfone derivatives at intermediate stage were determined by reverse acid-base titration.[258]

Synthesis of hyperbranched polyester polysulfonic acids with octadecyl tails

S16 was obtained as described in our previous study.[105] 4.14 g (14.0 mg-equiv.) of n-octadecylisocyanate was added to 3.28 g (28.0 mg-equiv.) of HBP-OH in 8 ml of DMF at 80 °C and reaction was held under stirring for 12 h till complete consumption of isocyanate groups (according to FT-IR spectroscopy). Following 2.58 g (14.0 mg-equiv) of 2-sulfobenzoic acid cyclic anhydride was added to the resultant solution and reaction was held under stirring during 20 h at 80 °C. The solvent was partially removed under reduced pressure (1-3 mm Hg) and the synthesized product was precipitated to acetonitrile followed by drying at 40-50 °C. The compound was purified by re-precipitation from acetone to acetonitrile and further dried at 40-50 °C till constant weight. Yield 4.88 g (49%). SO_3H content: 10.8% (calculated 11.4%). The product is a brown solid soluble in water, alcohols, DMF, DMSO and insoluble in acetonitrile, hexane, ether.

S8 was obtained by reaction between 1.52 g (13.0 mg-equiv) of HBP-OH and 2.88 g (9.8 mg-equiv) of n-octadecylisocyanate in 8 ml of DMF followed by acylation of the resultant product by 0.60 g (3.3 mg-equiv) of 2-sulfobenzoic acid cyclic anhydride. Yield 3.81 g

(76%). SO_3H content: 5.0% (calculated 5.3%). The product is a brown solid soluble in chloroform, alcohols, DMF, DMSO and insoluble in water, acetonitrile, hexane, ether.

Thermally responsive hyperbranched polyelectrolytes (HBPEs) based on hyperbranched polyester polysulfonic acids containing octadecyl tails.

S16P16 was synthesized by neutralizing 1.15 g (1.5 mg-equiv) of S16 with 3.85 g (1.5 mg-equiv) of PNIPAM in 10 ml of isopropyl alcohol. The solvent was partially removed under reduced pressure (1-3 mm Hg) followed by precipitation of the product to ether and drying at 40-50^{o}C. The compound was purified by re-precipitation from isopropyl alcohol to ether and further dried at 40-50°C till constant weight. Yield 4.81 (96%). The synthesized compound is light brown solid soluble in water (partially under heating), isopropyl alcohol, chloroform, THF, DMF, DMSO and insoluble in hexane, ether.

FT-IR: ν S=O (1000-1085 cm^{-1}), ν C=O amide I (1653 cm^{-1}), ν NHC=O, δ N-H amide II (1543 cm^{-1}), ν C=O of ester and urethane groups (1713, 1717, 1736 cm^{-1}), δ C-H of CH_2, δ as C-H of CH_3 (1458 cm^{-1}), δ sy C-H of CH_3 (1367, 1387 cm^{-1}), γ C-H of CH_3 (1090-1309 cm^{-1}), ν C-H of CH_2 (2876, 2929, 2972 cm^{-1}), ν ar C-H (3074 cm^{-1}), ν N-H of ammonium, amide and urethane groups (3130-3700 cm^{-1}).

^{1}H NMR: 0.74-1.11 ($CH(C\mathbf{H}_3)_2$, $CH_2C\mathbf{H}_3$, $C(CH_2CO(O))C\mathbf{H}_3$, 566H), 1.24 ($CH_2C\mathbf{H}_2CH_2$, 122H), 1.46 ($CH(C(O)NH)C\mathbf{H}_2$, 172H), 1.98 ($C\mathbf{H}(C(O)NH)CH_2$, 80H), 2.20-4.30 ($C\mathbf{H}_2$ of HBP core, $C\mathbf{H}_2S$, $NH_3^+C\mathbf{H}_2$, 48H), 3.48 ($OC(O)NHC\mathbf{H}_2$, 10H), 3.85 ($C\mathbf{H}(CH_3)_2$), 88H), 4.89 ($CH_2OC(O)N\mathbf{H}CH_2$, 3H), 7.00-7.90 (Ar, $CH(C(O)N\mathbf{H})CH_2$, 55H), 8.76 ($N\mathbf{H}_3^+$, 2H).

S8P8 was obtained as above by neutralization of 1.97 g (1.2 mg-equiv) of S8 with 3.03 g (1.2 mg-equiv) of PNIPAM. Yield 4.69 g (94%). The resultant compound is light brown solid soluble in isopropyl alcohol, chloroform, soluble under heating in DMF, DMSO, water (partially) and insoluble in hexane, ether.

FT-IR: ν S=O (1000-1092 cm^{-1}), ν C=O amide I (1649 cm^{-1}), ν NHC=O, δ N-H amide II (1543 cm^{-1}), ν C=O of ester and urethane groups (1709, 1737 cm^{-1}), δ C-H of CH_2, δ as C-H of CH_3 (1460 cm^{-1}), δ sy C-H of CH_3 (1367, 1387 cm^{-1}), γ C-H of CH_3 (1090-1309 cm^{-}

[1]), ν C-H of CH_2 (2853, 2874, 2924, 2972 cm^{-1}), ν ar C-H (3074 cm^{-1}), ν N-H of ammonium, amide and urethane groups (3130-3700 cm^{-1}).

^{1}H NMR: 0.76-1.14 ($CH(C\mathbf{H}_3)_2$, $CH_2C\mathbf{H}_3$, $C(CH_2CO(O))C\mathbf{H}_3$, 309H), 1.25 ($CH_2C\mathbf{H}_2CH_2$, 201H), 1.48 ($CH(C(O)NH)C\mathbf{H}_2$, 95H), 1.99 ($C\mathbf{H}(C(O)NH)CH_2$, 42H), 2.20-3.05, 3.65-4.30 ($C\mathbf{H}_2$ of HBP core, $C\mathbf{H}_2S$, $NH_3^+C\mathbf{H}_2$, 50H), 3.47 ($OC(O)NHC\mathbf{H}_2$, 13H), 3.85 ($C\mathbf{H}(CH_3)_2$, 44H), 4.85 ($CH_2OC(O)N\mathbf{H}CH_2$, 6H), 7.76-7.90 (Ar, $CH(C(O)N\mathbf{H})CH_2$, 51H), 8.78 ($N\mathbf{H}_3^+$, 2H).

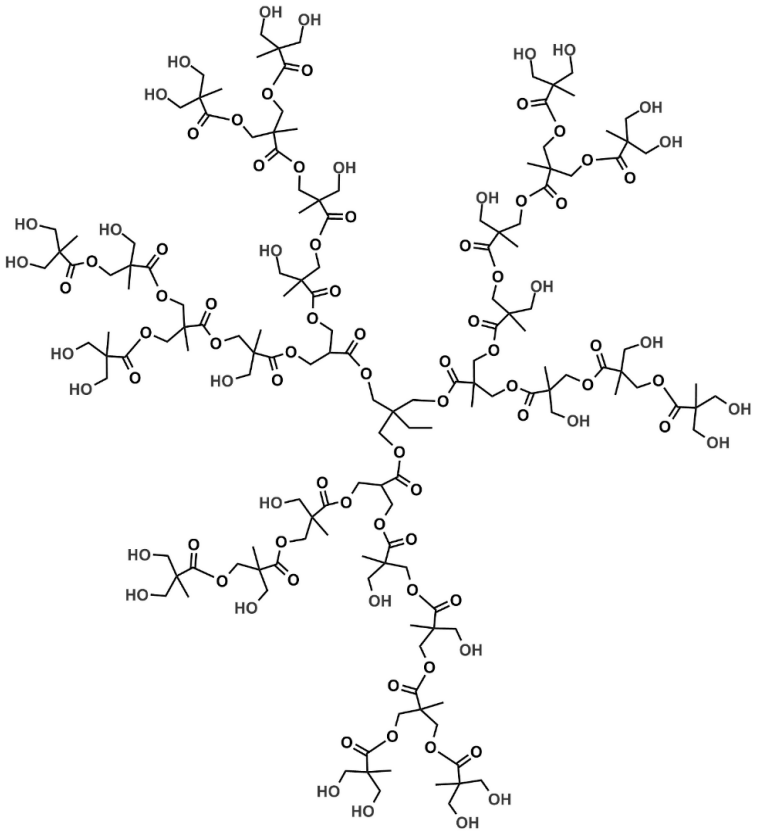

Figure S5.1. Chemical structure of hyperbranched polyester polyol (HBP-OH), Boltorn H30.

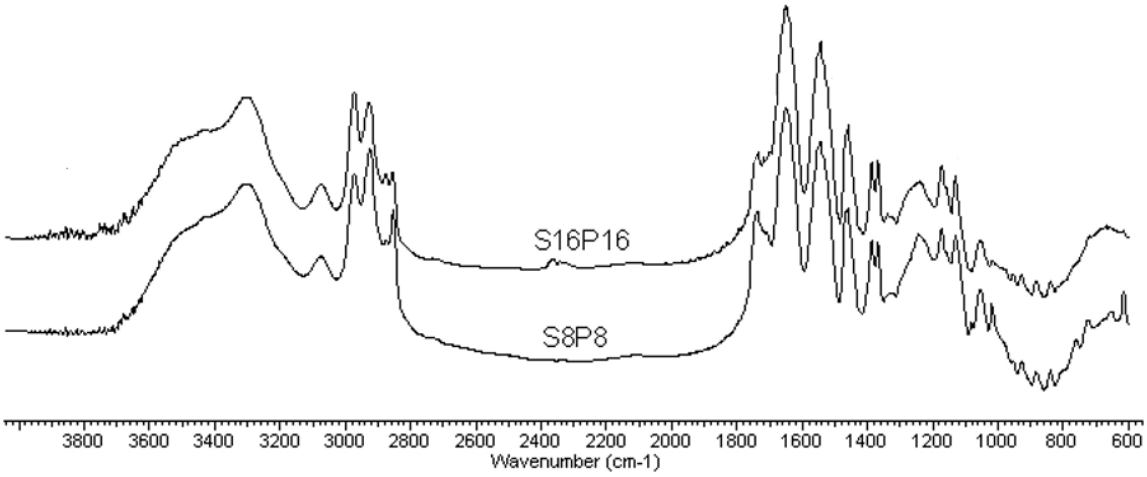

Figure S5.2. FT-IR spectra of the synthesized HBPEs.

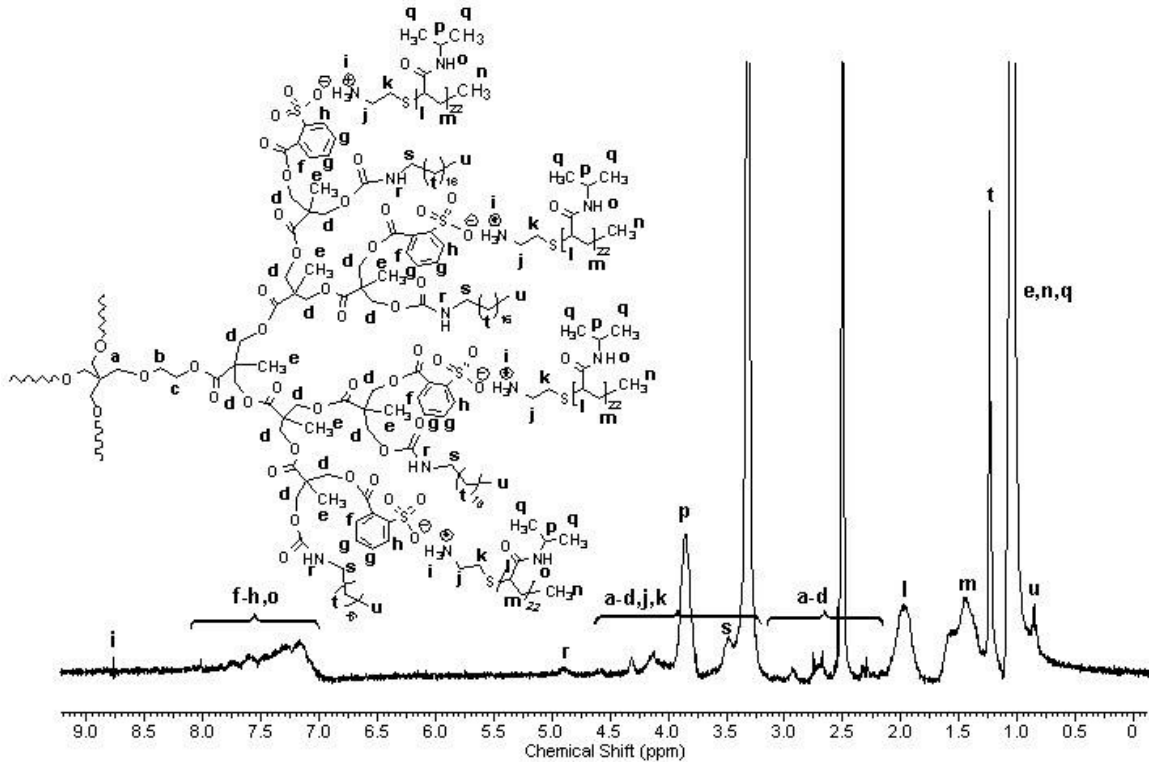

Figure S5.3. ^{1}H NMR spectrum of compound S16P16.

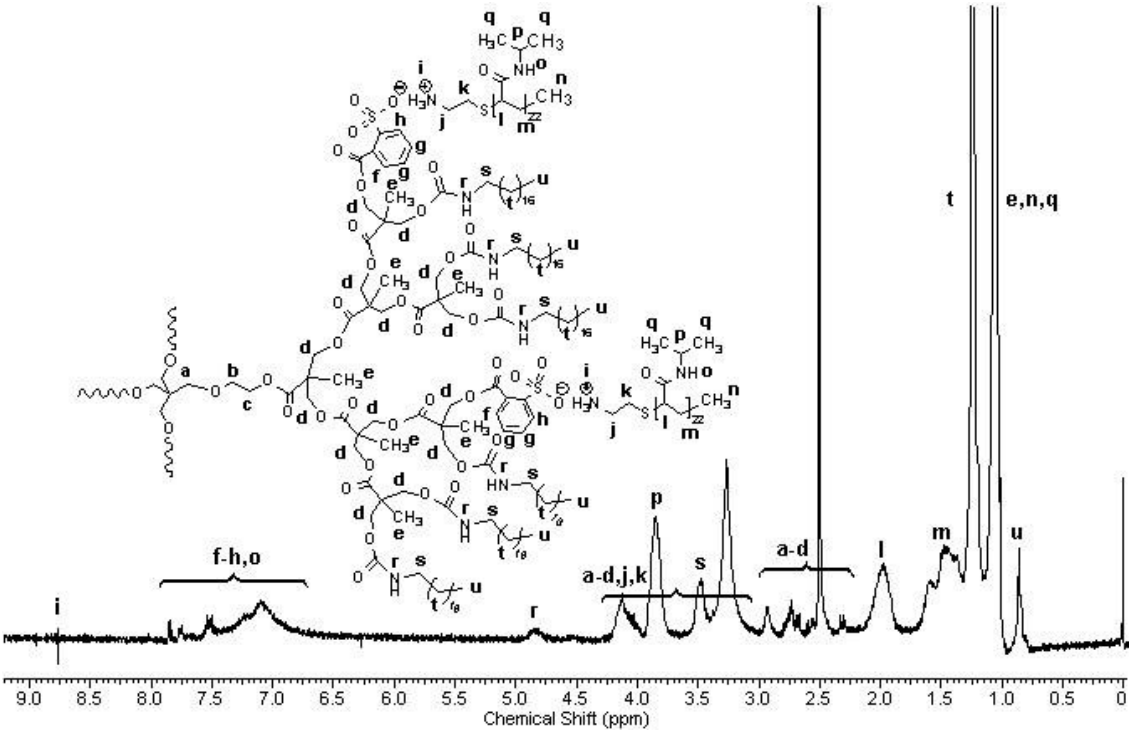

Figure S5.4. ^{1}H NMR spectrum of compound S8P8.

Differential scanning calorimetry (DSC)

DSC was conducted using Mettler Toledo STAR3 system DSC under a nitrogen atmosphere (80 mL/min) with the temperature range from −90 to 200 °C at the heating/cooling rate of 10°C/min twice. Materials were placed in standard Mettler aluminum crucibles with sample weight of ~ 5 mg. While the first heating run erased the previous thermal history of the samples, the second heating curves were used for determining the glass transition temperature (T_g).[189]

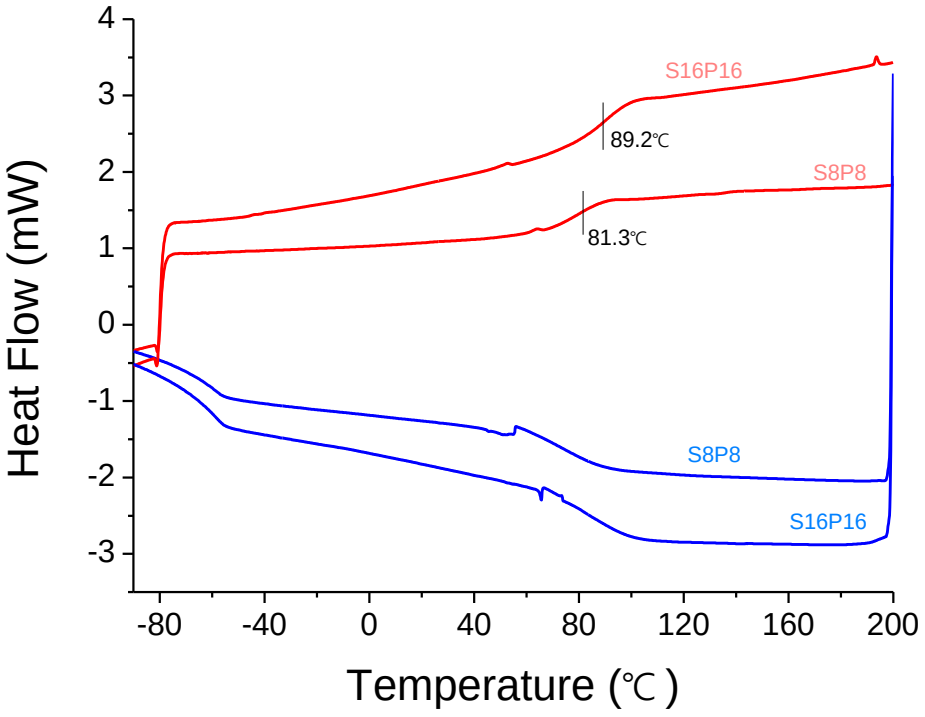

Figure S5.5. Dynamic scanning calorimetry curves of S8P8 and S16P16 HBPEs.

AFM images of the drop-cast films below LCST

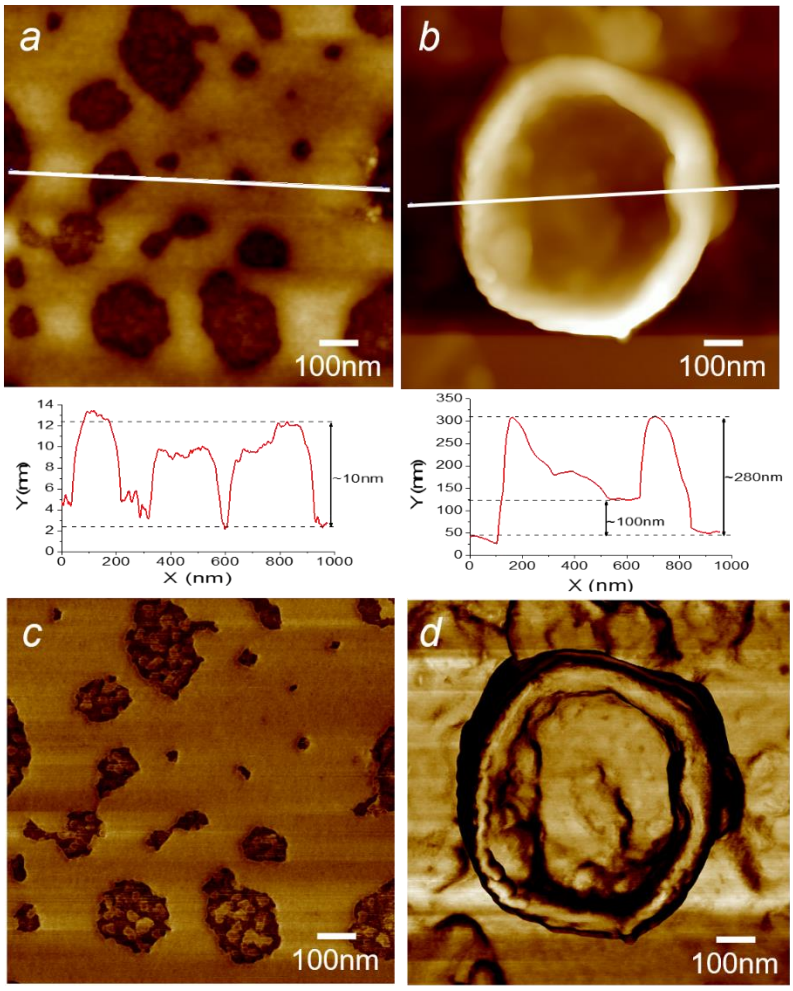

Figure S5.6. AFM topography images and corresponding height profiles (*a*,*b*) and phase images (*c*,*d*) of the drop-cast films of S8P8 (*a*,*c*) and S16P16 (*b*,*d*) solutions at ambient temperature. Z-scales are 20 nm, 400 nm, 30^{o} and 60^{o} respectively.

AFM images of drop-cast films above LCST

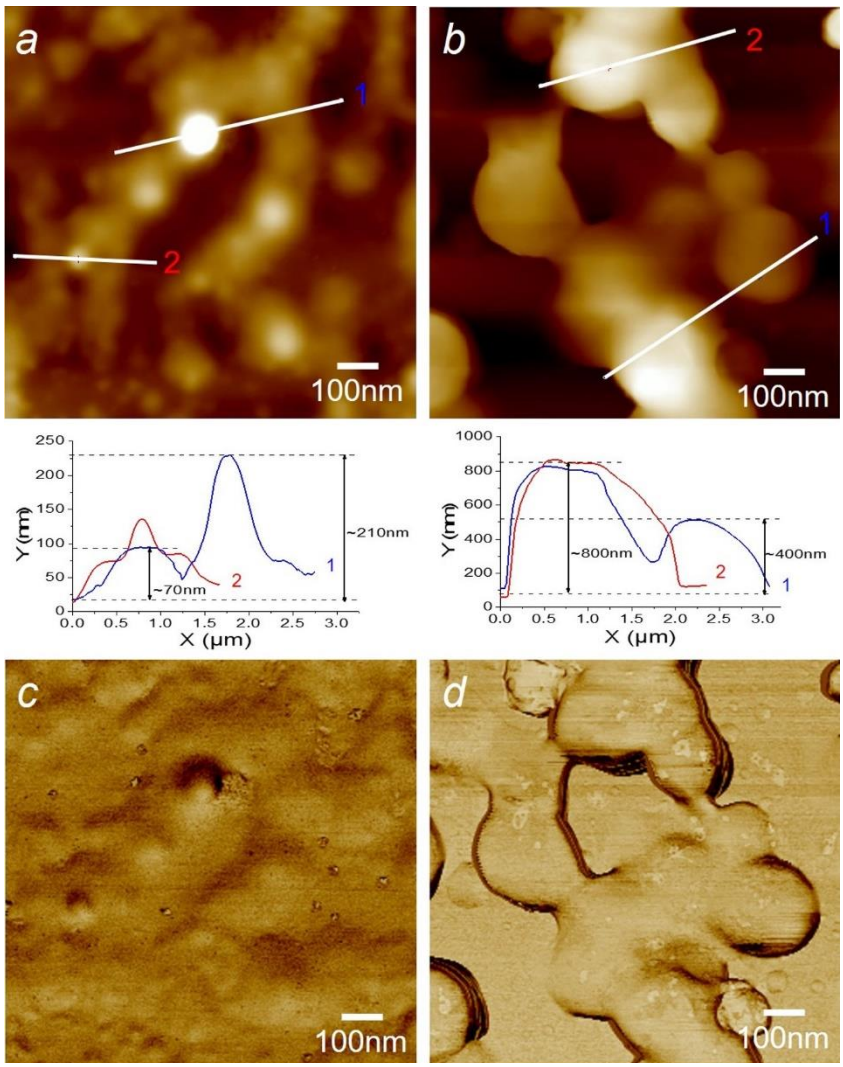

Figure S5.7. AFM topography images and corresponding height profiles (*a*,*b*) and phase images (*c*,*d*) of S8P8 (*a*,*c*) and S16P16 (*b*,*d*) at 50 ºC. Z-scales are 200 nm, 1,000 nm, 50º and 100º respectively.

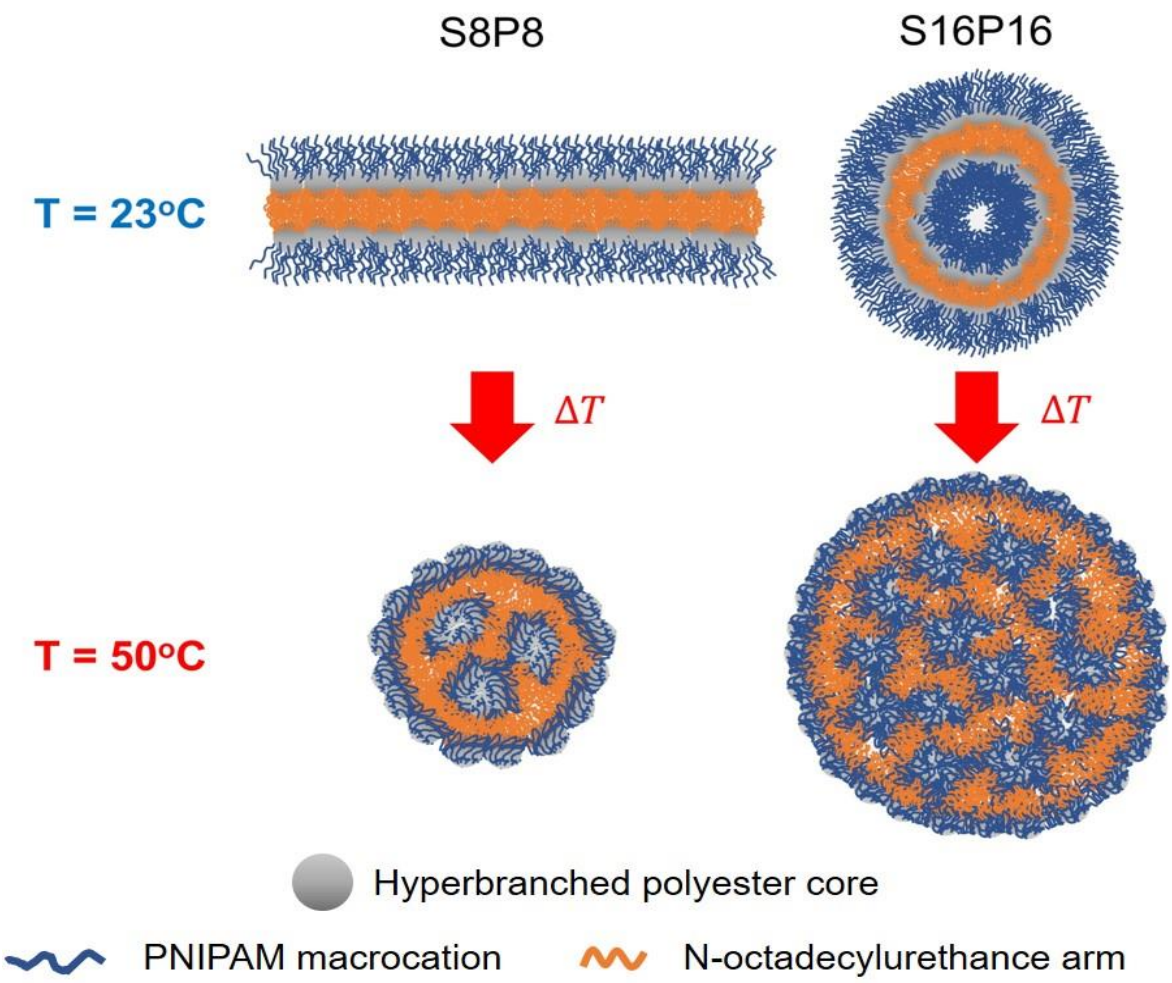

Figure S5.8. Schematic illustration of morphological transition of S8P8 and S16P16 HBPEs upon heating.

Effect of salts on the size and zeta potential distribution of hyperbranched polyelectrolyte assemblies

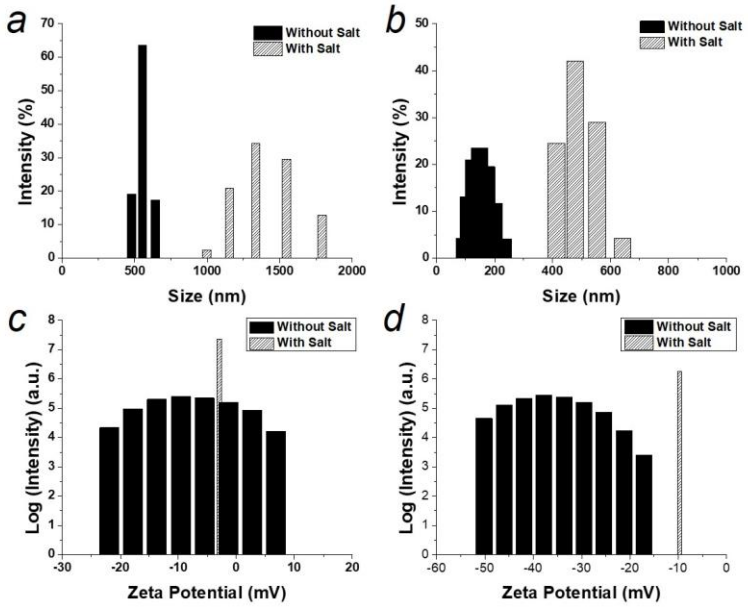

Figure S5.9. Distribution of size (*a*,*b*) and ζ-potential (*c*,*d*) of S8P8 (*a*,*c*) and S16P16 (*b*,*d*) HBPEs in aqueous media with and without 0.1 M NaCl at 25 ºC.

AFM topography images of the drop-cast films of HBPE solutions with 0.1M NaCl

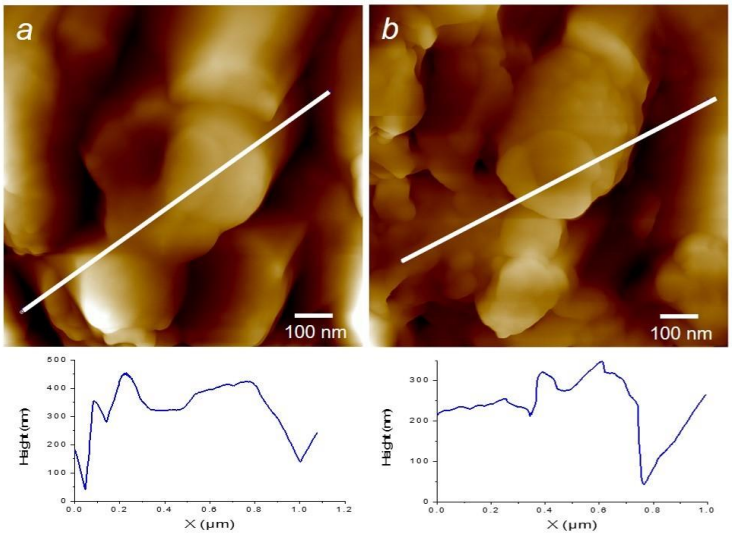

Figure S5.10. AFM topography images and corresponding height profiles of S8P8 (*a*) and S16P16 (*b*) at 23 ºC with 0.1M NaCl. Z-scales 500 nm for both images.

Molecular dynamic simulation of S16P16 assembly

Molecular Dynamics simulation was performed using AMBER 18 package.[315] Videos were recorded to show top and side view of the simulation system for 100 ns (**Movie S5.1-2**). Analyses of the trajectory were done using VMD[316] and the linear interaction energies were calculated using the CPPTraj [317] software packages. A single hyperbranched polyelectrolyte molecule was initially solvated in TIP3P box, energy minimized for 1000 steps, heated up to 300 K and simulated for 10 ns in NPT ensemble conditions. This relaxed structure was then stripped off the water molecules and used in the subsequent setup of the system with SiO_2 surface. A 409x210x25 $Å^3$ bonded SiO_2 surface having surface silanol density of 4.7 /nm^2 was constructed by translating the coordinates in the x and y directions as described in Ref 318.

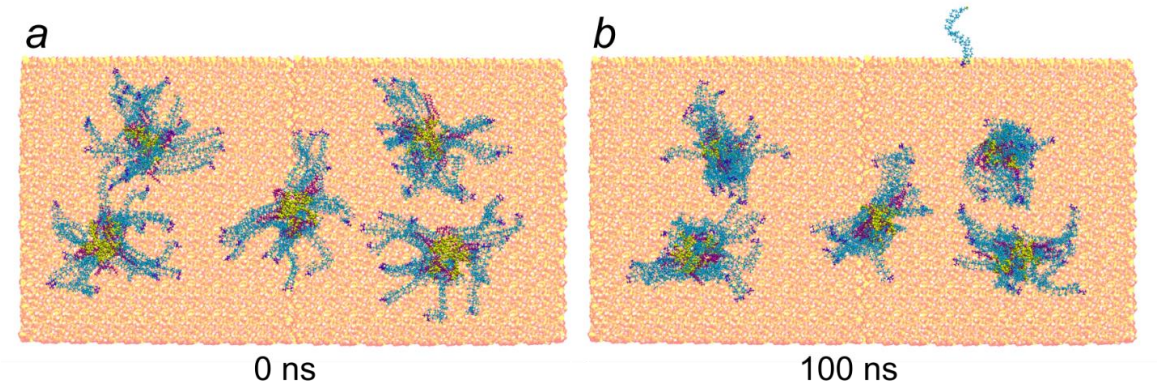

Figure S5.11. Top view of the simulation system containing five HBPEs on a SiO_2 surface (*a*) after minimization and equilibration (*b*) after 100 ns production simulation. Water molecules are hidden for clarity. Hyperbranched core in tan, PNIPAM macrocations in cyan, n-octadecyl urethane arms in red, terminal dimethyl acetamide groups in blue.

Figure S5.11 shows the top view of the simulation setup. Five molecules were set in random orientations above the SiO_2 surface in a configuration as the 5th face of a die. The particles at the sides have higher proximity to each other where the molecule at the center is relatively far from the other particles. The system was then solvated in TIP3P water box, using a buffer distance of 10 Å. The simulation was carried out at 300 K by using the Langevin thermostat with a collision frequency of 2 ps^{-1}. A constant pressure of 1 atm was

maintained by using the Monte-Carlo barostat[319] (if NPT ensemble). Periodic boundary conditions were applied. The initial structure was energy minimized, heated from 0 K to 300 K at a rate of 3 K/ps in NVT ensemble followed by an NVT equilibration step at 300 K for 0.3 ns with a timestep of 1fs. Because of the presence of a large rigid SiO_2 surface inside the simulation box, the subsequent NPT equilibration failed to adjust the box size automatically and left vacuum bubbles inside the box. The box size was manually reduced from the x, y, z directions and an NVT simulation was performed for 0.5 ns to equilibrate the water molecules. The process was repeated until the vacuum bubbles were eliminated. During this compression process, the size of the box was reduced from 453x250x161 $Å^3$ to 442x230x146 $Å^3$. An NPT simulation for 1 ns was run for further equilibration.

A harmonic restraint with a force constant of 10.0 kcal/mol/Å was applied on the SiO_2 surface during the all the steps of the simulation. The HBPE molecules were not harmonically restrained during the equilibration phase to facilitate the box compression. The NPT equilibration and the production simulations utilized the SHAKE algorithm[320] to covalent bonds involving hydrogen atoms with a timestep of 2fs. The intermolecular separation between the nearest PNIPAM macrocation of each HBP molecules and the SiO_2 surface were 5.53 Å, 2.35 Å, 2.10 Å, 7.73 Å and 1.20 Å after equilibration. Production simulations, from which all reported data was calculated, were performed in the NPT ensemble at 1 atm and 300 K for 100 ns.

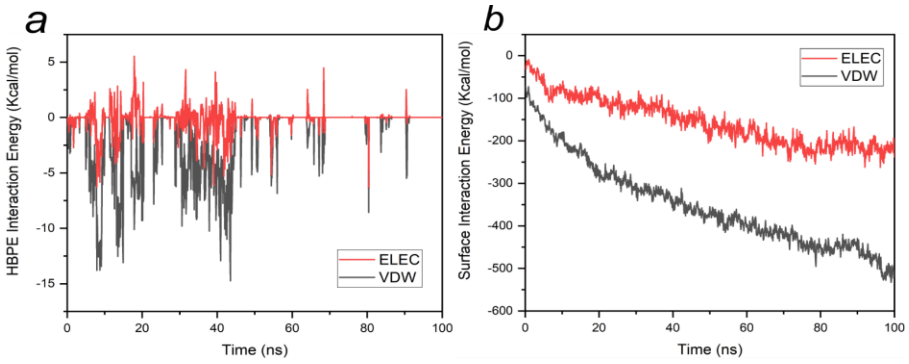

Figure S5.12. Time evolution of electrostatic and VDW components of linear interaction energy (*a*) between five HBP molecules (*b*) between five HBPE molecules and SiO_2 surface.

Figure S5.12 shows the time evolution of the van der Waals (VDW) and electrostatic interaction energy of the simulated system. The surface interaction energy was at least two orders of magnitude higher than the interparticle interaction energy. No pairwise interaction between the HBPE molecules is observed after 50 ns of the simulation due to the decrease in radius of gyration and increased anchoring to the SiO_2 surface. This stronger attraction towards the SiO_2 surface also prevented mobility of the HBPE molecules in the simulation.

Figure S5.13 shows the hopping lifetimes of the 80 PNIPAM macrocations of the 5 molecules. Movie S5.3 shows the hopping behavior of an individual macrocation. A 4 Å distance cutoff was used to determine whether the NH_3^+ group of the PNIPAM ion is within the vicinity of a target sulfonate site. The ions jump back and forth between the neighboring sulfonate sites. Out of total 80 ions, 36 ions (46% of the total) leave the original sulfonate site and do not return. The bars represent the time spent by the 44 ions that remained closer to their original sulfonate site. The error bars represent the maximum time spent on the original sulfonate site before the next hop. A smaller error bar represents higher hopping frequency while a bigger error bar represents a less mobile macrocation. In 1.25% case, they were able to entirely dissociate from the HBPE core.

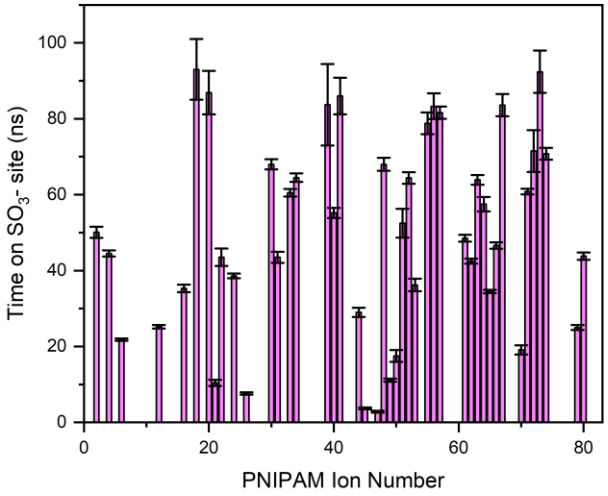

Figure S5.13. The 44 bars represent the time each NH_3^+ group of the 80 PNIPAM macrocations stayed on its original SO_3^- site. 36 ions do not return to their original SO_3^- sites. The error bars show the maximum time spent on a SO_3^- site before the next jump. A smaller error bar represents a higher hopping frequency.

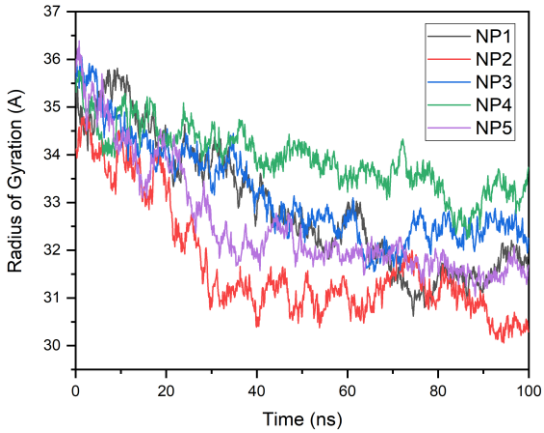

Figure S5.14. Time evolution of radius of gyration of the five HBPE molecules (excluding the dissociated macrocations).

Langmuir Isotherm of S8P8 and S16P16 monolayers

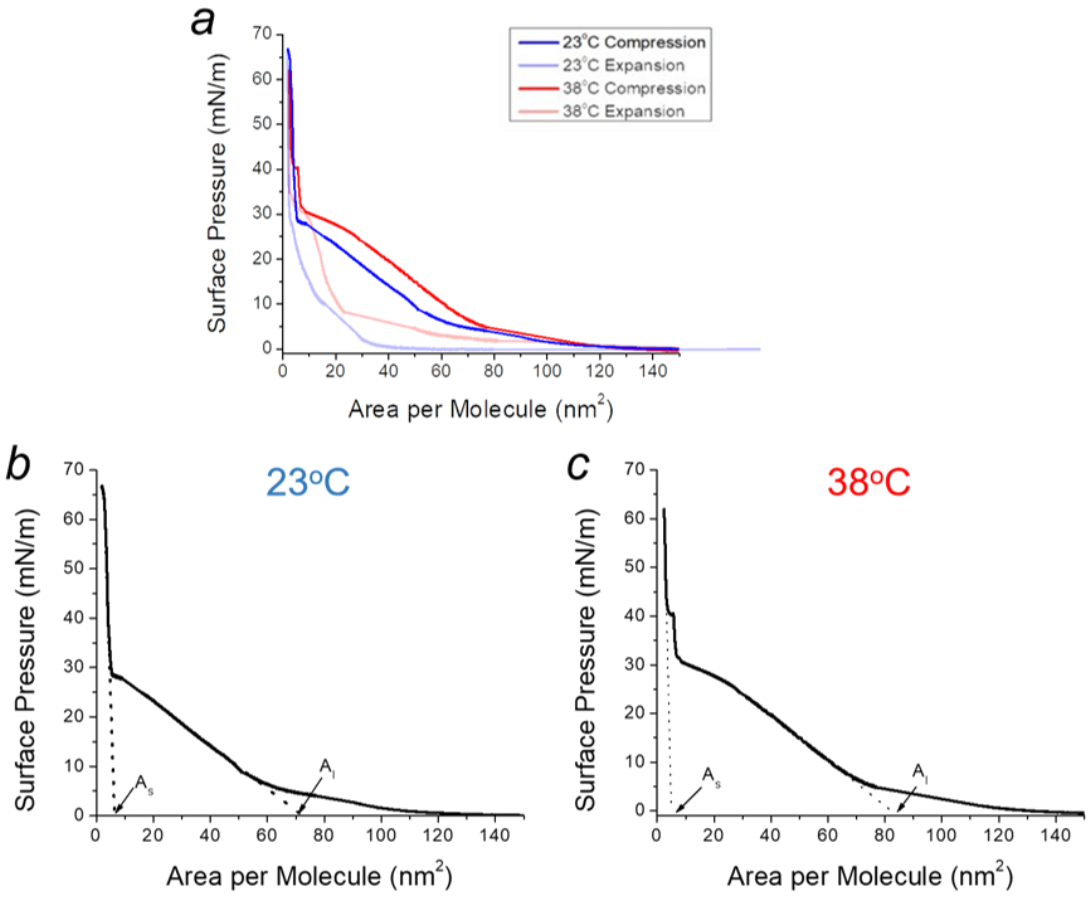

Figure S5.15. Langmuir isotherms of S8P8 HBPEs during first compression-expansion at different temperatures (*a*). Langmuir isotherm recorded at ambient temperature (*b*) and 38 ^{o}C (*c*), showing the limiting area per molecule in liquid and solid phases (A_l and $A_{s,}$ respectively).

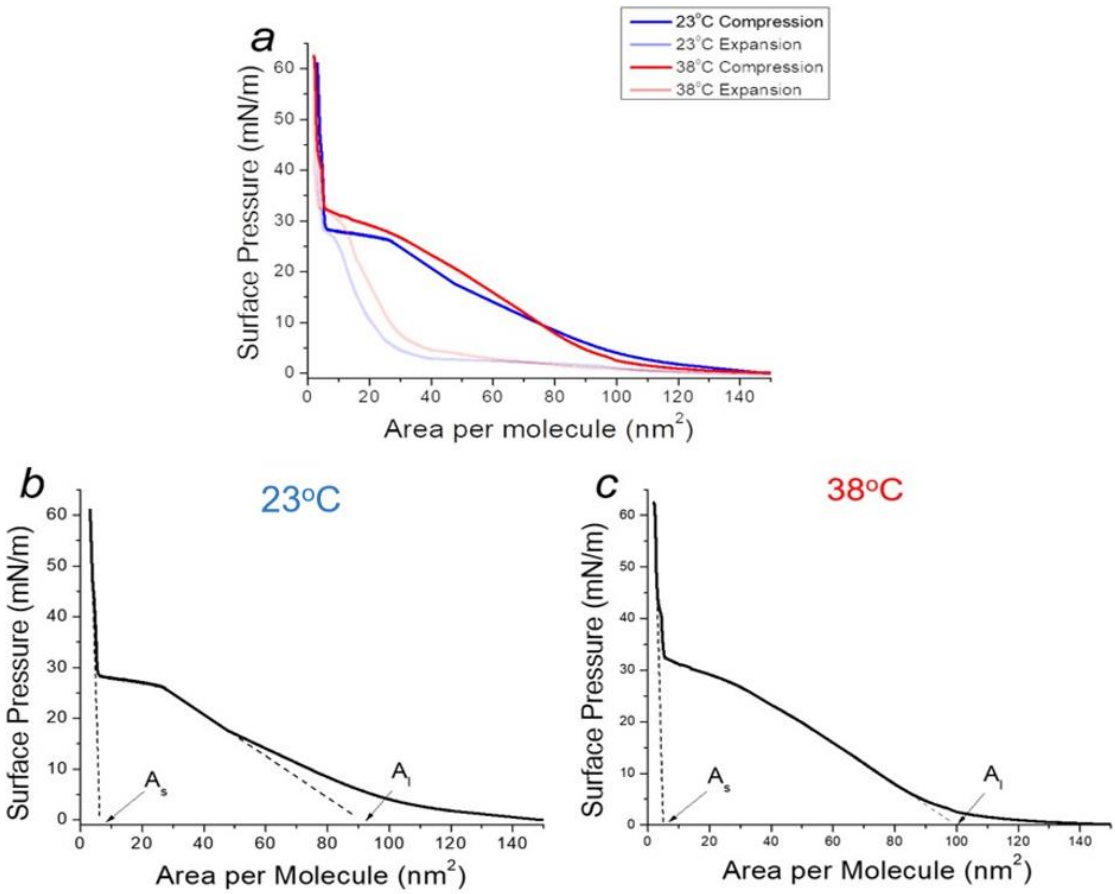

Figure S5.16. Langmuir isotherms of S16P16 HBPEs during first compression-expansion at different temperatures (*a*). Langmuir isotherm recorded at ambient temperature (*b*) and 38 °C (*c*), showing the limiting area per molecule in liquid and solid phases (A_l and A_s, respectively).

Langmuir isotherms for S8P8 and S16P16 below and above LCST during compression-expansion cycle

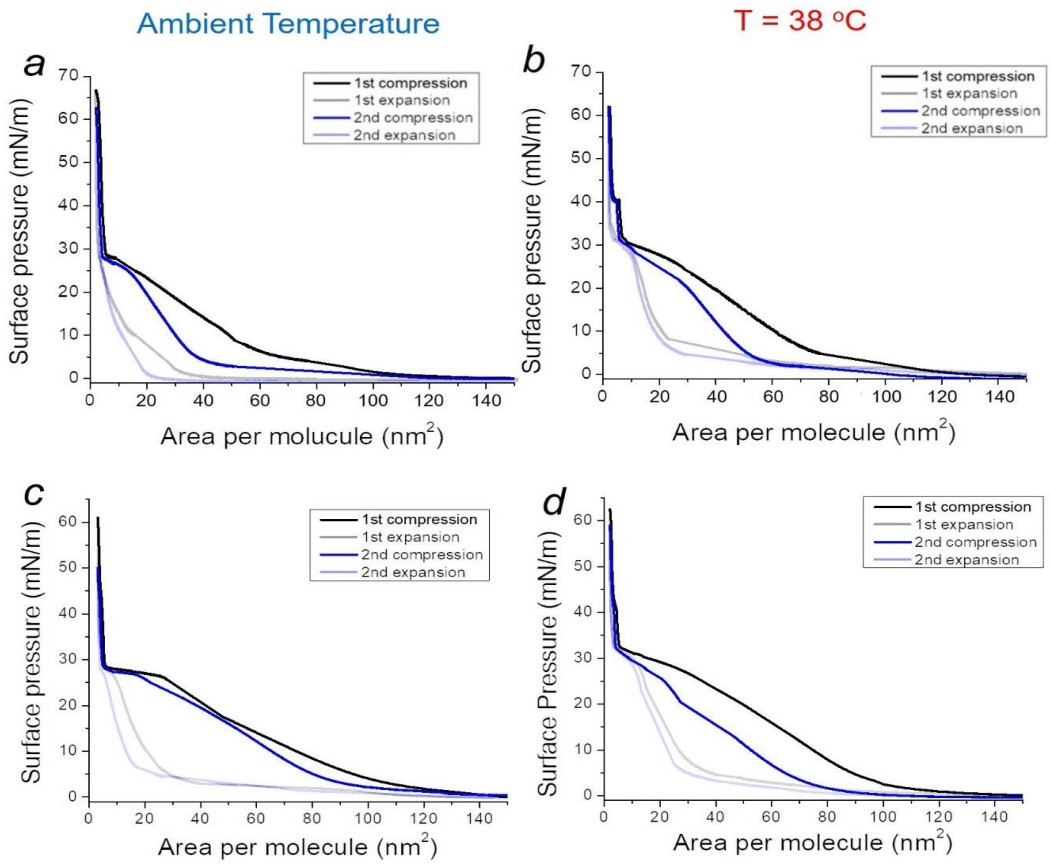

Figure S5.17. Langmuir isotherms of S8P8 (*a*,*b*) and S16P16 (*c*,*d*) HBPEs during compression-expansion cycles at different temperatures; ambient temperature (*a*,*c*) and 38°C (*b*,*d*).

Isotherm hysteresis appears for all isotherm curves during the compression-expansion cycles. Due to the intermolecular interaction and chain entanglement during compression, PNIPAM chains do not have enough time to recover their initial conformation during expansion.[61,321] The Langmuir isotherms during second compression were shifted toward smaller surface area since some HBPE molecules remained on the water surface from the initial monolayer compression and acted as nucleation sites for the domain formation during second compression.[225]

AFM topography images of S8P8 and S16P16 monolayers

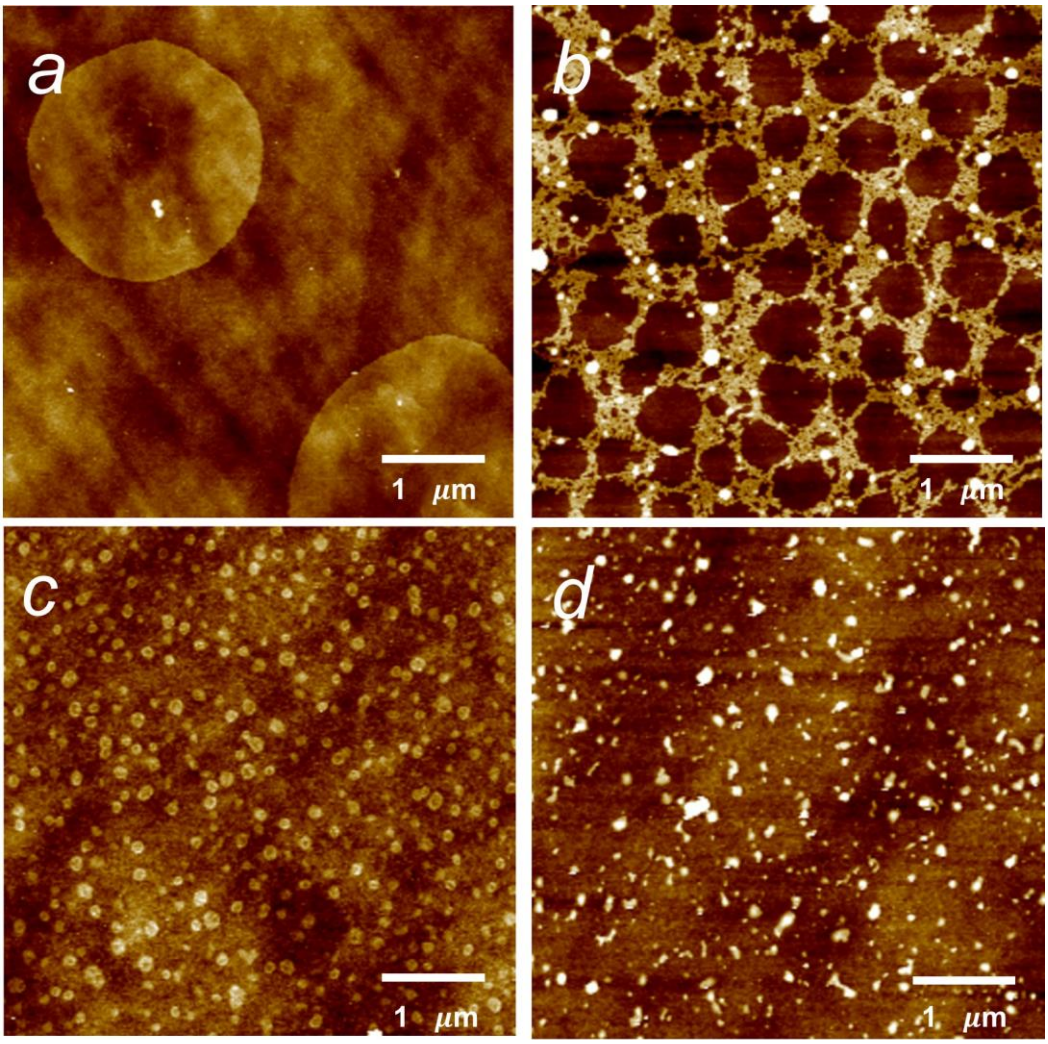

Figure S5.18. AFM topography images of LB monolayers of S8P8 (*a*,*b*) and S16P16 (*c*,*d*) at ambient temperature at different surface pressures: 20 mN/m (*a*,*c*) and 50 mN/m (*b*,*d*). Z scales are 10 nm for (*a*,*c*) and 15 nm for (*b*,*d*).

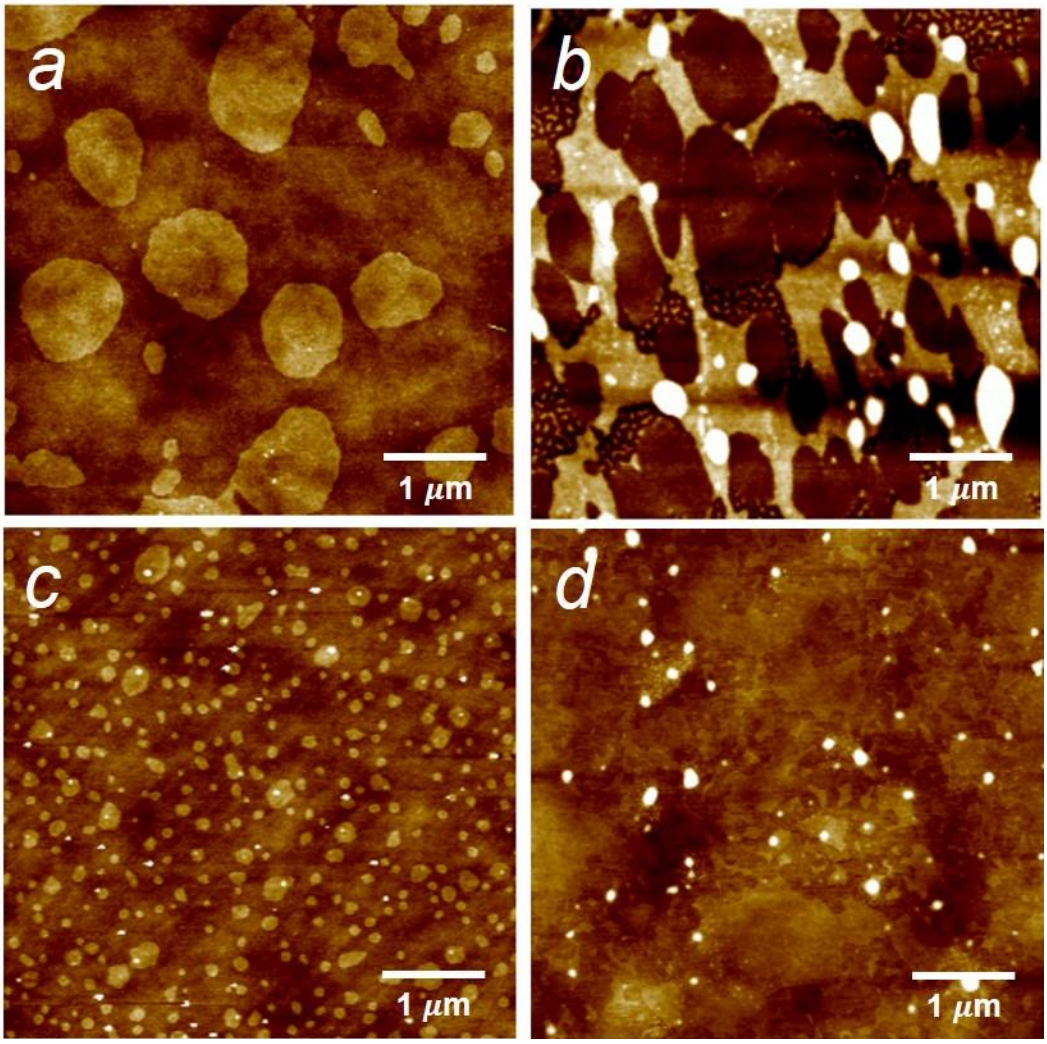

Figure S5.19. AFM topography images of LB monolayers of S8P8 (*a*,*b*) and S16P16 (*c*,*d*) at 38 °C at different surface pressures: 20 mN/m (*a*,*c*) and 50 mN/m (*b*,*d*). Z scales are 10 nm for (*a*,*c*) and 15 nm for (*b*,*d*).

AFM phase images of S8P8 and S16P16 monolayers

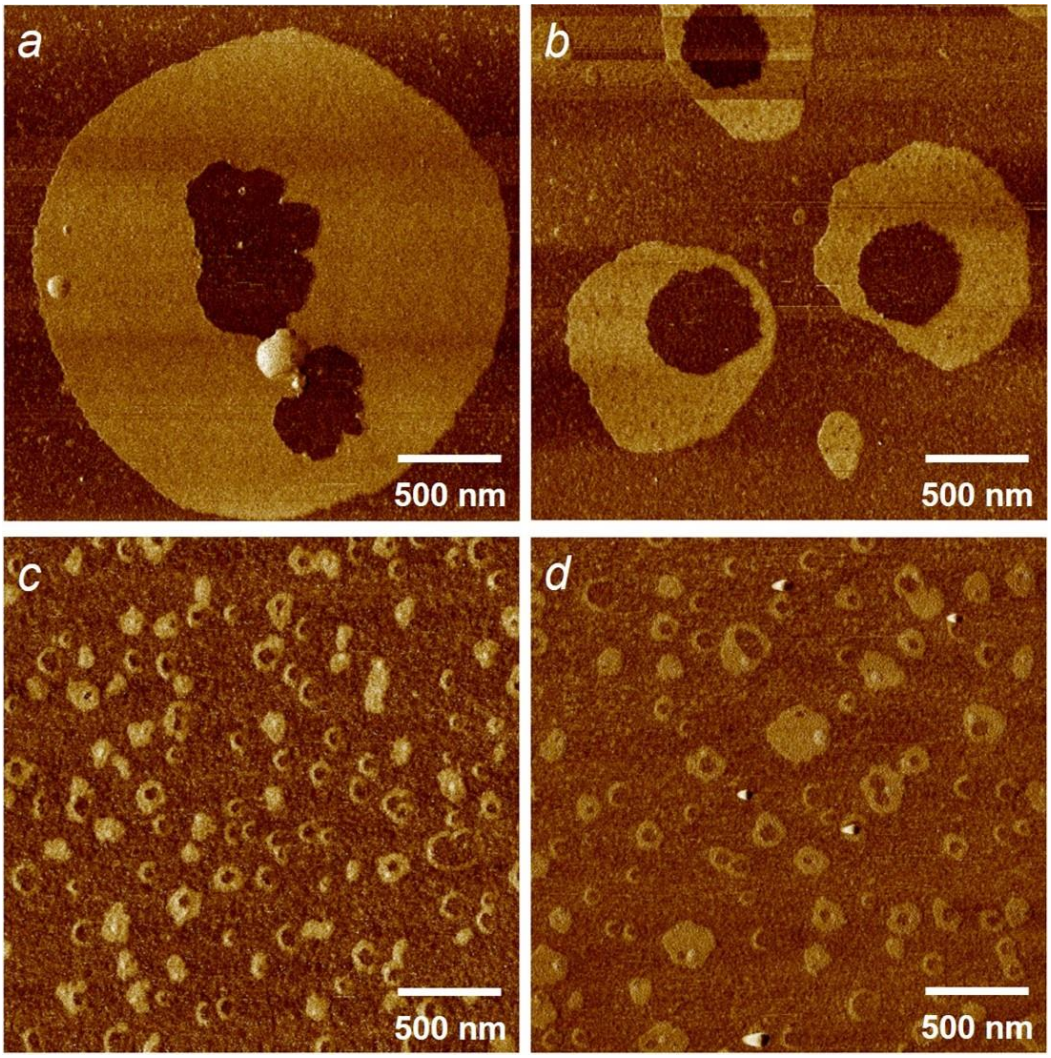

Figure S5.20. AFM phase images of S8P8 *(a,b)* and S16P16 (*c,d*) monolayers at 20 mN/m and at different temperatures; ambient temperature (*a,c*) and 38 ^{o}C (*b,d*). Z scales are 15^{o} and 3^{o} for (*a-c*) and (*d*), respectively.

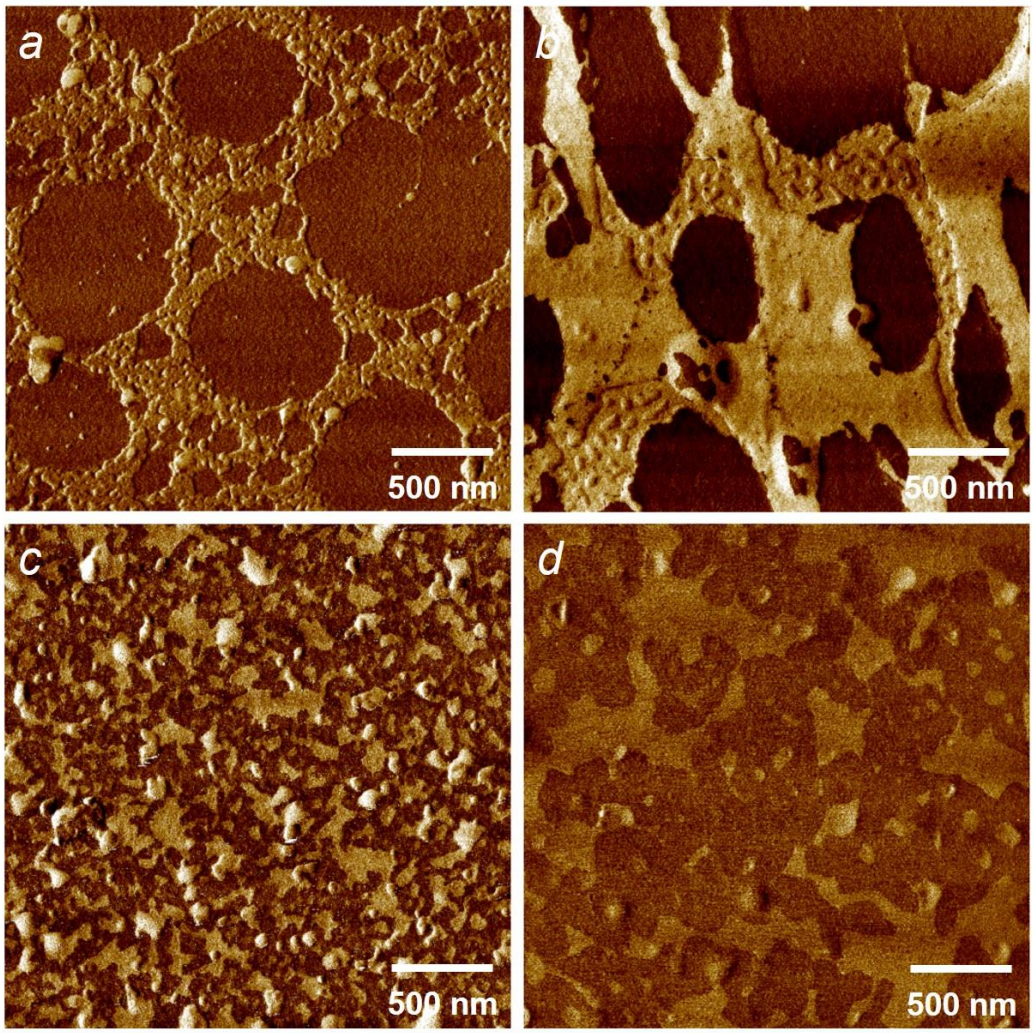

Figure S5.21. AFM phase images of S8P8 (*a*,*b*) and S16P16 (*c*,*d*) monolayers at 50 mN/m and at different temperatures; ambient temperature (*a*,*c*) and 38 ^{o}C (*b*,*d*). Z scales are 15^{o} for (*a*-*c*) and 3^{o} for (*d*).

AFM three-dimensional topography images of S8P8 and S16P16 monolayers

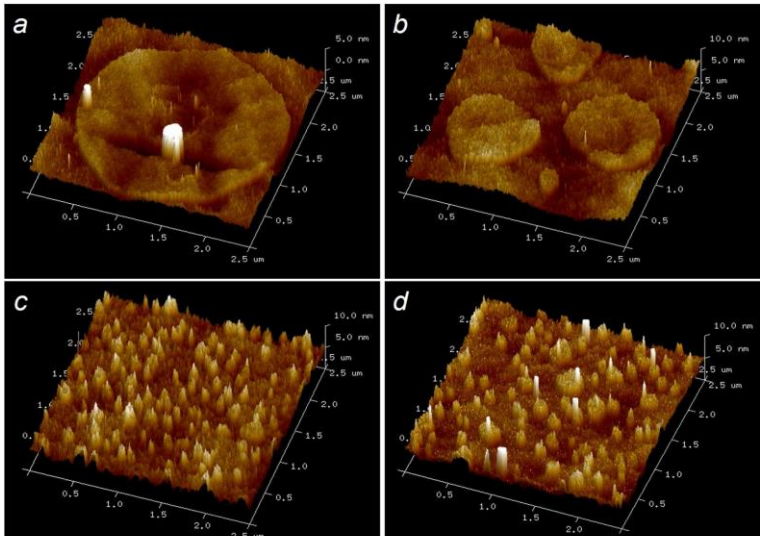

Figure S5.22. 3D AFM topography images of S8P8 (*a*,*b*) and S16P16 (*c*,*d*) monolayers at 20 mN/m and at different temperatures; ambient temperature (*a*,*c*) and 38 ^{o}C (*b*,*d*). Z scales are 10 nm for all images.

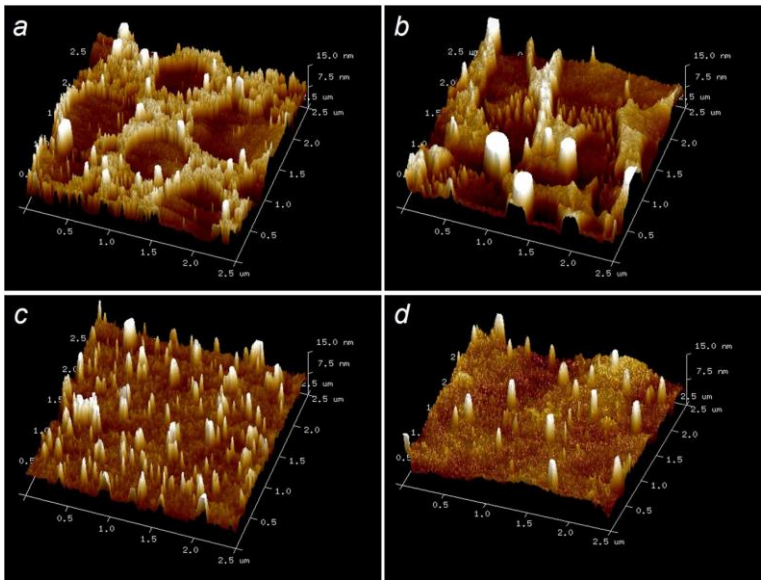

Figure S5.23. 3D AFM topography images of S8P8 (*a*,*b*) and S16P16 (*c*,*d*) monolayers at 50 mN/m and at different temperatures; ambient temperature (*a*,*c*) and 38 ^{o}C (*b*,*d*). Z scales are 15 nm for all images.

Thickness and roughness of S8P8 and S16P16 monolayers

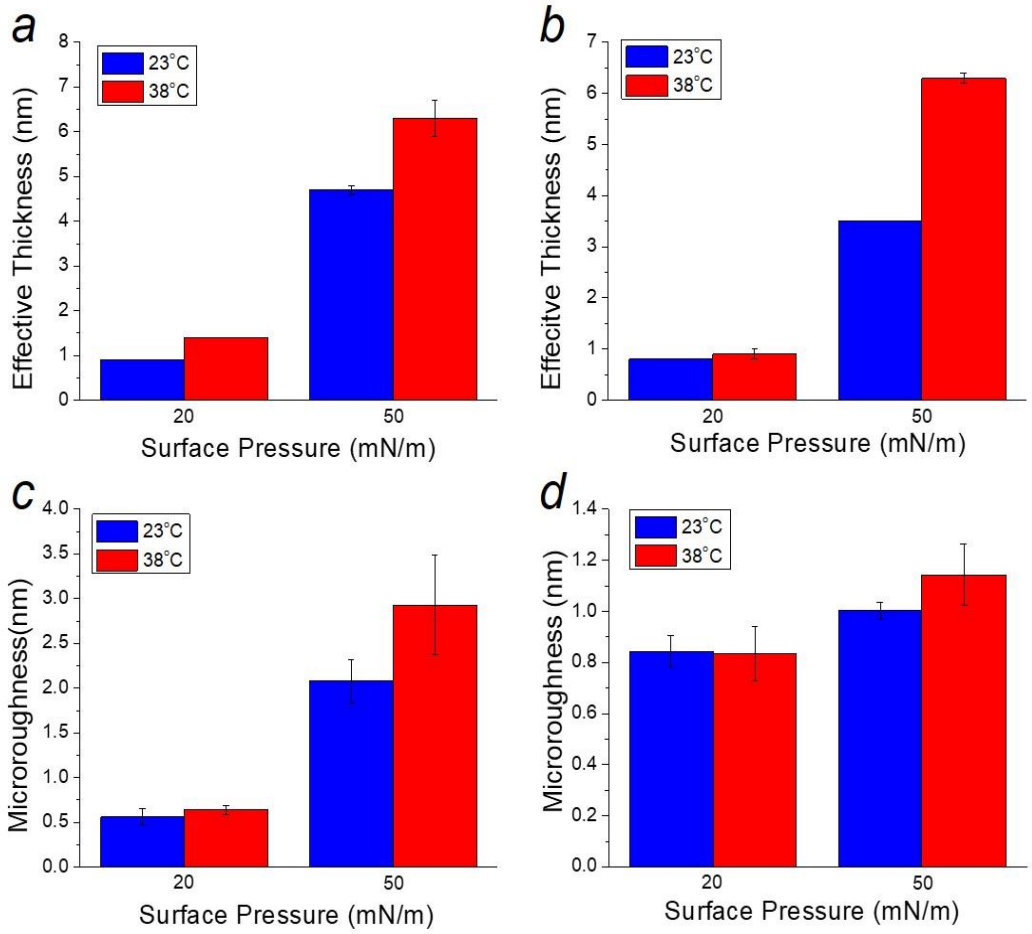

Figure S5.24. Effective thickness (*a*,*b*) and 1 μm x 1 μm microroughness (*c*,*d*) of S8P8 (*a*,*c*) and S16P16 (*b*,*d*) monolayers at different temperatures and surface pressures.

Topography, elastic modulus, adhesion and surface potential images obtained by Peak-Force Kelvin probe force microscopy.

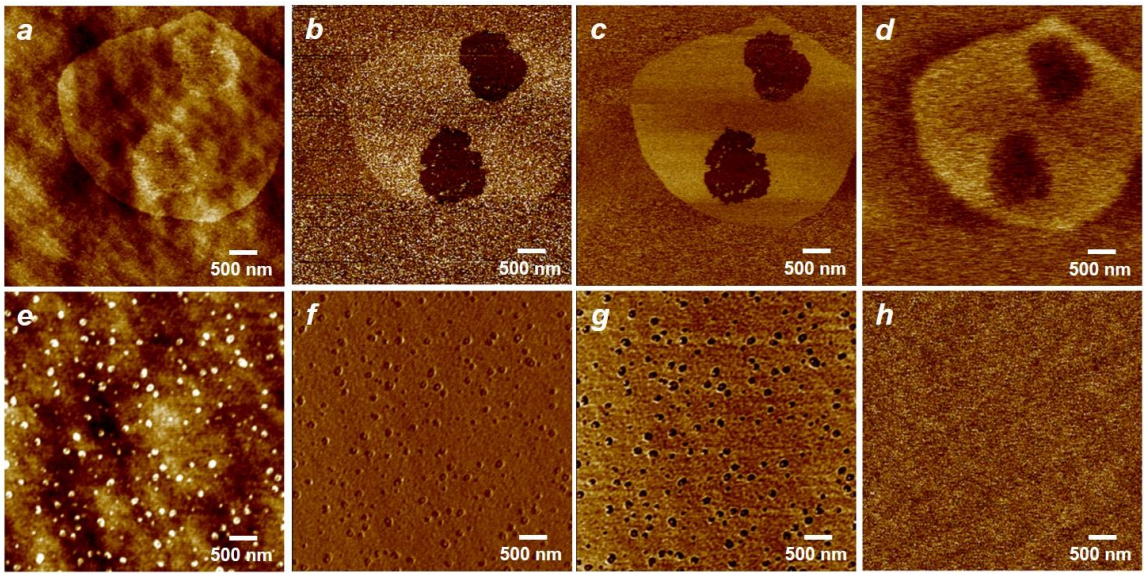

Figure S5.25. AFM topography (*a*,*e*), elastic modulus (*b*,*f*), adhesion (*c*,*g*) and surface potential (*d*,*h*) images and corresponding profiles of S8P8 (*a*-*d*) and S16P16 (*e*-*h*) monolayers at 20 mN/m and ambient temperature. Z scales are 7 nm for (*a*,*e*), 2 GPa for (*b*), 1 GPa for (*f*),1 nN for (*c*), 10 nN for (*g*), 1 V for (*d*), and 0.2 V for (*h*).

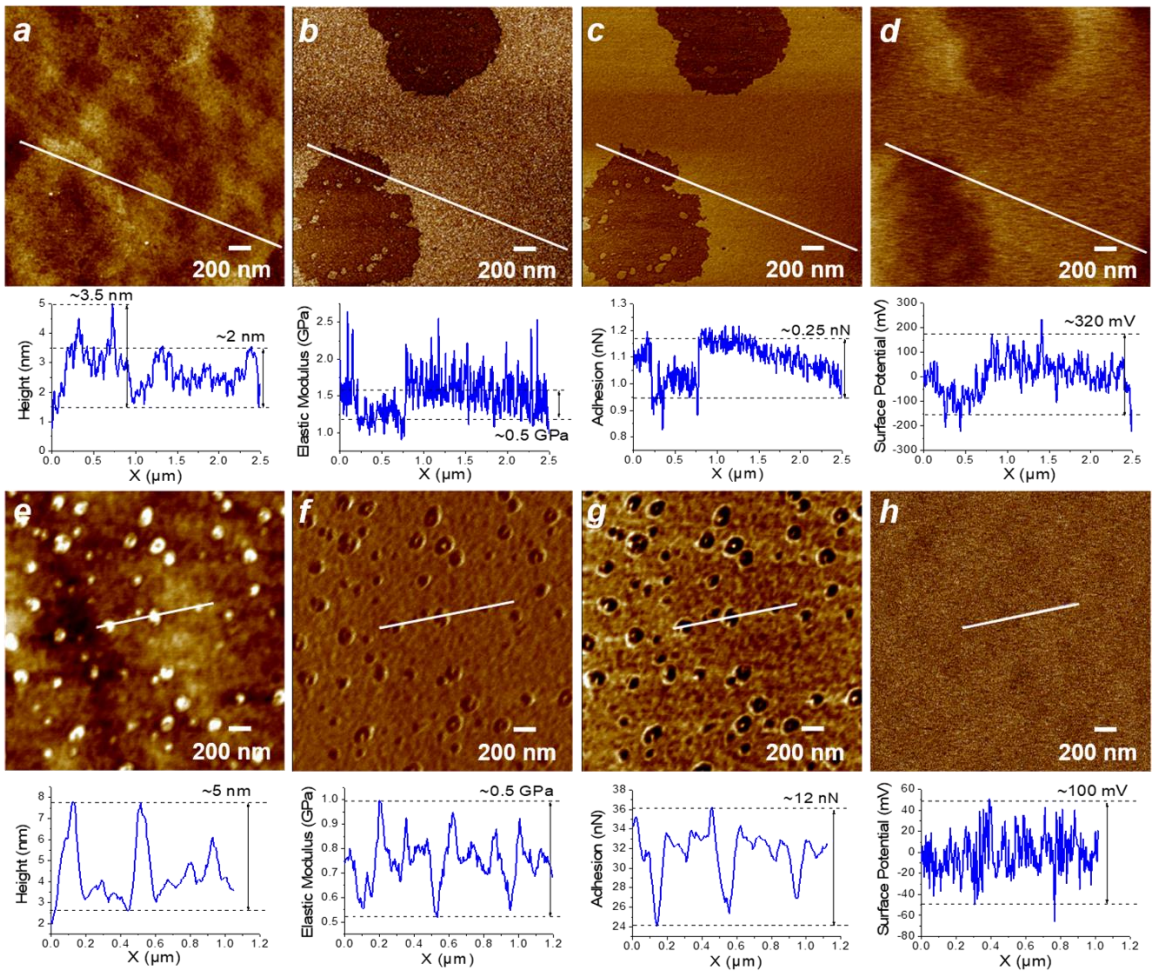

Figure S5.26. AFM topography (*a*,*e*), elastic modulus (*b*,*f*) and adhesion (*c*,*g*) and surface potential *(d*,*h*) images and corresponding profiles of S8P8 (*a*-*d*) and S16P16 (*e*-*h*) monolayers at 20 mN/m and ambient temperature. Z scales are 7 nm for (*a*,*e*), 2 GPa for (*b*), 1 GPa for (*f*),1 nN for (*c*), 10 nN for (*g*), 1 V for (*d*), and 0.2 V for (*h*).

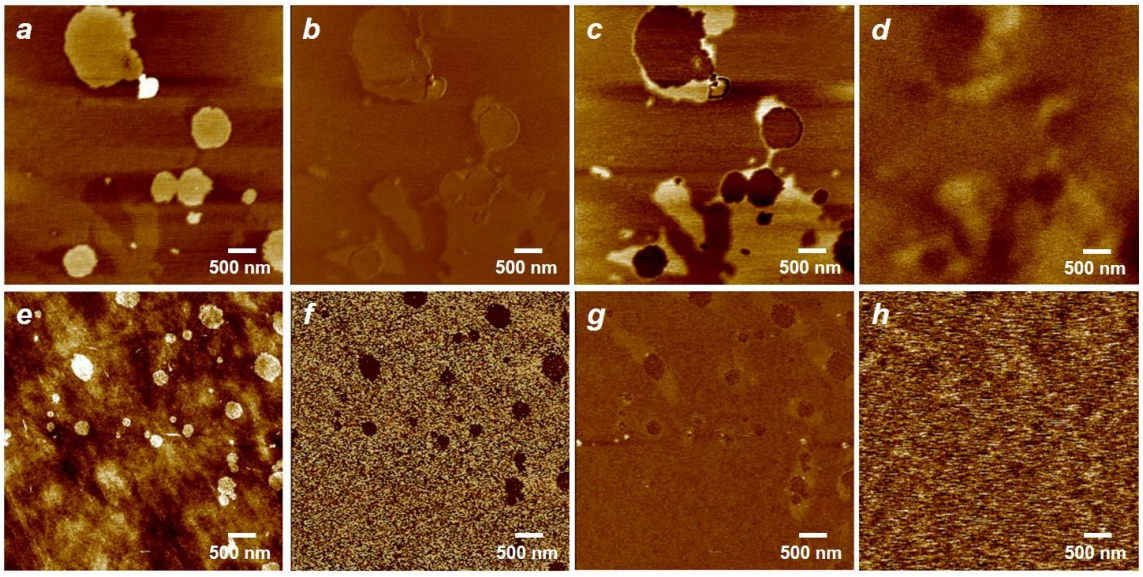

Figure S5.27. AFM topography (*a*,*e*), elastic modulus (*b*,*f*), adhesion (*c*,*g*) and surface potential (*d*,*h*) images and corresponding profiles of S8P8 (*a*-*d*) and S16P16 (*e*-*h*) monolayers at 20 mN/m and 38 ^{o}C. Z scales are 7 nm for (*a*,*e*), 0.5 GPa for (*b*), 5 GPa for (*f*),10 nN for (*d*), 2 nN for (*h*) and 0.6 V for (*d*,*h*).

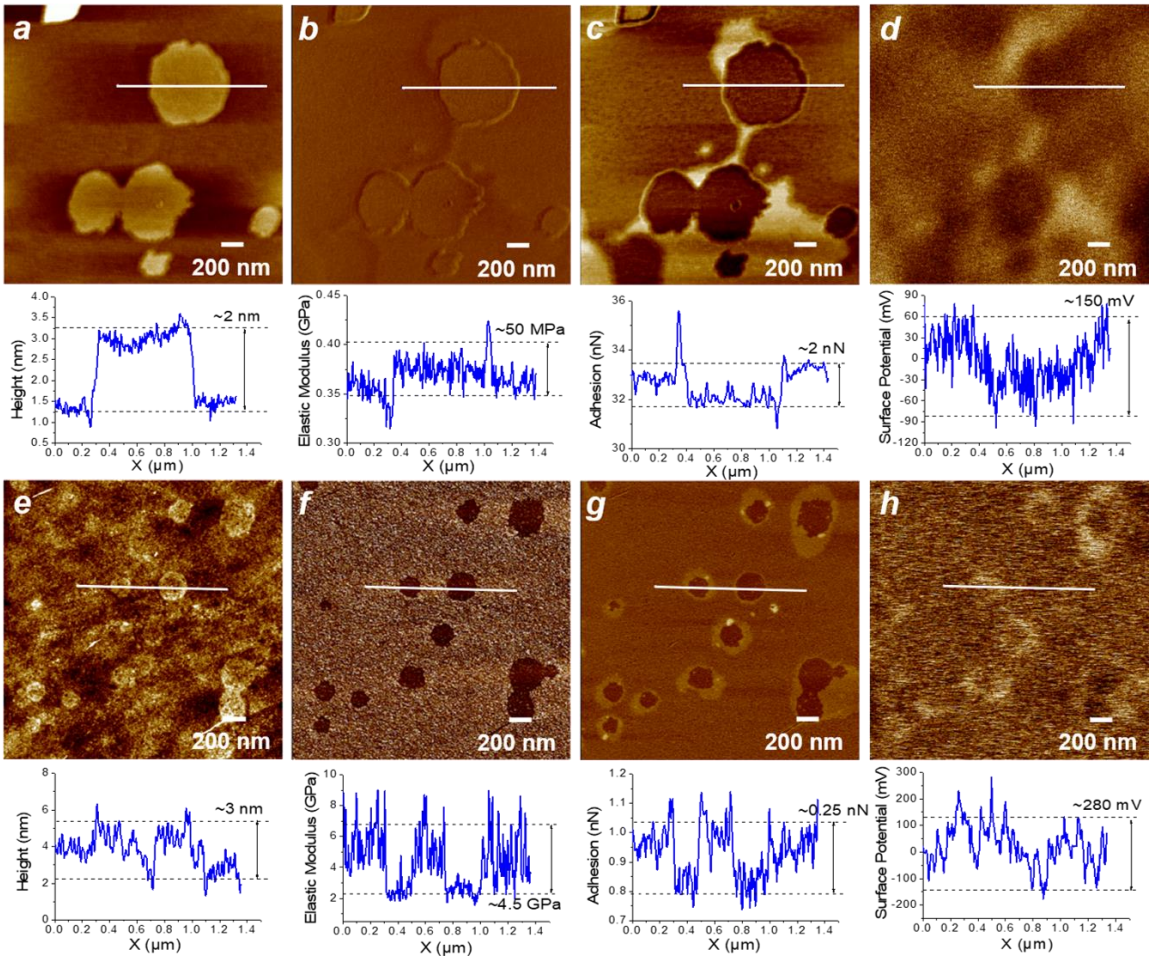

Figure S5.28. AFM topography (*a*,*e*), elastic modulus (*b*,*f*), adhesion (*c*,*g*) and surface potential (*d*,*h*) images and corresponding profiles of S8P8 (*a*-*d*) and S16P16 (*e*-*h*) monolayers at 20 mN/m and 38 ºC. Z scales are 7 nm for (*a*,*e*), 0.5 GPa for (*b*), 5 GPa for (*f*),10 nN for (*c*), 2 nN for (*g*) and 0.6 V for (*d*,*h*).

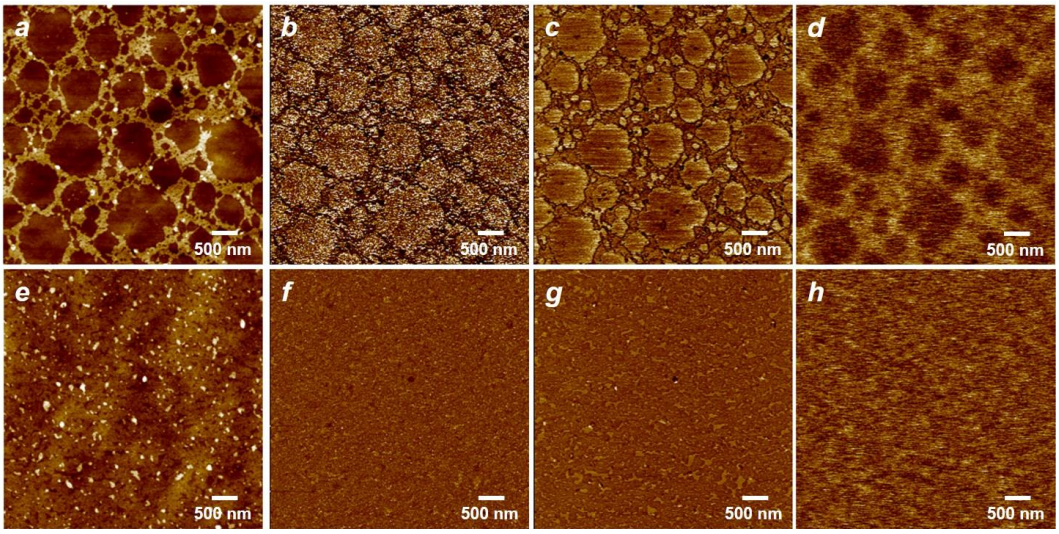

Figure S5.29. AFM topography (*a*,*e*), elastic modulus (*b*,*f*), adhesion (*c*,*g*) and surface potential (*d*,*h*) images and corresponding profiles of S8P8 (*a*-*d*) and S16P16 (*e*-*h*) monolayers at 50 mN/m and ambient temperature. Z scales are 15 nm for (*a*,*e*), 5 GPa for (*b*,*f*), 3 nN for (*c*,*g*), and 1 V (*d*,*h*).

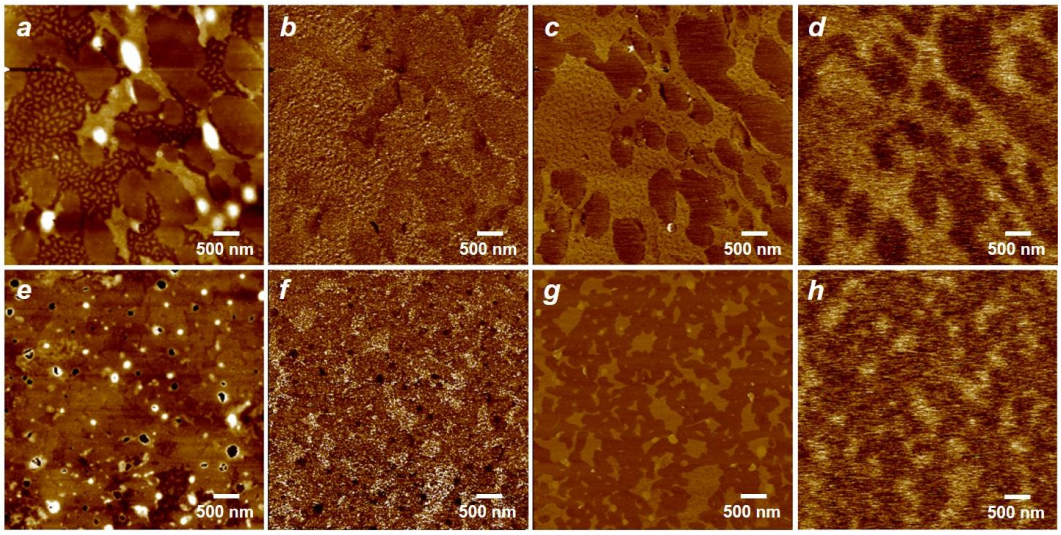

Figure S5.30. AFM topography (*a*,*e*), elastic modulus (*b*,*f*), adhesion (*c*,*g*) and surface potential (*d*,*h*) images and corresponding profiles of S8P8 (*a*-*d*) and S16P16 (*e*-*h*) monolayers at 50 mN/m and 38 ^{o}C. Z scales are 15 nm for (*a*), 30 nm for (*e*), 2.5 GPa for (*b*), 5 GPa for (*f*), 3 nN for (*c*,*g*), and 1 V for (*d*,*h*).

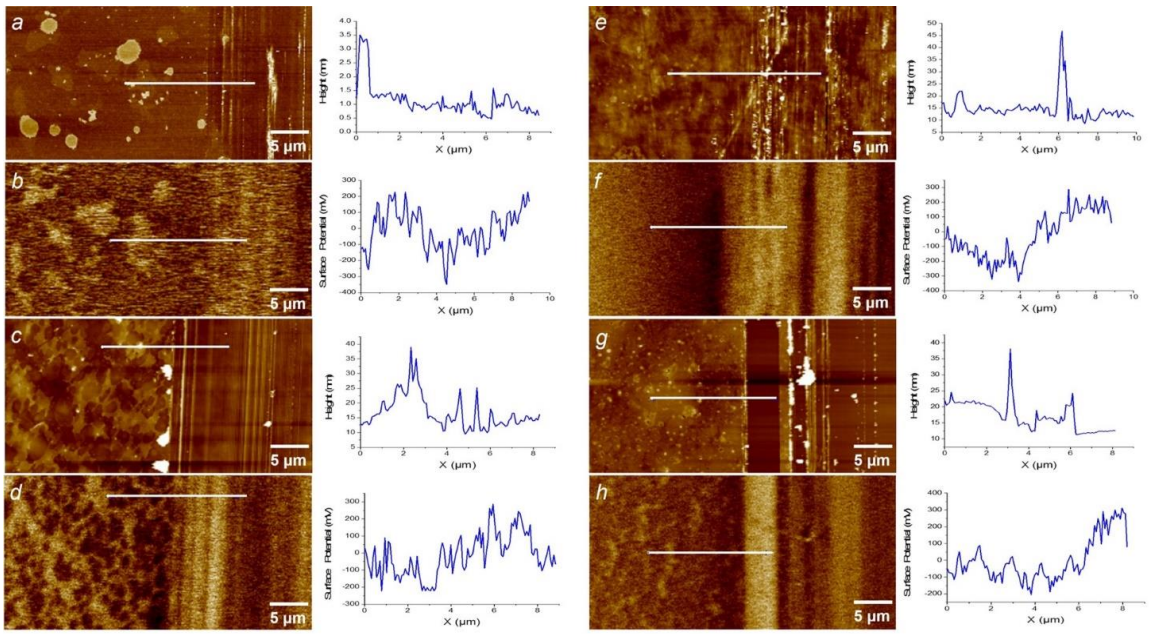

Figure S5.31. AFM topography (*a*,*c*,*e*,*g*), and surface potential (*b*,*d*,*f*,*h*) images and corresponding profiles of S8P8 (*a*-*d*) and S16P16 (*e*-*h*) monolayers with SiO_2-exposed region at 38 ^oC at different surface pressures: 20 mN/m (*a*,*b*,*e*,*f*) and 50 mN/m (*c*,*d*,*g*,*h*). Z scales are 7nm for (*a*), 30 nm for (*c*) 50 nm for (*e*,*h*), and 1 V for (*b*,*d*,*f*,*h*).

CHAPTER 6. SYNTHESIS AND ASSEMBLY OF REACTIVE AMPHIPHLIC APROTIC IONIC LIQUIDS BASED ON FUNCTIONALIZED OLIGOMERIC SILSESQUIOXANES

6.1 Introduction

Ionic liquids are organic salts with melting point below 100 ^{o}C and exhibit interesting properties, including a relatively high ionic conductivity, wide electrochemically stable window, negligible vapor pressure, and high chemical and thermal stabilities. [322] Polymerized ionic liquids have attracted great interest due to their unique properties derived from ionic liquid composition and possibilities for various practical applications, such as polymer electrolytes in electrochemical devices, building blocks in nanocomposites, innovative sensitive materials, and smart surfaces.[18,.323,324] Oligomeric ionic liquids (OILs) occupy an intermediate position between conventional low molecular weight ionic liquids and their polymeric analogues. Combining the unique properties of ionic liquids with the peculiarities of physical behavior of oligomers, these compounds can be considered as soft ion-conducting media for various electrochemical devices, antimicrobial additives for antifouling coatings, and solvents and immobilizing agents for heterogeneous catalysis.[322]

Among OILs, polyhedral oligomeric silsesquioxanes (POSS)-based OILs are of considerable interest. [325 , 326] POSS-OILs are typically composed of an inorganic, completely condensed polyhedral silsesquioxane core and an ionic group containing organic substituent.[327,328,329,330,331,332] POSS-OILs have advantages over conventional organic OILs since the introduction of inorganic silsesquioxane core increases thermal, chemical, and mechanical stability, and a star-like structure of POSS allows for generating an organic shell with a different number of spatially separated ionic groups for a certain functional purpose. Thus, POSS-OILs are promising for various applications, such as dopants of ion-exchange membranes and electrolytes for dye-sensitized solar cells.[69,70,71, 333 , 334] However, the assembly behavior of POSS-based OILs has been unexplored to date with a few studies reported on aprotic imidazolium-containing POSS-based polymeric or monomeric ionic liquids.[28,335,336]

One of directions for further development of chemistry of such organic-inorganic OILs is to suggest a facile, one-pot synthesis of their inorganic cores. This goal can be achieved by using a mixture of completely (cage) condensed polyhedral structures (specific to POSS) with incompletely condensed polyhedral structures and their linear and branched (open-chain) analogs. Many attempts have been made to obtain these mixtures by using a sol-gel process, and the ratio of the cage and open-chain structures can be controlled by adjusting the structure of organic shell of OILs and the conditions for the sol-gel process.[185,186,337,338,339,340,341] In addition, reactive oligomeric silsesquioxanes (OSS) with functional groups, such as epoxy, methacrylate groups as well as fragments containing aliphatic tertiary amine with hydroxyl groups, have been synthesized and utilized as an initial oligomer for following polymer synthesis.[161,337,338,370] While OSS-based ionic liquids (OSS-ILs) have been prepared by the sol-gel method,[339,340,341] the synthesis of amphiphilic OSS-ILs with functional groups and their oligomeric and polymeric analogs has not been reported.

In order to impart the organic-inorganic OSS-ILs with new functionalities, we develop a new approach to introduce an ionic group into the organic shell of OSS-ILs in combination with reactive groups and fragments of various functionalities. This process is carried out by modifying the organic shell of OSS, which contain a mixture of pre-synthesized silsesquioxane structures as an inorganic component, which is in contrast to the currently reported preparation methods for OSS-ILs by the sol-gel method with trialkoxysilanes bearing ionic groups.[339,340,341] This approach ensures the presence of an inorganic component and provides the possibility of further desired changes in the chemical structure and functionality of the organic shell.

In this work, OSSs with fragments containing aliphatic tertiary amine with hydroxyl groups (OSS(N+OH)) was selected as an initial compound since it can contain reactive groups of various types. The reactive groups of this compound allow for both various condensation reactions and introduction of ionic liquid groups by direct neutralization and quaternization reactions.[161] Using the new method developed here, amphiphilic cationic aprotic OSS-based OILs (OSS-OILs) were synthesized containing quaternary amino groups and hydrophobic alkyl substitutes of variable lengths in the organic shell. We investigated the

chemical structure, ionic conductivity and self-assembly behavior of the OSS-OILs with focus on the effects of hydrophilic-hydrophobic balance.

6.2 Experimental Section

6.2.1 Materials

(3-aminopropyl)triethoxysilane (99%), glycidol (96%), 1-bromopropane (99%), 1-bromodecane (98%), were purchased from Sigma-Aldrich and used as received. Dimethyl sulfoxide and acetonitrile were distilled before usage. The ultrapure water used in all experiments was prepared in a three-stage Millipore Milli-Q Plus 185 purification system (resistivity ≥18.2 MΩ·cm).

6.2.2 Synthesis of OSS-OILs

Synthesis of OSS(N+OH). The initial compound OSS(N+OH) was synthesized according to common technique by hydrolytic condensation of the product of interaction of 3-aminopropyl triethoxysilane with a twofold molar excess of glycidol.[185,186] The hydroxyl group content was 21.4% (calcd., 25.5%). The tertiary amino group content was 4.9% (calcd. 5.4%). The amounts of the initial substances were calculated from the actual content of tertiary amino groups in OSS(N+OH).

FTIR: ν Si-O-Si (1031 cm^{-1}), ν C-H bonds of CH and CH_2 groups (2765-3020 cm^{-1}), δ C-H bonds of CH and CH_2 groups (1462 cm^{-1}), ν O-H bonds of hydroxyl groups (3020-3723 cm^{-1}).

^{1}H NMR (DMSO-d_6): 0.51 ($[SiO_{1,5}]_n$–C***H₂***–), 1.50 (=N–CH_2–C***H₂***–), 2.38 and 2.78 (=N–C***H₂***–CH_2–), 3.34, 3.39, 3,56, 3.71 (=N–C***H₂***–CH(OH)–, –C***H₂***OH, –CH_2O***H***, –CH(O***H***)–) ppm.

Synthesis of OSS($C_3N^+Br^-$). The solution of 1.74 g (0.0142 g-equiv) 1-bromopropane in 2 mL DMSO was added to the solution of 4.05 g (0.0142 g-equiv) OSS(N+OH) in 8 mL DMSO. The reaction was held at 80 °C and stirring for 32 h. The solvent was partially removed under reduced pressure. Then the product was precipitated and washed twice with

acetonitrile. The obtained OSS-$C_3N^+Br^-$ was dried at 60 °C. Yield is 4,92 g (85%). The product is a clear, light brown viscous liquid.

FTIR: ν Si-O-Si (1023 cm^{-1}), ν C-H bonds of CH, CH_2 and CH_3 groups (2843-2987 cm^{-1}), δ C-H bonds of CH, CH_2 and CH_3 groups (1463 cm^{-1}), ν O-H bonds of hydroxyl groups (3020-3696 cm^{-1}).

^{1}H NMR (DMSO-d_6): 0.69 ($[SiO_{1,5}]_n$–C***H₂***–), 0.94 (-C***H₃***), 1.77 (=N^+–CH_2–C***H₂***–), 3.15 (=N^+–C***H₂***–CH_2–), 3.37, 3.48 (=N^+–C***H₂***–CH(OH)–, –C***H₂***OH, –CH_2O***H***, –CH(O***H***)–), 4.00 (–C***H***(OH)–) ppm.

Synthesis of OSS($C_{10}N^+Br^-$). This oligomer was synthesized in a similar way to **OSS-$C_3N^+Br^-$**. The solution of 2.37 g (0.0107 g-equiv) 1-bromodecane in 2 mL DMSO was added to the solution of 3.06 g (0.0107 g-equiv) OSS(N+OH) in 6 mL DMSO. Yield is 4.83 g (89%). The obtained OSS-$C_{10}N^+Br^-$ is a clear, light brown viscous liquid.

FTIR: ν Si-O-Si (1043 cm^{-1}), ν C-H bonds of CH, CH_2 and CH_3 groups (2832-2991 cm^{-1}), δ C-H bonds of CH, CH_2 and CH_3 groups (1462 cm^{-1}), ν O-H bonds of hydroxyl groups (3018-3690 cm^{-1}).

^{1}H NMR (DMSO-d_6): 0.69 ($[SiO_{1,5}]_n$–C***H₂***–), 0.86 (–C***H₃***), 1.25 (CH_3(C***H₂***)$_7$–), 1.77 (=N^+–CH_2–C***H₂***–), 3.18 (=N^+–C***H₂***–CH_2–), 3.38, 3.48 (=N^+–C***H₂***–CH(OH)–, –C***H₂***OH, –CH_2O***H***, –CH(O***H***)–), 4.03 (–C***H***(OH)–) ppm.

6.2.3 Characterization

FTIR spectra were recorded using a TENSOR 37 FT-IR spectrophotometer operated in 600-4000 cm^{-1} range. ^{1}H NMR spectra were recorded with a Varian VXR-400 MHz spectrometer using DMSO-d_6 (Cambridge Isotope Laboratories, Inc.) as a solvent.

The temperature dependence of the heat flow of the obtained compounds was studied on DSC Q2000 (TA Instruments, USA) in the temperature range from -40 to 80 °C at a heating rate of 20 °C/min under a nitrogen atmosphere. The heating and cooling cycle was repeated

twice and the data obtained during the second cycle was used to characterize the structure of the compound.

The temperature of the onset of thermal oxidative degradation ($T_{d5\%}$), which was taken as the temperature of 5% weight loss of the sample, was determined using TGA Q50 (TA Instruments, USA) in the temperature range from 20 to 700 °C at a heating rate of 20 °C/ min in air.

Self-assembly of OSS-OILs was studied in aqueous solutions at a concentration of 5 mg/mL. The size and zeta-potential of OSS-OILs in aqueous media was obtained using Zetasizer Nano ZS (described in Chapter 3).

To study the morphology of OSS-OIL assemblies, 100 μL of an aqueous solution of OSS-OILs was spin-casted onto a pre-cleaned silicon substrate (1.5 cm x 1.5 cm) at 3,000 rpm for 30 sec. The surface morphology of the spin-cast films was observed with an AFM (ICON, Bruker) in the soft tapping mode as described earlier in Chapter 3.

PeakForce QNM was performed on AFM (ICON, Bruker) to investigate surface adhesion of the OSS-OIL films as described earlier. The scanning rate was kept at 0.5 Hz and the resolution was 512 x 512 pixels. All AFM images were processed and analyzed using Nanoscope Analysis v.2.0 software (Bruker).

Ionic conductivity (σ_{dc}) of the synthesized OSS-OILs was measured by the dielectric relaxation spectroscopy technique using a dielectric spectrometer based on a P5083 AC bridge scheme (0.1–100 kHz) and a two-electrode stainless steel cell (measurement accuracy of 0.03%). The samples were dried for 30 min at 100 °C under nitrogen flow before the measurements. The measurements were performed under a dry nitrogen atmosphere at a temperature from 40 to 120 °C.

6.3 Results and Discussion

6.3.1 Synthesis and Characterization of OSS-OILs

The initial OSS(N+OH) compounds are a mixture of silsesquioxane nanoparticles, composed of an inorganic component bearing a combination of cage and open-chain structures and an organic component containing aliphatic hydroxyl and tertiary amino groups in the ratio N:OH = 1:4 (Figure 6.1).[161,162] The size distribution of these nanoparticles is relatively narrow and their average size measured by TEM is 2.7 nm, and this size corresponds to that of a single silsesquioxane-based nanoparticle consisting of 12-18 Si atoms, considering the size of the organic shell of OSS (N+OH) (0.5-1.5 nm).[161] Amphiphilic reactive cationic aprotic OSS-OILs were synthesized by the reaction of quaternization of tertiary amino groups of OSS(N+OH) with 1-bromopropane or 1-bromodecane at the ratio N: Br = 1: 1, resulting in the preparation of OSS($C_3N^+Br^-$) or OSS($C_{10}N^+Br^-$), respectively. The synthesized OSS-OILs exhibit different hydrophilic-hydrophobic balance due to different lengths of the introduced alkyl radical. They are viscous brown liquids, soluble in water, DMF, DMSO, insoluble in acetonitrile, acetone, ethyl acetate, hexane, chloroform, THF, diethyl ether, and toluene. For OSS($C_{10}N^+Br^-$), it also dissolves in ethanol upon heating.

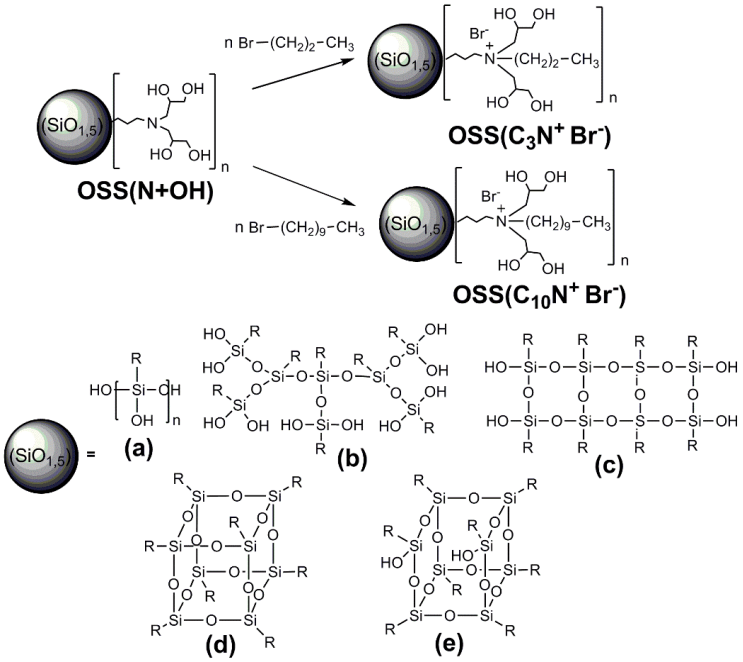

Figure 6.1. Scheme for the synthesis of reactive cationic OILs based on OSS(N+OH) and structures of the silsesquioxane core: linear (a), branched (b), completely condensed polyhedral (d) and incompletely condensed polyhedral (e) structures.

FTIR spectra of the initial and final compounds, OSS (N+OH) and OSS-OILs, are similar (Figure 6.2a). They contain absorption bands of stretching vibrations of Si-O-Si bonds (1023-1043 cm^{-1}), C-H bonds of CH, CH_2 and CH_3 groups (2765-3020 cm^{-1}), OH bonds of hydroxyl groups (3018-3723 cm^{-1}), deformation vibrations of C-H bonds of CH, CH_2 and CH_3 groups (1462-1463 cm^{-1}). The synthesized OSS-OILs contain alkyl chains of various lengths covalently bound to the quaternary ammonium atom in the organic shell. Thus, an increase in the relative intensities of the absorption bands corresponding to the stretching (2765-3020 cm^{-1}) and deformation (1462-1463 cm^{-1}) vibrations of CH bonds is observed in the IR spectra of the OSS-OILs.[342]

The ^1H NMR spectrum of the initial compound OSS(N+OH) contains signals of the protons of the CH_2 groups at α- (2.38 and 2.78 ppm), β- (1.50 ppm) and γ- (0.51 ppm) positions to the tertiary nitrogen atom, signals of the protons of CH and CH_2 groups in the α-position to hydroxyl groups and signals of protons of hydroxyl groups in the range of 3.25-4.00 ppm (Figure 6.2b).[342]

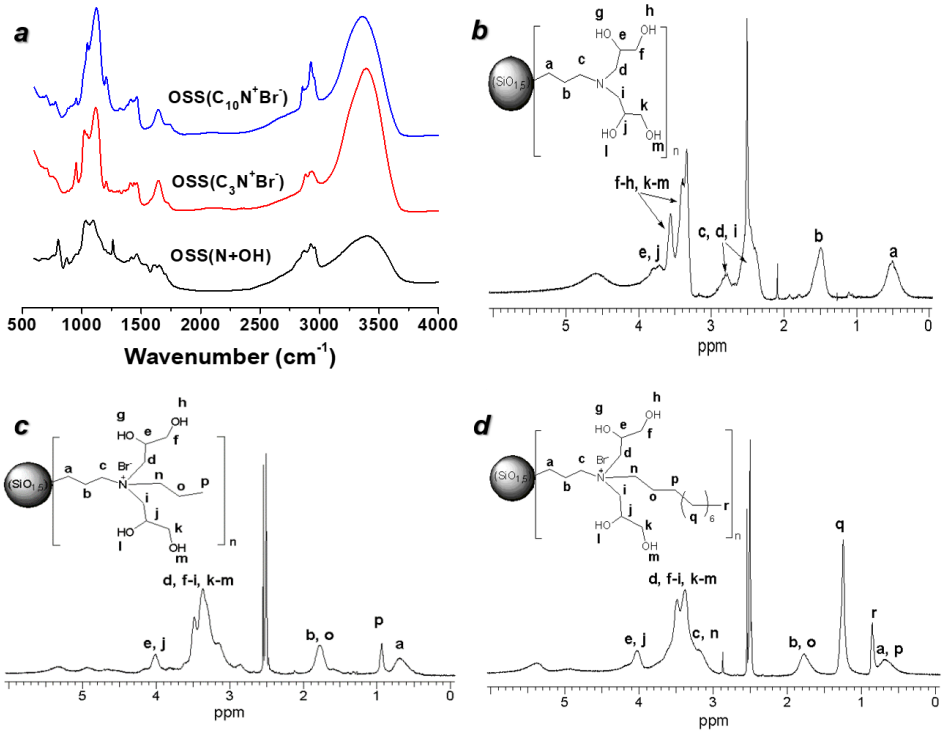

Figure 6.2. (a) FTIR spectra of OSS(N+OH) and OSS-OILs. (b-d) ^1H NMR spectra of OSS(N+OH) (b), OSS($C_3N^+Br^-$) (c) and OSS($C_{10}N^+Br^-$) (d).

In the ^{1}H NMR spectra of OSS-OILs, the signals of the protons of CH_2 groups in the α-position towards nitrogen atoms are shifted towards the weak field (3.37 ppm for OSS ($C_3N^+Br^-$) and 3.38 ppm for OSS($C_{10}N^+Br^-$)) compared with those in the OSS(N+OH) spectrum. In addition, signals of CH_3 group protons appear (0.94 ppm for OSS($C_3N^+Br^-$) and 0.86 ppm for OSS($C_{10}N^+Br^-$)), and a signal of repeating CH_2 groups of the alkyl chain attached to the nitrogen atom during quaternization is observed for OSS ($C_{10}N^+Br^-$) (1.25 ppm) (Figure 6.2c-d).

Table 6.1. Characteristics of OSS (N+OH), OSS-OILs and their aqueous solutions.

Samples	M_n theor* (g/mol)	Content of ionic groups (meq/g)	T_g (°C)	$T_{d5\%}$ (°C)	Size, (DLS) (nm)	Zeta potential (mV)	σ_{dc} (S/cm)			
							40 °C	80 °C	100 °C	120 °C
OSS(N+OH)	4040	-	25	190						
OSS($C_3N^+Br^-$)	6000	2.63	-25	195	152±7	+62.9±3.4	$3\cdot10^{-5}$	$2.4\cdot10^{-4}$	$6.7\cdot10^{-4}$	$1.4\cdot10^{-3}$
OSS($C_{10}N^+Br^-$)	7570	2.09	-4	158	165±16	+52.0±3.5	$2.2\cdot10^{-8}$	$3.6\cdot10^{-6}$	$1.2\cdot10^{-5}$	$1.3\cdot10^{-4}$

6.3.2 Thermal Properties of OSS-OILs

DSC results show that the initial OSS(N+OH) and obtained OSS-OILs are amorphous substances due to the irregular structure of their inorganic cores (Figure 6.3a). It has been demonstrated that ionic liquids containing a mixture of OSS as an inorganic core and trimethylammonium bis(trifluoromethanesulfonyl) imide groups in an organic shell was amorphous with a glass transition temperature (T_g) value of 15 °C, while their counterparts with POSS inorganic cores are semi-crystalline with a melting point of 172 °C.[339,341] This result supports that the irregular structure of inorganic parts results in the transition from semi-crystalline to amorphous compounds. The T_g value of the initial OSS(N+OH) is

25 °C (Table 6.1).[343] The introduction of ionic groups and aliphatic substituents into its organic shell shifts the T_g value to below 0 °C. The T_g value of OSS($C_3N^+Br^-$) and OSS($C_{10}N^+Br^-$) is -25 °C and -4 °C, respectively (Table 6.1), which are lower than those of aprotic ammonium OSS-ILs (T_g = 15 °C,[339,341]) or POSS-ILs (2.7 °C and 24.6 °C[331]). The lower T_g value of OSS($C_3N^+Br^-$) compared to that of OSS($C_{10}N^+Br^-$) can be explained by the decrease in the intensity of intermolecular interactions with the shorter alkyl radical, resulting in the decrease in the rigidity and packing density.[331,344,345,346]

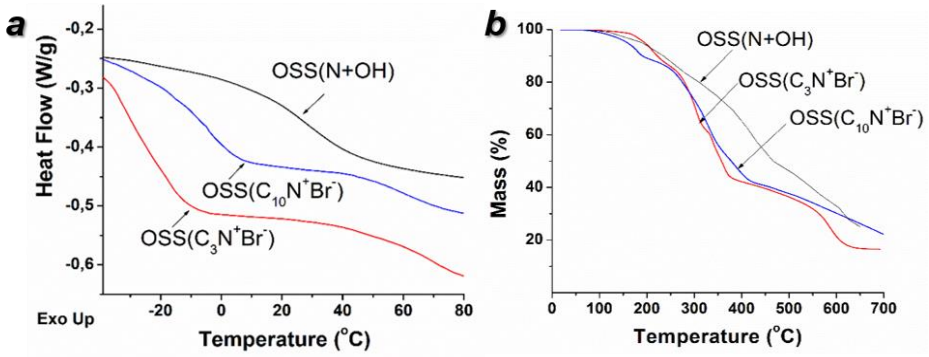

Figure 6.3. DSC (a) and TGA (b) curves for OSS(N+OH) and OSS-IL.

TGA data shows that the temperature of the onset of decomposition ($T_{d5\%}$) of the OSS-OIL with shorter alkyl substituents, OSS($C_3N^+Br^-$) is close to that of the initial OSS(N+OH). (Figure 6.3b, Table 6.1). The $T_{d5\%}$ value significantly decreases with increasing the length of alkyl substituents. The thermal stability of the synthesized OSS-OILs is comparable to those of ionic POSS with iodide anions (207-253 °C).[331] On the other hand, their resistance to thermal oxidative degradation is weaker compared to alkylurethane-containing non-ionic OSS with the same composition of inorganic components, indicating that the presence of ionic groups reduces thermal stability.[343]

6.3.3 Colloidal Properties and Assembly Behavior of OSS-OILs

The assembly behavior of the OSS-IL in aqueous media were first investigated by the DLS method (Figure 6.4). According to DLS data, bimodal size distribution was observed for OSS($C_3N^+Br^-$), showing the formation of aggregates with an average size of 152 ± 7 nm (Figure 6.4a). A different aggregation was observed for the aqueous solution of OSS($C_{10}N^+Br^-$). OSS($C_{10}N^+Br^-$) showed multimodal size distribution with three peaks

(Figure 6.4.b). This result suggests that the length of the alkyl substituents of OSS-OILs affects the assembly behavior in aqueous solutions, resulting in the formation of more diverse morphologies with longer alkyl substituent.

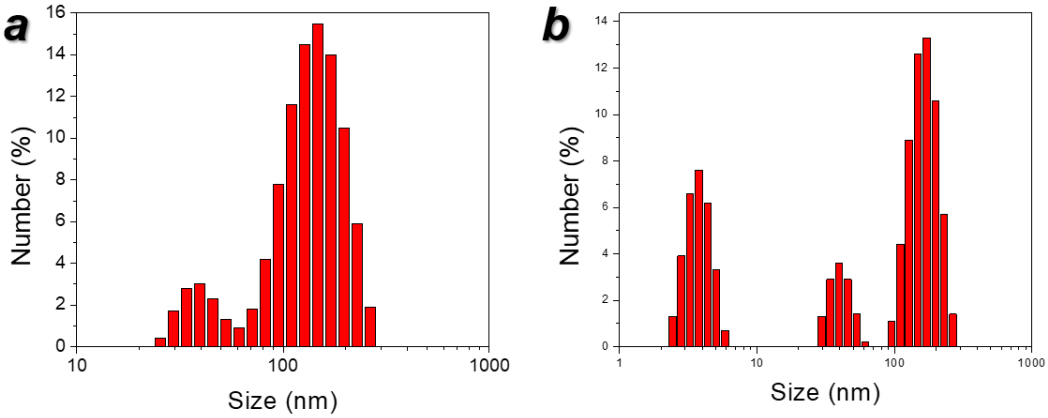

Figure 6.4. Size distribution of OSS($C_3N^+Br^-$) (a) and OSS($C_{10}N^+Br^-$) (b) assemblies in aqueous solutions.

The surface morphology of OSS-OIL films obtained by spin-casting from the solutions was studied using AFM (Figure 6.5). Spherical flat micelles were formed from OSS($C_3N^+Br^-$) with an average diameter of 229 ± 92 nm and an average height of 2 nm (Figure 6.5a-d). On the other hand, the AFM images of OSS($C_{10}N^+Br^-$) films show polydisperse micellar morphologies, which is in good agreement with the DLS result, and a majority of the morphologies exhibit elongated, worm-like structures with an average height of 2 nm (Figure 6.5e-h). Such difference in surface morphology between these two OSS-OIL films can be explained by variation in hydrophobicity of OSS-OILs depending on the length of the alkyl substituents which governs their molecular organization to minimize unfavourable interactions between the hydrophobic alkyl substitutes and water molecules. The morphological transition from spherical to worm-like micelles have been reported for amphiphilic polymers by increasing their hydrophobicity.[347,348] Since the self-assembly of amphiphilic polymers is driven by the minimization of free energy in their system, the morphology of their self-assembled structures can be primarily predicted by the so-called packing parameter ($p = v/a_0l_c$), where v is the volume fraction of hydrophobic segments, a_0 is the equilibrium area of the hydrophilic surface group, and l_c is the maximum effective chain length of the individual amphiphilic molecule.[349] It has been demonstrated

that spherical micelles are generated for $p \leq 1/3$ whereas cylindrical micelles for $1/3 \leq p \leq 1/2$.[350] OSS-OILs with longer alkyl substitutes have a greater volume fraction of hydrophobic segments and thus a higher value of packing parameter, compared to those for OSS-OILs with shorter alkyl substitutes. Accordingly, OSS-ILs with longer alkyl substitutes predominantly form microscopic, worm-like domains whereas spherical micelles were constructed with shorter alkyl substitutes.

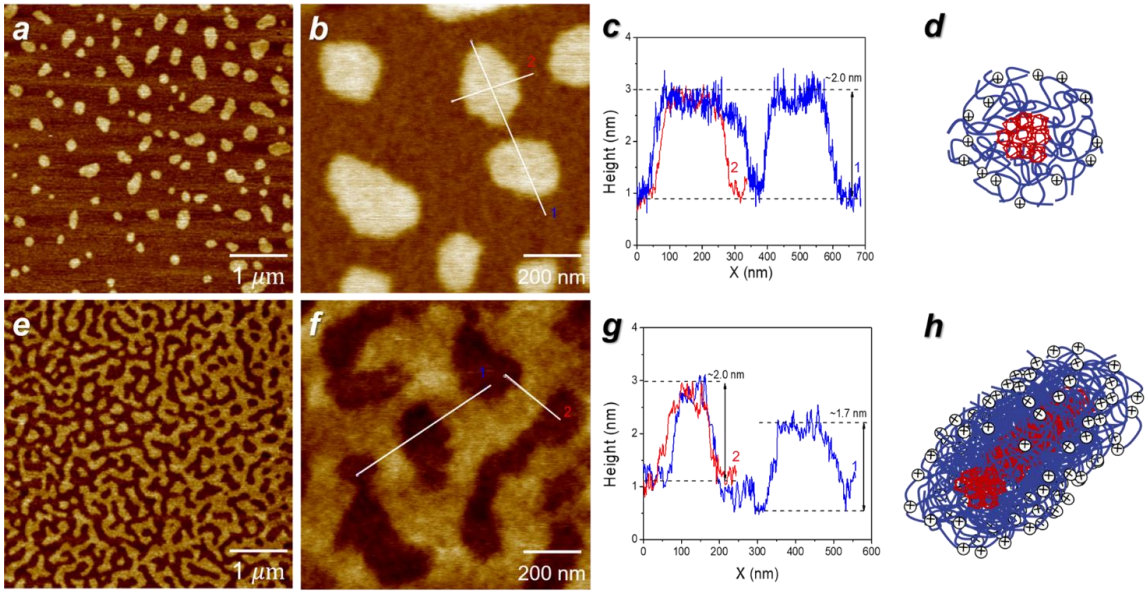

Figure 6.5. AFM topography images of spin-cast films of OSS($C_3N^+Br^-$) (a-b) and OSS ($C_{10}N^+Br^-$) (e-f) and the corresponding height profiles along the indicated lines (c and g). Z scale of all AFM images is 5 nm. (d-h) Schematic representation of OSS($C_3N^+Br^-$) (g) and OSS($C_{10}N^+Br^-$) (h) assemblies.

In addition, mapping of surface adhesion of the OSS-OIL films was investigated by performing PF-QNM imaging (Figure 6.6). The surface of spherical flat domains of OSS($C_3N^+Br^-$) show much higher adhesion compared to interdomain region (Figure 6.6b). On the other hand, OSS($C_{10}N^+Br^-$) morphologies show no remarkable contrast in surface adhesion between the worm-like domains and interdomain region (Figure 6.7d). As mentioned earlier, the hydrophobicity of OSS-OILs increases with longer alkyl substitutes, resulting in the decreased adhesion with hydrophilic AFM probes.[91,351] This result indicates that not only surface morphology but also surface mechanical response (surface adhesion) can be tuned by adjusting the length of the peripheral alkyl substitutes of OSS-OILs.

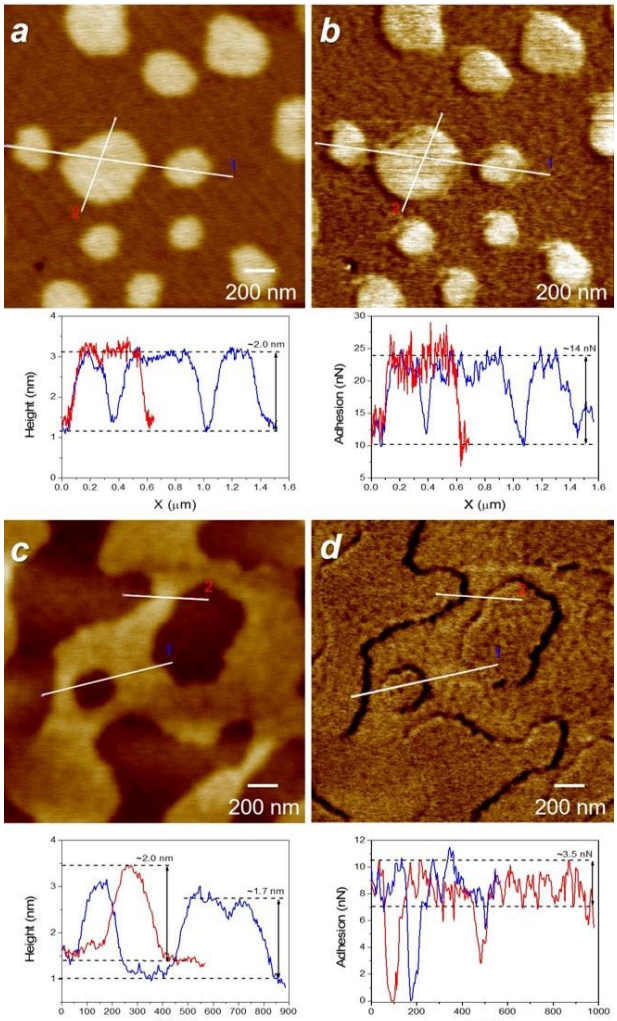

Figure 6.6. Topography (a,c) and adhesion (b,d) images and corresponding profiles of the OSS($C_3N^+Br^-$) (a,b) and OSS($C_{10}N^+Br^-$) (c-d) films. Z scale is 5 nm for (a,c), 30 nN for (b) and 15 nN for (d).

The high values of the zeta-potential of the OSS($C_3N^+Br^-$) and OSS($C_{10}N^+Br^-$) particles in aqueous media are associated with the presence of positively charged quaternary ammonium groups on their surface (Table 6.1). The lower value of zeta-potential of the OSS($C_{10}N^+Br^-$) particles as compared to OSS($C_3N^+Br^-$) is probably due to the charge screening by longer alkyl substituent at the quaternary nitrogen atom. Since colloidal systems with zeta-potential values above 30 mV are considered as a highly stable system,[352] the OSS($C_3N^+Br^-$) and OSS($C_{10}N^+Br^-$) particles are resistant to aggregation in an aqueous solution.

6.3.4 Ionic Conductivity of OSS-OILs

Based on the structure of the synthesized OSS-OILs, they can be classified as electrolytes with a single-ion conduction mechanism provided mainly by Br^- anions. In this work, we investigated the dc conductivity (σ_{dc}) of the OSS-OILs under anhydrous conditions in the temperature range of 40–120 °C. An increase in the value of σ_{dc} with increasing temperature indicates ionic nature of conductivity (Figure 6.7. and Table 6.1).[55] The conductivity of OSS($C_3N^+Br^-$) is higher compared to OSS($C_{10}N^+Br^-$) due to the higher mobility of charge carriers in its composition. The maximum value of σ_{dc} is obtained to be 1.4×10^{-3} S/cm for OSS($C_3N^+Br^-$) at 120 °C.

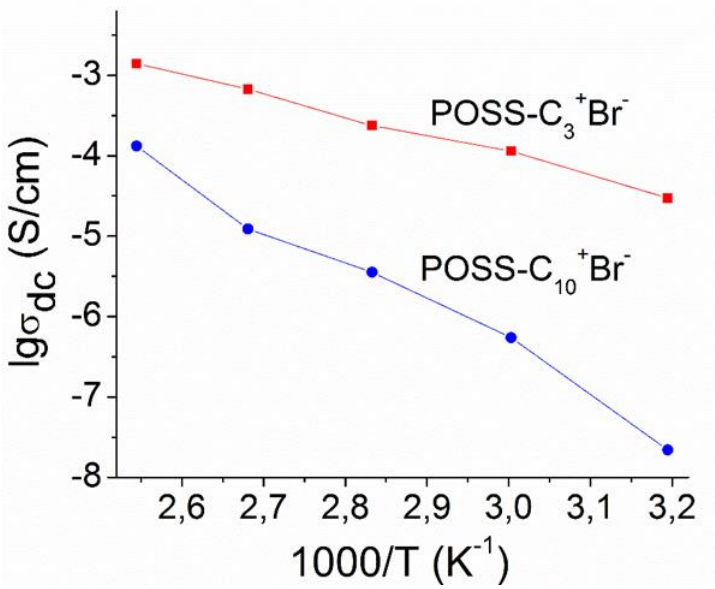

Figure 6.7. Temperature dependence of conductivity of the synthesized OSS-OILs.

As the temperature rises, a sharper increase in the conductivity of OSS($C_{10}N^+Br^-$) was observed, compared to OSS($C_3N^+Br^-$). The σ_{dc} values of OSS($C_3N^+Br^-$) are three orders of magnitude higher at 40 °C but only one order of magnitude higher at 120 °C. It should be noted that there is a correlation between the T_g and the conductivity of the OSS-OILs. In fact, OSS($C_3N^+Br^-$) has a higher conductivity and lower T_g, compared to OSS($C_{10}N^+Br^-$). It has been reported that POSS-IL and OSS-IL with T_g values (-22 °C and -25 °C, respectively) close to that of OSS($C_3N^+Br^-$) (T_g = -25 °C) possess σ_{dc} is in the range of 10^-

^{4} – 10^{-3} S/cm at 100 °C. This level is comparable to that of OSS($C_3N^+Br^-$), supporting the correlation between the *Tg* and $\sigma_{dc.}$ [340]

6.4 Conclusions

In this work, a method for producing organo-inorganic amphiphilic reactive aprotic cationic ionic liquids was proposed based on the quaternization reaction of a mixture of oligosilsesquioxane polyhedral (cage) structures and their analogs with an open-chain structures containing a tertiary amine and primary and secondary hydroxyl groups in an organic shell with n-bromopropane or n-bromodecane. The influence of the inorganic component composition and the degree of amphiphilicity in the synthesized OSS-OILs on their physical properties as well as self-organization in aqueous solutions and into thin films at solid surfaces were investigated.

In aqueous solutions, an increase in the length of the hydrophobic alkyl substitutes of the OSS-OILs leads to an increase in the polydispersity of the size distribution of their assemblies. Their average size is 150-170 nm. At the same time, the high values of their zeta-potentials indicate a high aggregate stability. A different character of self-organization between OSS($C_3N^+Br^-$) and OSS($C_{10}N^+Br^-$) was also observed in a thin film on solid silicon substrates. OSS($C_3N^+Br^-$) forms disk-like structures with a diameter of several hundred nanometers and a thickness of 2 nm, while OSS($C_{10}N^+Br^-$) with higher hydrophobicity constructs worm-like structures with the same thickness (2 nm). Surface mechanical properties mapping shows that not only surface morphology but also surface mechanical response can be tuned by adjusting the amphiphilicity of OSS-OILs.

The synthesized OSS-OILs are amorphous with the T_g values below 0 °C. The ionic conductivity of these compounds is comparable to that of traditional imidazolium-containing POSS-OILs. The increase in length of the alkyl substituent leads to a decrease in the conductivity. The lower T_g facilitates higher ionic conductivity. In fact, the maximum conductivity value obtained from these two OSS-OILs is 1.4×10^{-3} S/cm at 120 °C from OSS($C_3N^+Br^-$) with lower T_g than that of OSS($C_{10}N^+Br^-$).

In conclusion, the organization and properties of OSS-OILs are modulated by varying the structure of their ionic groups and its content, as well as the structure of the organic shells as a whole. In particular, the ionic conductivity of the OSS-OILs above 1 mS/cm gives these materials great potential as polymer electrolytes for various electrochemical applications, such as batteries, supercapacitors and sensors.

CHAPTER 7. SHAPE-PERSISTENT, HIGHLY CONDUCTIVE IONOGELS REINFORCED WITH THE NETWORK OF CELLULOSE NANOCRYSTALS AND POLY(IONIC LIQUID)S

7.1 Introduction

Ionic liquids are pure molten salts capable of being a new potential electrolyte material, which have low melting points typically below 100 ^{o}C.[353,354,355,356] They have attracted considerable attention due to their unique properties—high ionic conductivity, high chemical and thermal stability, a large electrochemical window, and low vapor pressure—which can be tuned by choosing different combinations of cations and anions. While taking advantages of these interesting features of ionic liquids, they have been studied as high-performance electrolytes for electrochemical applications in devices such as batteries, fuel cells, and solar cells.[357,358,359] However, their viscous fluidic nature impedes their ability to sustain a self-supporting, free-standing shape; instead, they require solid confinement, which compromises their portability and leads to the issues of leakage.[360] Ionic liquids can be solidified by direct polymerization of ionic liquids or post-modification of polymer chains with ionic liquids.[55,82,96,105,361] However, the ionic conductivity of polymerized ionic liquids is generally reduced significantly compared to that of monomeric ionic liquids.[18, 362 , 363 , 364] Therefore, there has been increasing demand for non-covalently immobilizing ionic liquids in solid states to allow for facile handling without compromising their unique properties.

One common strategy for ionic liquid immobilization in handleable materials without a significant sacrifice in their desired properties is via the formation of ionogels in which ionic liquids are encapsulated within a solid matrix such as inorganic and polymeric matrices.[143,365] However, as ionic conductivity and mechanical strength are inversely coupled, highly conductive ionogels have been obtained only at the expense of mechanical strength.[146,147] Block copolymers consisting of an ion-conducting block and a rigid block have been explored to prepare mechanically strong and conductive ionogels. However, most block copolymer ionogels possess insufficient ionic conductivity and low mechanical strength (e.g., room-temperature ionic conductivity of 10^{-4} S cm^{-1} and storage modulus well

below MPa range)[366,367] to meet the needs for solid batteries, which limit the use of the ionogels.[148,149,150,151, 368 , 369] Another approach for producing mechanically strong and highly conductive ionogels is using ionic polymers as an ionogel matrix.[152,153,154, 370 , 371 , 372 , 373] For example, the ionogels composed of zwitterionic copolymers displayed high room-temperature ionic conductivities above 1 mS cm^{-1} and compressive elastic moduli in the range of several MPa.[370]

Examples of biopolymers used for robust ionogels include cellulose,[167,374] gelatin,[375] and chitosan.[376,377] However, biopolymer-based ionogels show low mechanical stability and low ionic liquid loading since the traditional method for producing biopolymer-based ionogels involves dissolution and regeneration of biopolymers in ionic liquids, leading to the loss of structural integrity.

High aspect ratio and outstanding mechanical properties of nanocellulose-based materials allow for the formation of mechanically robust ionogels.[166,171,180,378,379,380,381] Ionic liquids can be entrapped into the readily formed network of nanocellulose, resulting in materials with enhanced mechanical stability and/or ionic liquid loading without the dissolving/regeneration process of cellulose. For example, ionogels prepared with nanofibrillar methyl cellulose exhibited high strength with storage moduli in the MPa range and high ionic liquid content of 90 wt% but at the cost of greatly reduced ionic conductivities compared to that of pure ionic liquids making them uncompetitive as solid electrolytes.[166] Ionogels based on cellulose nanocrystals (CNCs) grafted with poly(ionic liquid)s showed good mechanical stability.378 However, CNC-incorporated ionogels exhibited a limited ionic liquid loading up to 40 wt% and very low ionic conductivity of 10^{-3}-10^{-1} mS cm^{-1}.[171,]378

Here, we propose a strategy for producing robust and shape-persistent ionogels with both high mechanical strength and ionic conductivity by using cellulose nanocrystals and hyperbranched polymeric ionic liquid (PIL) as matrix materials (Figure 7.1). The PIL with 32 sulfonate terminal groups and imidazolium counterions was selected to enhance compatibility with CNCs and the ionic liquid (1-ethyl-3-methylimidazolium bis(trifluoromethylsulfonyl)imide, ([EMIM][TFSI])). Integrating CNC and PIL resulted

in robust shape-persistent matrices which can hold ionic liquid up to 95 wt%. The unique continuous nano-porous morphology of CNC/PIL ionogels suggested here facilitates efficient ion transport with high ionic conductivity up to 7.8 mS cm^{-1}, which is accomplished in tandem with high mechanical strength with a compressive elastic modulus of up to 5.6 MPa, which well exceeds those reported to date.

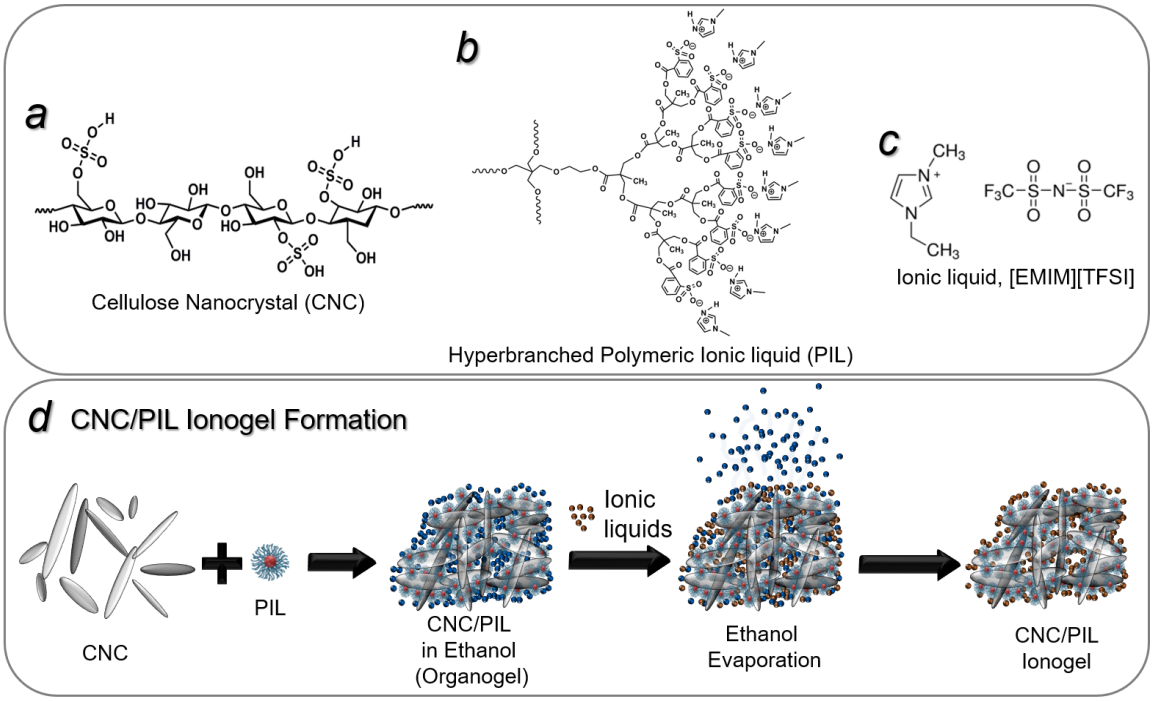

Figure 7.1. (a-c) Chemical structure of CNC/PIL ionogel components: (a) cellulose nanocrystal (CNC), (b) hyperbranched polymeric ionic liquid (PIL), and (c) ionic liquid, 1-ethyl-3-methylimidazolium bis(trifluoromethylsulfonyl)imide ([EMIM][TFSI]). (d) Schematic illustration for CNC/PIL ionogel formation.

7.2 Experimental Section

7.2.1 Materials

N-methylimidazole (MIM) (Aldrich, 99%) and 2-sulfobenzoic acid cyclic anhydride (Aldrich, ≥95%), were used as received. Oligo(ethylene glycol) (OEG) with weight average molecular weight (M_n) of 1000 (Aldrich) was dried under vacuum conditions using rotary pump (1-3 mmHg vacuum pressure) at 80-90 ^oC for 4 hrs. Hyperbranched aliphatic

polyether polyol (HBP) Boltorn H30 (Perstorp) with M_w = 3500 (an equivalent molecular weight measured by hydroxyl groups via acetylation technique 117 g eq^{-1}) was purified by precipitation of dimethylformamide (DMF) solution in diethyl ether followed by vacuum drying at 25-30^{o}C for 6 hrs. DMF, diethyl ether, acetone, isopropyl alcohol, acetonitrile, and chloroform were dried and distilled before use. Ionic liquid, [EMIM][TFSI] (99%) was purchased from Iolitec Ionic Liquids Technologies.

7.2.2 Synthesis of Polymeric Ionic Liquids

Polymeric ionic liquids used in this study were synthesized as described in our previous study. [382] Sulfonate hyperbranched polymeric ionic liquids with imidazolium counterions (PIL) were prepared as follows: hyperbranched sulfonic acids were firstly synthesized by reaction of HBP and 2-sulfobenzic acid in DMF and were reacted with MIM (Figure 7.1b). For linear polymeric ionic liquid with imidazolium counterions (L-PIL), OEG with sulfonate end groups was synthesized by reacting initial OEG and 2-sulfobenzoic acid and then reacted with MIM. Hyperbranched polymeric sulfonic acid with potassium salt (PA-K) was prepared by adding KOH solution in water to a solution of hyperbranched sulfonic acid in ethanol under vigorous stirring, followed by solvent evaporation (see details in Supporting Information).

7.2.3 Preparation of CNC suspension

CNCs were prepared using the common sulfuric acid hydrolysis method (described earlier).[187,188] In this study, hardwood pulp (Georgia Pacific LLC) was used as a starting materials. CNC aqueous suspension was concentrated to 3 wt% by evaporating water.

7.2.4 Preparation of Ionogels

Firstly, 0.9 mL of CNC suspension (3 wt%) was mixed with 0.1 mL of aqueous solution of hyperbranched polymeric ionic liquids (PILs) with imidazolium counterions at different concentrations (0, 3, 6, and 12 wt%). Water was firstly exchanged to ethanol by gently adding ethanol on top of the solutions/hydrogels and replacing it twice a day for 1 week. The absence of refractive index gradients at the sol/gel interface was used as an indicator

for the completion of solvent exchange.[383,384] 0.6 g of ionic liquid, [EMIM][TFSI] was mixed with 0.5 mL ethanol, added into the samples and left undisturbed overnight. CNC/PIL ionogels with a diameter of ~ 1 cm and a height of ~ 1 cm were finally prepared after slowly evaporating ethanol for 2 weeks, followed by vacuum-drying at 70 °C overnight (Figure 7.1d). The CNC concentration of the ionogels is 4.5 wt%, and the PIL concentration varies from 0 to 2.0 wt% (Table 7.1).

Table 7.1. Composition for CNC/PIL ionogels.

Ionogels	CNC (wt%)	PIL (wt%)	Ionic liquid content (wt%)	
			Theoretical	Measured
CNC/PIL-0.0	4.5	0.0	95.5	95.3
CNC/PIL-0.5		0.5	95	95.3
CNC/PIL-1.0		1.0	94.5	95.1
CNC/PIL-2.0		2.0	93.5	94.5

To determine the ionic liquid content of the ionogels, we collected samples after adding ethanol but before adding ionic liquids and dried them at 40 °C overnight. Then, we measured and averaged out the weight of these dried samples (m_1). The weight of the ionogels (m_2) was also measured and averaged. The ionic liquid content (%) of the ionogels was obtained from $\frac{m_2-m_1}{m_1} \times 100$, where m_1 and m_2 are the weight of a dried sample without adding ionic liquids and a corresponding ionogel, respectively.

The measured values of the ionic liquid content are different from theoretical values calculated with assumption of no mass loss during the ionogel formation process. We

found 4-7 wt% mass loss during the water-to-ethanol solvent exchange, which results in the discrepancy between the theoretical and measured values of ionic liquid content**.**

7.2.5 Characterization

Atomic Force Microscopy (AFM). AFM images were obtained with the scan rate of 0.5-1.0 Hz and resolution of 512 x 512 or 1024 x 1024 pixels. AFM probes (MikroMasch, HQ:XSC11/AL BS) were used with a tip radius of 8 nm and spring constant of 1.5-2.2 N/m. For sample preparation, 0.1 mL of CNC/PIL aqueous solution or hydrogel was drop-cast onto a pre-cleaned silicon substrate and air-dried prior to AFM imaging. In case of the ionogel samples, they were sliced into thin films and placed onto the silicon substrate.

Scanning Electron Microscopy (SEM). SEM images were obtained using Hitachi SU8230 SEM with a 5.0 kV accelerating voltage. Samples were sputter coated with gold/platinum for 60 s using Hummer 6 Gold/Palladium sputter coater (Anatech).

Attenuated Total Reflectance Fourier Transform Infrared (ATR-FTIR). Attenuated total reflectance Fourier transform infrared (ATR-FTIR) spectra were obtained in range of 4000-600 cm^{-1}. 0.1 mL of the CNC/PIL aqueous mixture was directly deposited and air-dried into a film on the ATR crystal. In case of the ionogel samples, sliced ionogels were placed onto the ATR crystal.

Thermal analysis. Thermal gravimetric analysis (TGA) and dynamic scanning calorimetry (DSC) were conducted using TGAQ50 (TA Instruments) and a Mettler Toledo STARe system DSC 3 (Mettler Toledo), respectively. For CNC/PIL aqueous mixtures, they were air-dried to form films. TGA and DSC measurements were carried out as described earlier in Chapter 3.

Mechanical Compression Test. Compression mechanical tests were conducted using a Shimadzu EZ-SX tester at a crosshead speed of 0.5 mm min^{-1} with a maximum strain of 75%. The cylindrical samples of CNC/PIL gels collected after adding ethanol but before adding ionic liquids or CNC/PIL ionogels with a diameter of 9 mm and a height of 8 mm were tested. Three samples were collected for each test. Compressive elastic modulus of

the samples was calculated on the initial linear slope of the stress-strain curves at 5-10% strain.[385] The maximum compressive strength was also reported at 75% strain. For the ionogels, the compressive yield strength was determined using an offset-yield method in which a line is drawn parallel to the initial linear slope of the stress-strain curve but offset by 2% along the strain axis. The corresponding stress value at which the offset line crossed the stress-strain curve was defined as the compressive yield strength.[386,387,388,389]

Broadband Dielectric Spectroscopy (BDS). Solid, freestanding ionogel films were placed in a capacitor between two gold coated electrodes and dried under vacuum at 70 °C for 24 hours. Dried ionogel films were then immediately transferred to the dielectric sample chamber and annealed at 110 °C for 30 minutes under a dry nitrogen atmosphere.

The dielectric spectra were measured using a Novocontrol Concept 80 system, including an Alpha-A impedance analyzer, a ZGS active sample cell interface, and a Quatro cryosystem temperature control unit. An AC voltage of 0.1 V was applied, and the dielectric response was measured over a frequency range of 10^{-2}-10^{6} Hz and a temperature range of 163-383 K (recorded from high to low temperatures). Following sample equilibration at 383 K, BDS measurements showed a steady-state response. Samples were then cooled in increments of 5 K and the corresponding complex conductivity spectra $\sigma^*(\omega) = \sigma'(\omega) + i\sigma''(\omega)$ were recorded for each temperature, where ω is the angular frequency. Reported values of the dc conductivity $\sigma_{dc}(T)$ for each measurement are determined from the frequency-independent plateau of the real conductivity σ'.

7.3 Results and Discussion

To elucidate how integrating small amounts of CNC and PIL forms a mechanical supporting matrix for ionogels, we compared CNC/PIL composites with composites of CNC and two different ionic polymers: linear polymeric ionic liquids with imidazolium counterions (L-PIL), which is a linear counterpart of PIL, and hyperbranched polymeric sulfonic acid with potassium salt (PA-K), which have the same chemical structure as PIL but with different counterions (Scheme S7.1). CNCs were extracted from wood pulp via the well-established sulfuric acid hydrolysis method.[187,188] AFM image of CNCs shows that they possess a length of 167±59 nm and a diameter of 6±1 nm (Figure 7.2a). AFM

images of PIL show that spherical microdroplets were formed with several hundred nm in sizes (Figures 7.2b and S7.1a). Spherical assemblies were also observed for L-PIL and PA-K with different sizes (Figure S7.1b-c).

7.3.1 Interactions between CNCs and PILs

Depending on the PIL content, CNC/PIL aqueous mixtures remained in solution state or became hydrogels (Figures 7.2c). Immediate gelation occurred when the PIL concentration was 1.2 wt% or higher in aqueous media. At a lower concentration of PIL (0.6 wt%), a hydrogel was also formed, but at a slower rate (Figure 7.2c, Scheme S7.2). It should be noted that although both CNC and PIL possess negatively charged groups (sulfate or sulfonate groups, respectively),[390] the mixing of CNC and PIL results in gelation without phase separation. The gelation behavior of CNC/PIL samples was further investigated by performing time sweep rheological analysis (Figure S7.2). At 0.3 wt% PIL, the storage modulus is greater than loss modulus after 225 s, indicating liquid-to-gel transition (Figure S2a).[175,391] When PIL content is 0.6 wt% or higher, the storage modulus is greater than the loss modulus over entire time period, suggesting the occurrence of gelation before the measurements (Figure S2b-c). However, the gelled solutions with 0.3 and 0.6 wt% PIL are very weak with storage moduli below 25 Pa, thus flowing when the tubes containing the solutions were flipped as shown in the visual investigation (Figure 2c). Additionally, significant increase in storage modulus (250-550 Pa) for the sample with 1.2 wt% PIL demonstrates that the addition of 1.2 wt% PIL facilitates the formation of a mechanically strong hydrogel.

To unravel the origin of interactions between CNC and PIL, gelation behavior of CNC with L-PIL or PA-K was studied (Figure S7.3). Despite the presence of negatively charged surface functional groups, L-PIL and PA-K solutions were well-mixed with the CNC suspension, forming hydrogels at high concentrations. When L-PIL was added, immediate gelation was not observed, and a hydrogel was slowly generated only at the L-PIL content of 1.2 wt%. Gelation behavior between CNC and PA-K is similar to that between CNC and PIL (Figure S7.3 and Scheme S7.2). We suggest that, compared to linear ionic

polymers, a greater number of functional groups in hyperbranched counterparts enhances its interactions with CNCs, facilitating its faster gelation.

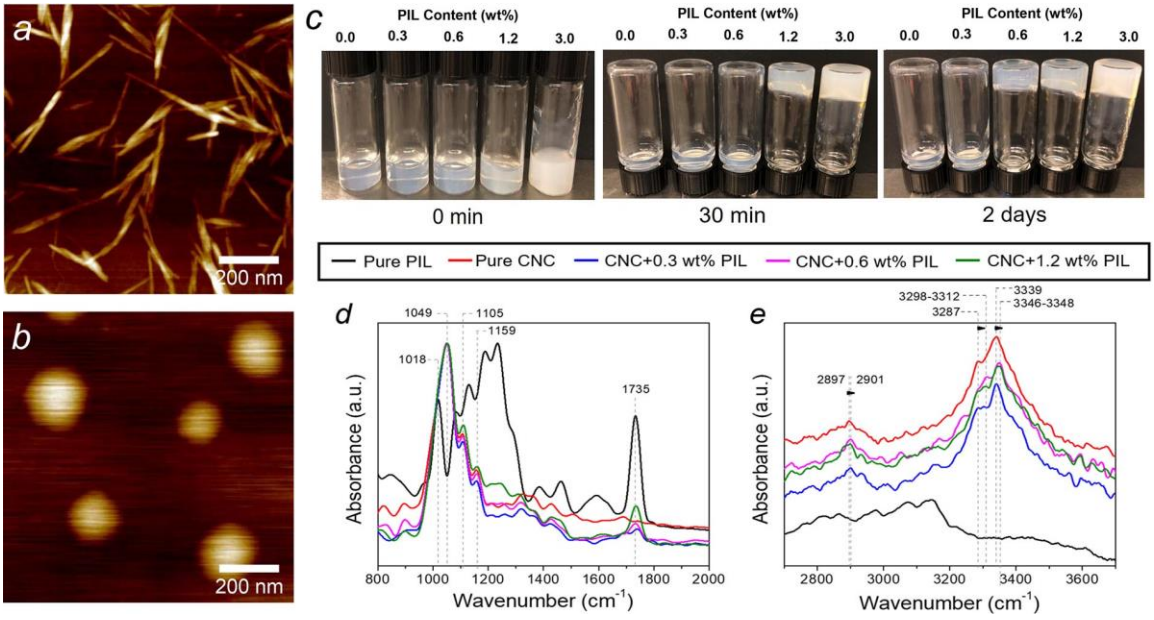

Figure 7.2. AFM topography images of CNC (a) and PIL (b) with z scale of 17 nm. (c) Photos of the aqueous mixtures of CNC and PIL, showing gelation behavior. (d-e) FTIR spectra of CNC, PIL and CNC/PIL with different PIL contents at (d) 800-2000 cm^{-1} and (e) 2700-3700 cm^{-1}. CNC concentration of the samples for (c-e) was 3 wt%.

Zeta-potential values confirm that CNC and all ionic polymers (PIL, L-PIL and PA-K) have a negative surface charge (Figure S7.4). Overall, the zeta-potential value increased with increasing concentration of ionic polymers due to the higher zeta-potential value of the ionic polymers compared to that of CNC, irrespective of the type of the ionic polymers. This result suggests that CNC surfaces are partially covered by the ionic polymers as further confirmed with FTIR (Figures 7.2d-e and S7.5-6).

The FTIR spectra of all samples are dominated by that of CNC, showing the characteristic peaks of cellulose. The peaks at 1049 cm^{-1}, 1105 cm^{-1} and 1159 cm^{-1} were observed, which are assigned to C-O stretching, ring stretching in plane, C-O-C stretching at the β-(1,4)-glycosidic linkage of cellulose, respectively (Figures 7.2d and S7.6).[392,393] For CNC/PIL samples, the intensity of the C=O stretching peak for PIL at 1734 cm^{-1} increased without peak shift as the PIL concentration increased in comparison with a reference peak of

unchanged C-O groups of CNC at 1049 cm^{-1}. Specifically, the intensity ratio of C=O to C-O peaks increased from 0.08 to 0.2 with increasing PIL content from 0.3 to 1.2 wt% (Figure 7.2d). This result confirms the increased PIL amount and suggests an insignificant effect of C=O groups on intermolecular interactions between CNC and PIL.

In addition, a broad peak of O-H stretching shifts to higher wavenumber (blue-shifted) when the PIL concentration was 0.6 wt% or higher (Figure 7.2e). The characteristic peaks of pure CNCs at 3287 cm^{-1} and 3339 cm^{-1}, corresponding intermolecular hydrogen bonding, were shifted by 11-25 cm^{-1} and 7-9 cm^{-1}, respectively, with the addition of PIL component.[392,394] The peak related to C-H stretching centered at 2897 cm^{-1} was also slightly blue-shifted by 4 cm^{-1} for the samples with PIL (Figure 7.2e). The blue shift of O-H and C-H stretching peaks suggests that original intermolecular hydrogen bonding in CNCs was broken,[395] and that CNC and PIL formed intermolecular interactions via unusual hydrogen-bonding, called "blue-shifted" hydrogen bonding. The blue shift for C–H···π type hydrogen bonding has been theoretically and experimentally investigated.[396,397,398,399] We suggest that the X-H···π type H-bonding ability is extended to the CNC/PIL samples where H-X··· $[C\text{-}H]^+$ interactions can be formed between X-H groups of CNCs and $[C\text{-}H]^+$ in π^+-cloud of the imidazolium ring of the PILs.[20] Furthermore, the FTIR spectra of the samples with L-PIL showed the blue shift of intermolecular hydrogen bonding peaks, while the characteristic H-bond peaks of the samples with PA-K were red-shifted (Figures S7.5-6). This result indicates that the counterion type determines the type of hydrogen bonding formed between CNC and the ionic polymers.

AFM images of cellulose nanocrystal/polymer composite films show uniform dispersion of the ionic polymers and CNC without phase separation, regardless of the type of the ionic polymers (Figures 7.3 and S7.7-9). AFM images of pure CNC film exhibit anisotropic arrangement due to the self-assembly behavior of CNCs into a chiral nematic phase (Figures 7.3b,f and S7.7a,e).[400] With increasing PIL concentration, AFM images of CNC/PIL films show a change in CNC orientation to a nematic and then an isotropic phase featuring network structures. Using the hyperbranched ionic polymers (PIL and PA-K), the apparent network structures were observed when the PIL or PA-K concentration reached

0.6 wt% (Figures 7.3c-e, g-i, S7.7b-d, f-h and S7.8-9d-f). For the samples with L-PIL, a higher L-PIL content was needed to create the network structure (Figures S7.8-9a-c). It should be noted that the content of ionic polymers needed for the network structure formation corresponds to the content at which the hydrogel formation and the shift of hydrogen bonding vibrations occurred. Therefore, we can conclude that at a critical content of ionic polymer, a percolating networking support was formed via hydrogen bonding between cellulose nanocrystals and ionic polymers. The intermolecular interactions between CNC and PIL suppress the self-organization of CNCs into an anisotropic state and instead promote CNC orientation in an isotropic state, which results in the formation of the network structure.

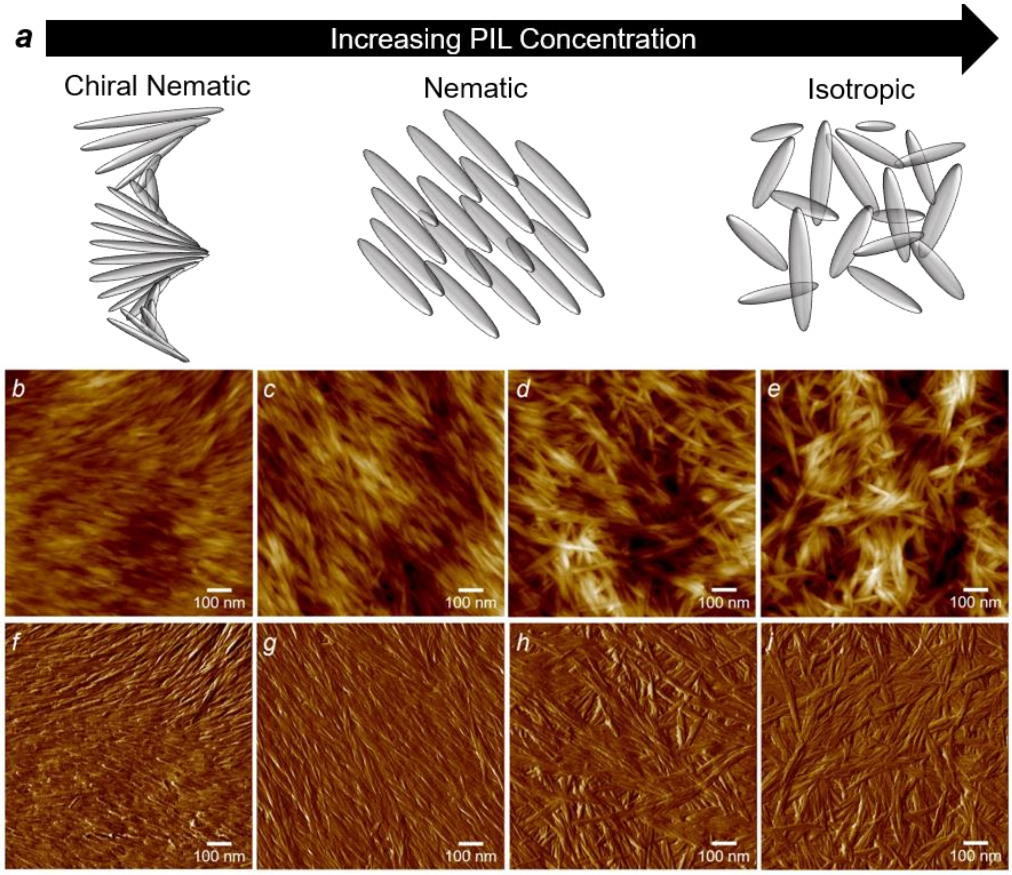

Figure 7.3. (a) Schematic illustration of CNC orientation change with increasing PIL content. AFM topography (b-e) and phase (f-i) images of CNC/PIL films with different PIL content: (b,f) 0 wt%, (c,g) 0.3 wt%, (d,h) 0.6 wt%, and (e,i) 1.2 wt%. Z scale for (b-e) and (f-i) is 40 nm and 30°, respectively.

Circular dichroism (CD) spectroscopy analysis was performed to quantitatively investigate how incorporation of the ionic polymers affects the alignment of CNC with the calculation of the anisotropic dissymmetry factor, called g-factor, determining the extent of CNC anisotropic alignment in the CNC/PIL composites. Overall, CD spectra of all composite samples exhibit peaks with positive ellipticity, indicating that the composites retain a left-handed helical structure of CNC (Figure S7.10a,c,e). However, the intensity of the peaks is very weak compared to that of pure CNC, confirming that the introduction of the ionic polymers disrupts the self-organization of CNCs into an anisotropic chiral nematic phase as shown in the AFM images (Figures 7.3 and S7.7). The g-factor also rapidly decreases with the addition of PIL and PA-K, while the relatively gradual decrease in g-factor was observed for the samples with the addition of L-PIL (Figure S7.10b,d,f). This result demonstrates that the incorporation of hyperbranched ionic polymers facilitate the formation of the matrix with a random network structure (Figures 7.3 and S7.7-9).

In addition, thermal behavior of CNC/PIL samples was studied using TGA and DSC (Figure S7.11). TGA curves of pure CNC show a two-step decomposition process as indicated by a major weight loss at 173 ^{o}C and a minor loss at 387 ^{o}C, which is consistent with TGA results for CNC prepared via sulfuric acid hydrolysis in literature.[401,402] Due to a higher thermal stability of PIL with a thermal decomposition temperature of 318 ^{o}C, the CNC/PIL composites are more thermally stable. The major weight loss occurred at a higher temperature around 245 ^{o}C for the composite with 1.2 wt% PIL content (Figure S7.11a). This result demonstrates that PILs protect CNCs from lower-temperature thermal decomposition, supporting the zeta-potential measurement result which suggests that the surfaces of CNC can be saturated by PILs (Figure S6.3). The content of PIL in the CNC/PIL composites also affects DSC results. Samples with 0.6 wt% or higher PIL showed a noticeable glass transition at around -20 ^{o}C, which is lower than that of neat PIL at -9 ^{o}C (Figure S7.11b).[382]

7.3.2 Formation of CNC/PIL Ionogels

As described above, PIL with 32 sulfonated terminal groups and imidazolium counterions was exploited to generate a supporting matrix with CNC for ionogels due to its capability

of forming multiple interactions. Ionogels based on CNC and PIL were successfully prepared with various PIL contents via two-step solvent exchange, followed by the evaporation of volatile solvent (ethanol) (Figures 7.1, 7.4 and S7.12). During the solvent exchange, despite mass loss (4-7wt%), CNC and PIL were preserved well as revealed by XPS data on the samples collected after adding ethanol but before adding the ionic liquid (Figures S7.13-15). The ionogels discussed below are coded as CNC/PIL-0.0, CNC/PIL-0.5, CNC/PIL-1.0, and CNC/PIL- 2.0. The number indicates the weight concentration of PILs in the final ionogels in wt%.

After volatile solvent evaporation, shape-persistent solid ionogels were formed with high ionic liquid content of around 95 wt%. Despite the extremely high ionic liquid content, the CNC/PIL ionogels are freestanding and strong enough to withstand a weight 400 times heavier than themselves without macroscopically visible damage (Figure 7.4a,b). The dimension of the ionogels can be adjusted by simply changing the volume of their components in solutions. Indeed, ionogels with sub-mm thickness were successfully prepared, and these ionogels are semi- transparent with optical transmittance of up to 50% measured by UV-Vis spectroscopy, allowing objects to be seen clearly though them due to the intrinsic optical transparency of CNC (Figure 7.4c and S7.16). The ionogel shape can be also altered by varying the shape of the container used for ionogel preparation as not only circular but also rectangular-shaped ionogels were produced (Figure S7.12e). Additionally, the ionogel preparation method proposed here can be expanded for the ionogels with all types of ionic liquids although ionogel properties strongly depend on the type of ionic liquids. In fact, ionogel films with two other ionic liquids (bis(trifluoromethylsulfonyl)imide lithium salt and 1-butyl-3-methylimidazolium bromide) were successfully prepared using the same method for the ionogel with [EMIM][TFSI]. The ionogel film containing the ionogel containing bis(trifluoromethylsulfonyl)imide lithium salt was mechanically stable enough to grab it using a tweezer, while the one containing 1-butyl-3-methylimidazolium bromide was very soft and lost their shape when grabbed with the tweezer (Figure S7.12f-g). Furthermore, the ionogels can be also used as a conducting channel to light up a yellow light-emitting-diode (LED), demonstrating their high conductivity (Figure 7.4d, Video S7.1).

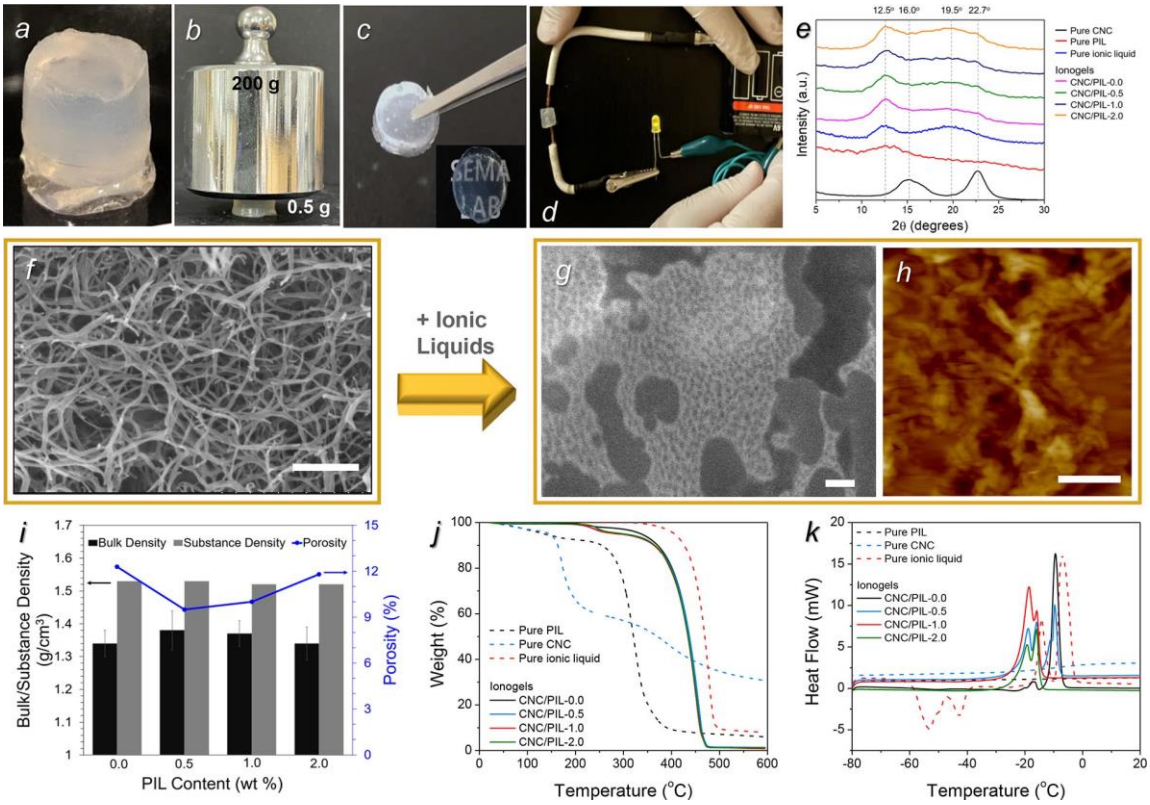

Figure 7.4. (a-d) Photos of CNC/PIL ionogels. (e) XRD spectra of CNC/PIL Ionogels. (f,g) SEM images of CNC/PIL aerogel (f) and CNC/PIL-2.0 ionogel (g). (h) AFM topography image of CNC/PIL-2.0 ionogel (z scale : 150 nm). Scale bar is 500 nm for (e-g). (i) Bulk and substance densities and porosity, (j) TGA and (k) DSC curves of CNC/PIL ionogels.

The FTIR and XPS spectra of the CNC/PIL ionogels are similar to those of pure ionic liquid [EMIM][TFSI], confirming the dominating presence of the ionic liquids (Figures S7.17-19).[403] Additionally, XPS peaks are shifted toward lower binding energy compared to those of pure [EMIM][TFSI],[404] and the shifted peaks include C1s peaks related to CF_3 of [TFSI] anions and the end of ethyl groups of [EMIM] cations and N1s peaks related to [EMIM] and [TFSI] ions (see detail in Supporting Information, Figure S7.17c-f and S7.18a). These peak shifts indicate that ionic liquids are entrapped within the CNC/PIL network by forming interactions with CNC and PIL. Similar XPS peak shift was reported for the ionic liquid confined in silica nanopores, confirming the interactions between ionic liquids and the silica pore wall surface.[405]

X-ray diffraction (XRD) spectra of the CNC/PIL ionogels show amorphous features with weak diffraction peaks, further confirming the dominance of ionic liquids in the ionogels (Figure 7.4e). Although the significant amorphous signal originating from the ionic liquids, [EMIM][TFSI], makes it different to distinguish crystalline peaks for CNCs, peak fitting analysis of the XRD spectra demonstrates the retention of crystalline structures of CNCs within the ionogels. Crystalline peaks of cellulose I ($[1\bar{1}0]$ peak at 14.8°, [110] peak at 16.1°, and [200] peak at 22.6°) are identified with two amorphous bands associated with the ionic liquid, [EMIM][TFSI].[383,393,406] An amorphous band assigned to PIL is also observed for the ionogels containing PIL (Figure S7.20-21).

The bulk and substance densities of samples before and after adding ionic liquids were calculated to investigate the effects of integrating CNC, PIL and ionic liquid on the physical properties of the ionogels. The bulk density (ρ_B) was calculated by measuring the dimensions and weight of the samples, and the substance density (ρ_S) was determined by considering only solid and liquid matters within the samples. The bulk densities (ρ_B) of the CNC/PIL gels retaining ethanol without ionic liquids are in the range of 0.83-0.99 g/cm^3, which are greater than the substance densities (ρ_S) of 0.81-0.82 g/cm^3 (Table S7.1). This result suggests that the water-to-ethanol exchange causes the densification of the CNC/PIL gels. Similarly, the increased density of CNC gels achieved through solvent exchange to ethanol was reported and may be attributed to the change in solvation energy to be less negative than pure water.'[407] Interestingly, the bulk densities of the CNC/PIL ionogels (1.34-1.38 g/cm^3) are smaller than their substance densities of 1.52-1.53 g/cm^3 (Table 7.2 and Figure 7.4i). This result suggests that the introduction of the ionic liquids leads to the formation of solid ionogels with porous structures. The porosity (ε) can be estimated from bulk and substance densities using the following equation: $\varepsilon = \left(1 - \frac{\rho_B}{\rho_S}\right) \times 100\ (\%)$, where ε, ρ_B and ρ_S are the porosity, bulk density, and substance density, respectively.[408] The estimated porosity of the CNC/PIL ionogels is 9.5-12.3% (Table 7.2).

Table 7.2. Physical and mechanical properties and ionic conductivities of CNC/PIL ionogels.

Ionogels	ρ_B (g/cm^3)	ρ_s (g/cm^3)	ε (%)	E (MPa)	σ_y (kPa)	$\sigma_{75\%}$ (kPa)	Ionic Cond. at 30 °C (mS cm^{-1})
CNC/PIL-0.0	1.34±0.04	1.53	12.3	0.6±0.2	55±13	320±40	5.4
CNC/PIL-0.5	1.38±0.06	1.53	9.5	2.1±0.2	141±5	830±100	5.9
CNC/PIL-1.0	1.37±0.04	1.52	10.0	3.1±1.0	190±20	710±170	6.2
CNC/PIL-2.0	1.34±0.05	1.52	11.8	5.6±1.4	260±60	790±150	7.8

* ρ_B, ρ_S and ε are the bulk density, substance density, and porosity, respectively. E, σ_y and $\sigma_{75\%}$ are the compressive elastic modulus, yield strength, and compressive strength at 75% strain, respectively.

7.3.3 Microstructures of CNC/PIL Ionogels

Due to the high ionic liquid content of the CNC/PIL ionogels, it was very challenging to conduct SEM imaging on the ionogels. Thus, SEM imaging of CNC/PIL aerogels obtained via CO_2 supercritical drying was performed first. All CNC/PIL aerogels show a porous network structure, which can effectively confine ionic liquids (Figures 7.4f and S7.22). The CNC aerogel without PIL possesses a relatively discontinuous network, reflecting the anisotropic arrangement of CNCs (Figure S7.22a). The PIL incorporation facilitates the formation of a continuous and percolating network (Figures 7.4f and S7.22b-c). Such PIL-dependent structural alternation of the aerogels resembles the change in orientation of CNC with various PIL contents as found in the AFM images (Figures 7.3 and S7.6). Despite the technical difficulty in SEM imaging of the ionogels, we were able to obtain a SEM image of the CNC/PIL ionogel with 2.0 wt% PIL, showing the presence of nanopores which were

not observed in the aerogels (Figure 7.4g). Their surface morphology taken by AFM also showed a networking morphology of nanopores (Figures 7.4h and S7.23). The SEM and AFM images show that added ionic liquid is confined and concentrated near the interfaces of CNC/PIL due to the strong ionic interactions between ionic liquids and the CNC/PILs.

7.3.4 Thermal Properties of CNC/PIL Ionogels

Thermal properties of the ionogels were studied using TGA and DSC (Figure 7.4j,k). TGA curves show that all ionogels have a high thermal stability (Figure 7.4j). The onset thermal decomposition temperature (~10% mass loss) of the ionogels was around 370 ^{o}C, and the maximum thermal decomposition occurred around 455 ^{o}C. Such high thermal stability of the ionogels is due to the high thermal stability of the neat ionic liquid [EMIM][TFSI] with onset and maximum thermal decomposition temperatures at 426 ^{o}C and 476 ^{o}C, respectively, which is in good agreement with the literature data for [EMIM][TFSI].[409,410]

The DSC curve of the pure ionic liquid shows multiple peaks of melting and cold crystallization, indicating the ordering of ionic liquids into different phases.[405,411,412] The melting peaks were shifted toward lower temperatures compared to those of the pure ionic liquid, and the cold crystallization peaks disappeared (Figure 7.4k). This result indicates the change in molecular ordering of the ionic liquid upon confinement, confirming interactions between the ionic liquid and the CNC/PIL matrix. Similar changes in the melting and crystallization peaks have been reported for confined or tethered ionic liquids due to strong intermolecular interactions between ionic liquids and supporting network, which introduce an energy barrier for melting ionic liquids.[143,405,413,414,415]

7.3.5 Mechanical Properties of CNC/PIL Ionogels

Despite the extremely high content of ionic liquid, our ionogels are not liquids but shape-persistent monolithic specimens with high resistance to mechanical stresses. These monolithic ionogels are too brittle to perform tensile mechanical tests due to inherent high elastic modulus of CNCs (110-220 GPa).[416,417] Instead, compressive mechanical tests were carried out to investigate the mechanical properties of the ionogels. The compressive stress-strain curves of the ionogels show that stress linearly increases at low strains, reaches

a plateau value at intermediate strains, and then sharply rises at high strain (Figures 7.5b-c and S7.24). The appearance of these three distinct regions in the stress-strain curves—namely, the linear elastic region, plateau collapse region and densification region—indicates that the ionogels have a porous morphology.[388,389,418,419,420,421] Upon compression, the ionogels undergo a linear elastic deformation process upon application of a steadily increasing, small initial strain. Further compression causes fracture of CNC/PIL matrix scaffold, resulting in the initial collapse of porous morphology corresponding to the plastic deformation in the plateau region of the stress-strain curve. At high strains, the pores collapse and the ionogels are compacted significantly, leading to the rapid increase in stress in the last regime (Figure 7.5a,b).

The stress-strain curves of the ionogels are different from those of the samples retaining ethanol without the ionic liquid, which exhibit two linear regions with flat and steep slopes as observed from traditional non-porous gels (Figures 7.5b and S7.24-26).[422,423,424] This result suggests that the addition of ionic liquids causes the formation of porous ionogels, presumably due to ionic association mediated by electrostatic ionic interactions between CNC, PIL and ionic liquids. Compressive elastic modulus (E) and compressive strength at 75% strain ($\sigma_{75\%}$) of the ionogels are one to two orders of magnitude, respectively, higher than those of the samples without the added ionic liquid (Table 7.2, Figures 7.5c and S7.25b-c). The enhanced mechanical properties of the ionogels suggest that the added ionic liquid create additional strong electrostatic interactions with CNCs and PILs, which can act as physical cross-links.

Moreover, the presence of PIL component plays a positive role on the enhancement of the mechanical properties of the ionogels (Table 7.2, Figure 7.5b-c). With increasing PIL content, compressive elastic modulus of the ionogels increases from 0.6 MPa to 5.6 MPa. Compressive yield strength (σ_y) also increases from 55 kPa to 260 kPa. Similarly, compressive strength at 75% strain of the CNC ionogel without PIL is 320 kPa, while the CNC/PIL ionogels have a much higher compressive stress in the range of 710-830 kPa (Figure 7.5c). It should be noted that all PIL-containing ionogels show remarkably high mechanical properties compared to existing polymer-based ionogels with compressive elastic moduli in kPa range, despite their high ionic liquid content of ~95wt%.[161,425,426] We

suggest that ionic pairing and crosslinking causes the enhancement of mechanical properties, as suggested for ionogels based on ionic polymers with positively and negatively charged functional groups.[154,370,371]

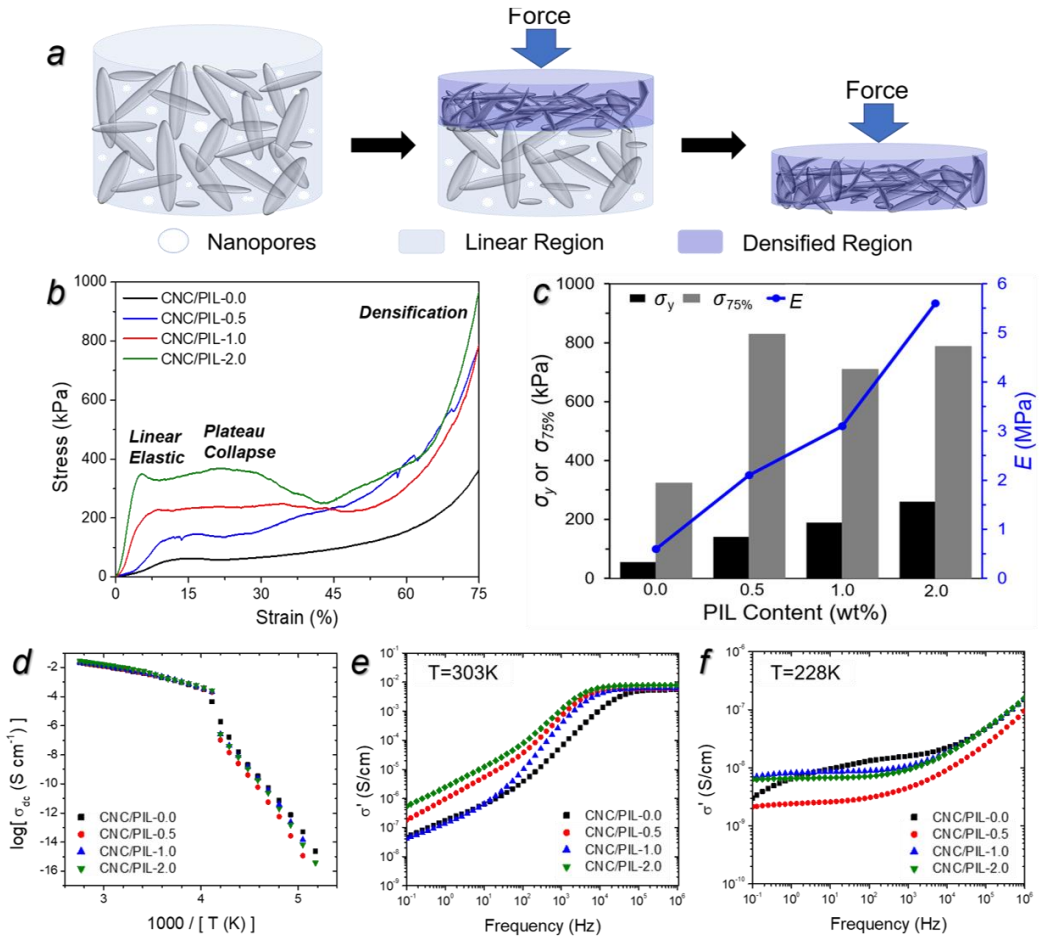

Figure 7.5. (a) Schematic illustration of the structural change of CNC/PIL ionogels under compression showing collapse of nanopores at high strains. (b) Representative compressive stress-strain curves, (c) compressive elastic modulus (E), yield strength (σ_y) and compressive strength at 75% strain ($\sigma_{75\%}$) of CNC/PIL ionogels. (d) Ionic conductivity of CNC/PIL ionogels as a function of temperature. (e-f) The real part of conductivity (σ') of the ionogels at 303K (e) and 228K (f).

The mechanical properties of the ionogels were further probed by nanoscale dynamic mechanical analysis (nano-DMA).[427] As we observed, storage (G') and loss (G'') moduli of all ionogels are almost completely independent of frequency, and the values of storage moduli are higher than those of loss moduli over the entire frequency ranges, confirming

that the ionogels are solid-like, elastic gels (Figure S7.27).[428,429] The CNC ionogels without PIL exhibited a storage modulus of 15 MPa, while those with PIL have storage moduli of 45-60 MPa. These values are much higher than those for other ionic liquid-rich polymer-based ionogels with storage moduli in kPa range.[148,430,431,432] Therefore, the CNC/PIL ionogels possess remarkable mechanical strength due to the physical crosslinking of CNC/PIL network and ionic liquids in additional to incorporation of mechanically strong nanocrystals.

7.3.6 Ion Transport Properties of CNC/PIL Ionogels

To evaluate the ion transport of the ionogels, the dc conductivity, σ_{dc} was determined from broadband dielectric spectroscopy (BDS) over a wide range of temperatures (Figure 7.5d). The temperature dependence of σ_{dc} was qualitatively similar for all samples, regardless of the PIL content, and exhibited typical super-Arrhenius behavior at high temperatures, followed by an abrupt drop near the ionic liquid crystallization temperature, and then an Arrhenius dependence at the low temperatures.[433,434]

The dc ion conductivity is defined as the real part of the complex conductivity (σ') in the frequency-independent plateau region.[82] Notably, ionic conductivities of all ionogels prepared in this study were in the order of 5-8 mS cm^{-1} at 30 ^{o}C (Figure 7.5e). CNC ionogel without PIL showed ionic conductivity of 5.4 mS cm^{-1}, and the ionic conductivities of CNC/PIL ionogels increased from 5.9 mS cm^{-1} to 7.8 mS cm^{-1} as the PIL content increased (Table 7.2). These values are much higher than that of PIL (6.44 $\times 10^{-2}$ mS cm^{-1} at 20 ^{o}C) but comparable to that of pure ionic liquid, [EMIM][TFSI] (~10.9 mS cm^{-1}).[382,435, 436] This result demonstrates that the high ionic conductivity of the ionogels arises from their high content of ionic liquids, and the mechanical fortification afforded by confining ionic liquid into CNC/PIL network negligibly diminishes the conductivity relative to that of the pure ionic liquid (10.9 mS cm^{-1}).[435,436]

At low temperatures, there are notable differences between the conductivity spectra of the CNC ionogels and the CNC/PIL ionogels. A complete presentation of the σ′ data for the ionogels is provided in the SI (Figure S7.28). Namely, the characteristic frequency-independent conductivity plateau is distorted for the ionogel without PIL, corresponding

to a broader distribution of ion hopping rates (Figure 7.5f).[437] This behavior has also been observed in ionic liquids confined to silica nanopores and is attributed to a distribution of pore sizes as well as the disparity in ion transport rates near the silica interfaces.[437,438,439,440] The ions near the CNC interfaces are expected to have different dynamics compared to those in the bulk due to the electrostatic and hydrogen-bonding interactions between CNC and ionic liquids. In addition, conductivity in crystalline phase, in amorphous phase, and at their interfaces will be different. This results in heterogeneous ion dynamics observed in the dielectric spectra. On the other hand, the narrower ion relaxation times and stable conductivity plateau observed for the CNC/PIL ionogels suggests that the addition of PIL leads to more homogenous ion environments by forming continuous ion conducting channels. The results therefore demonstrate how functionalization of CNCs with ionic polymers can be used to tailor the heterogenous dynamic environments in composite materials.

7.3.7 Mechanism for Ionogel Formation

Next, we suggest that there are multiple interactions created between CNC, PIL and ionic liquids (Figure 7.6). CNC and PIL can form various interactions and construct the nano-network matrix for trapping large amounts of ionic liquids. Since CNC and PIL are both negatively charged with negative values of zeta potential, we suppose that the major interaction between CNC and PIL is governed by hydrogen bonding rather than ionic interactions. They can interact via hydrogen bonding possibly between C-H and O-H of CNC and π^+-cloud in the imidazolium ring of PIL, as confirmed by FTIR and XPS analysis (Figures 7.2e and S7.14). PILs can also interact themselves via electrostatic ionic interaction between anionic sulfonate terminal groups and imidazolium counter-cations, forming ionic clusters which can serve as physical cross-links.[441]

In the presence of ionic liquids, the interactions become complicated since ionic liquids can form additional ionic interactions with CNC and PIL (Figure S7.17-18). For example, ionic liquid cations can interact with negatively charged terminal groups of PIL, and ionic liquid anions can create ionic interactions with imidazolium counter-cations of PIL, providing ionic bridges between PIL and ionic liquids. It has been reported that upon

addition of halide ions (X^-), cationic polymeric ionic liquids can form intra- and/or inter-chain cross-linking among the polymer chains through ionic bridges with the halide ions, leading to the formation of a cross-linked hydrogel.[442,443] [TFSI] anions of the ionic liquids can also form hydrogen bonding with C-H or O-H of CNCs owing to the presence of S=O and C-F in [TFSI].[444] Therefore, ionic liquids are concentrated near the CNC/PIL interfaces, resulting in further ionic association between CNC and PIL. Thus, the concentrated ionic liquids provide continuously connected ion conducting networks and nanopore formation that facilitate fast and un-hindered ion transport of small ions.

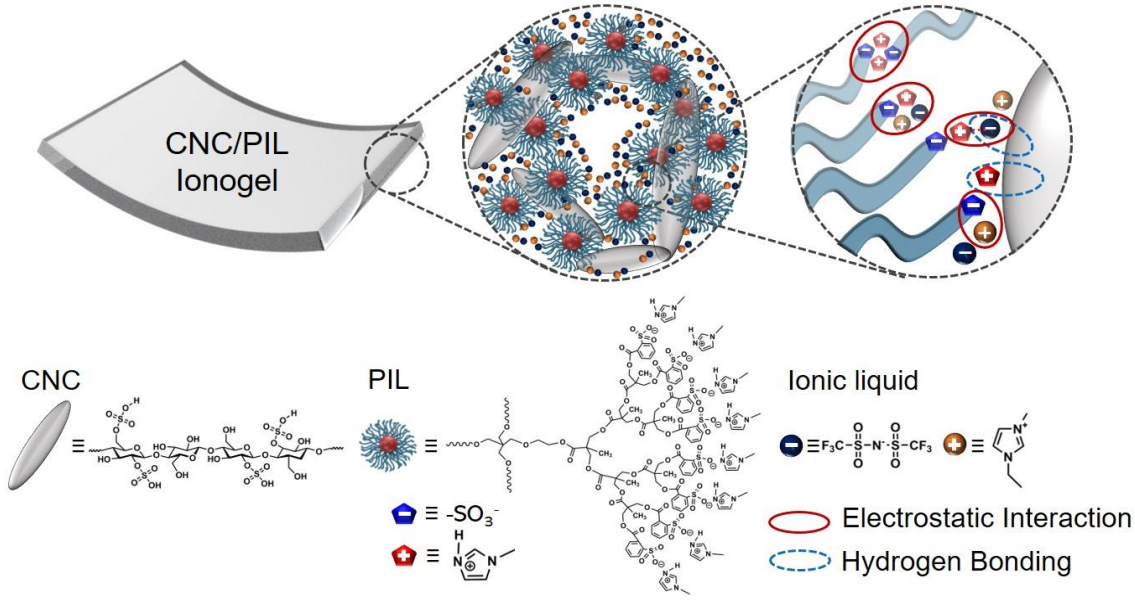

Figure 7.6. Schematic illustration of CNC/PIL ionogel formation mechanism through via interactions between CNC, PIL and ionic liquids.

7.4 General Discussion and Conclusions

It is important to note that a majority of solid electrolytes and ionogels reported to date demonstrate an inverse correlation between mechanical strength and ionic conductivity.[146,147] Among the electrolyte materials, the maximum mechanical strength in terms of elastic modulus is observed from inorganic solid electrolytes, but their ionic conductivities are very low, in the range of 10^{-5}-10^{-4} S cm^{-1}.[445] In fact, the corresponding

Ashby plot shows an enhancement in mechanical strength at the expense of the ionic conductivity (Figure 7.7, see Table S7.2-3 for the references of the Ashby plot).

To demonstrate the exceptional combination of mechanical and ion transport properties of CNC/PIL ionogels designed here, we compare the ionic conductivity and compressive/tensile elastic modulus of existing electrolyte materials (Figure 7.7). In general, polymer and hybrid organic-inorganic solid electrolytes possess high elastic moduli on the order of 10^3 to 10^6 Pa but very low ionic conductivities in order of 10^{-5} to 10^{-1} mS cm^{-1}. Traditional ionogels have higher ionic conductivities of 10^{-2} to 10^1 mS cm^{-1} but lower elastic moduli of 10^0 to 10^5 Pa. The Ashby analysis reveals that the trade-off between mechanical strength and ionic conductivity is exaggerated when the ionic conductivities reach above 1 mS cm^{-1}, which is ~10% of the ionic conductivity of [EMIM][TFSI].

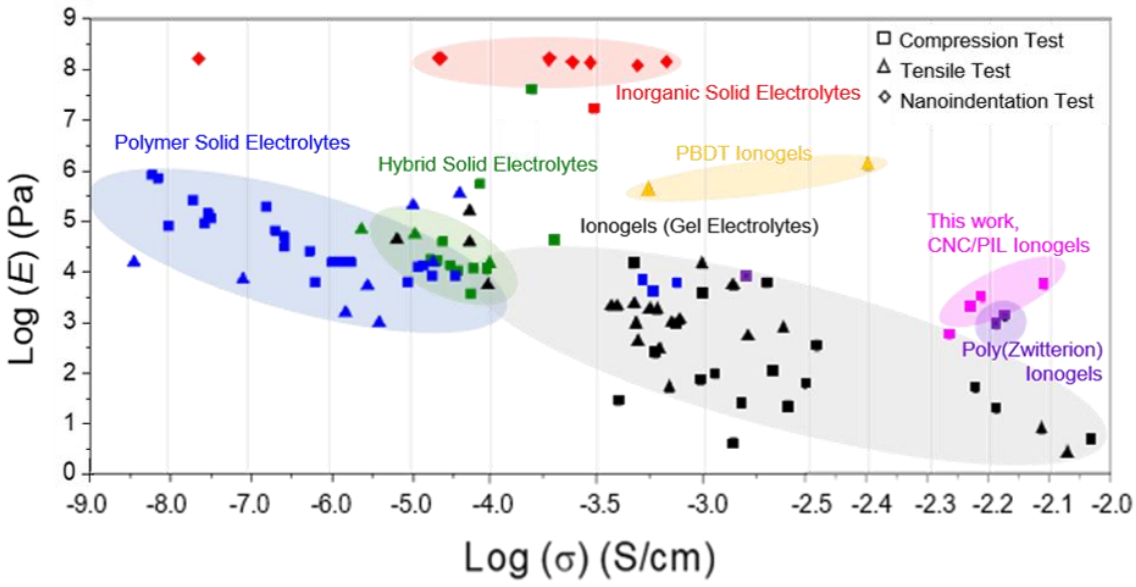

Figure 7.7. Ionic conductivity vs compressive/tensile elastic modulus comparison for solid electrolytes and ionogels (gel electrolytes) (References in Table S7.2-7.3).

Notably, this trade-off is broken for the CNC/PIL ionogels prepared in this study even though their ionic conductivity is as high as ~70% of the ionic conductivity of neat ionic liquid. The CNC/PIL ionogels possess reasonably high elastic moduli comparable to

conventional solid-state electrolytes as well as high ionic conductivity comparable to liquid-state electrolytes (ionic liquid) (Figure 7.7). Very few ionogels show higher or comparable elastic moduli in comparison to those of the CNC/PIL ionogels. Ionogels composed of a rigid-rod sulfonated polymer, poly(2,2′-disulfonyl-4,4′-benzidine terephthalamide) (PBDT) exhibit elastic moduli higher than those of CNC/PIL ionogels due to high modulus of PBDT combined with the collective ionic (electrostatic) interactions. However, their ionic conductivities are only 25-35% of those of pure ionic liquids.[372,373] Additionally, poly(zwitterion)-based ionogels display both good elastic moduli in MPa range and ionic conductivities up to ~6.7 mS cm^{-1} (~60% of ionic conductivity of pure ionic liquid), comparable to those of the CNC/PIL ionogels.[370,371] This supports the positive effects of the electrostatic interactions between ionic moieties of polymers on enhancement of both mechanical and ion transport properties of ionogels.

In summary, we report the shape-persistent, ionic liquid-rich ionogels by using cellulose nanocrystals and polymerized ionic liquids as a supporting network. First, high mechanical strength of the ionogels with a compressive elastic modulus up to 5.6 MPa is caused by the mechanical reinforcement achieved by CNC/PIL network formation. Moreover, these robust CNC/PIL ionogels show high ionic conductivity up to 7.8 mS cm^{-1}, similar to that of free ionic liquids and well exceeding those of traditional gel electrolyte materials, due to their unique continuous nanoporous morphology without interruption of the percolating conductive pathway. The strong and conductive CNC/PIL ionogels have potential as robust electrolyte components for high-performance energy harvesting and storage devices where their high mechanical compression strength can suppress dendrite growth in battery electrodes. Finally, we suggest that the reinforced and conductive ionogels developed here introduces a foundation for the development of novel mechanically robust, highly conductive electrolyte materials for energy storing devices capable of breaking the mechanical strength versus ionic conductivity dilemma.

Chapter 7 Appendix: Supporting Information

Synthesis of Ionic Poylmers (PIL, L-PIL, and PA-K).

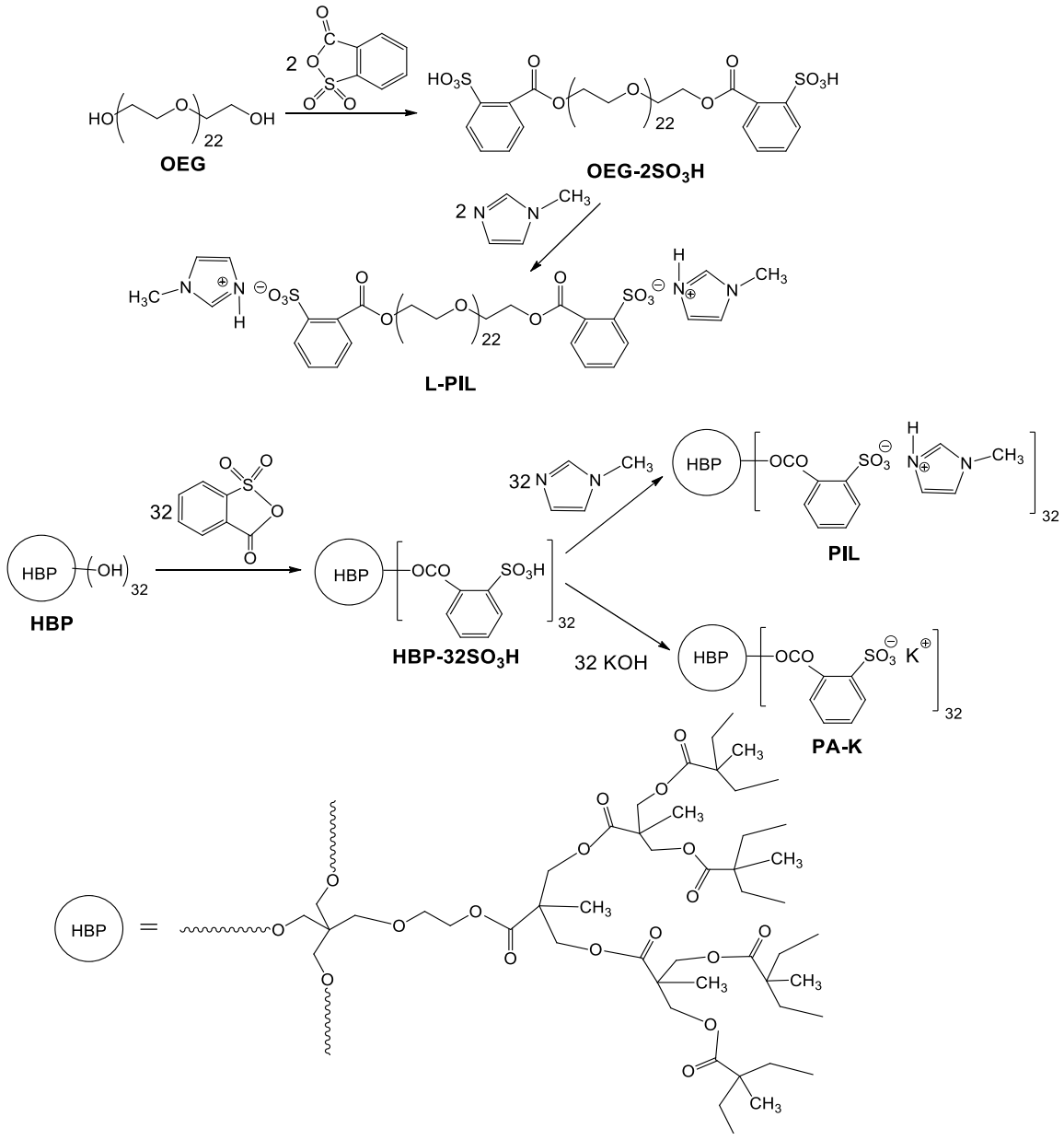

Scheme S7.1. Synthesis of imidazolium-containing polymeric ionic liquids of linear (L-PIL) and hyperbranched (PIL) structure and of hyperbranched polymeric sulfonic acid with potassium salt (PA-K).

Synthesis of linear polymeric ionic liquid L-PIL

Linear polymeric ionic liquid **L-PIL** was synthesized according to previously reported technique.[382] At first stage linear oligomeric α,ω-disulfonic acid OEG-2SO_3H was obtained as follows. 4.96 g (4.96 mmol) of polyethylene glycol OEG M_n 1000 g/mol and 1.83 g (9.92 mmol) of 2-sulfobenzoic acid cyclic anhydride were reacted in a bulk under nitrogen flow and stirring at 75 ^oC for 2 h. The resultant oligomeric linear acid OEG-2SO_3H was first washed with diethyl ether and then dried under vacuum using rotary pump (1-3 mm Hg vacuum pressure) at 50 ^oC. Yield: 6.07 g (85%). SO_3H groups content: determined 11.3%; calculated 11.84%. At second stage the linear polymeric ionic liquid L-PIL was synthesized by neutralising the synthesized linear oligomeric acid OEG-2SO_3H with N-methylimidazole. A solution of 2.68 g (1.96 mmol) of OEG-2SO_3H and 0.32 g (3.92 mmol) of N-methylimidazole in 5-10 ml of ethanol was intensively stirred at room temperature for 5-10 min. The solvent was then evaporated at 50-60 ^oC and the obtained viscous transparent brownish liquid was washed with diethyl ether and dried in vacuum using rotary pump (1-3 mm Hg vacuum pressure) at 40-50 ^oC. Yield: 2.43 g (81%). The structure of the obtained polymeric ionic liquid L-PIL was confirmed by FTIR and ^1H NMR spectra provided in Ref.382.

Synthesis of hyperbranched polymeric ionic liquid

The hyperbranched polymeric ionic liquid **PIL** was synthesized in two stages as above according to our previous Ref.382. At first stage the oligomeric sulfonic acid HBP-32SO_3H of hyperbranched structure with terminal acidic groups was obtained by exhaustive acylation of aliphatic hyperbranched polyester polyol HBP containing 32 terminal primary hydroxyl groups by 2-sulfobenzoic acid cyclic anhydride. 1.51 g (0.0135 g-equivalent) of HBP-32OH was reacted with 2.49 g (0.0135 g-equivalent) of 2-sulfobenzoic acid cyclic anhydride in 7 ml of DMF at 80^oC for 8-10 h. The solvent was partially removed under reduced pressure (1-3 mm Hg) and the synthesized product HBP-32SO_3H was precipitated to ether with subsequent drying at 40-50^oC. Then the product was purified by reprecipitation from ethanol to ether and further dried at 40-50°C till constant weight. Yield: 3.87 g (97%). SO_3H groups: determined 25.1%; calculated 26.8%.

At second stage the hyperbranched polymeric ionic liquid PIL was obtained by neutralizing the synthesized oligomeric sulfonic acid HBP-32SO_3H with N-methylimidazole. 3.40 g (0.0105 g-equivalents) of HBP-32SO_3H and 1.30 (0.0158 g-equivalent) of 1-methylimidazole were added to 13 ml of DMF and intensively stirred at room temperature for 5-10 min. The solvent was then removed under reduced pressure and the remaining transparent brownish liquid was washed with acetone and dried under 60-70 ^oC in vacuum using rotary pump (1-3 mm Hg vacuum pressure). Yield: 3.37 g (79%). The structure of the obtained polymeric ionic liquid PIL was confirmed by FTIR and ^1H NMR spectra provided in Ref.382.

Synthesis of hyperbranched polymeric sulfonic acid with potassium salt PA-K

Hyperbranched polymeric sulfonic acid with potassium salt **PA-K** was synthesized by neutralizing the oligomeric sulfonic acid HBP-32SO_3H of hyperbranched structure obtained by exhaustive acylation of polyester polyol HBP-OH by 2-sulfobenzoic acid cyclic anhydride as above with KOH. A solution of 0.138 g (2.47 mmol) of KOH in 1 ml of water was added dropwise to a solution of 0.846 g (2.47 mg-equivalents) of HBP-32SO_3H in 15 ml of ethanol under vigorous stirring at ambient temperature for 5-10 min. The neutral pH of the solution was determined using litmus paper Then water was evaporated at 75-80 ^oC and the resultant product was washed with acetone and dried at 60-70 ^oC in vacuum using rotary pump (1-3 mm Hg vacuum pressure) till constant weight. Yield: 0.778 g (83%).

AFM Images of PIL, L-PIL, and PA-K

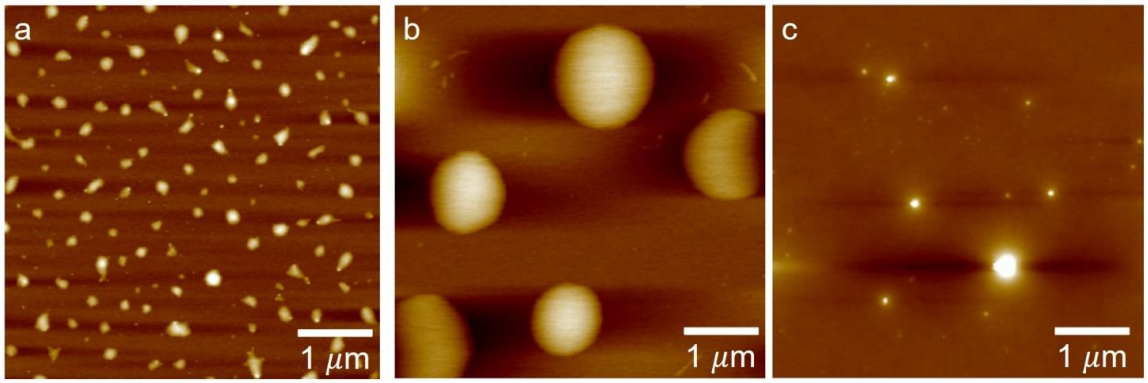

Figure S7.1. AFM topography images of (a) PIL, (b) L-PIL and (c) PA-K. Z scale is 15 nm, 30 nm and 50 nm for (a), (b), and (c), respectively.

AFM images were taken on thin films of ionic polymers (PIL, L-PIL and PA-K). The thin films were prepared using spin-coating at 3,000 rpm for 1 min and air-dried before AFM imaging. 100 μL of 1 wt% aqueous solution of ionic polymers was used for each sample.

Rheological Analysis for CNC/PIL Samples

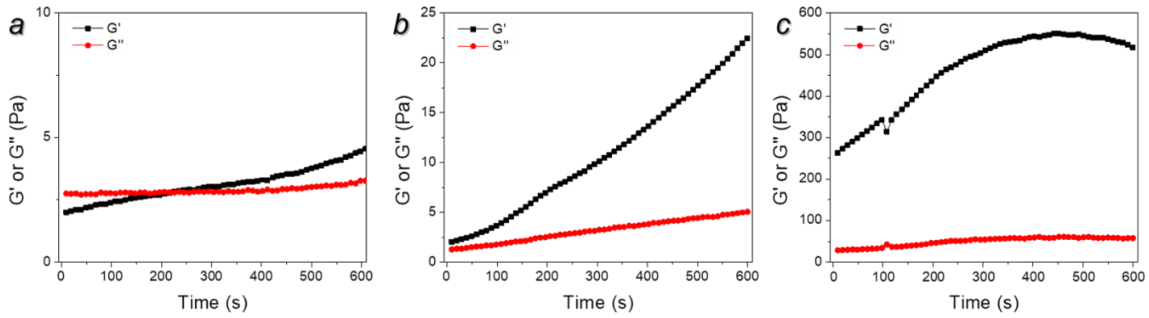

Figure S7.2. Storage modulus (G') and loss modulus (G'') of CNC/PIL samples as function of time. The samples contain different PIL contents: (a) 0.3 wt%, (b) 0.6 wt% and (c) 1.2 wt%.

Experimental Section for Rheological Analysis

An oscillation time sweep experiment was performed using an AR2000EX rheometer (TA Instruments) to record the storage modulus (G′) and the loss modulus (G") as function of time. The oscillation frequency was set to 1 Hz and a shear strain of 3% was applied. 3 wt% CNC suspension without PIL was too fluidic to run rheological measurements. The CNC/PIL samples were placed on a sample stage and tested with a 25 mm parallel plate at a temperature of 25 ^{o}C.

Gelation of CNC/L-PIL and CNC/PA-K Samples

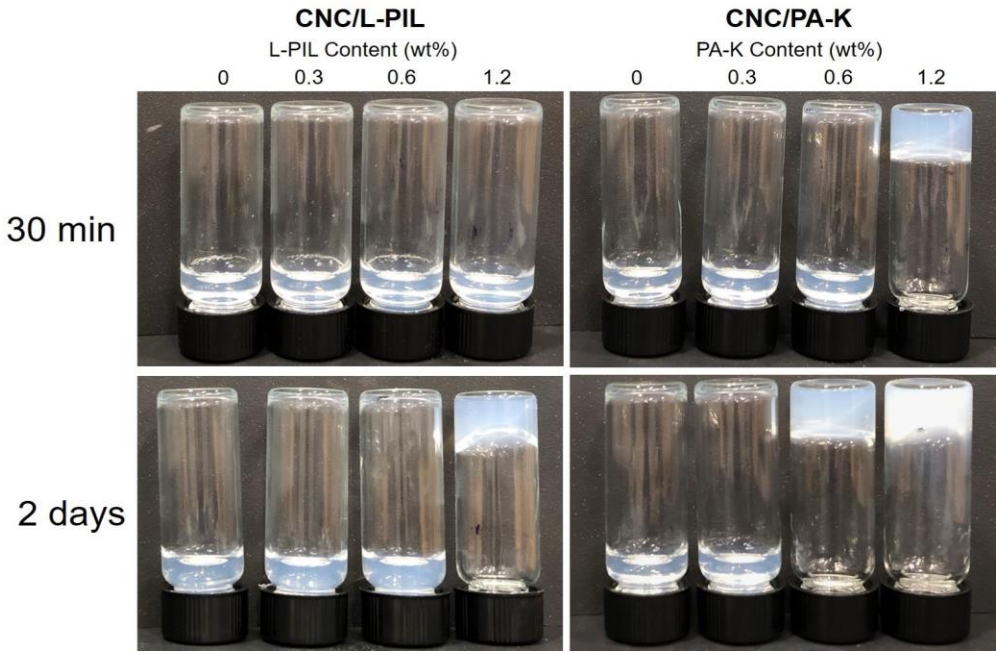

Figure S7.3. Photos of CNC/L-PIL (left) and CNC/PA-K (right) aqueous mixtures. Photos were taken 30 min (top) and 2 days (bottom) after mixing CNC and ionic polymers (L-PIL or PA-K). CNC concentration of all samples is 3 wt%.

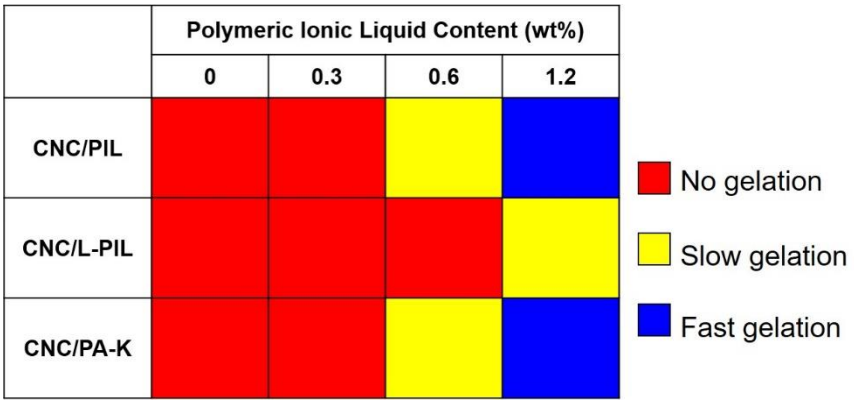

Scheme S7.2. Summary of gelation behavior of CNC/PIL, CNC/L-PIL, and CNC/PA-K aqueous mixtures. CNC concentration for all samples is 3 wt%.

Zeta-potential Values of CNC/PIL, CNC/L-PIL and CNC/PA-K Samples

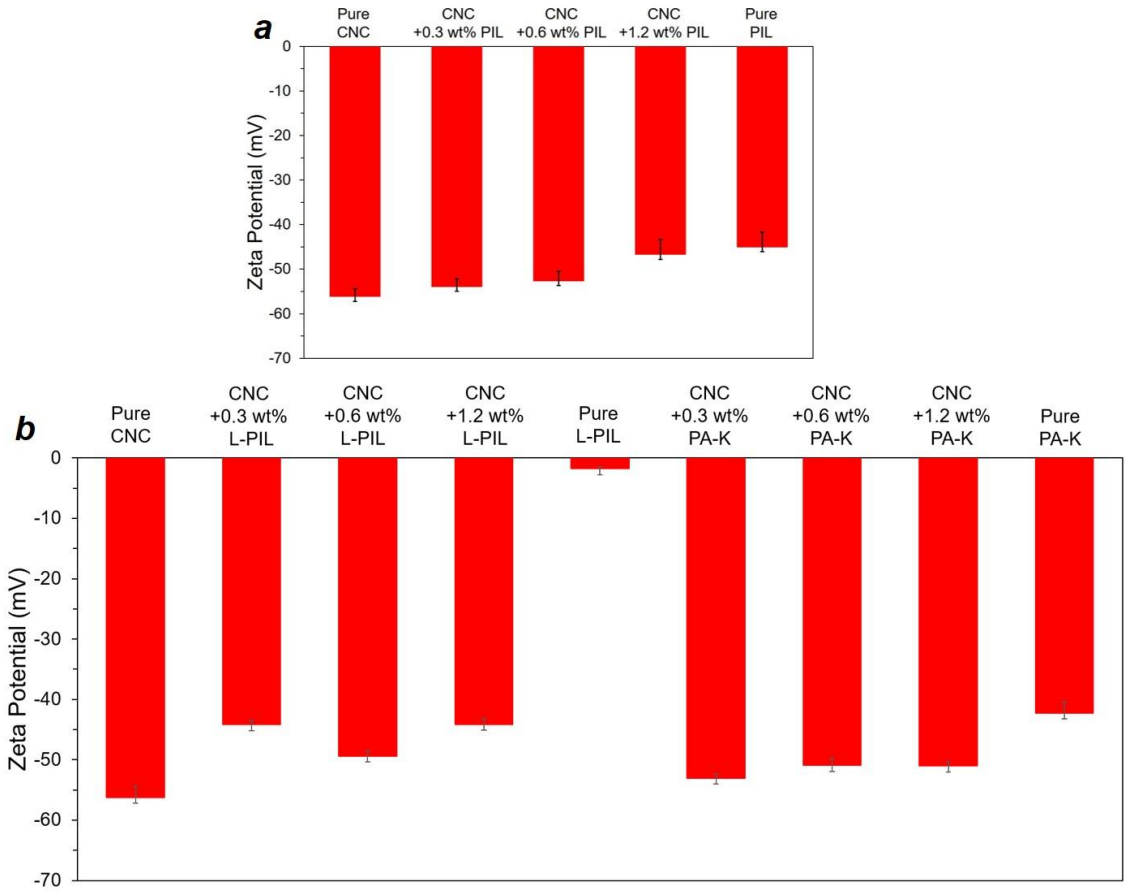

Figure S7.4. Zeta potential values of (a) CNC/PIL, (b) CNC/L-PIL, and CNC/PA-K aqueous mixtures. CNC concentration for all samples is 3 wt% before dilution.

Zeta-potential values of CNC/PIL, CNC/L-PIL and CNC/PA-K aqueous mixtures with different contents of ionic polymers were measured using Zetasizer Nano ZS (Malvern) by averaging three independent measurements of 20 runs each. All samples were diluted 30 times for the measurements.

FTIR Analysis of CNC/PIL, CNC/L-PIL and CNC/PA-K Samples

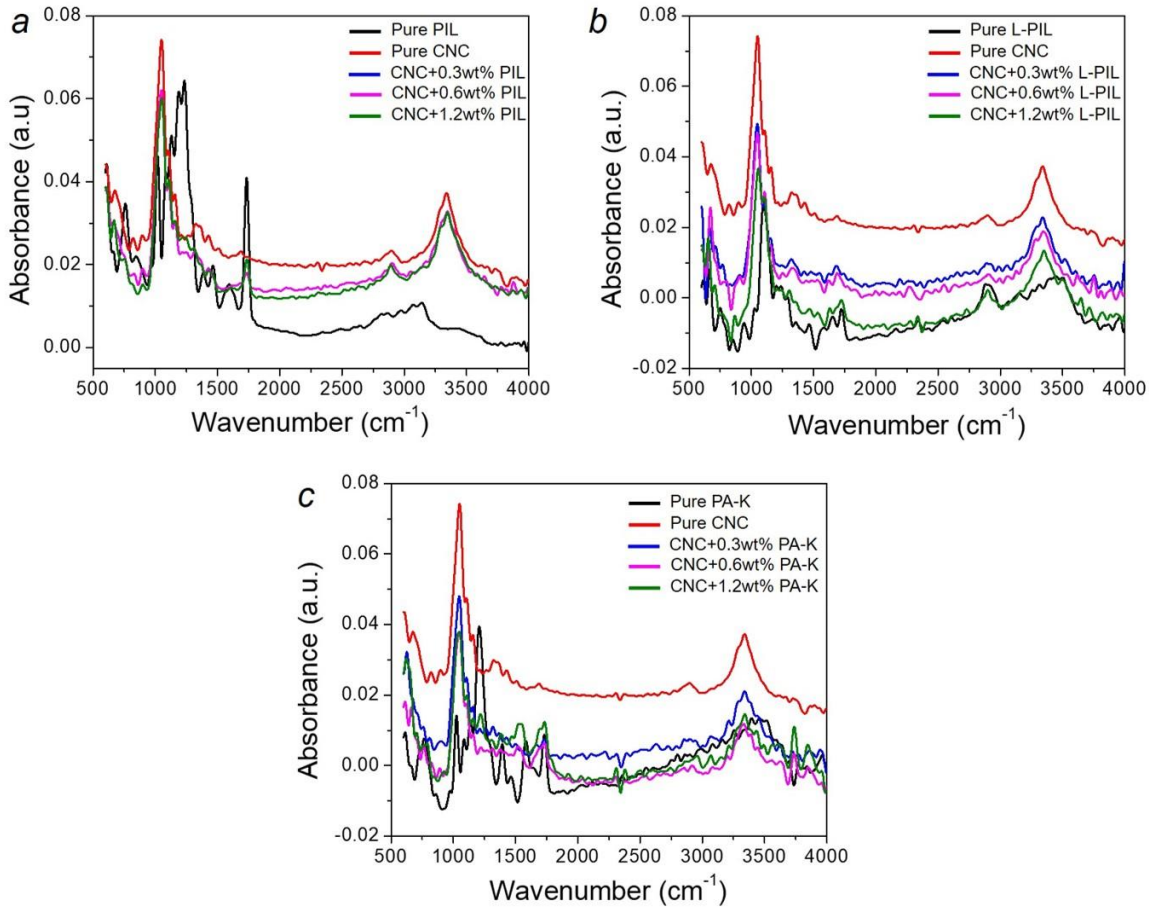

Figure S7.5. FTIR spectra of (a) CNC/PIL, (b) CNC/L-PIL, and (c) CNC/PA-K at 600-4000 cm^{-1}. CNC concentration for all samples is 3 wt%.

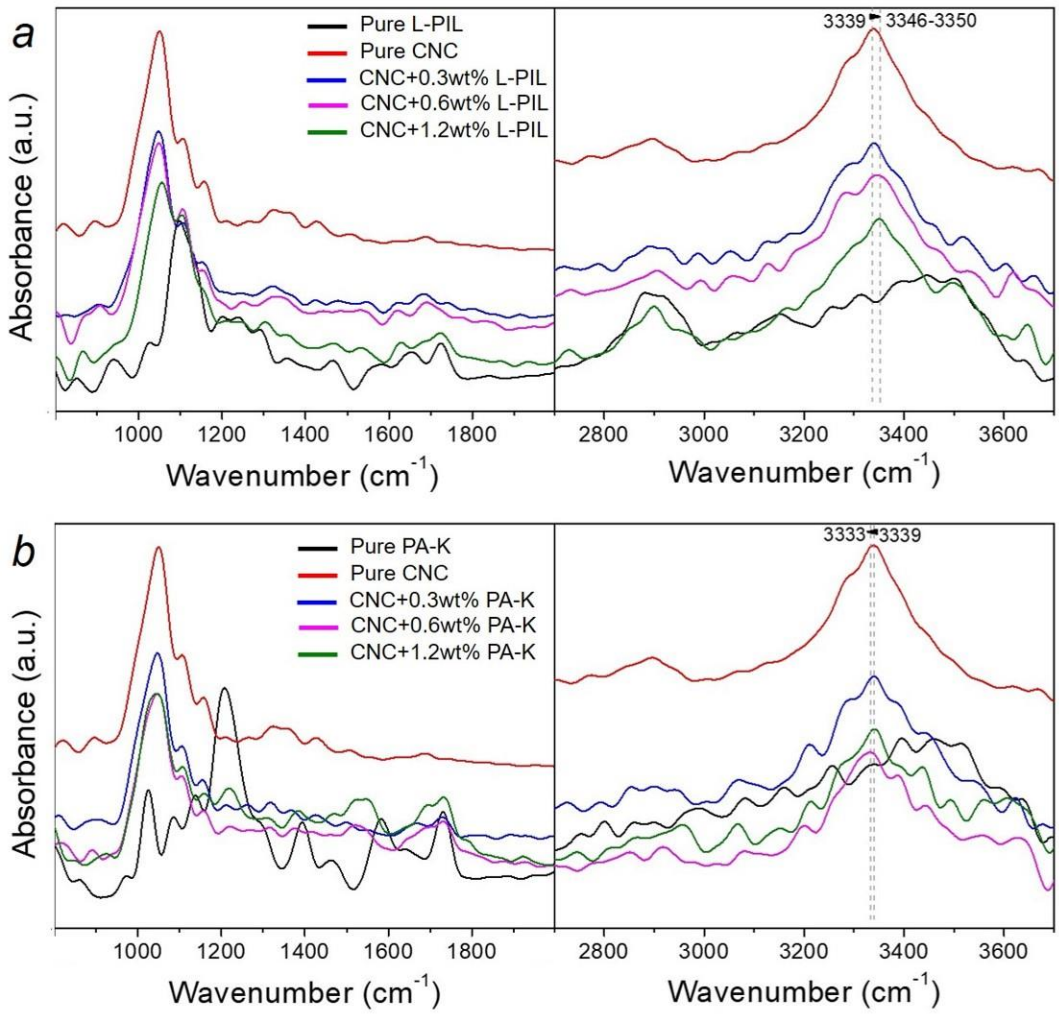

Figure S7.6. FTIR spectra of (a) CNC/L-PIL and (c) CNC/PA-K at 800-2000 cm^{-1} (left) and 2700-3700 cm^{-1} (right). CNC concentration for all samples is 3 wt%.

AFM Images of CNC/PIL, CNC/L-PIL and CNC/PA-K Films

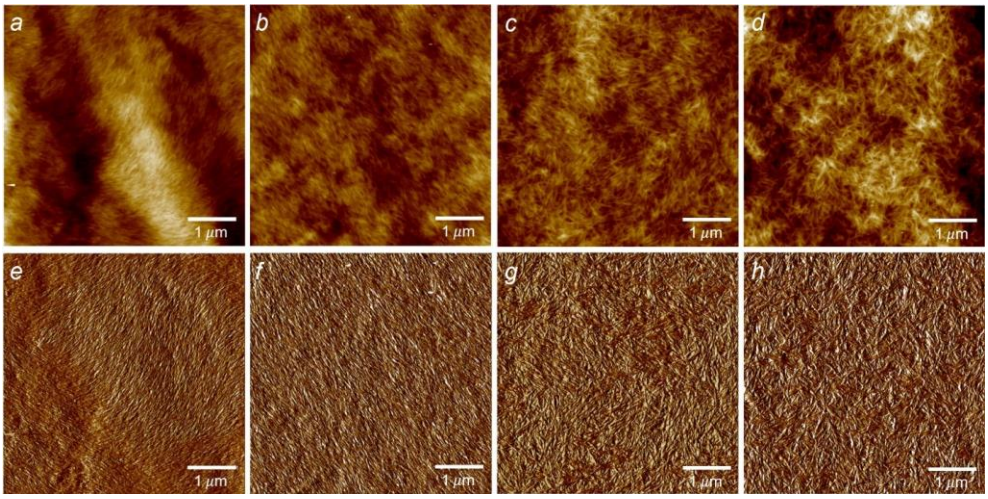

Figure S7.7. 5μm x 5μm AFM topography (a-d) and phase (e-h) images of (a,e) pure CNC, (b-d and f-h) CNC/PIL films with different ionic polymer contents: (b,f) 0.3 wt%, (c,g) 0.6 wt%, and (d,h) 1.2 wt%. CNC concentration is 3 wt% for all samples. Z scale for (a-d) and (e-h) is 80 nm and 30^{o}.

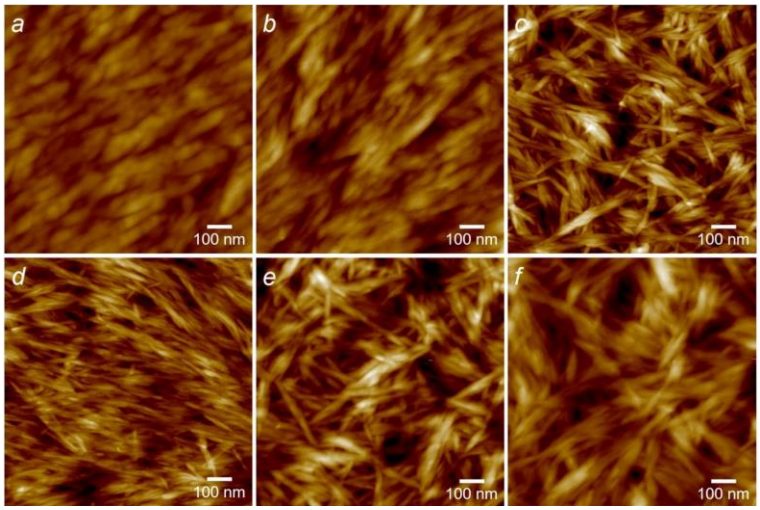

Figure S7.8. 1μm x 1μm AFM topography images of (a-c) CNC/L-PIL and (d-f) CNC/PA-K films with different contents of ionic polymers: (a,d) 0.3 wt%, (b,d) 0.6 wt%, and (c,f) 1.2 wt%. CNC concentration is 3 wt% for all samples. Z scale is 30 nm for (a-e) and 50 nm for (f).

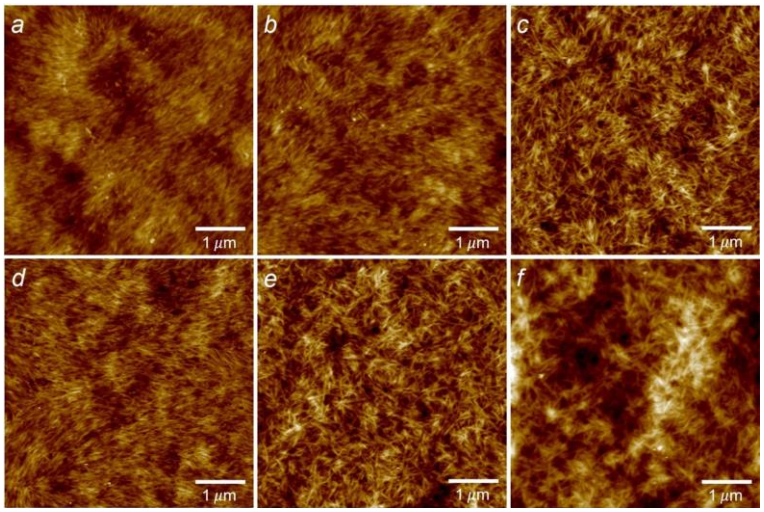

Figure S7.9. 5μm x 5μm AFM topography images of (a-c) CNC/L-PIL and (d-f) CNC/PA-K films with different contents of ionic polymers: (a,d) 0.3 wt%, (b,d) 0.6 wt%, and (c,f) 1.2 wt%. CNC concentration is 3 wt% for all samples. Z scale is 50 nm for (a-e) and 100 nm for (f).

CD Analysis of CNC/PIL, CNC/L-PIL and CNC/PA-K Samples

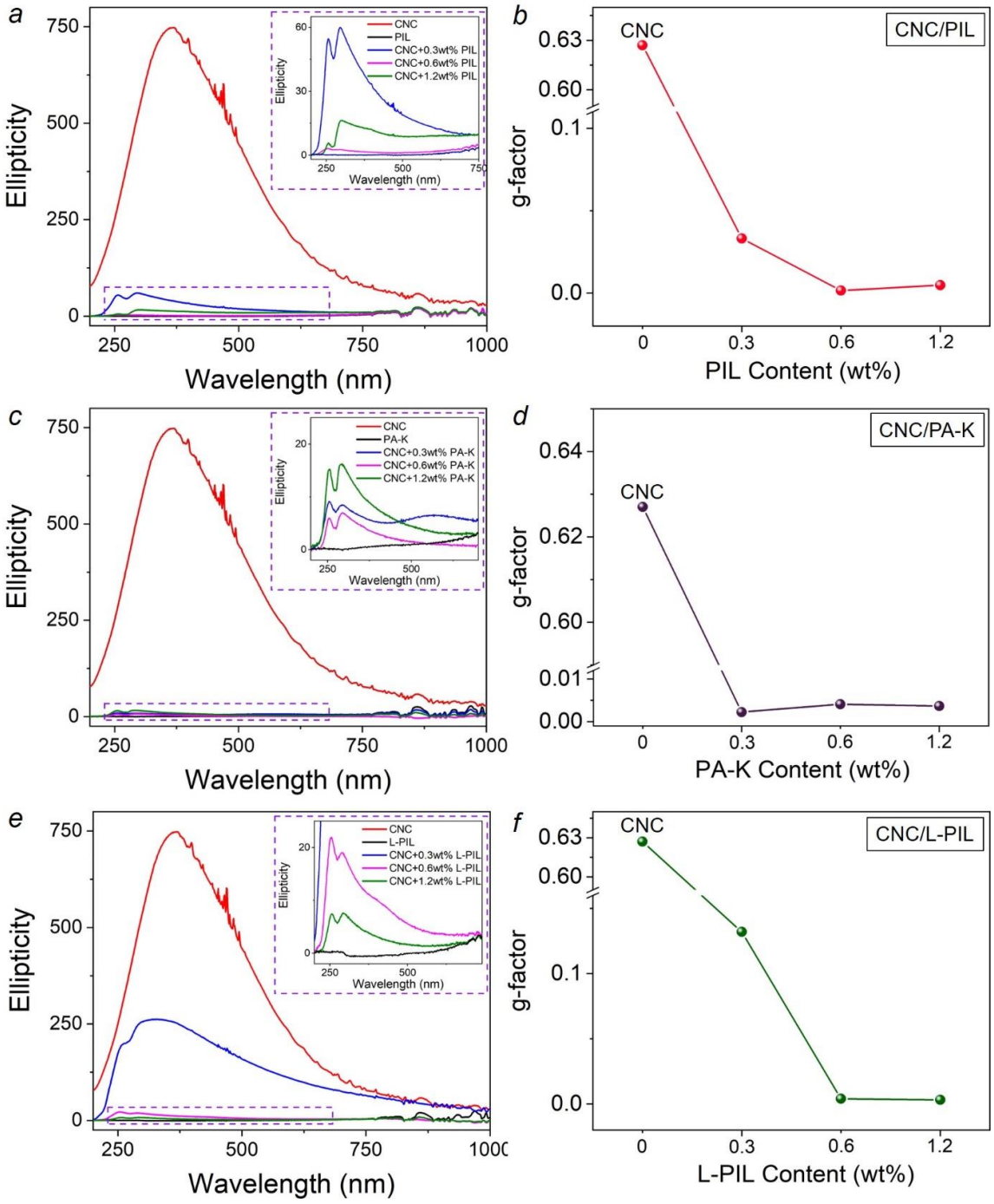

Figure S7.10. (a,c,e) CD spectra and (b,d,f) g-factor for (a,b) CNC/PIL, (c,d) CNC/PA-K, and (e.f) CNC/L-PIL composites. CNC concentration for all samples is 3 wt%.

The g-factor, anisotropy factor, is a parameter presented as a ratio of the strength of CD to the strength of light absorption of a chiral sample at specific wavelengths.[446] that is employed to identify the enantiomeric purities of optically active materials.446 More specifically, the g-factor displays the difference of the absorption of the sample against left- and right-circularly polarized lights obtained from CD measurements at a given absorption band.[447, 448] Additionally, the CD spectroscopy analysis is performed to investigate how incorporation of ionic polymers with different architectures (Linear vs Hyperbranched) and counterions (K^+ or IM^+) affects the alignment of CNC. CD spectra of the composites of CNC and imidazolium-containing hyperbranched polymeric ionic liquid (PIL) exhibit peaks with positive ellipticity, indicating that the composites retain a left-handed helical structure (Figure S7.10a). The g-factor rapidly decreases as the PIL content increases to 0.6 wt%, illustrating that anisotropic CNC becomes isotropically aligned. Interestingly, when the PIL content further increases to 1.2 wt%, g-factor of the composite increases by 206% compared to the composite of 0.6 wt% PIL, demonstrating that the extent of anisotropic alignment of CNC increases with further PIL incorporation (Figure S7.10b). As evident above, AFM images show that CNC ordering changes from anisotropic to isotropic with PIL (Figures S7.7). The g-factor and CD spectra of the composites combined with AFM images provide a more detailed picture regarding the alignment of CNC in the composites. The anisotropic alignment has partially maintained with decreased extent in the composite even with the incorporation of 1.2 wt% PIL. An extent of anisotropic alignment of CNC increased in the composites when PIL content is higher than 0.6 wt%. The samples with different ionic polymers (L-PIL and PA-K) also present the similar trend of CD spectra and g-factor (Figure S7.10c-f). All composites depict the weak positive spectra in the CD spectra, meaning that left-handed structure is preserved. The g-factor of CNC/PIL-K rapidly decreases until 0.3 wt% incorporation of PA-K (Figure S7.10d). In the case of CNC/L-PIL samples, it shows continuous decrease of g-factor, meaning that extent of CNC anisotropic alignment in the composites continuously decreases with continuous addition of L-PIL (Figure S7.10f). However, it is worth noting the highest extent of CNC anisotropic alignment is observed at the 0.3 wt% incorporation of L-PIL compared to those for the samples with the hyperbranched ionic polymers (PIL and PA-K), followed by rapid decreases. Thus, all these experiments

demonstrate that incorporation of the ionic polymers with hyperbranched architecture has stronger power to decrease the extent of anisotropic alignment of CNC in the ionogel composite, giving rise to porous structures with partial anisotropic alignment.

Experimental Section for Circular Dichroism.

CD spectra are collected using an Applied Photophysics Chirascan™-plus with films mounted perpendicularly to the beam path and using solid composite in a wavelength range between 200 and 1000 nm. For sample preparation, 20 μL of solutions were deposited and air-dried on a quartz (1 cm x 0.5 cm).

The g- factor is obtained using following expression:

$$g_{abs} = \frac{\Delta A}{A}$$

where ΔA is absorbance difference between left and right circularly polarized light and A is absorbance band at the CD peak.[449,450,451]

TGA and DSC Analysis of CNC/PIL Samples

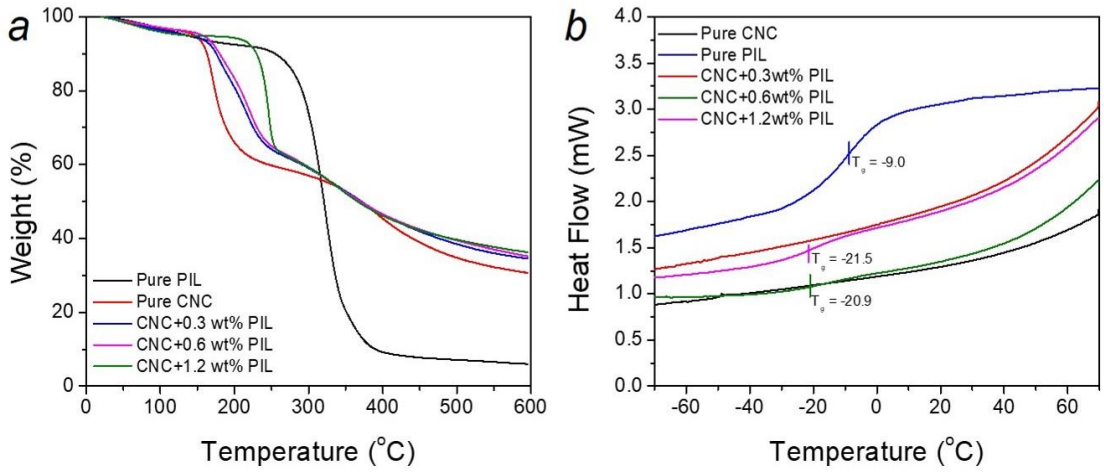

Figure S7.11. (a) TGA and (b) DSC curves of CNC/PIL with different PIL contents. DSC curves were collected during second heating cycle. CNC concentration for all samples is 3 wt%.

Photos of CNC/PIL Ionogels

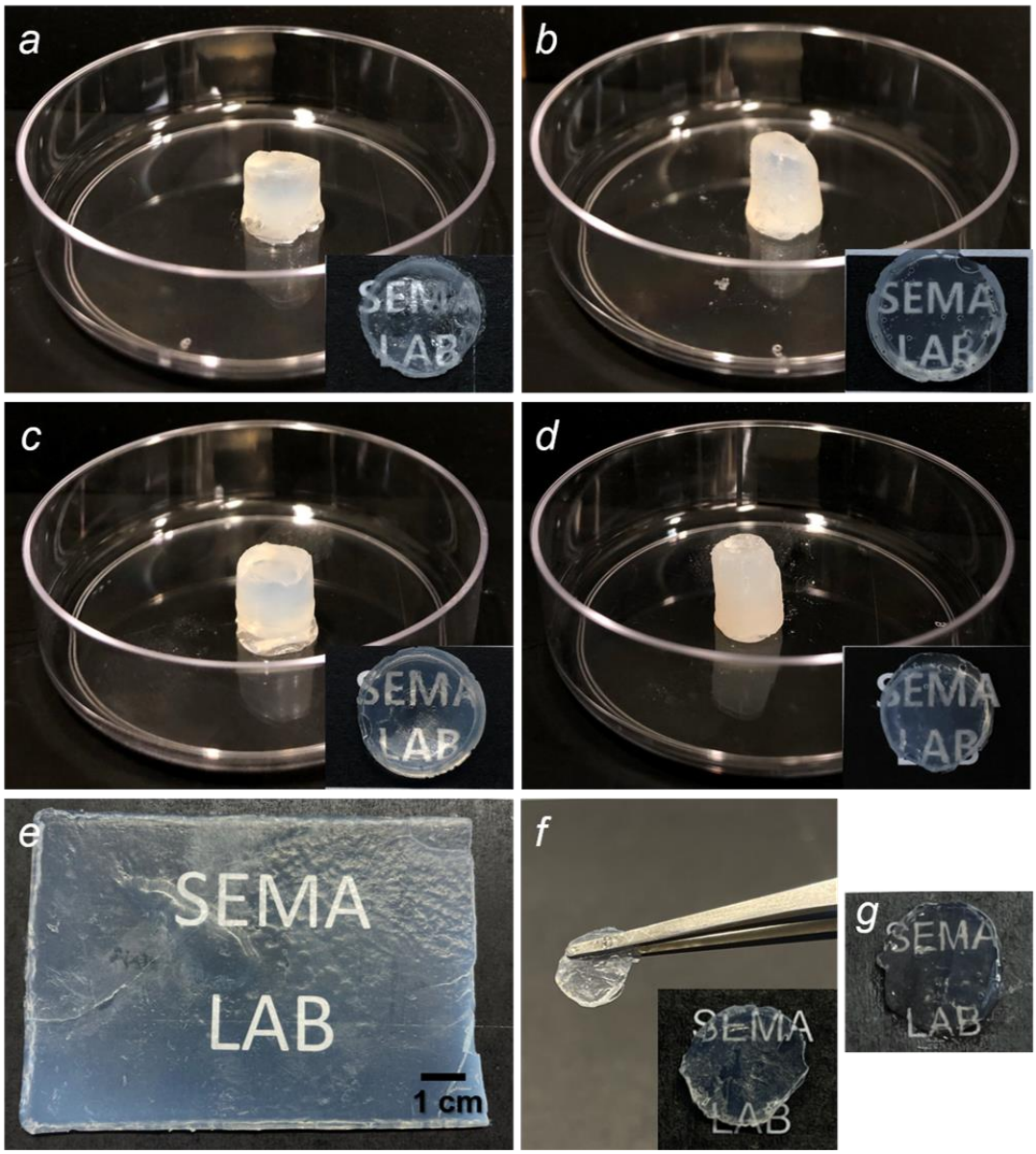

Figure S7.12. (a-e) Photos of (a) CNC/PIL-0.0, (b) CNC/PIL-0.5, (c) CNC/PIL-1.0, (d) CNC/PIL-2.0 ionogels, and (e) rectangular-shaped CNC/PIL-1.0 ionogels (10 cm x 7 cm x 0.2 cm). Inserts of (a-d) show the ionogels with height of ~1 mm. (f-g) CNC/PIL ionogels containing different types of ionic liquids: (f) bis(trifluoromethylsulfonyl)imide lithium salt and (g) 1-butyl-3-methylimidazolium bromide.

XPS Analysis of CNC/PIL Gels in Ethanol Without Adding Ionic Liquids

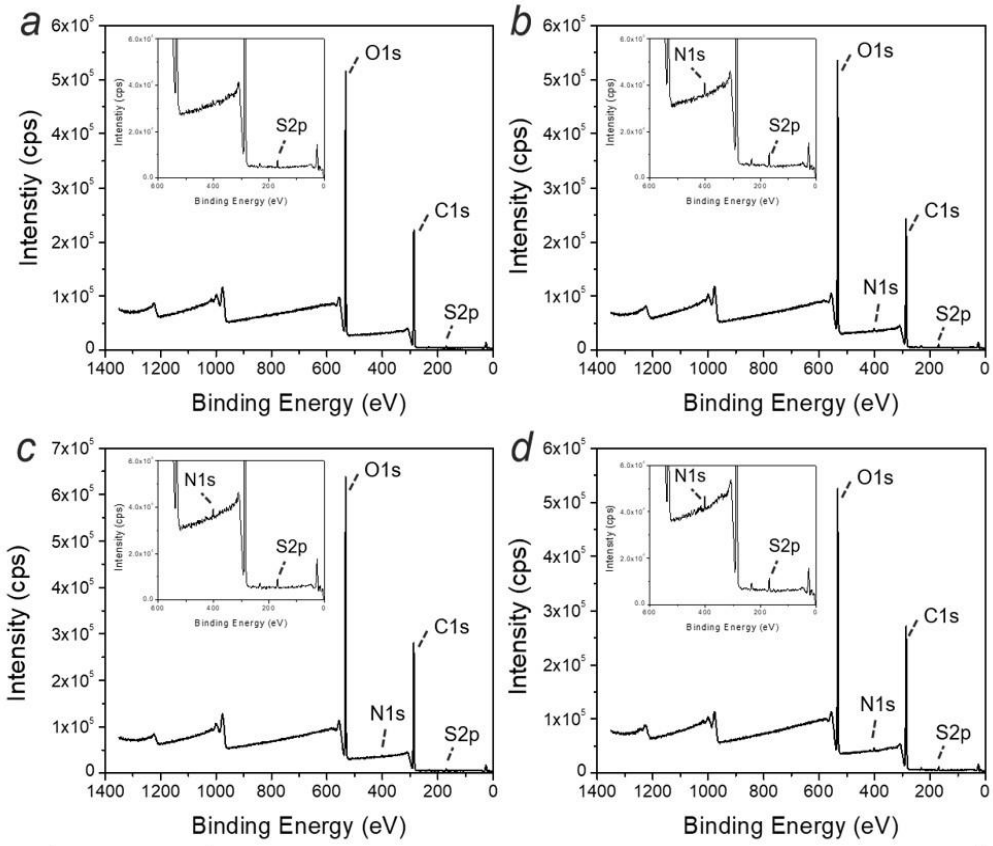

e

PIL Content (wt%)	Atomic Concentration (%)			
	C1s	O1s	S2p	N1s
0.0	40.2±2.5	59.2±2.5	0.6±0.1	0.0±0.0
0.3	57.8±1.4	41.0±1.8	0.7±0.1	0.5±0.4
0.6	55.6±0.2	43.3±0.1	0.6±0.0	0.5±0.1
1.2	60.6±1.4	37.9±1.5	0.8±0.1	0.7±0.1

Figure S7.13. (a-d) XPS survey spectra and (e) elemental compositional data of the CNC/PIL gels in ethanol collected before adding ionic liquid. The PIL contents of the samples are 0 wt%, 0.3 wt%, 0.6 wt%, and 1.2 wt%, for (a), (b), (c) and (d), respectively. Inserts of (a-d) show the spectra in the binding energy range of 0-600 eV. CNC concentration for all samples is 3 wt%.

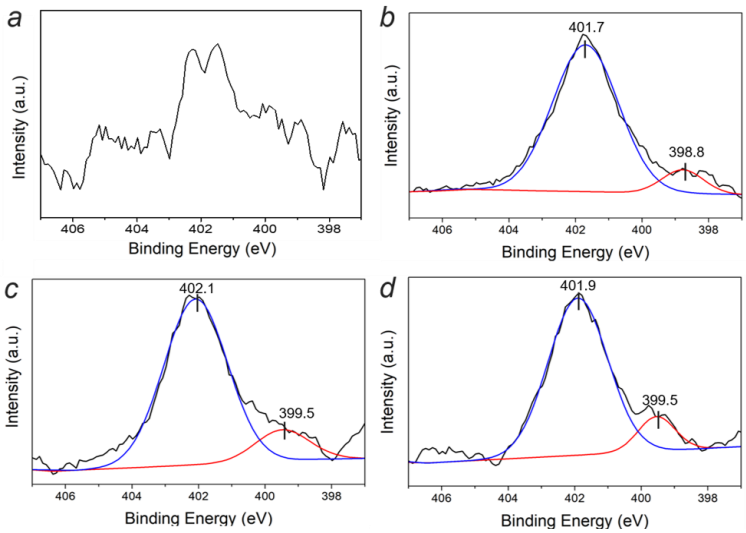

Figure S7.14. High-resolution N1s spectra of CNC/PIL gels in ethanol collected before adding ionic liquid. The PIL contents of the samples are 0 wt%, 0.3 wt%, 0.6 wt%, and 1.2 wt%, respectively. CNC concentration for all samples is 3 wt%.

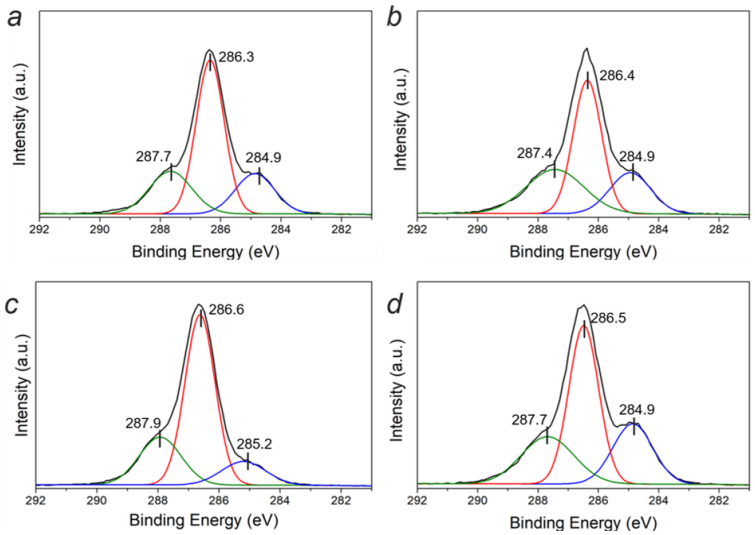

Figure S7.15. High-resolution C1s spectra of CNC/PIL gels in ethanol collected before adding ionic liquid. The PIL contents of the samples are 0 wt%, 0.3 wt%, 0.6 wt%, and 1.2 wt%, respectively. CNC concentration for all samples is 3 wt%.

The XPS survey spectra of the samples collected before adding the ionic liquid show peaks corresponding to C1s, O1s and S2p (Figure S7.13). The high resolution C1 spectra of all samples exhibit three main chemical environments of carbon, having one major peak at

286.5 eV related to C-O or C-N bonds, a peak at 285 eV related to C-C bonds and a peak at 288 eV related to O-C-O, C=O or C=N bonds (Figure S7.15).[452,453] Only for the samples prepared with PIL, a major peak at 402 eV assigned to charged imidazolium rings was found in the high-resolution N1 spectra, confirming the existence of PIL.[454] A small peak at 400 eV was also observed in the high-resolution N1 spectra, which suggests the presence of neutral nitrogen (imide) (Figure S7.14).[452,455] This peak is attributed to the contribution of the imidazolium rings of PIL to the formation of intermolecular interactions with CNC, resulting in partial neutralization of imidazolium ions.

Optical Transmittance of CNC/PIL Ionogels

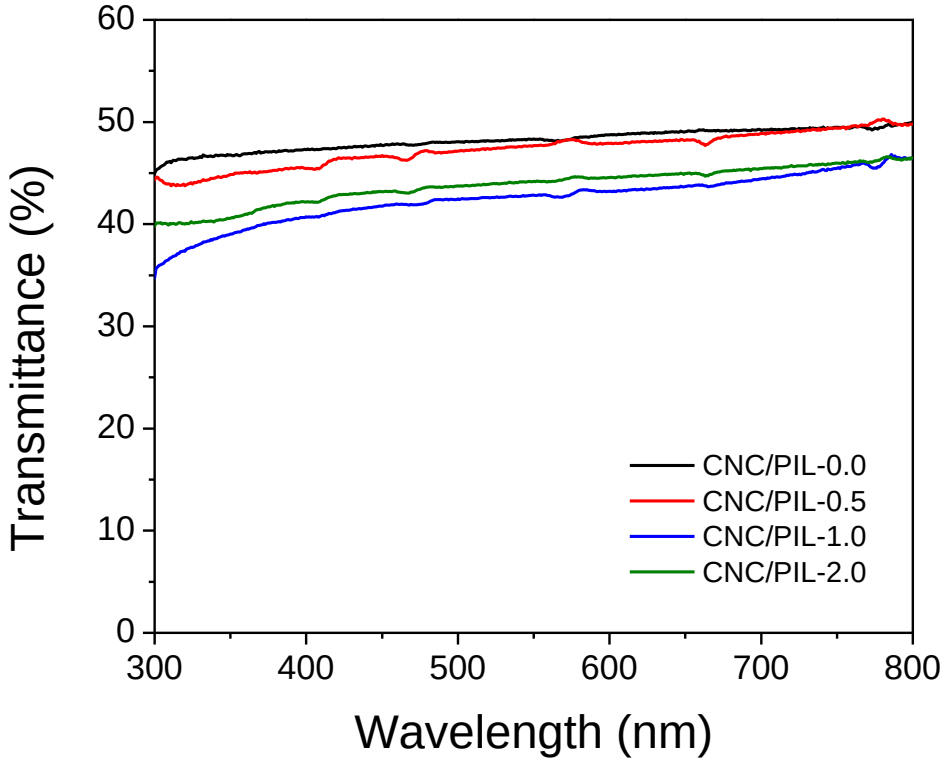

Figure S7.16. Optical transmittance of CNC/PIL ionogels with different PIL contents.

XXPS Analysis of CNC/PIL Ionogels

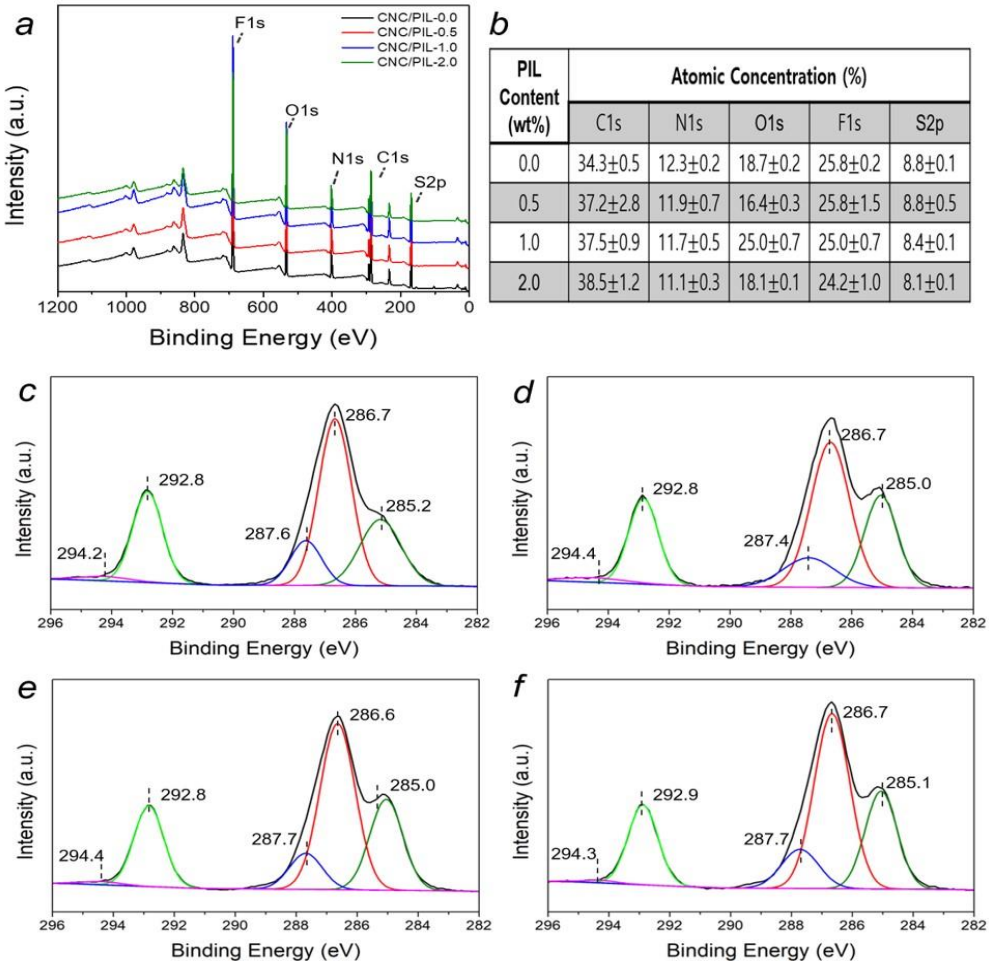

PIL Content (wt%)	Atomic Concentration (%)				
	C1s	N1s	O1s	F1s	S2p
0.0	34.3±0.5	12.3±0.2	18.7±0.2	25.8±0.2	8.8±0.1
0.5	37.2±2.8	11.9±0.7	16.4±0.3	25.8±1.5	8.8±0.5
1.0	37.5±0.9	11.7±0.5	25.0±0.7	25.0±0.7	8.4±0.1
2.0	38.5±1.2	11.1±0.3	18.1±0.1	24.2±1.0	8.1±0.1

Figure S7.17. (a) XPS survey spectra, (b) elemental compositional data and (c-f) high resolution C1s spectra of the CNC/PIL ionogels with different PIL contents: (c) CNC/PIL-0.0, (d) CNC/PIL-0.5, (e) CNC/PIL-1.0, and (f) CNC/PIL-2.0 ionogels.

The XPS survey spectra of all ionogels exhibit peaks of C1s, N1s, O1s, F1s, and S2p, confirming the presence of the ionic liquid, [EMIM][TFSI] (Figure S7.17a-b). The peak related to CF_3 of the [TFSI] anion was seen at a lower binding energy (292.8 eV) than that of neat [EMIM][TFSI] at 293.2 eV.[404] The peak corresponding to the end of ethyl groups of [EMIM] cations (C1s aliphatic chain) was also shifted toward a lower binding energy (285.0-285.2 eV) than that of neat IL at 285.6 eV (Figure S7.17c-f).[404] Similarly, N1s peaks related to the [TFSI] anion (at 399.4 eV) and to the [EMIM] cation (at 402.0 eV) were found at lower binding energy compared to those of neat [EMIM][TFSI] (399.7 eV and

402.3 eV, respectively) (Figure S7.18a).[404] These peak shifts suggest that ILs form interactions with CNC/PIL upon confinement.

Experimental Section for X-ray Photoelectron Spectroscopy (XPS).

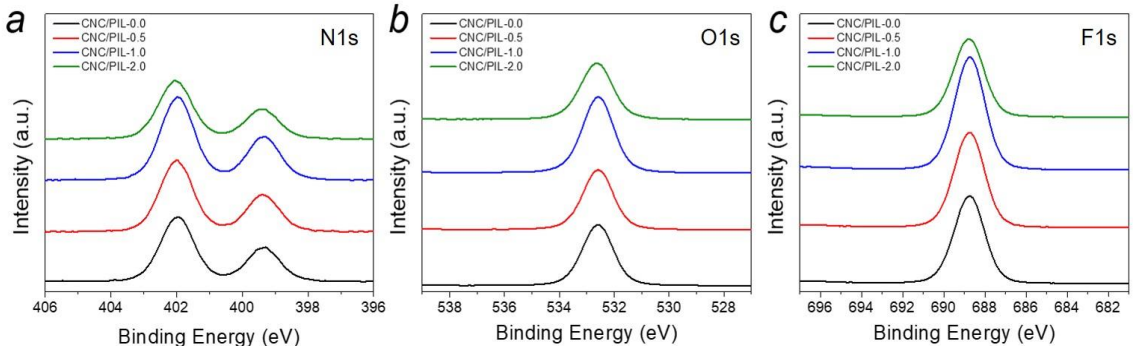

Figure S7.18. High resolution (a) N1s, (b) O1s and (c) F1s spectra of the CNC/PIL ionogels with different PIL contents.

XPS analysis was performed to determine the surface composition of the CNC/PIL samples collected before and after adding ionic liquids using a Thermo K-Alpha XPS instrument. Dried CNC/PIL samples were used for XPS analysis. Survey spectra were taken with two scans at 1 eV step size while high resolution spectra were averaged over five scans. OriginPro8.5 was used to deconvolute and fit the high-resolution spectra via the Fit Peaks (Pro) function.

FTIR Analysis of CNC/PIL Ionogels

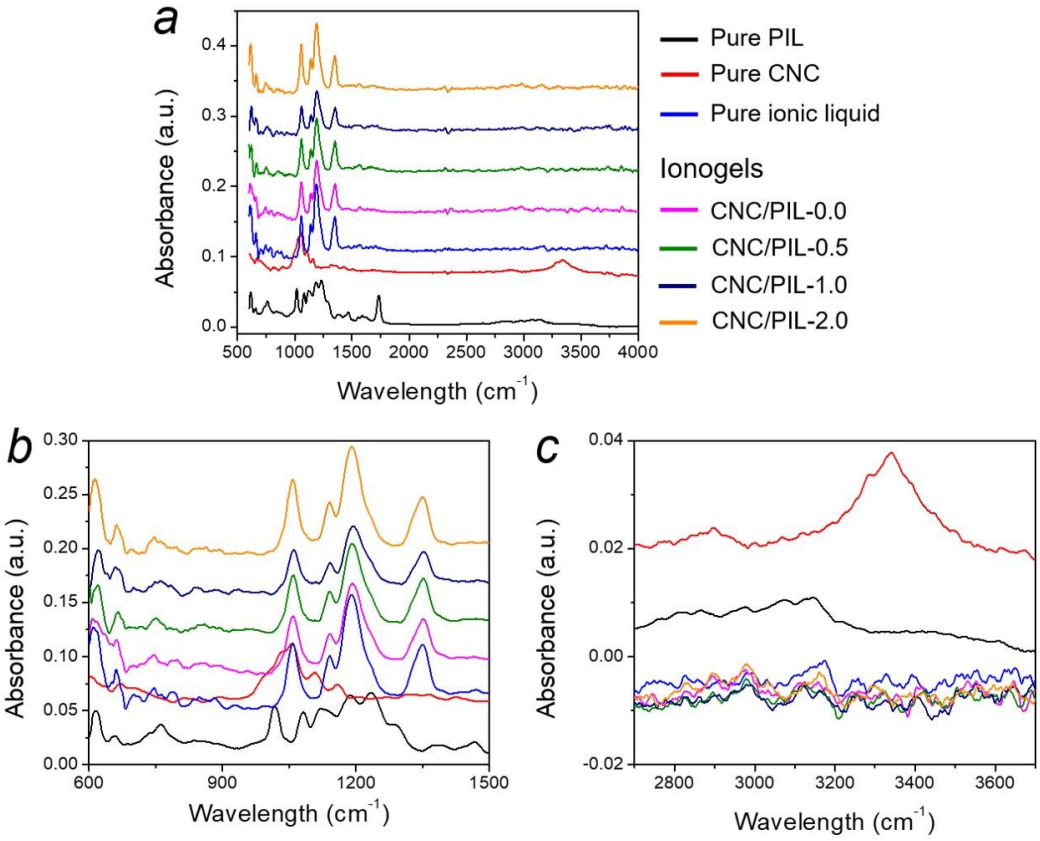

Figure S7.19. FTIR spectra of CNC, PIL, ionic liquid and CNC/PIL ionogels at (a) 600-4000 cm^{-1}, (b) 600-1500 cm^{-1} and (c) 2700-3700 cm^{-1}.

FTIR spectra of CNC/PIL ionogels are dominated by ionic liquids (ILs), [EMIM][TFSI] due to the high ionic liquid content. The spectra of the ionogels are almost the same as that of pure ionic liquids. The characteristic peaks for the ionic liquids are observed, including a SO_2 antisymmetric bending (609 cm^{-1}), a S–N–S bending (650 cm^{-1}) and a CF_3 symmetric bending (746 cm^{-1}). In the region between 1000 and 1400 cm^{-1}, all the spectra show a S–N–S antisymmetric stretching at 1057 cm^{-1}, a SO_2 symmetric stretching at 1132 cm^{-1}, CF_3 antisymmetric stretching at 1190 cm^{-1} and SO_2 antisymmetric stretching at 1351 cm^{-1}.[456]

XRD Analysis of CNC/PIL Ionogels

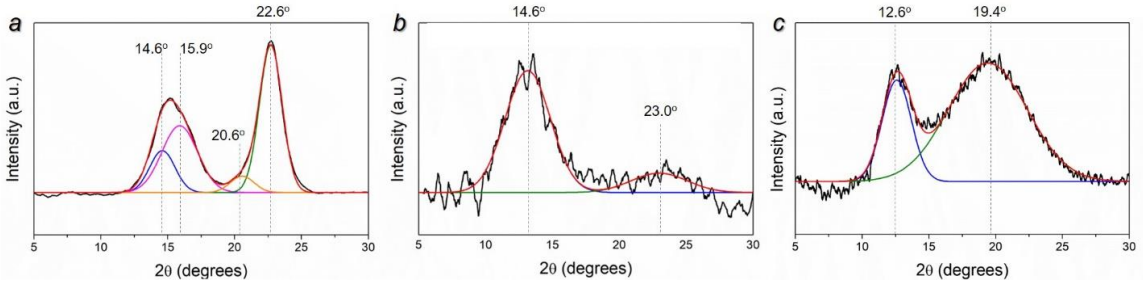

Figure S7.20. XRD spectra and the corresponding peak deconvolution for (a) CNC, (b) PIL and (c) ionic liquid, [EMIM][TFSI].

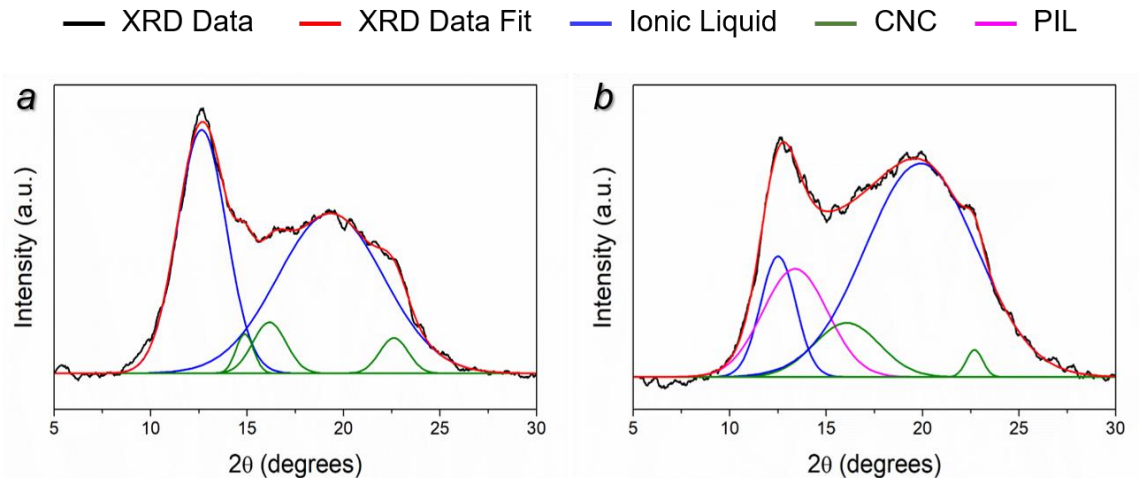

Figure S7.21. XRD spectra and the corresponding peak deconvolution for (a) CNC/PIL-0.0 and (b) CNC/PIL-2.0 ionogels.

Experimental Section for X-ray Diffraction Analysis

XRD analysis was performed to investigate the physical state of the CNC/PIL ionogels using a Malvern Panalytical Empyrean instrument. XRD spectra were collected in the 2θ range of 5-30^{o} with step size of 0.026^{o} and time per step of 152s. OriginPro8.5 was used to deconvolute and fit the XRD spectra via the Fit Peaks (Pro) function.

SEM Images of CNC/PIL Aerogels

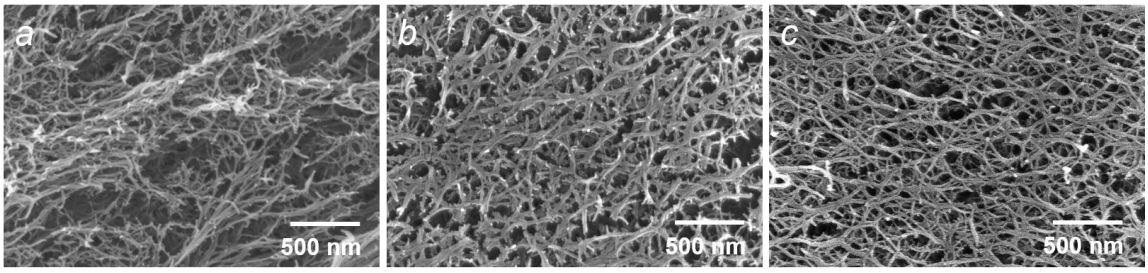

Figure S7.22. SEM images of CNC/PIL aerogels with different PIL contents: (a) 0 wt%, (b) 0.3 wt%, and (c) 0.6 wt%.

AFM Images of CNC/PIL Ionogels

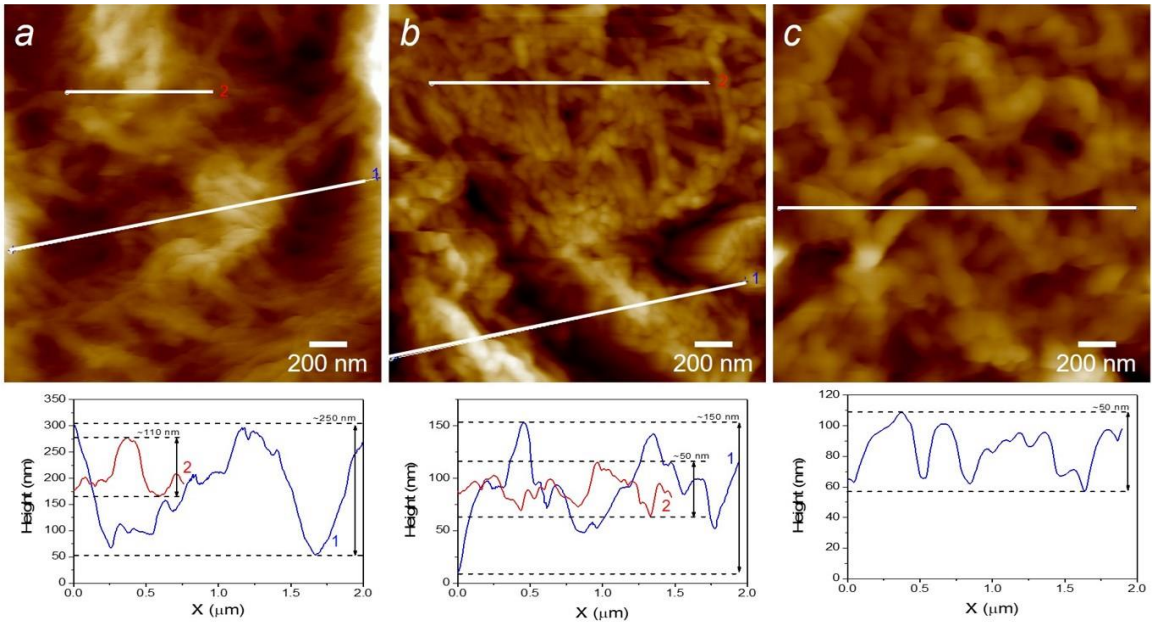

Figure S7.23. AFM topography images and corresponding height profiles of (a) CNC/PIL-0.0, (b) CNC/PIL-0.5, and (c) CNC/PIL-1.0 ionogels. Z scale is 450 nm for (a) and 150 nm for (b-c).

Compressive Mechanical Test of CNC/PIL Ionogels

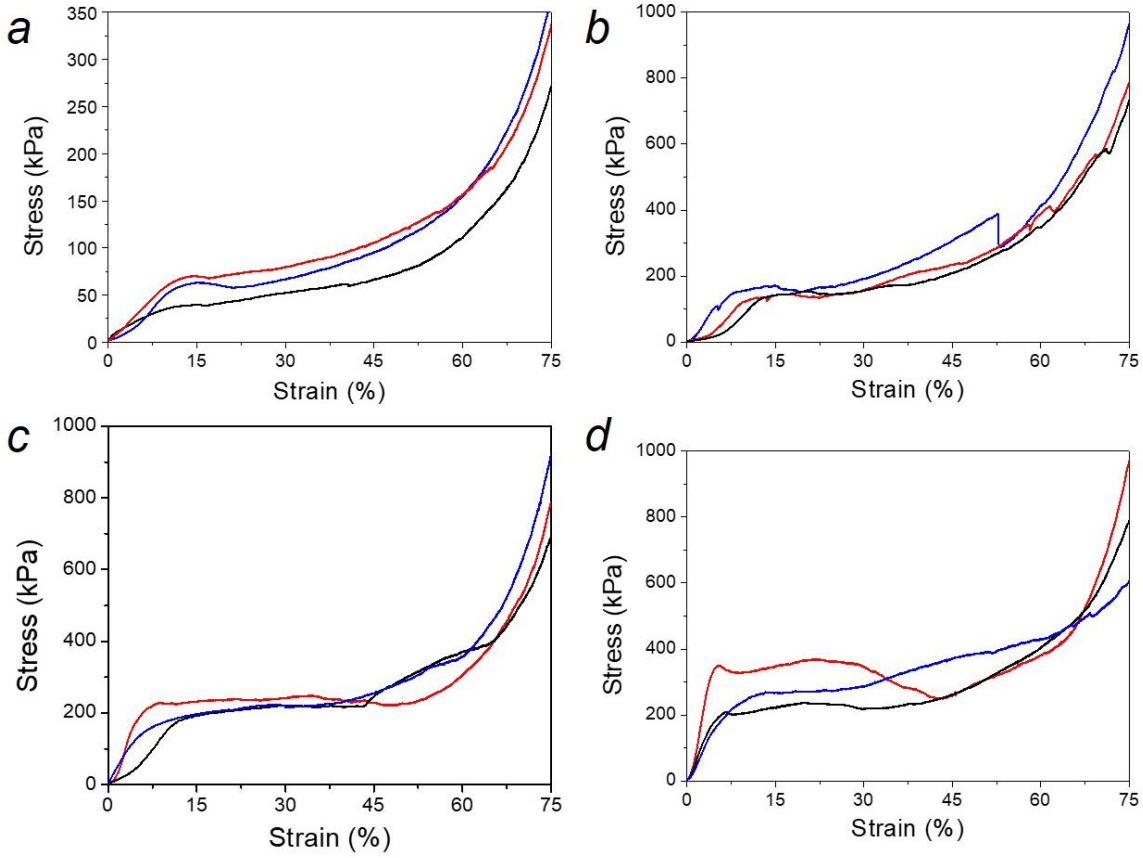

Figure S7.24. Compressive stress-strain curves of (a) CNC/PIL-0.0, (b) CNC/PIL-0.5, (c) CNC/PIL-1.0 and (d) CNC/PIL-2.0 ionogels.

Compressive Mechanical Test of CNC/PIL Gels in Ethanol Without Adding Ionic Liquids

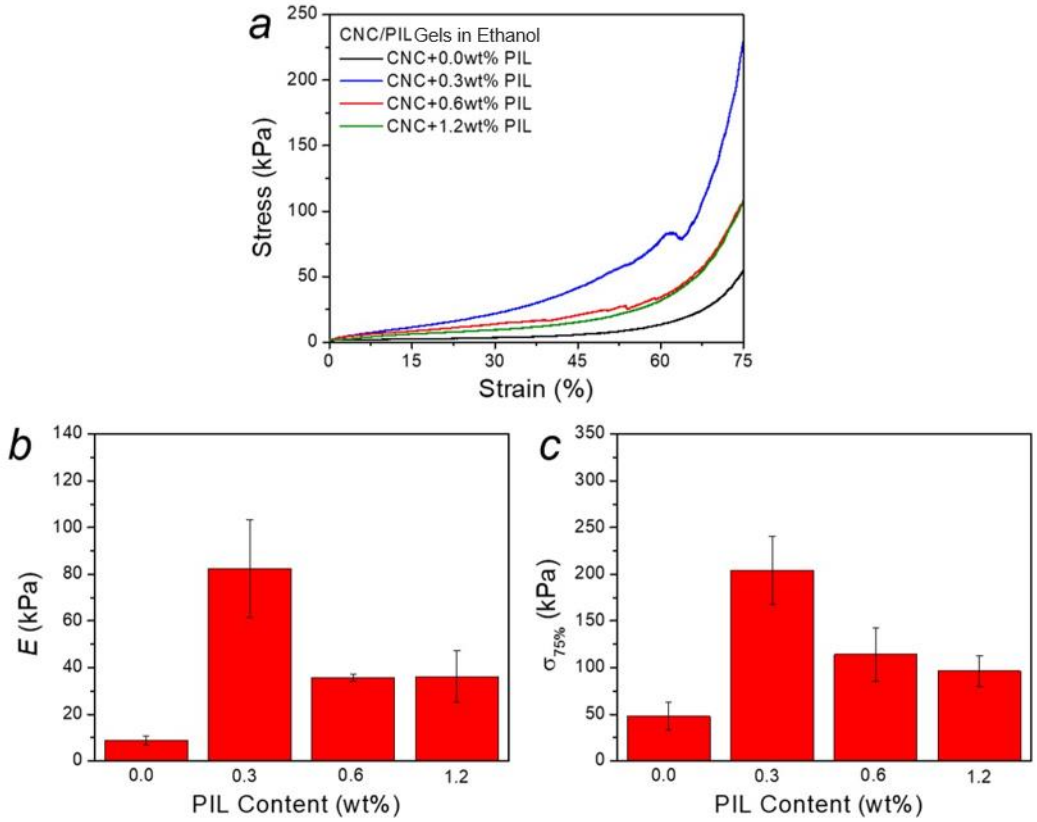

Figure S7.25. (a) Representative compressive stress-strain curves, (b) Young's modulus (*E*), and (c) compressive stress at 75% strain ($\boldsymbol{\sigma}_{75\%}$) of CNC/PIL gels in ethanol with different PIL contents collected before adding ionic liquids. CNC concentration for all samples is 3 wt%.

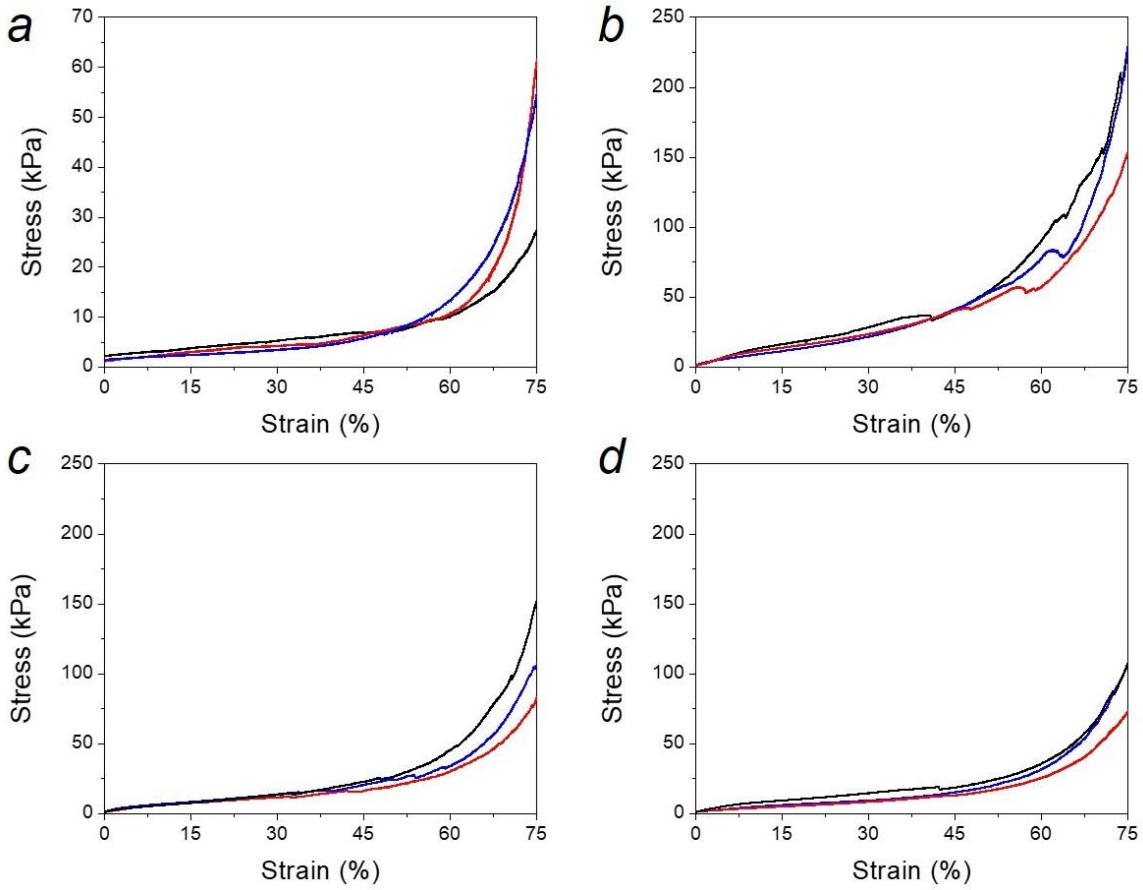

Figure S7.26. Compressive stress-strain curves of CNC/PIL gels in ethanol with different PIL contents collected before adding ionic liquids: (a) 0 wt%, (b) 0.3 wt%, (c) 0.6 wt% and (d) 1.2 wt%. CNC concentration of all samples is 3 wt%.

Nano-Dynamic Mechanical Analysis (nano-DMA) of CNC/PIL Ionogels

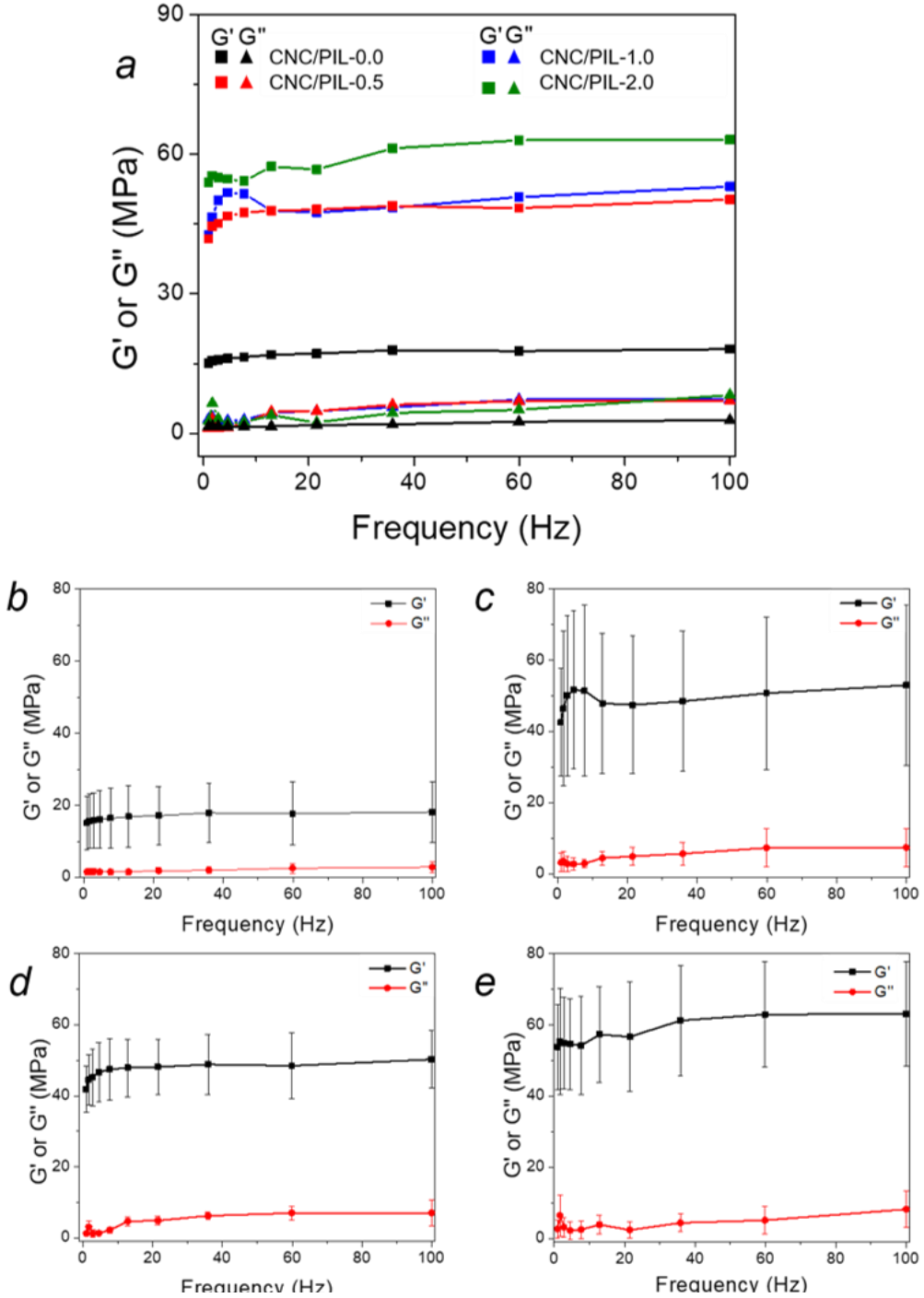

Figure S7.27. Isothermal frequency sweep of storage (G') and loss (G'') moduli of (a) CNC/PIL ionogels with various PIL contents, (b) CNC/PIL-0.0, (c) CNC/PIL-0.5, (d) CNC/PIL-1.0, and (e) CNC/PIL-2.0 ionogels.

Experimental Session for Nano-Dynamic Mechanical Analysis (nano-DMA).

AFM-based nanoscale DMA (nano-DMA) was performed using an ICON Dimension microscope (Bruker). AFM-based nano-DMA optimized probes (RTESPA 150-30) were used with a pre-calibrated spring constant of 5 N/m and tip radius of 33 nm. Nanoscale viscoelastic properties of CNC/PIL ionogels were measured at ambient temperature with a preload of 10 nN as a function of frequency of 0.1-100 Hz. At least 20 points were selected for each sample to calculate average storage and loss moduli. All data for nano-DMA were analyzed using Bruker Nanoscope Analysis 2.0 software.

Ionic Conductivity of CNC/PIL Ionogels at Different Temperatueres

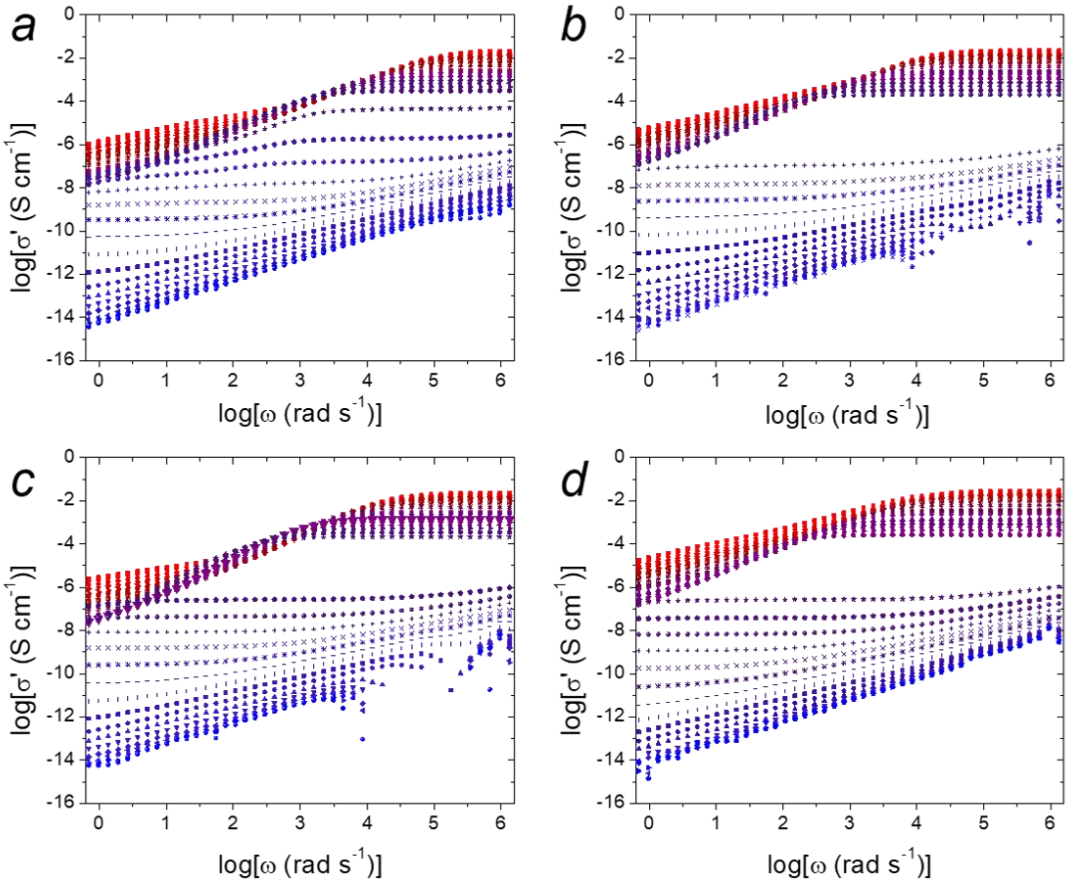

Figure S7.28. The frequency dependence of the real part of the complex conductivity (***σ***'), plotted at different temperatures (363K to 163K) for (a) CNC/PIL-0.0, (b) CNC/PIL-0.5, (c) CNC/PIL-1.0, and (d) CNC/PIL-2.0 ionogels. Red and blue color indicates high and low temperatures, respectively.

Table S7.1. Bulk and substance densities and densification degree of CNC/PIL Gels in Ethanol

PIL Content (wt%)	Bulk density (g/cm^3)	Substance density (g/cm^3)	Densification (%)
0.0	0.83±0.02	0.81	3.2
0.3	0.86±0.03	0.82	4.6
0.6	0.90±0.04	0.81	11.8
1.2	0.99±0.02	0.81	21.9

Table S7.2. Elastic moduli and ionic conductivities of solid electrolytes for Figure 7.7.

Electrolyte Type	Material	Elastic Modulus (MPa)	Ionic Conductivity (mS/cm)	References
Polymer Electrolytes	Poly(ethylene Oxide) (PEO)	780[b]	0.0000059	457
		690[b]	0.000007	
		77[b]	0.0000095	
		250[b]	0.000019	
		87[b]	0.000026	
		140[b]	0.000029	
		110[b]	0.000032	
		43[b]	0.00013	
		30[b]	0.00026	
		25[b]	0.00053	
		15[b]	0.0011	

Table S7.2. continued.

Electrolyte Type	Material	Elastic Modulus (MPa)	Ionic Conductivity (mS/cm)	References
Polymer Electrolytes	Poly(ethylene Oxide) (PEO)	15[b]	0.0013	457
		15[b]	0.0017	
	PEO/LiTFSI	6.8[a]	0.000079	458
	PEO	189[b]	0.000153	459
	PEO/$LiCF_3SO_3$	63[b]	0.0002	
		48[b]	0.000254	
		6[b]	0.000623	
		15[b]	0.001	
	PEO/$LiCF_3SO_3$/Polyethylene glycol (PEG)	6[b]	0.00873	
		12[b]	0.0113	
		13[b]	0.0133	

Table S7.2. continued.

Electrolyte Type	Material	Elastic Modulus (MPa)	Ionic Conductivity (mS/cm)	References
Polymer Electrolytes	PEO/$LiCF_3SO_3$/Polyethylene glycol (PEG)	8[b]	0.0171	459
	PEO/LiCF3SO3/dioxyphthalate (DOP)	8[b]	0.0337	
		7[b]	0.522	
		4[b]	0.593	
		6[b]	0.76	
	PEO/LiTFSI	15[a]	3.5475E-06	460
	poly(vinylidene fluoride-co-hexafluoropropylene) (PVDF-HFP)/LiTFSI	5.1[a]	0.00275	461
	PEO/LiTFSI	0.952[a]	0.0038	462

Table S7.2. continued.

Electrolyte Type	Material	Elastic Modulus (MPa)	Ionic Conductivity (mS/cm)	References
Polymer Electrolytes	Hydroxypropyl trimethylammonium bis(trifluoromethane) sulfonimide chitosan salt (HACC-TFSI)/PEO/LiTFSI	14.8[a]	0.0177	462
	Poly(ethylene glycol) methacrylate (PEGMA) /Poly(ethylene glycol) diacrylate (PEGDA)	338[a]	0.0376	463
	Poly(ethylene glycol) diglycidyl ether *a*-1,4-butanedithiol)) (PEGDGE-a-BDT)-MIM/TSFI/PVDF-HEP/LiTFSI	200,000[a]	0.01	464
	poly(diallyldimethylammonium) bis(trifluoromethanesulfonyl)imide)	~1520[a]	0.0146	465
Hybrid Organic-Inorganic Electrolytes	PEO/LiTFSI/exfoliated vermiculite sheets	13.1[b]	0.029	458

Table S7.2. continued.

Electrolyte Type	Material	Elastic Modulus (MPa)	Ionic Conductivity (mS/cm)	References
Hybrid Organic-Inorganic Electrolytes	PEO/$LiCF_3SO_3$/Al_2O_3	17[b]	0.0163	459
		16[b]	0.0202	
		10[b]	0.0365	
		11[b]	0.0864	
	PEO/LITFSI/$Li_{0.33}La_{0.557}TiO_3$ (LLTO) particles	38.4[b]	0.0235	460
	PEO/LITFSI/$Li_{0.33}La_{0.557}TiO_3$ (LLTO) framework	46[b]	0.204	
	PVDF-HFP/LiTFSI/ $Li_{6.5}La_3Zr_{1.5}Ta_{0.5}O_{12}$ (LLZTO)	12.8[a]	0.088	461
	PEGMA-PEGDA/Silica	529[b]	0.0677	463
	PEO/g-C_3N_4	65.7[a]	0.0023	466

Table S7.2. continued.

Electrolyte Type	Material	Elastic Modulus (MPa)	Ionic Conductivity (mS/cm)	References
Hybrid Organic-Inorganic Electrolytes	PEO/Hydroxyapatite (HAP)	53[a]	0.0105	467
	PEO/LiALTi$(PO_4)_3$	3.6[b]	0.052	468
	PEO/LiTFSI/PEG grafted polymer-like quantum dots	11.4[b]	0.0553	469
	Epoxy polymer/ $Li_{1.4}Al_{0.4}Ge_{1.6}(PO_4)_3$ (LAGP).	42,000[b]	0.16	470
Inorganic Electrolytes	Li_2S/P_2S_5	170,000[b]	0.31	471,472
	Li7La3Zr2O12 (LLZO)	156,000[c]	2.23E-05	445
	Li7-3xAlxLa3Zr2O12 (Al-LLZO)	162,000[c]	0.0208	
		163,000[c]	0.0221	
		161,000[c]	0.189	
		142,000[c]	0.245	

Table S7.2. continued.

Electrolyte Type	Material	Elastic Modulus (MPa)	Ionic Conductivity (mS/cm)	References
	Li7-yLz3Zr2-yTayO12 Ta-LLZO)	141,000[c]	0.297	
		124,000[c]	0.493	
		149,000[c]	0.68	

[a] Elastic modulus is measured using tensile mechanical test.

[b] Elastic modulus is measured using compressive mechanical test.

[c] Elastic modulus is measured using nanoindentation method.

Table S7.3. Solid content, elastic moduli, and ionic conductivities of ionogels for Figure 7.7.

Ionic liquid	Materials	Solid content (wt%)	Elastic Modulus (MPa)	Ionic Conductivity (mS/cm)	References
EMIM TFSI	Tetramethoxysilane (TMOS)	56.6	1[b]	0.0053	435
		15.4	0.0846[b]	4.9	
	Poly(2-phenylethyl methacrylate)-grafted cellulose nanocrystals	70	42[a]	0.00631	378
	PEO Epoxy	50 vol%	5.711[a]	0.09	473
		40 vol%	1.1[a]	0.78	
		43.3 vol%	0.525[a]	1.63	
	PEGDA	50	2.1[a]	0.375[a]	465
		50	0.96[a]	0.489	

Table S7.3. continued.

Ionic liquid	Materials	Solid content (wt%)	Elastic Modulus (MPa)	Ionic Conductivity (mS/cm)	References
EMIM TFSI	PEGDA	50	0.43[a]	0.498	465
		50	1.9[a]	0.569	
		50	1.8[a]	0.61	
		50	0.3[a]	0.631	
	PEDGA/PEGMA	50	1[a]	0.712	
		50	0.9[a]	0.743	
	PEGDA	50	2.04[a]	0.4	474
		25	0.77[a]	2.4	
	PEDGA	45	15[b]	0.47	425
		7.6	0.05[b]	6	
	PVDF-HFP	50	2.4[a]	0.48	475

Table S7.3. continued.

Ionic liquid	Materials	Solid content (wt%)	Elastic Modulus (MPa)	Ionic Conductivity (mS/cm)	References
EMIM TFSI	PVDF-HFP	N/A	0.05[a]	0.7	476
	PVDF-HFP/triallyl isocyanurate	N/A	5.2[a]	1.4	
	Poly(styrene) (PS) -ran-Poly(methyl methacrylate) (PMMA)	30	0.072[b]	0.98	477
	Poly[S-ran-1-(4-vinylbenzyl)-3-methylimidazolium hexafluorophosphate]	40	0.1[b]	1.15	478
	$(PMMA\text{-}b\text{-}PS)_6$	30	0.025[b]	1.54	479
	PEGDA	25	6[b]	2	480
		25	0.35[b]	3.3	

Table S7.3. continued.

Ionic liquid	Materials	Solid content (wt%)	Elastic Modulus (MPa)	Ionic Conductivity (mS/cm)	References
EMIM TFSI	Poly(sulfobetaine vinylimidazole) (SBVI)	20 mol%	1.3[b]	6.7	371
	Poly(methacryloyloxyethyl phosphorylcholine) (MPC)	20 mol%	0.023[b]	2.5	
	Poly(SBVI)	34 vol%	0.9[b]	6.5	370
	Poly(sulfobetaine methylimidazole)	34 vol%	0.02[b]	6.5	
	Tetra-PEG	4.4	0.0077[a]	7.7	481
		3.2	0.0028[a]	8.5	

Table S7.3. continued.

Ionic liquid	Materials	Solid content (wt%)	Elastic Modulus (MPa)	Ionic Conductivity (mS/cm)	References
BMIM BF4	Hydroxyethyl methacrylate (HEMA)/TiO_2	10.2	4.1[b]	1.4	161
EMIM Cl	HEMA/Chitosan	20	28.65[b]	0.4	165
EMIM Ac	Cellulose/Chitosan	16	253[b]	0.6	426
EMI DCA	Poly 3-dimethyl (methacryloyloxyethyl) ammonium propane sulfonate (DMAPS)-co-AA)	30.9	3900[b]	1	482
EMIM TCB	Polydimethylsiloxane	20	60[b]	3.1	483
EMIM TFO	Sulfonated all-aromatic polyamide (sulfo-aramid, PBDT)	20	~1340 000[a]	4	372

Table S7.3. continued.

Ionic liquid	Materials	Solid content (wt%)	Elastic Modulus (MPa)	Ionic Conductivity (mS/cm)	References
LITFSI/PyrTFSI	PBDT	10	410000[a]	0.56	373
LiTFSI/BMP TFSI	P(SBVI-co-MPC)	12.5	14300[b]	1	484
BMP TFSI	P(SBVI-co-MPC)	15 mol%	8000[b]	1.6	154
LiTFSI	Isotropic PEG	100	3100000[a]	0.14	485
		60	37200[a]	0.05	
	Anisotropic PEG	80	1320000[a]	N/A	
		60	153000[a]	0.05	

[a] Elastic modulus is measured using tensile mechanical test.

[b] Elastic modulus is measured using compressive mechanical test.

CHAPTER 8. GENERAL CONCLUSIONS AND BROAD IMPACT

8.1 Summary of Major Research Results

In the field of the assembly of ionic polymers, the vast majority of work focused on simple ionic polymers with linear architecture and small organic molecules as cations/anions although intensive research has been done on the synthesis of ionic polymers with various chain architectures. The role of branched polymer architecture and interplay of the core-arm functionalities on the assembly, interfacial behavior, percolation limits, and molecular reorganization remain largely unexplored to date and more focused research is needed.

The results in this research provide fundamental insight to address this gap in knowledge. We focused on the effect of polymer chain architecture and peripheral chemical composition on the assembly, interfacial behavior and resulting morphologies of nanostructures of polyelectrolytes and poly(ionic liquid)s. The branched polyelectrolytes and poly(ionic liquid)s studied in this work include hyperbranched polyelectrolytes with different ratios of covalently-linked, hydrophobic alkyl arms and ionically-linked hydrophilic, thermo-responsive macrocations and star-shaped polyelectrolytes with alkyl substituents of variable lengths. These branched polyelectrolytes have ability to generate diverse nanostructures such as spherical core-shell type micelles, cylindrical micelles, vesicles, planar structures, two-dimensional circular micelles and ridge-like structures. Their morphology can be further changed by responding to external environments (solvent ionic strength, temperature, surface pressure, or concentration) through molecular reorganization and phase transformation as was explored in this research.

We investigated the assembly of hyperbranched polyelectrolytes with stimuli-responsive properties behavior in solution and at different interfaces (air-water and air-solid interfaces). The surface morphology and properties of ultrathin monolayer films of hyperbranched polyelectrolytes were studied with emphasis on the conformational change and molecular organization at liquid-air and solid-air interfaces in conjunction with comprehensive surface characterization.

We also studied the responsive behavior of hyperbranched polyelectrolytes with ionically bound thermo-responsive macrocations. The labile ionic bonding enables the macrocations to hop between terminal ionic groups, promoting the domain morphological transition of the hyperbranched polyelectrolytes under changing external environmental conditions, which is inaccessible to traditional covalently tethered polymer arms.

Moreover, we successfully demonstrated the fabrication of functional composites by integrating hyperbranched poly(ionic liquid)s, monomeric ionic liquids and mechanically strong nanocrystals. The multiple functionalities of the hyperbranched poly(ionic liquid)s facilitate the formation of interactions with the nanocrystals and ionic liquids, resulting in the enhancement of mechanical and ion transport properties of the resulting composites. The detail summary concerning critical technical findings and developments in this work are presented below.

Firstly, hyperbranched polyelectrolytes with 24 hydrophobic n-octadecylurethane arms and 8 hydrophilic, thermo-responsive PNIPAM macrocations were studied. Stable Langmuir monolayers were formed at the air-water interface and transferred to solid substrates to form Langmuir Blodgett monolayer films with diverse morphologies. Well-defined disk-like domains were observed in a liquid phase and transformed into almost uniform monolayers with a network of ridge-like structures in a solid phase. The disk-to-ridge transformation is dissimilar from the transformations commonly observed for linear amphiphilic block copolymers, known as ‘pancake-to-brush’ or ‘carpet-to-brush’ transition. The branched architecture and asymmetry in chemical composition of the polyelectrolytes allowed the disk-like domains to preserve their shape under high lateral compression, resulting in the formation of ridge-like network structures in a solid phase. In addition, the morphology of LB monolayers can be tuned by changing temperature due to LCST transition of PNIPAM; for example, elevated individual islands were formed only above LCST in a solid phase due to the aggregation of hydrophobized PNIPAM macrocations. Moreover, we examined the mechanical contrast distribution of the monolayer surface in both dry and wet conditions. In a dry state, the monolayer surface showed a relative uniformity of mechanical response irrespective of constituents and for all temperatures; all molecular components are in a collapsed state. In contrast, a clearly heterogeneous

mechanical response was observed in water, indicating molecular reorganization. Further change in mechanical contrast distribution was found above LCST. The distribution of mechanical properties changed from highly contrasted two-phase distribution below LCST to near uniform distribution above LCST, confirming the critical role of thermo-responsive and labile PNIPAM macrocations in the monolayer organization.

Secondly, we studied thermo-responsive hyperbranched polyelectrolytes of symmetric and asymmetric types with emphasis of the role of highly mobile PNIPAM macrocations of oligomeric type on the dynamic assembly of the hyperbranched polyelectrolytes. The hyperbranched polyelectrolytes are composed of covalently-bound hydrophobic alkyl arms and ionically-bound PNIPAM macrocations with variable contents. The presence of terminal PNIPAM macrocations provides the polyelectrolytes with stimuli-triggered responsive ability due to not only their thermo-responsive behavior but also labile ionic bonding, allowing for morphological transition under changing temperature and ionic strength. Indeed, about 90% of the PNIPAM macrocations can hop between terminal sulfonate groups of the core of the hyperbranched polyelectrolytes, probed by molecular dynamic simulation. In addition, variation of peripheral chemical composition of the hyperbranched polyelectrolytes plays a crucial role on determining surface morphologies as well as mechanical and electrical response of their monolayers. In particular, the presence of fraction of negatively charged sulfonate terminal groups at the substrate/monolayer interface causes the formation of a dipole layer, facilitating surface potential contrast caused by the difference in dipole distribution between domains.

Thirdly, we exploited star-shaped oligomeric ionic liquids with inorganic cores and organic shells. The oligomeric ionic liquids contain a mixture of polyhedral oligosilsesquioxane (POSS) and their analogs with open chain structures as inorganic cores and tertiary ammonium groups with variable lengths of hydrophobic alkyl substitutes as organic shells. The increase in the length of the alkyl substituents increases peripheral hydrophobicity which affects their self-organization in aqueous media and into a thin film on a solid surface. Morphological transition from disk-like to microscopic, worm-like domains was observed with decreased surface adhesion by increasing the length of alkyl

substituents which leads to the change in molecular organization to minimize unfavorable interactions between the hydrophobic substitutes and water molecules.

Lastly, we successfully demonstrated that hyperbranched poly(ionic liquid)s can be used as a "binding" functional component to fabricate functional composite materials which show simultaneous enhancement in mechanical stability and ionic conductivity. Abundant functional groups of hyperbranched poly(ionic liquid)s enables the formation of multiple physical interactions with cellulose nanocrystals bearing anionic groups, facilitating the formation of mechanically strong network structures with an interrupted ion-conducting pathway. The use of these robust network structures as a supporting frame for ionic liquids results in the fabrication of ionogels with unique continuous nanoporous morphology. The shape-persistent robust ionogels have uninterrupted ion-conducting network, resulting in an exceptional combination of high elastic modulus and ionic conductivity, which has not been achieved from conventional solid electrolytes and fluidic electrolytes. Thus, these novel ionogel materials developed in this work offer a significant insight for utilizing branched polyelectrolytes and poly(ionic liquid)s to develop mechanically robust, highly conductive solid electrolyte materials that are shape-persistent and appropriate for energy harvesting and storage devices.

8.2 Proposed Future Work and Trends.

The work in this dissertation elucidates the stimuli-responsive assembly behavior of branched polyelectrolytes and their morphology and phase transformation. However, there are still many unresolved questions needed to be addressed to obtain complex nanostructures with tunable morphology and tailored transport properties from branched polyelectrolytes. In particular, the branched polyelectrolytes can be assembled into interconnected network morphologies with potentially switchable percolating behavior, such as on-off connectivity/ion transport, by incorporating functional components, such as stimuli-responsive macrocations or terminal groups. Future studies should focus efforts on various asymmetrical, molecular architectures by choosing different grafting compositions, molecular weights of branches and nature of macroions as well as terminal and pendant functionalities in order to promote the formation of continuous morphologies beyond

simple, discrete spherical organization. For example, based on enthalpic considerations, branched polyelectrolytes with strong aggregation of cores, which favors the formation of discrete domains, and weak segregation of different arm components, which favors to poorly organized morphologies, might be able to create intermediate balances, which are favorable for generating interconnected elongated domains and continuous network if combined with asymmetric composition. The addition of functional components, such as thermo-responsive macrocations and photoresponsive terminal groups, would enable local molecular reorganization caused by change in intra/intermolecular bonding, resulting in reversible reorganization at meso- and microscale and thus switchable transformation of the domain network connectivity under external stimuli.

Although the results discussed in this dissertation demonstrate the tunability of the assembly and morphologies of branched polyelectrolytes by adjusting external environmental conditions (e.g., temperature and surface pressure), there are many additional critical environmental factors whose effects on the assembly of branched polyelectrolytes are not fully understood. For example, although substrate-polymer interactions are one of the most significant factors for directing polymer assembly behavior and nanostructure orientation and uniformity, the substrate effects on the assembly of branched polyelectrolytes are unknown. The vast majority of existing studies on polymer assembly consider static substrates with less attention paid on dynamic substrates. Dynamic substrates can deform their surface chemistry or/and structure in response to external stimuli such as pH, temperature, and light as well as the association with macromolecules.[486, 487] The surface reconfiguration of the dynamic substrates can maximize favorable interactions with assembling polymer molecules, thereby lowering the energy barrier for polymer assembly.[487] Employing dynamic substrates provides a level of control on polymer organization and morphology beyond that achieved by using static substrates. Future studies can consider preparing stimuli-responsive ionogels as a dynamic substrate matrix to elucidate the potential of utilizing dynamic substrates for realizing dynamic assembly of branched polyelectrolytes. The non-volatile nature and chemical/thermal stability of the ionic liquid would enable the ionogels to keep their responsive properties intact. Unlike static solid materials, the stimuli-responsive ionogels

can change their microstructures in response to external stimuli, leading to the transformation in morphology and properties of branched polyelectrolyte assembled on the ionogels.

Finally, because this work suggests a great potential of branched polyelectrolytes as a building block material for fabricating functional polymer composites with both high mechanical stability and ionic conductivity via multiple ionic interactions, future studies should focus on the using the mechanism of ionic interactions of these ionic polymers to develop novel inorganic-organic composite materials with ionic components capable of forming highly organized phases in contrast to usual disordered, amorphous materials from traditional polyelectrolytes with random-coil organization.

Due to the presence of multiple ionic groups, polyelectrolytes have abilities to strongly adsorb inorganic ions, confining the ions within polyelectrolytes,[488] and thus serve as amorphous phase templates for in-situ synthesis of inorganic nanoparticles.[489,490,491] On the other hand, functional templates formed by branched polyelectrolytes with multiple functionalities have a great potential to create organized structures with responsive properties, as demonstrated in this dissertation. In addition, ionic liquids are capable of creating crystalline phases.[492] Their polymeric analogs, poly(ionic liquid)s can have crystalline structures with a few examples of liquid crystalline poly(ionic liquid)s reported.[493,494] Therefore, the use of branched polyelectrolytes and poly(ionic liquid)s which can form highly ordered, possibly crystalline, phases can open up new possibilities to produce nanoparticles with unusual morphology and properties. For example, the nanoparticles synthesized with organized continuous network structures would exhibit unique properties, such as superior photocatalytic activity and high molecule adsorption.[495,496]

For one, polyelectrolytes can be used as a template for in-situ growth of metal-organic frameworks (MOFs), which are novel three-dimensional porous materials composed of inorganic metal nodes linked by rigid organic ligands.[497] MOFs are an important class of materials formed via ionic interactions for various applications such as chemical separation, molecular storage and heterogenous catalysis.[498,499,500] Polyelectrolytes provide ionic sites

where metal ions can strongly interact, facilitating the nucleation and growth of MOFs with highly crystalline and porous lattice.[501,502] Selection of polyelectrolytes with different chain architectures and functionalities can introduce novel morphology and functionality to the resulting MOF/polyelectrolyte composites.

As an initial stage of preliminary research for future researchers in the field of organized ionic materials far beyond ionic organics and polymers studied to date, we attempted to explore 1D cellulose nanocrystals bearing sulfate groups which have an ability to self-assemble into chiral nematic structures for generating MOF/CNC composites with new functionalities, including multi-scale porosity, unusual crystal lattice, and induced chirality. In initial first attempts, we successfully fabricated MOF/CNC composites with MOF grown not only on the surface but also inside the CNC film (Figure 8.1). We used a widely studied MOF, zeolitic imidazolate framework-8 (ZIF-8), as a proof of concept, which is built up from connecting zinc ions and 2-methylimidazole linkers.[503] First, CNC films were prepared as an ionic, chiral bio-template which provides ionic sites to concentrate zinc ions for nucleation and subsequent growth as well as endows the final composite film with chirality. ZIF-8 precursors (zinc nitrate and 2-methylimidazole) were filled into the CNC films using vacuum-assisted filtration under careful control over time for filtration and drying.

The resulting ZIF-8/CNC films became white-colored but iridescent, suggesting ZIF-8 growth with chirality preserved in the films. Cross-sectional SEM images of the ZIF-8/CNC films clearly show nanoparticles grown on CNCs, suggesting that ZIF-8 was fabricated inside the CNC films (Figure 8.1b). Cross-sectional images of ZIF-8/CNC films exhibit helicoidal Bouligan morphology, supporting the retention of chiral structures in the ZIF-8/CNC films (Figure 8.1b).[504] Transmission electron microscopy (TEM) images of ZIF-8/CNC also confirm the synthesis of ZIF-8 nanoparticles on CNCs, showing necklace-like morphology, which is different from the need-like morphology of pure CNC and micro-sized hexagonal morphology of conventional ZIF-8 particles (Figure 8.1c). This result suggests that the use of CNC template effectively regulates the synthesis of ZIF-8 in regard to shape and size.

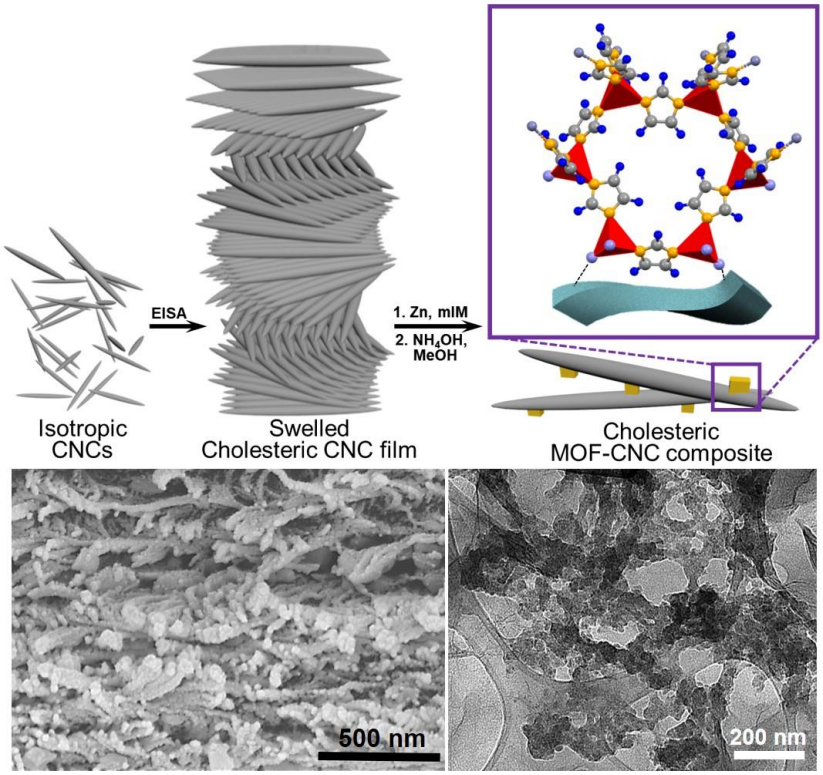

Figure 8.1. (a) Schematic illustration of fabrication of ZIF-8/CNC composite film via in-situ growth of ZIF-8 on CNC surface. (b) Cross-sectional SEM and (c) TEM images of ZIF-8/CNC films.

Finally, X-ray and neutron scattering characterizations confirm the structural changes in ZIF-8/CNC composites compared to pure CNC and ZIF-8 (Figure 8.2). A XRD spectrum of ZIF-8/CNC composites shows characteristic peaks of both CNC and MOF, including the characteristic diffraction peaks at 2θ = 7.3°, 10.4°, 12.7°, 14.7°, 16.4°, 18.0°, 26.7° and 29.6° which can be assigned to (011), (002), (112), (022), (013), (222), (134) and (044) planes for ZIF-8, respectively,[505,506] and three crystalline peaks of cellulose ($(1\bar{1}0)$ at 14.8°, (110) at 16.1°, and (200) at 22.6°).[393] This result reveal that the presence of ZIF-8 on the surface of CNCs without a significant change in the crystalline structure of CNCs (Figure 8.2a). The relative peak intensity of ZIF-8/CNC is different from that of pure ZIF-8, especially the (011) plane, probably due to the interruption of CNCs to the ZIF-8 growth process. Some diffraction peaks are slightly shifted toward to higher diffraction angles,

indicating a slight compression of ZIF-8 unit cells during nucleation and growth at the CNC surfaces (Figure 8.2a).[507]

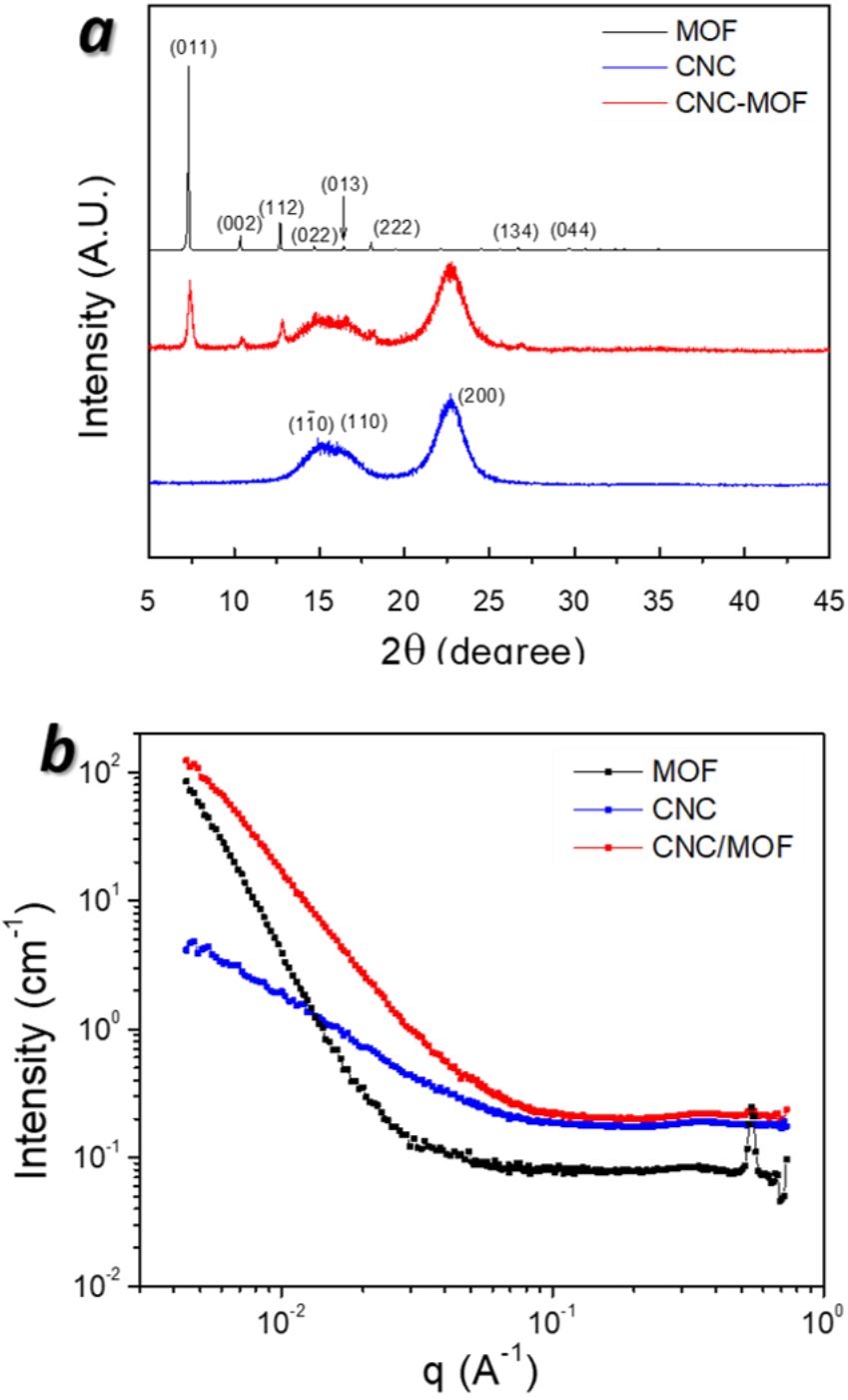

Figure 8.2. (a) XRD data and (b) SANS data of ZIF-8 (MOF) powder and CNC and ZIF-8/CNC films.

In addition, small-angle neutron scattering (SANS) identified the change in physical structures (Figure 8.2b). SANS data for ZIF-8/CNC composite films are well-fitted by using a combined model of Unified power law model and Debye-Andersen-Brumberger (DAB) model, suggesting that the ZIF-8/CNC composites are a randomly distributed, two-phase morphology.[508] Notably, in a high q regime, ZIF-8/CNC composite films exhibit a peak at q = 0.543 Å^{-1}, indicating the crystalline ordering of structural features with d-spacing of 1.16 nm as calculated by $d = 2\pi/q$.[509] A sharp peak at the same q value was found for pure ZIF-8, while pure CNC film does not show the peak (Figure 8.2b). This result supports that the original crystalline structures of ZIF-8 are preserved in the composite films. The power law exponent value of ZIF-8/CNC film is significantly different from those of CNC film and ZIF-8 particles. ZIF-8/CNC film show a power law exponent of 2.7 consistent with mass fractal morphology. CNC film has a power law exponent of 1.9 close to that of two-dimensional objects (e.g., sheets), while a power law exponent of ZIF-8 particles was 4.1, indicating surface fractal materials (compact three-dimensional scattering objects) with smooth surface (Figure 8.2b).[510,511] Such different nature of internal morphology suggests that the growth of ZIF-8 on CNC surfaces causes the structural changes from sheet-like morphology to fractal-like aggregation configuration.

These ZIF-8/CNC composites with high porosity and chirality can be used for enantioselective absorption and separation, which cannot be achieved from conventional MOF materials. Thus, these studies will bring fundamental scientific knowledge regarding the construction of novel, chiral MOF composites.

In total, future studies should consider the use of branched polyelectrolytes with different functionalities as templates for in-situ growth of MOFs and other inorganic and hybrid materials. Branched polyelectrolytes with various functionalities have shown a promise to generate complex organized phases and morphologies, including percolating network, which are difficult to obtain from linear polyelectrolytes. Introducing a complex organized morphology, for example, percolating network structures would enhance the properties of the hybrid materials, such as catalytic efficiency and separation/adsorption capability of molecules. Since branched polyelectrolytes have a capability of multi-stimuli responsive behavior, the combination of branched polyelectrolytes and inorganic components endows

the resultant hybrid materials with novel smart functions. This type of multi-responsive hybrid materials is attractive in prospective advanced applications, such as targeted drug delivery/imaging, tunable catalysis, highly precise sensing, and switchable optics. Further developments for the responsive hybrid materials to a higher level of performance, such as stepwise responses to one stimulus, selective response to a stimulus under precisely defined conditions, and high on-off switching ratio, are expected with emerging achievements on the synthesis of branched polyelectrolytes with increasing complexity in chain architectures (e.g., branched-linear and branched-core star architectures) and chemical composition.

8.3 Dissemination of Work

The work presented in this dissertation has been summarized in the following major publications.

[1] **Lee, H.**; Erwin, A.; Buxton, M. L.; Kim, M.; Stryutsky, A. V.; Shevchenko, V. V.; Sokolov, A. P.; Tsukruk, V. V. Shape-Persistent, Highly Conductive Ionogels from Ionic Liquids Reinforced with Cellulose Nanocrystal Network. **2021**, *Accepted to Advanced Functional Materials.*

[2] Shevchenko, V. V.; Gumenna, M. A.; **Lee, H.;** Klimenko, N. S.; Stryutsky, A. V.; Tsukruk, V. V. Reactive amphiphilic aprotic ionic liquids based on functionalized oligomeric silsesquioxanes. **2021**, *Under revision at Bull. Chem. Jpn. Soc.*

[3] **Lee, H.**; Stryutsky, A. V.; Mahmood, A.-U.; Singh, A.; Shevchenko, V. V.; Yingling, Y. G.; Tsukruk, V. V. Weakly Ionically Bound Thermo-sensitive Hyperbranched Polymers. *Langmuir* **2021,** *37*, 2913 *(***Selected as Cover***).*

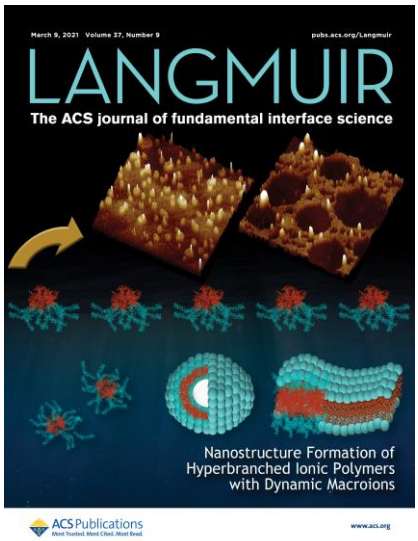

[4] **Lee, H.**; Stryutsky, A. V.; Korolovych, V. F.; Mikan, E.; Shevchenko, A. V.; Tsukruk, V. V. Transformations of Thermo-Sensitive Hyperbranched Poly(ionic liquid)s Monolayers. *Langmuir* **2019,** *35*, 11809.

[5] Erwin, A. J.; **Lee, H.**; Ge, S.; Zhao, S.; Korolovych, V. F.; He, H.; Matyjaszewski, K.; Sokolov, A.P.; Tsukruk, V. V. Viscoelastic properties and ion dynamics in star-shaped polymerized ionic liquids. *Euro. Polym. J.* **2018**, *109*, 326.

[6] Korolovych, V. F.; Erwin, A.; Stryutsky, A. V.; **Lee, H.**; Heller, W. T.; Shevchenko, V. V.; Bulavin, L. A.; Tsukruk, V. V. Thermally Responsive Hyperbranched Poly(ionic liquid)s: Assembly and Phase Transformations. *Macromolecules* **2018**, *51*, 4923.

The following publications are related to the work in this dissertation:

[1] Kim, M.;‡ **Lee, H.**;‡ Adstedt, K.; Pierce, K.; Heller, W.; Buxton, M.; Tsukruk, V. V. *In-situ* Synthesis of Chiral metal-organic frameworks enabled by an ionic bio-template with photonic structures. *Manuscript in preparation.*

[2] Kim, M.; **Lee, H**.; Snipes, R. T.; Han, M. J.; Tsukruk, V. V. Bio-Synthetic Optically-Active Adhesive with Strong and Dynamic Polarized Luminescence. **2021**, *Submitted to Advanced Functional Materials*.

[3] Kim, M.; **Lee, H**.; Krecker, M. C.; Bukharina, D.; Nepal, D.; Bunning, T. J.; Tsukruk, V. V. Switchable Photonic Bio-Adhesive Materials. **2021**, *Accepted to Advanced Materials*.

[4] Kang, S.; Biesold, G. M.; **Lee, H.**; Bukharina, D.; Lin, Z.; Tsukruk, V. V. Dynamic chiro-optics of bio-inorganic nanocomposite via seamless co-assembly of semiconducting nanowires and biological nanocrystals. **2021**, *Accepted to Advanced Functional Materials.*

[5] Kang, S.;‡ Li, Y,;‡ Bukharina, D.; Kim, M.; **Lee, H.**; Buxton, M. L.; Nepal, D.; Bunning, T. J.; Tsukruk, V. V. Alternating circularly polarized light emission with on-demand handedness in photochromically-doped biophotonic materials. **2021**, *Accepted to Advanced Materials*.

[6] Xiong, R.; Singh, A.; Yu, S.; Zhang, S.; **Lee, H.**; Yingling, Y. G.; Nepal, D. Bunning, T. J.; Tsukruk, V. V. Co-assembling Polysaccharide Nanocrystals and Nanofibers for Robust Chiral Iridescent Films. *ACS Appl. Mater. Interfaces* **2020**, *12, 31*, 35345.

Conference presentations related to this dissertation:

[1] Breaking Mechanical Strength vs Ionic Conductivity Dilemma of Ionogels by Reinforcement with Cellulose Nanocrystal Network. 262nd ACS National Meeting, Atlanta GA, 2021 (***Oral***, Accepted).

[2] Shape-persistent, highly conductive ionogels from ionic liquids reinforced by cellulose nanocrystals. GT Student Polymer Network Symposium, Atlanta GA 2021.

[3] Strong and conductive ionogel: polymeric ionic liquids reinforced with cellulose nanocrystals. GT MRS Poster Session, Atlanta GA 2021.

[4] Temperature-induced transformation of amphiphilic thermo-sensitive hyperbranched poly(ionic liquid)s, 257th ACS National Meeting, Orlando, FL, 2019 ***(Oral).***

[5] Hybrid ionogels by complexation of poly(ionic liquid)s with nanocellulose, 257th ACS National Meeting, Orlando, FL, 2019 ***(Oral).***

[6] Transformation of thermo-sensitive hyperbranched poly(ionic liquid)s monolayers, GT MRS Poster Session, Atlanta, GA, 2019.

REFERENCES

[1] Wang, Y.; Hosta-Rigau, L.; Lomas, H.; Caruso, F. *Phys. Chem. Chem. Phys.* **2011**, *13*, 4782.

[2] Zhao, J.; Lee, V. E.; Lui, R.; Priestley, R. D. *Annu. Rev. Chem. Biomole. Eng.* **2019**, *10*, 361.

[3] Dolce, C.; Mériguet, G. *Colloid Polym. Sci.* **2017**, *295*, 279.

[4] Dobrynin, A. V.; Rubinstein, M. *Prog. Polym. Sci.* **2005**, *30*, 1049.

[5] Colby, R. H. *Rheol. Acta* **2010**, *49*, 425.

[6] Wnag, R.-Y.; Park, M. J. *Annu. Rev. Mater. Res.* **2020**, *50*, 521.

[7] Jo, G.; Ahn, H.; Park, M. J. *ACS Macro Lett.* **2013**, *2*, 990.

[8] Jung, H. Y.; Mandal, P.; Jo, G.; Kim, O.; Kim, M.; Kwak, K.; Park, M. J. *Macromolecules* **2017**, *50, 8*, 3224.

[9] Micka, U.; Holm, C.; Kremer, K. *Langmuir* **1999**, *15*, 4033.

[10] Wang, Z,-G. *J. Phys. Chem. B* **2008,** *112*, 16205.

[11] Nakamura, I.; Balsara, N. P.; Wang, Z.-G. *Phys. Rev. Lett.* **2011,** *107*, 198301.

[12] Sing, C. E.; Zwanikken, J. W.; de la Cruz, M. O. *Nat. Mater.* **2014**, *13,* 694.

[13] Zhai, C.; Zhou, H.; Gao, T.; Zhao, L.; Lin, S. *Macromolecules* **2018**, *51*, 4471.

[14] Green, O.; Grubjesic, S.; Lee, S.; Firestone, M. A. *Polym. Rev.* **2009**, *49*, 339.

[15] Yuan, J.; Mecerreyes, D.; Antonietti, M. *Prog. Polym. Sci.* **2013**, *38*, 1009.

[16] Nishimura, N.; Ohno, H. *Polymer* **2014**, *55*, 3289.

[17] Meek, K. M.; Elabd, Y. A. *J. Mater. Chem. A* **2015**, *3*, 24187.

[18] Mecerreyes, D. *Prog. Polym. Sci.* **2011,** *36*, 1629.

[19] Jung, Y.; Park, M. J. *Soft Matter* **2017**, *13*, 250.

[20] Matthews, R. P.; Welton, T.; Hunt, P. A. *Phys. Chem. Chem. Phys.* **2014**, *16*, 3238.

[21] Wang, G.; Zhuo, S.; Lin, Y. *J. Appl. Polym. Sci.* **2013**, *127*, 2574.

[22] Cordella, D.; Debuigne, A.; Jérôme, C.; Kochovski, Z.; Taton, D.; Detrembleur, C. *Macromol. Rapid Commun.* **2016**, *37*, 1181.

[23] Ye, Y.; Choi, J.-H.; Winey, K. I.; Elabd, Y. A. *Macromolecules* **2012**, *45*, 7027.

[24] Weber, R. L.; Ye, Y.; Schmitt, A. L.; Banik, S. M.; Elabd, Y. A.; Mahanthappa, M. K. *Macromolecules* **2011**, *44*, 5727.

[25] Liu, S.; Xu, T. *Macromolecules* **2016**, *49*, 16, 6075.

[26] May, A. W.; Shi, Z.; Wjayasekara, D. B.; Gin, D. L.; Bailey, T. S. *Polym. Chem.* **2019**, *10*, 751.

[27] Zhang, W.; Kochovski, Z.; Lu, Y.; Schmidt, B. V. K. J.; Antonietti, M.; Yuan, J. *ACS Nano* **2016**, *10*, 7731.

[28] Dule, M.; Biswas, M.; Paira, T. K.; Mandal, T. K. *Polymer* **2015**, *77*, 32.

[29] He, H.; Rahimi, K.; Zhong, M.; Mourran, A.; Luebke, D. R.; Nulwala, H. B.; Möller, M.; Matyjaszewski, K. *Nat. Commun.* **2017**, *8*, 14057.

[30] Choi, J.-H.; Ye, Y.; Elabd, Y. A.; Winey, K. I. *Macromolecules* **2013**, *46*, 5290.

[31] Minko, S.; Kiriy, A.; Gorodyska, G.; Stamm, M. *J. Am. Chem. Soc.* **2002**, *124*, 3218.

[32] Zhulina, E. B.; Borisov, O. V. *Macromolecules* **2005**, *38*, 6726.

[33] Kocak, G.; Tuncer, C.; Bütün, V. *Polym. Chem.* **2017**, *8*, 144.

[34] Lovett, J. R.; Warren, N. J.; Ratcliffe, L. P. D.; Kocik, M. K.; Armes, S. P. *Angew. Chem.* **2015**, 54, 4, 1279.

[35] Chroni, A.; Pispas, S.; Forys, A.; Trzebicka, B. *Macromol. Rapid Commun.* **2019**, *40, 24,* 1900477.

[36] Pincus, P. *Macromolecules* **1991**, *24*, 2912.

[37] Pispas, S.; Hadjichristidis, N. *Macromolecules*, **2003**, *36*, 8732.

[38] Stubenrauch, K.; Voets, I.; Fritz-Popovski, G.; Trimmel, G. *J. Polym. Sci. Part A Polym. Chem.* **2009**, *47, 4,* 1178.

[39] Skandalis, A.; Pispas, S. *Polymer* **2018**, *147*, 9.

[40] Hales, K.; Pochan, D. J. *Curr. Opin. Colloid Interface Sci.* **2006**, *11*, 330.

[41] Stuart, M. A. C.; Hofs, B.; Voets, I. K.; de Keizer, A. *Curr. Opin. Colloid Interface Sci.* **2005**, *10*, 30.

[42] Borisov, O. V.; Zhulina, E. B. *Langmuir* **2005**, *21*, 3229.

[43] Li, N. K.; Fuss, W. H.; Tang, L.; Gu, R.; Chillkoti, A.; Zauscher, S.; Yingling, Y. G. *Soft Matter* **2015**, *11*, 8235.

[44] Liu, L.-Y.; Xia, G.; Feng, Z.-J.; Hao, Q.-H.; Tan, H.-G. *Soft Matter* **2019**, *15*, 3689.

[45] Zhong, J.; Luo, H.; Tang, Q.; Lei, Z.; Tong, Z. *Macromol. Chem. Phys.* **2019**, *229*, 1800554.

[46] Xu, Y.; Borisov, O. V.; Ballauff, M.; Müller, A. H. *Langmuir* **2010**, *26*, 6919.

[47] Larin, S. V.; Pergushov, D. V.; Xu, Y.; Darinskii, A. A.; Zezin, A. B.; Müller, A. H.; Borisov, O. V. *Soft Matter* **2009**, *5*, 4938.

[48] Furukawa, T.; Ishizu, K. *Macromolecules* **2005**, *38*, 2911.

[49] Xu, W.; Ledin, P. A.; Plamper, F. A.; Synatschke, C. V.; Müller, A. H.; Tsukruk, V. V. *Macromolecules* **2014**, *47*, 7858.

[50] A. Hanisch, A. H. Gröschel, M. Förtsch, M. Drechsler, H. Jinnai, T. M. Ruhland, F. H. Schacher and A. H. E. Müller. *ACS Nano* **2013**, *7*, 4030.

[51] Bayoudh, S.; Laschewsky, A.; Wischerhoff, E. *Colloid. Polym. Sci.* **1999**, *277*, 519.

[52] Pu, K. Y.; Li, K.; Shi, J.; Liu, B. Fluorescent Single-Molecular Core−Shell Nanospheres of Hyperbranched Conjugated Polyelectrolyte for Live-Cell Imaging. *Chem. Mater.* **2009**, *21*, 3816−3822.

[53] Mishra, M. K.; Kobayashi, S., Eds. Star and Hyperbranched Polymers; Marcel Dekker: New York, **1999**; Vol. 53.

[54] Peleshanko, S.; Tsukruk, V. V. *Prog. Polym. Sci.* **2008**, *33*, 523.

[55] Xu, W.; Ledin, P. A.; Shevchenko, V. V.; Tsukruk, V. V. *ACS Appl. Mater. Interfaces* **2015**, *7*, 12570.

[56] Choi, I.; Malak, S. T.; Xu, W.; Heller, W. T.; Tsitsilianis, C.; Tsukruk, V. V. *Macromolecules* **2013**, *46*, 1425.

[57] Jusufi, A.; Likos, C.; Löwen, H. *Phys. Rev. Lett.* **2001**, *88*, 018301.

[58] Likos, C.; Löwen, H.; Watzlawek, M.; Abbas, B.; Jucknischke, O.; Allgaier, J.; Richter, D., *Phys. Rev. Lett.* **1998**, *80*, 4450.

[59] Chremos, A.; Douglas, J. F. *J. Chem. Phys.* **2015**, *143*, 111104.

[60] Xu, W.; Choi, I.; Plamper, F. A.; Synatschke, C. V.; Müller, A. H.; Melnichenko, Y. B.; Tsukruk, V. V. *Macromolecules* **2014**, *47*, 2112.

[61] Xu, W.; Ledin, P. A.; Iatridi, Z.; Tsitsilianis, C.; Tsukruk, V. V. *Macromolecules* **2015,** *48*, 3344.

[62] Erwin, A. J.; Korolovych, V. F.; Iatridi, Z.; Tsitsilianis, C.; Ankner, J. F.; Tsukruk, V. V. *Macromolecules* **2018**, *51*, 4800.

[63] Julthongpiput, D.; Lin, Y. Teng, J.; Zubarev, E. R.; Vladimir, V. V. *J. Am. Chem. Soc.* **2003**, *125*, 15912.

[64] Gorodyska, G.; Kiriy, A.; Minko, S.; Tsitsilianis, C.; Stamm, M. *Nano Lett.* **2003**, *3*, 365.

[65] Iatridi, Z.; Tsitsilianis, C. *Chem. Commun.* **2011**, *47*, 5560.

[66] Hillmyer, M. A.; Lodge, T. P. *Langmuir* **2006**, *22*, 9409.

[67] Liu, C.; Hillmyer, M. A.; Lodge, T. P. *Langmuir* **2009**, *25, 24*, 13718.

[68] Liu, H.; Li, C.; Liu, H.; Liu, S. *Langmuir* **2009**, *25, 8*, 4724.

[69] Zhou, H.; Yea, Q.; Xu, J. *Mater. Chem. Front.* **2017,** *1*, 212.

[70] Chen, F.; Lin, F.; Zhang, Q.; Cai, R.; Wu, Y.; Ma, X. *Macromol. Rapid Commun.* **2019**, *40, 17,* 1900101.

[71] Dong, F.; Lu, L.; Ha, C. *Macromol. Chem. Phys.* **2019**, *220, 3*, 1800324.

[72] Ultah, A.; Ultah, S.; Khan, G. S.; Shah, S. M.; Hussain, Z.; Muhammad, S.; Siddiq, M.; Hussain, H. *Eur. Polym. J.* **2016**, *75,* 67.

[73] Ni, C. H.; Wu, G.; Zhu, C. P.; Yao, B. L. *J. Phys. Chem. C* **2010**, *114, 32,* 13471.

[74] Wang, W.; Fei, M.; Jie, X.; Wang, P.; Cao, H.; Yu, J. *Polym. Bull.* **2010**, *65*. 863.

[75] Huang, H.; Ren, D.; Qu, J. *Colloid. Polym. Sci.* **2020**, *298*, 1515.

[76] Ma, L.; Geng, H.; Song, J.; Li, J.; Chen, G.; Li, Q. *J. Phys. Chem. B* **2011**, *115*, 10586.

[77] Xu, Y.; Chen, M.; Xie, J.; Li, C.; Yang, C.; Deng, Y.; Yuan, C.; Chang, F. C.; Dai, L. *React. Funct. Polym.* **2013**, *73*, 1646.

[78] Bai, Y.; Wei, J.; Yang, ,L.; He, C.; Lu, X. *Colloid Polym. Sci*. **2012**, *209*, 504.

[79] Mori, H.; Ebina, Y.; Kambara, R.; Nakabayashi, K. *Polym. J.* **2012**, *44,* 550.

[80] He, Z.; Zhong, M.; Yang, Y.; Wu, C.; Yang, J. *J. Polym. Res.* **2016**, *23*, 243.

[81] Erwin, A. J.; Xu, W.; He, H.; Matyjaszewski, K.; Tsukruk, V. V. *Langmuir* **2017**, *33*, 3187.

[82] Erwin, A. J.; Lee, H.; Ge, S.; Zhao, S.; Korolovych, V. F.; He, H.; Matyjaszewski, K.; Sokolov, A. P.; Tsukruk, V. V. *Eur. Polymer J.* **2018**, *109*, 326

[83] Maksym, P.; Tarnacka, M.; Wolnica, K.; Dzienia, A.; Zieba, A.; Kaminski, K.; Paluch, M. *J. Polym. Sci. Part A: Polym. Chem.* **2018**, *56,* 2681.

[84] Zhoum N.; Wang, Y.; Zhou, Y.; Shen, J.; Zhou, Y.; Yang, Y. *Electrochimica Acta* **2019**, *301*, 284.

[85] Gao, C.; Yan, D. *Prog. Polym. Sci.* **2004**, *29*, 183.

[86] Tian, H.; Chen, X.; Lin, H.; Deng, C.; Zhang, P.; Wei, Y.; Jing, X. *Chem. Eur. J.* **2006**, *12*, 4305.

[87] Luo, S.; Han, M.; Cao, Y.; Ling, C.; Zhang, Y. *Colloid. Polym. Sci.* **2011**, *289,* 1243.

[88] Roy, S. G.; De, P. *Polym. Chem.* **2014**, *5*, 6365.

[89] Yu, C.; Ma, L.; Li, K.; Li, S.; Liu, Y.; Zhou, Y.; Yan, D. *Langmuir* **2017**, *33*, 388.

[90] Pispas, S.; Floudas, G.; Pakula, T.; Lieser, G.; Sakellariou, S.; Hadjichristidis, N. *Macromolecules* **2003**, *36*, 759.

[91] Lee, H.; Stryutsky, A. V.; Korolovych, V. F.; Mikan, E.; Shevchenko, V.; Tsukruk, V. V. *Langmuir* **2019**, *35*, 11809.

[92] Jo, Y. M.; Park, C. W.; Jung, B.; Yang, H.-M.; Kim, J.-D. *Macromol. Chem. Phys.* **2010**, *211*, 2434.

[93] Mariani, G.; Moldenhauer, D.; Schweins, R.; Gröhn. F. *J. Am. Chem. Soc.* **2016**, *138*, 1280.

[94] Pocovi-Martinez, S.; KemmerJonas, U.; Perez-Prieto, J.; Frey, H.; Stiriba, S.-E. *Macromol. Chem. Phys.* **2014**, *215,* 2311.

[95] Hernandez-Ainsa, S.; Fedeli, E.; Barbera, J.; Marcos, M.; Sierra, T.; Serrano, J. L. *Soft Matter* **2014**, *10*, 281.

[96] Korolovych, V. F.; Erwin, A.; Stryutsky, A.; Lee, H.; Heller, W. T.; Shevchenko, V. V.; Bulavin, L. A.; Tsukruk, V. V. *Macromolecules* **2018**, *51*, 4923.

[97] Schwab, E.; Mecking S. *J. Polym. Sci. A Polym. Chem.* **2005***, 43*, 4609.

[98] Tamaki, M.; Taguchi, T.; Kitajyo, Y.; Takahashi, K.; Sakai, R.; Kakuchi, T.; Satoh, T. *J. Polym. Sci. Part A* **2009,** *47*, 7032.

[99] Schüler, F.; Kerscher, B.; Beckert, F.; Thomann, R.; Mülhaupt, R. *Angew. Chem. Int. Ed.* **2013**, *52*, 455.

[100] Huang, J.-F.; Luo, H.; Liang, C.; Sun, I.-W.; Baker, G. A.; Dai, S. *J. Am. Chem. Soc.* **2005,** *127,* 12784.

[101] Fan, Y.; Zhang, D.; Wang, J.; Jin, H.; Zhou, Y.; Yan, D. *Chem. Commun.* **2015**, *51*, 7234.

[102] Zhang, J.; Chen, S.; Qin, B.; Zhang, D.; Guo, P.; He, Q. *Polymer* **2019**, *164,* 154.

[103] Wieddmann, S.; Luitz, M.; Kerscher, B.; Lutz, J.-F.; Mulhaupt, R. *Macromolecules* **2019**, *52*, 9672.

[104] Chen, C.; Fang, X. *J. Appl. Polym. Sci.* **2010**, *117,* 3539.

[105] Korolovych, V. F.; Ledin, P. A.; Stryutsky, A.; Shevchenko, V. V.; Sobko, O.; Xu, W.; Bulavin, L. A.; Tsukruk, V. V. *Macromolecules* **2016**, *49*, 8697.

[106] Yu, J.; Jackson, N. E.; Xu, X.; Brettmann, B. K.; Ruths, M.; de Pablo, J. J.; Tirrell, M. *Sci. Adv.* **2017**, *3*, eaao1497.

[107] Hao, Q.-H.; Cheng, J.; Liu, L.-X.; Tan, H.-G.; Wei, T.; Liu, L.-Y.; Miao, B. *Macromolecules* **2020,** *53, 16,* 7187.

[108] Wang, M.; Zou, S.; Guerin, G.; Shen, L.; Deng, K.; Jones, M.; Walker, G. C.; Scholes, G. D.; Winnik, M. A. *Macromolecules* **2008**, *41*, 6993.

[109] Lee, H.-I.; Boyce, J. R.; Nese, A.; Sheiko, S. S.; Matyjaszewski, K. *Polymer* **2008**, *49*, 5490.

[110] Ruthard, C.; Maskos, M.; Yildiz, H.; Grohn, F. *Macromol. Rapid Commun.* **2011**, *32*, 523.

[111] Xu, Y.; Borisov, O. V.; Ballauff, M.; Muller, A. H. E. *Langmuir* **2010**, *26, 10*, 6919.

[112] Kent, E. W.; Lewoczko, E. M.; Zhao, B. *Langmuir* **2020**, *36*, 13321.

[113] Cao, Q.; Zuo, C.; LI, L.; He, H. *Soft Matter* **2011**, *7,* 6522.

[114] Chang, H.-Y.; Lin, Y.-L.; Sheng, Y.-J.; Tsao, H.-K. *Macromolecules* **2013**, *46,* 5644.

[115] Yao, K.; Chen, Y.; Zhang, J.; Bunyard, C.; Tang, C. *Macromol. Rapid Commun*. **2013**, *34*, 645.

[116] Ghelichi, M.; Eikerling, M. H. *J. Phys. Chem. B* **2016**, *120,* 2859.

[117] Lin, W.; Galletto, P.; Borkovec, M. *Langmuir* **2004**, *20*, 7465.

[118] Lyulin, S. V.; Vattulainen, I.; Gurtovenko, A. A. *Macromolecules* **2008**, *41*, 4961.

[119] Hernández-Ainsa, S.; Fedeli, E.; Barbera, J.; Marcos, M.; Sierra, T.; Serrano, J. L. *Soft Matter* **2014,** *10*, 281.

[120] Mariani, G.; Moldenhauer, D.; Schweins, R.; Grohn, F. *J. Am. Chem. Soc.* **2016**, *138*, 1280.
[121] Mariani, G.; Schweins, R.; Grohn, F. *Macromolecules* **2016**, *49*, 8661.
[122] Qin, T.; Li, X.; Chen, J.; Zeng, Y.; Yu, T.; Yang, G.; Li, Y. *Chem. Asian J.* **2014**, *9*, 3641.
[123] Hayouni, S.; Robert, A.; Maes, C.; Conreux, A.; Marin, B.; Mohamadou, A.; Bouguillon, S. *New J. Chem.* **2018**, *42*, 18010.
[124] Rodríguez-Prieto, T.; Fattori, A.; Caamejo, C.; de la Mata, F. J.; Cano, J.; Ottaviani, M. F.; Gomez, R. *Eur. Polym. J.* **2020**, *133*, 109748.
[125] Liu, C.; Rouhi, J. *RSC Adv.* **2021**, *11*, 9933.
[126] Simone, P. M.; Lodge, T. P. *Macromolecules* **2008**, *41*, 1753–.
[127] Simone, P. M.; Lodge, T. P. *ACS Appl. Mater. Interfaces* **2009**, *1*, 2812.
[128] Gwee, L.; Choi, J.-H.; Winey, K. I.; Elabd, Y. A. *Polymer* **2010**, *51*, 5516.
[129] Tamate, R.; Hashimoto, K.; Ueki, T.; Watanabe, M. *Phys. Chem. Chem. Phys.* **2018**, *20*, 25123.
[130] Chen, S.; Wu, G.; Wang, X.; Chen, X.; Nealey, P. *ACS Appl. Polym. Mater.* **2020**, *2*, 427.
[131] Bennett, T. M.; Jack, K. S.; Thurecht, K. J.; Blakey, I. *Macromolecules* **2016**, *49*, 205.
[132] Chen, X.; Zhou, C.; Chen, S.-J.; Craig, G. S. W.; RinconDelgadillo, P.; Dazai, T.; Miyagi, K.; Maehashi, T.; Yamazaki, A.; Gronheid, R.; Stoykovich, M. P.; Nealey, P. F. *ACS Appl. Mater. Interfaces* **2018**, *10*, 16747.
[133] Bennett, T. M.; Chambers, L. C.; Thurecht, K. J.; Jack, K. S.; Blakey, I. *Macromolecules* **2018**, *51*, 8979.
[134] Virgili, J. M.; Hexemer, A.; Pople, J. A.; Balsara, N. P.; Segalman, R. A. *Macromolecules* **2009**, *42*, 4604.
[135] Kim, S. Y.; Kim, S. H.; Park, M. J. *Nat. Commun.* **2010**, *1*, 88.
[136] Hoarfrost, M. L.; Segalman, R. A. *Macromolecules* **2011**, *44*, 5281.
[137] Virgili, J. M.; Hoarfrost, M. L.; Segalman, R. A. *Macromolecules* **2010**, *43*, 5417.
[138] Kim, O.; Kim, S. Y.; Lee, J.; Park, M. J. *Chem. Mater.* **2016**, *28*, 318.
[139] Kim, S. Y.; Yoon, E.; Joo, T.; Park, M. J. *Macromolecules* **2011**, *44*, 5289.
[140] Jung, H. Y.; Kim, O.; Park, M. J. *Macromol. Rapid Commun.* **2016**, *37*, 1116.
[141] Kim, O.; Kim, S. Y.; Ahn, H.; Kim, C. W.; Rhee, Y. M.; Park, M. J. *Macromolecules* **2012**, *45*, 8702.
[142] Lu, J.; Yan, F.; Texter, J. *Prog. Polym. Sci.* **2009**, *34,* 431.
[143] Le Bideau, J.; Viau, L.; Vioux, A. *Chem. Soc. Rev.* **2011**, *40*, 907.
[144] Shi, Y.; Wang, Y.; Gu, Y.; Zheng, L.; Ma, S.; Xu, X. *Chem. Eng. J.* **2020**, *392*, 123645.
[145] Vioux, A.; Viau, L.; Volland, S.; Le Bideau, J. *Comptes Rendus Chimie* **2010**, *13*, 242.
[146] Quartarone, E.; Mustarelli, P. *Chem. Soc, Rev.* **2011**, *40*, 2525.
[147] Thapaliya, B. P.; Popov, I.; Dai, S. *ACS Appl. Energy Mater.* **2020**, *3*, 1265.
[148] He, Y.; Boswell, P. G.; Bühlmann, P.; Lodge, T. P. *J. Phys. Chem. B* **2007,** *111,* 4645.
[149] Miranda, D. F.; Versek, C.; Tuominen, M. T.; Russell, T. P.; Watkins, J. J. *Macromolecules* **2013**, *46*, 9913.
[150] Zhang, S.; Lee, K. H.; Frisbie, C. D.; Lodge, T. P. *Macromolecules* **2011**, *44*, 940.
[151] Mizuno, H.; Hashimoto, K.; Tamate, R.; Kokubo, H.; Ueno, K.; Li, X.; Watanabe, M. *Polymer* **2020**, *206*, 122849.
[152] Ding, Y.; Zhang, J.; Chang, L.; Zhang, X.; Liu, H.; Jiang, L. *Adv. Mater.* **2017**, *29, 47,*

1704253.

[153] Sun, N.; Gao, X.; Wu, A.; Lu, F.; Zheng, L. *J. Mol. Liq.* **2017**, *248*, 759.

[154] Qin, H.; Panzer, M. J. *Chem. Mater.* **2020**, *32, 18*, 7951.

[155] Pont, A.-L.; Marcilla, R.; De Meatza, I.; Grande, H.; Mecerreyes, D. *J. Power Sources* **2009**, *188*, 558 – 563.

[156] Gu, Y.; Lodge, T. P. *Macromolecules* **2011**, *44*, 1732.

[157] Rao, J.; Wang, X.; Yunis, R.; Ranganathan, V.; Howlett, P. C.; MacFarlane, D. R.; Forsyth, M.; Zhu, H. *Electrochimica Acta* **2020**, *346*, 136224.

[158] Wang, Z.; Zhang, J.; Liu, J.; Hao, S.; Song, H.; Zhang, J. *ACS Appl. Mater. Interfaces* **2021**, *13, 4,* 5614.

[159] Dupont, J.; Meneghetti, M. R. *Curr. Opin. Colliod Interface Sci.* **2013**, *18*, 54.

[160] Song, H.; Luo, Z.; Zhao, H.; Luo, S.; Wu, X.; Gao, J.; Wang, Z. *RSC Adv.* **2013**, *3*, 11665.

[161] Liu, X.; He, B.; Wang, Z.; Tang, H.; Su, T.; Wang, Q. *Sci. Rep.* **2014**, *4*, 6673.

[162] Gayet, F.; Viau, L.; Leroux, F.; Mabille, F.; Monge, S.; Robin, J.-J.; Vioux, A. *Chem. Mater.* **2009**, *21*, 5575.

[163] Wang, M.; Li, R.; Feng, X.; Dang, C.; Dai, F.; Yin, X.; He, M.; Liu, D. Qi, H. *ACS Appl. Mater. Interfaces* **2020**, *12*, 27545.

[164] Liu, X.; Wen, Z.; Wu, D.; Wang, H.; Yang, J.; Wang, Q. *J. Mater. Chem. A* **2014**, *2*, 11569.

[165] Liu, X.; Wu, D.; Wang, H.; Wang, Q. *Adv. Mater.* **2014**, *26*, 4370.

[166] Mantravadi, R.; Chinnam, P. R.; Dikin, D. A.; Wunder, S. L. *ACS Appl. Mater. Interfaces* **2016**, *8*, 13426.

[167] Kadokawa, J. I.; Murakami, M. A.; Kaneko, Y. *Carbohydr. Res.* **2008**, *343*, 769.

[168] Chereddy, S.; Aguirre, J. Dikin, D.; Wunder, S. L.; Chinnam, P. R. *ACS Appl. Energy Mater.* **2020**, *3*, 279.

[169] Smith, C. J. III; Wagle, D. V.; O'Neil, H. M.; Evans, B. R.; Baker, S. N.; Baker, G. A. *ACS Appl. Mater. Interfaces* **2017**, *9*, 38042.

[170] Eichhorn, S. J.; Dufresne, A.; Aranguren, M.; Marcovich, N. E.; Capadona, J. R.; Rowan, S. J.; Weder, C.; Thielemans, W.; Roman, M.; Renneckar, S.; Gindl, W.; Veigel, S.; Keckes, J.; Yano, H.; Abe, K.; Nogi, M.; Nakagaito, A. N.; Mangalam, A.; Simonsen, J.; Benight, A. S.; Bismarck, A.; Berglund, L. A.; Peijs, T. *J. Mater. Sci.* **2010**, *45*, 1.

[171] Shi, Q. X.; Xia, Q.; Xiang, X.; Ye, Y. S.; Peng, H. Y. ; Xue, Z. G.; Xie, X. L.; Mai, Y. M. *Chem. Eur. J.* **2017**, *23*, 11881.

[172] Chau, M.; Sriskandha, S. E.; Pichugin, D.; Thérien-Aubin, H.; Nykypanchuk, D.; Chauve, G.; Méthot, M.; Bouchard, J.; Gang, O.; Kumacheva, E. *Biomacromolecules* **2015**, *16*, 2455.

[173] Huang, L.; Ye, Z.; Berry, R. *ACS Sustainable Chem. Eng.* **2016**, *4*, 4937.

[174] Hörenz, C.; Bertula, K.; Tiainen, T.; Hietala, S.; Hynninen, V.; Ikkala, O. *Biomacromolecules* **2020**, *21*, 830.

[175] Oechsle, A.-L.; Lewis, L.; Hamad, W. Y.; Hatzikiriakos, S. G.; MacLachlan, M. J. *Chem. Mater.* **2018**, *30*, 376.

[176] Jena, K. K.; Raju, K V. S. N.; Prathab, B.; Aminabhavi, T. M. *J. Phys. Chem. B* **2007**, *111*, 8801.

[177] Milliman, H. W.; Boris, D.; Schiraldi, D. A. *Macromolecules* **2012**, *45,* 1931.

[178] Fink, J. K. In Reactive Polymers Fundamentals and Applications; William Andrew Inc: New York, **2013**; 303.

[179] Yagi, Y.; Inomata, H.; Saito, S. *Macromolecules* **1992**, *24*, 2997.

[180] Moon, R. J.; Martini, A.; Nairn, J.; Simonsen, J.; Youngblood, J. *Chem. Soc. Rev.* **2011**, *40*, 3941.

[181] Domingues, R. M. A.; Gomes, M. E.; Reis, R. L. *Biomacromolecules* **2014**, *15*, 2327.

[182] Lagerwall, J. P. F.; Schutz, C.; Salajkova, M.; Noh, J.; Park, J. H.; Scalia, G.; Bergstrom, L. *NPG Asia Mater.* **2014**, *6*, e80.

[183] Liu, P.; Guo, X.; Nan, F.; Duan, Y.; Zhang, J. *ACS Appl. Mater. Interfaces.* **2017**, *9*, 3085.

[184] Huang, S.; Wang, X; Shen, J.; Wu, R.; Zhao, H.; Wang, Y.; Wang, Y.; Xia, Y. *Carbohydr. Polym.* **2017**, *157*, 1426.

[185] Mori, H.; Lanzendörfer, M. G.; Müller, A. H. E.; Klee, J. E. *Macromolecules* **2004**, *37*, 5228.

[186] Gunawidjaja, R.; Huang, F.; Gumenna, M.; Klimenko, N.; Nunnery, G.A.; Shevchenko, V.; Tannenbaum, R.; Tsukruk, V. V. *Langmuir* **2009**, *25,* 1196.

[187] Habibi, Y.; Lucia, L. A.; Rojas, O. J. *Chem. Rev*. **2010**, *110,* 3479.

[188] Xiong, R.; Yu, S.; Kang, S.; Adstedt, K. M.; Nepal, D.; Bunning, T. J.; Tsukruk, V. V. *Adv. Mater.* **2020,** *32, 2*, 1905600.

[189] Ojijo, V.; Ray, S. S.; Sadiku, R. *ACS Appl. Mater. Interfaces* **2013**, *5*, 4266.

[190] Blanazs, A.; Armes, S. P.; Ryan, A. J. *Macromol. Rapid Commun.* **2009**, *30*, 267.

[191] Orski, S. V.; Fries, K. H.; Sontag, S. K.; Locklin, J. *J. Mater. Chem.* **2011**, *21*, 14135.

[192] Shi, Y.; Peng, L.; Ding, Y.; Zhao, Y.; Guihua, Y. *Chem. Soc. Rev.* **2015**, *44*, 6684.

[193] Barrat, J. L.; Joanny, J. F. *Adv. Chem. Phys.* **1996**, *94*, 1.

[194] Vizintin, A.; Guterman, R.; Schmidt, J.; Antonietti, M.; Dominko, R. *Chem. Mater.* **2018**, 5444.

[195] Peleshanko, S.; Jeong, J.; Gunawidjaja, R.; Tsukruk, V. V. *Macromolecules* **2004**, *37*, 6511.

[196] Inoue, K. *Prog. Polym. Sci.* **2000**, *25*, 453.

[197] Korolovych, V. F.; Erwin, A.; Stryutsky, A.; Milan, E. K.; Shevchenko, V. V.; Tsukruk, V. V. *Bull. Chem. Soc. Jpn.* **2017**, *90*, 919.

[198] Wang, D.; Jin, Y.; Zhu, X.; Yan, D. *Prog. Polym. Sci.* **2017**, 64, 114.

[199] Connal, L. A.; Li, Q.; Quinn, J. F.; Tjipto, E.; Caruso, F.; Qiao, G. G. *Macromolecules* **2008**, *41*, 2620.

[200] Du, J. Z.; Long, H. Y.; Yuan, Y. Y.; Song, M. M.; Chen, L.; Bi, H.; Wang, J. *Chem. Commun.* **2012**, *48*, 1257.

[201] Choi, I.; Suntivich, R.; Plamper, F. A.; Synatschke, C. V.; Müller, A. H. E.; Tsukruk, V. V. *J. Am. Chem. Soc.* **2011**, *133,* 9592.

[202] He, C.; Zhao, C.; Guo, X.; Guo, Z.; Chen, X.; Zhuang, X.; Liu, S.; Jing, X. *J. Polym. Sci., Part A: Polym. Chem.* **2008**, *46*, 4140.

[203] Iatridi, Z.; Lencina, M. M. S.; Tsitsilianis, C. *Polym. Chem.* **2015**, *6*, 3942.

[204] Magurudeniya, H. D.; Ringstrand B. S.; Seifert S.; Firestone, M. A. *Polym. Chem.* **2018**, *9*, 5200.

[205] Benetti, E. M.; Zapotoczny, S.; Vancso, J. *Adv. Mater.* **2007**,*19*, 268.

[206] Jones, D. M.; Smith, J. R.; Huck, W. T. S.; Alexander, C. *Adv. Mater.* **2002**, *14*, 1130.

[207] Yu, Y.; Kieviet, B. D.; Liu, F.; Siretanu, I.; Kutnyánszky, E.; Vansco, G. J.; de Beer, S. *Soft Matter* **2015**, *11*, 8508.

[208] Khanna, K.; Varshney, S.; Kakkar, A. *Polym. Chem.* **2010**, *1*, 1171.

[209] Grayer, V.; Dormidontova, E.; Hadziioannou, G.; Tsitsilianis, C. A. *Macromolecules* **2000**, *33*, 6330.

[210] Tsitsilianis. C.; Alexandridis, P.; Lindman, B. *Macromolecules* **2001**, *34*, 5979.

[211] Kim. H.; Kang, B. G.; Choi, J.; Sun, Z.; Yu, D. M.; Mays, J.; Russell, T. P. *Macromolecules* **2018**, *51*, 1181.

[212] Kim, H.; Arras, M. M.; Mahalik, J. P.; Wang, W.; Yu, D. M.; Chernyy, S.; Goswami, M.; Kumar, R.; Sumpter, B. G.; Hong, K.; Smith, G. S.; Russell, T. P. *Macromolecules* **2018**, *51*, 7491.

[213] Jiang, G; Wang, L.; Chen, T.; Yu, H.; Wang, C.; Chen, C. *Polymer* **2005**, *46*, 5351.

[214] Du, Y.; Chen, Q.; Shen, L.; Xing, Y.; Dai, J. *J. Appl. Polym. Sci.* **2011**, *121*, 2927.

[215] Liu, L.; Moon, K. S.; Gunawidjaja, R.; Lee, E.; Tsukruk, V. V.; Lee, M. *Langmuir,* **2008**, *24*, 3930.

[216] Joncheray, T. J.; Bernard, S. A.; Matmour, R.; Lepoittevin, B.; El-Khouri, R. J.; Taton, D.; Gnanou, Y.; Duran, R. S. *Langmuir,* **2007**, *23*, 2531.

[217] Zhao, L.; Lin, Z. *Soft Matter*, **2011**, *7*, 10520.

[218] Borner, H. G.; Beers, K.; Matyjaszewski, K.; Sheiko, S. S.; Moller, M. *Macromolecules* **2001**, *34*, 4375.

[219] Zhao, L.; Byun, M.; Rzayev, J.; Lin, Z. Q. *Macromolecules* **2009**, *42*, 9027.

[220] Hofle, G.; Steglich, W.; Vorbrüggen, H. *Angew. Chem. Int. Ed. Engl.* **1978**, *17*, 569.

[221] McConney, M. E.; Singamaneni, S.; Tsukruk, V. V. *Polym. Rev.* **2010**, *50*, 235.

[222] Chyasnavichyus, M.; Young, S. L.; Tsukruk, V. V. *Langmuir* **2014**, *30*, 10566.

[223] Zhai, X.; Peleshanko, S.; Klimenko, N. S.; Genson, K. L.; Vaknin, D.; Vortman, M. Ya.; Shevchenko, V. V.; Tsukruk, V. V. *Macromolecules* **2003**, *36*, 3101.

[224] Žagar, E.; Žigon, M. *Macromolecules* **2002**, *35,* 9913.

[225] Joncheray, T. J.; Denoncourt, K. M.; Mathieu, C.; Meier, M. A. R.; Schubert, U. S.; Duran, R. S. *Langmuir* **2006**, *22*, 9264.

[226] Denmark, D. J.; Bradley, J.; Alonso, M. J.; Shakespeare, S.; Bernal, N.; Phan, M. H.; Srikanth, H.; Witanachchi, S.; Mukherjee, P. *RCS Adv.* **2016**, *6*, 5641.

[227] Wang, L.; Wu, Y.; Men, Y.; Shen, J.; Liu, Z. *RSC Adv.* **2015**, *5*, 70758.

[228] Boutris, C.; Chatzi, E. G.; Kiparissides, C. *Polymer* **1997**, *38*, 2567-.

[229] Chen, G.; Hoffman, A. S. *Nature* **1995**, *373*, 49.

[230] Dhanabalan, A.; Dabke, R. B.; Kumar, N. P.; Talwar, S. S.; Major, S.; Lal, R.; Contractor, A. Q. *Langmuir* **1997**, *13*, 4395.

[231] Matsuoka, H.; Uda, K. *Langmuir* **2016**, *32*, 8383.

[232] Gunawidjaja R.; Peleshanko, S.; Tsukruk, V. V. *Macromolecules* **2005**, *38*, 8765.

[233] Zhu, J.; Eisenberg, A.; Lennox, R. B. *Macromolecules* **1992**, *25*, 6547.

[234] Wang X.; Ma, X.; Zang, D. *Soft Matter* **2013**, *9*, 443.

[235] Fang, J. Y.; Gaul, D. F.; Chumanov, G.; Cotton, T. M. *Langmuir* **1995**, *11*, 4366.

[236] Li, Z.; Ma, X.; Guan, X.; Qiang, X.; Zang, D.; Chen, F. *Colloid. Polym. Sci.* **2017**, *295*, 157.

[237] Seo, Y.; Paeng, K.; Park, S. *Macromolecules* **2001**, *34*, 8735.

[238] Joncheray, T. J.; Denoncourt, K. M.; Meier, M. A. R.; Schubert, U. S.; Duran, R. S. *Langmuir* **2007**, *23*, 2423.

[239] Clarke, C. J.; Zhang, L.; Zhu, J.; Yu, K.; Lennox, R. B.; Eisenberg, A. *Macromol. Symp.* **1997**, *118*, 647.

[240] Faure´, M. C.; Bassereau, P.; Lee, L. T.; Menelle, A.; Lheveder, C. *Macromolecules* **1999**, *32*, 8538.

[241] Zhao, L.; Goodman, M. D.; Bowden, N. B.; Lin, Z. *Soft Matter* **2009**, *5*, 4698.

[242] Mouri, E.; Matsumoto, K.; Matsuoka, H. *J. Polym. Sci., Part B: Polym. Phys.* **2003**, *41*, 1921.

[243] Kaewsaiha, P.; Matsumoto, K.; Matsuoka, H. *Langmuir* **2007**, *23*, 7065.

[244] Cox, J. K.; Yu, K.; Eisenberg, A.; Lennox, R. B. *Phys. Chem. Chem. Phys.* **1999**, *1*, 4417.

[245] Sidorenko, A.; Zhai, X. W.; Simon, F.; Pleul, D.; Tsukruk, V. V. *Macromolecules* **2002**, *35*, 5131.

[246] Tsukruk, V. V.; Bliznyuk, V. N.; Hazel, J.; Visser, D.; Everson, M. P. *Langmuir* **1996**, *12*, 4840.

[247] Oishi, Y.; Umeda, T.; Kuramori, M.; Suehiro, K. *Langmuir* **2002**, *18*, 945.

[248] Ornatska, M.; Peleshanko, S.; Genson, K. L.; Rybak, B.; Bergman, K. N.; Tsukruk, V. V. *J. Am. Chem. Soc.* **2004**, *126*, 9675.

[249] Perrin, F. X.; Panaitescu, D. M.; Frone, A. N.; Radovici, C.; Nicolae, C. *Polymer* **2013**, *54*, 2347.

[250] Tagit, O.; Tomczak, N.; Vancso, G. J. *Small* **2008**, *4*, 119.

[251] Harmon, M. E.; Kuckling, D.; Pareek, P.; Frank, C. W. *Langmuir* **2003,** *19*, 10947.

[252] Shulha, H.; Zhai, X.; Tsukruk, V. V. *Macromolecules* **2003**, *36*, 2825.

[253] Young, S. L.; Gupta, M.; Hanske, C.; Fery, A.; Scheibel, T.; Tsukruk, V. V. *Biomacromolecules* **2012**, *13*, 3189.

[254] Funk, L.; Brehmer, M.; Zentel, R.; Kang, H.; Char, K. *Macromol. Chem. Phys.* **2008,** *209,* 52.

[255] Russell, T. P. *Science* **2002**, *297*, 964.

[256] Cheng, X.; Canavan, H. E.; Stein, M. J.; Hull, J. R.; Kweskin, S. J.; Wagner, M. S.; Somorjai, G. A.; Castner, D. G.; Ratner, B. D. *Langmuir* **2005**, *21*, 7833.

[257] Schmidt, S.; Zeiser, M.; Hellweg, T.; Duschl, C.; Fery, A.; Möhwald, H. *Adv. Funct. Mater.* **2010**, *20*, 3235.

[258] Kim, D.; Park, H.; Rhim, J.; Lee, Y. *Solid State Ionics* **2005**, *176*, 117.

[259] Peak Force QNM User Guide. http://www.torontomicrofluidics.ca/cms/mzanuals/peak_force.pdf p.77, (accessed Apr. 21, 2019).

[260] Derjaguin, B. V.; Muller, V. M.; Toporov. Yu. P. *J. Colloid. Interface Sci.* **1975**, *53*, 314.
[261] Johnson, K. L.; Kendall, K.; Roberts, A. D. *Proc. R. Soc. Lond. A.* **1971**, *324*, 301.
[262] Soo, P. L.; Eisenberg, A. *J. Polym. Sci. Part B. Polym. Phys.* **2004**, *42*, 923.
[263] Wang, X.; Hong, K.; Baskaran, D.; Goswami, M.; Sumpter, B.; Mays, J. *Soft Matter* **2011**, *7*, 7960.
[264] Wang, X.; Goswami, M.; Kumar, R.; Sumpter, B. G.; Mays, J. *Soft Matter* **2012**, *8*, 3036.
[265] Uhlík, F.; Košovan, P.; Zhulina, E. B.; Borisov, O. V. *Soft Matter* **2016**, *12*, 4846.
[266] Chopade, S. A.; Au, J. G.; Li, Z.; Schmidt, P. W.; Hillmyer, M. A.; Lodge, T. P. *ACS Appl. Mater. Interfaces* **2017**, *9*, 14561.
[267] Iatridi, Z.; Tsitsilianis, C. *Polymers* **2011**, *3*, 1911.
[268] Schwarz, B.; Schönhoff, M. *Langmuir* **2002**, *18*, 2964.
[269] Miller, M. D.; Bruening, M. L. *Chem. Mater.* **2005**, *17*, 5375.
[270] Tagliazucchi, M. E.; Calvo, E. J. *J. Electroanal. Chem.* **2007**, *599*, 249.
[271] Beneselfelt, T.; Pattersson, T.; Wagberg, L. *Langmuir* **2017**, *33*, 968.
[272] Tagliazucchi, M.; Calvo, E. J. *Chem. Phys. Chem.* **2010**, *11*, 2957.
[273] Zhu, Y.; Yao, C.; Ren, J.; Liu, C.; Ge, L. *Coll. Surf. A Physicochem. Eng. Asp.* **2015**, *465*, 26.
[274] Calvo, E. J.; Flexer, V.; Tagliazucchi, M.; Scodeller, P. *Phys. Chem. Chem. Phys.* **2010**, *12*, 10033.
[275] Zhang, F.; Wu, Q.; Chen, Z.-C.; Li, X.; Jiang, X.-M.; Lin, X.-F. *Langmuir* **2006**, *22*, 8458.
[276] Mergel, O.; Kühn, P. T.; Schneider, S.; Simon, U.; Plamper, F. A. *Electrochim. Acta* **2017**, *232*, 98.
[277] Dionzou, M.; Morère, A.; Roux, C.; Lonetti, B.; Marty, J.-D.; Mingotaud, C.; Joseph, P.; Goudounèche, D.; Payré, B.; Léonetti, M.; Mingotaud, A.-F. *Soft Matter* **2016**, *12*, 2166.
[278] Hess, M.; Jones, R. G.; Kahovec, J.; Kitayama, T.; Kratochvil, P.; Kubisa, P.; Mormann, W.; Stepto, R. F. T.; Tabak, D.; Vohlidal, J.; Wilks, E. S. *Pure Appl. Chem.* **2006**, *78, 11,* 2067.
[279] Ting, J. M.; Wu, H.; Herzog-Arbeitman, A.; Srivastava, S.; Tirrell, M. V. *ACS Macro Lett.* **2018**, *7*, 726.
[280] Fehér, B.; Zhu, K.; Nyström, B.; Varga, I.; Pedersen, S. *Langmuir* **2019**, *35, 42*, 13614.
[281] Bodycomb, J.; Hara, M. *Macromolecules* **1995**, *28,* 8190.
[282] Qiao, X.; Weiss, R. A. *Macromolecules* **2013**, *46*, 2417.
[283] Huang, C.; Chen, Q.; Weiss, R. A. *Macromolecules* **2017***, 50*, 424.
[284] Brenner, A. R.; Voit, B. I. *Macromol. Symp.* **1996**, *102*, 47.
[285] Qui, T.; Tang, L.; Fu, Z.; Tuo, X.; Li, Y.; Liu, D.; Yang, W. *Polym. Adv. Technol.* **2004**, *15*, 65.
[286] Schwab, E.; Mecking, S. *Organometallics* **2005**, *24*, 3758.
[287] Biswas, C. S.; Patel, V. K.; Vishwakarma, N. K.; Tiwari, V. K.; Maiti, B.; Maiti, P.; Kamigaito, M.; Okamoto, Y.; Ray, B. *Macromolecules* **2011**, *44*, 5822.
[288] Makharza, S.; Auisa, J.; Abu Sharkh, S.; Ghabboun, J.; Faroun, M.; Dweik, H.; Sultan, W.; Sowwan, M. *Int. J. Polym. Anal. Char.* **2010**, *15*, 254.
[289] Ito, M.; Ishizone, T. *J. Polym. Sci. A Polym. Chem.* **2006**, *44,* 4832.
[290] Shi, Z.; Yongfeng, Z.; Yan, D. *Macromol. Rapid Commun.* **2008**, *29*, 412.
[291] Žagar, E.; Huskić, M.; Grdadolnik, J.; Žigon, M.; Zupančič-Valant. A. *Macromolecules* **2005**, *38*, 3933.

[292] Dumitrascu, A.; Sarkar, A.; Chai, J.; Zhang, T.; Bubeck, R. A.; Howell, B. A.; Smith, P. B. *J. Therm. Anal. Calorim.* **2018**, *131*, 273.
[293] Halperin, A.; Kröger, M.; Winnik, F. M. *Angew. Chem. Int. Ed.* **2015**, *54*, 15342.
[294] Lapworth J. W.; Hatton, P. V.; Rimmer, S. *RCS Adv.* **2013**, *3*, 18107.
[295] Rimmer, S. Carter, S.; Rutkaite, R.; Haycock, J. W.; Swanson, L. *Soft Matter* **2007**, *3*, 971.
[296] Feil, H.; Bae, Y. H.; Feijen, J.; Kim, S. W. *Macromolecules* **1993**, *26*, 2496.
[297] Weng, Y.; Ding, Y.; Zhang, G. *J. Phys. Chem. B* **2006**, *110*, 11813.
[298] Chee, C-K.; Hunt, B. J.; Rimmer, S.; Rutkaite, R. Soutar, I.; Swanson, L. *Soft Matter* **2009**, *5*, 3701.
[299] Yim, H.; Kent, M. S.; Huber, D. L.; Satija, S.; Majewski, J.; Smith, G. S. *Macromolecules* **2003**, *36*, 5244.
[300] Plunkett, K. N.; Zhu, X.; Moore, J. S.; Leckband, D. E. *Langmuir* **2006**, *22*, 4259.
[301] Zhou, Y.; Yan, D.; Dong, W.; Tian, Y. *J. Phys. Chem. B* **2007**, *111,* 1262.
[302] Han, Q.; Chen, X.; Niu, Y.; Zhao, B.; Wang, B.; Mao, C.; Chen, L.; Shen, J. *Langmuir* **2013**, *29*, 8402.
[303] Pamies, R.; Zhu, K.; Volden, S.; Kjoniksen, A.; Karlsson, G.; Glomm, W. R.; Nystrom, B. *J. Phys. Chem. C* **2010**, *50*, 21960.
[304] Karjalainen, E.; Chenna, N.; Laurinmäki, P.; Butcher, S. J.; Tenhu, H. *Polym. Chem.* **2013**, *4*, 1014.
[305] Blanazs, A.; Armes, S. P.; Ryan, A. J. *Macromol. Rapid Commun.* **2009**, *30*, 264.
[306] Holder, S. J.; Sommerdijk, N. A. J. M. *Polym. Chem.* **2011**, *2*, 1018.
[307] Lombardo, D.; Kiselev, M. A.; Magazu, S.; Calandra, P. *Adv. Cond. Matter Phys.* **2015**, *2015,* 151683.
[308] Mai, Y.; Eisenberg, A. *Chem. Soc. Rev.* **2012**, *41*, 5949.
[309] Dai, Y.; Wang, H.; Zhang, X. *J. Nanopart. Res*. **2017**, *19*, 298.
[310] Brozowska, A.; Paczesny, J.; Parzuchowski, P.; Kusznerczuk, M.; Nikiforov, K.; Rokicki, G.; Gregorowicz, J. *Macromolecules* **2014**, *47*, 5256.
[311] Pochan, D. J.; Gido, S. P.; Pispas, S.; Mays, J. W. *Macromolecules* **1996**, *29*, 5099.
[312] Lee, G.; Shin, Y.-H.; Son, J. Y. *J. Am. Chem. Soc.* **2009**, *131*, 1634.
[313] Salerno, M.; El Merhie, A.; Diaspro, A.; Dante, S. *Thin Solid Films* **2018**, *660*, 253.
[314] Wu, Y.; Hayashi, K.; Saito, N.; Sugimura, H.; Takai, O. *Surf. Interface Anal.* **2003**, *35*, 94.
[315] Case, D. A.; Cheatham, T. E.; Darden, T.; Gohlke, H.; Luo, R.; Merz, K. M.; Onufriev, A.; Simmerling, C.; Wang, B.; Woods, R. J. *J. Comput. Chem.* **2005**, *26*, 1668.
[316] Humphrey, W.; Dalke, A.; Schulten, K. *J. Mol. Graph.* **1996**, *14*, 33.
[317] Roe, D. R.; Cheatham, T. E. *J. Chem. Theory Comput.* **2013**, *9*, 3084.
[318] Emami, F. S.; Puddu, V.; Berry, R. J.; Varshney, V.; Patwardhan, S. V.; Perry, C. C.; Heinz, H. *Chem. Mater.* **2014**, *26*, 2647.
[319] Åqvist, J.; Wennerström, P.; Nervall, M.; Bjelic, S.; Brandsdal, B. O. *Chem. Phys. Lett.* **2004**, *384*, 288.
[320] Ryckaert, J.-P.; Ciccotti, G.; Berendsen, H. J. C. *J. Comput. Phys.* **1977**, *23*, 327.
[321] Liu, G.; Yang, S. *J. Phys. Chem. B* **2007**, *111*, 3633.
[322] Dupont, J.; de Souza, R. F.; Suarez, P. A. Z. *Chem. Rev*. **2002**, *102*, 3667.

[323] Shaplov, A. S.; Ponkratov, D. O. ; Vygodskii, Ya. S. *Polym. Sci.* **2016,** *58,* 73.

[324] Shaplov, A. S.; Ponkratov, D. O.; Vlasov, P. S.; Lozinskaya, E. I.; Komarova, L. I.; Malyshkina, I. A.; Vidal, F.; Nguyen, G. T. M.; Armand, M.; Wandrey, C.; Vygodskii, Ya. S. *Polym. Sci. Ser. B.* **2013**, *55*, 122.

[325] Tanaka, K.; Chujo, Y. *J. Mater. Chem.* **2012**, *22*, 1733.

[326] Tanaka, K.; Chujo, Y. *Bull. Chem. Soc. Jpn.* **2013**, *86*, 1231

[327] Chojnowski, J.; Fortuniak, W.; Rościszewski, P.; Werel, W.; Łukasiak, J.; Kamysz, W.; Hałasa, R. *J. Inorg. Organomet. Polym. Mater.* **2006**, *16*, 219.

[328] Kaneko, Y.; Shoiriki, M.; Mizumo, T. *J. Mater. Chem.* **2012**, *22,* 14475.

[329] Tokunaga, T.; Shoiriki, M.; Mizumo, T.; Kaneko, Y.; *J. Mater. Chem. C.* **2014**, *2*, 2496.

[330] K. Tanaka, F. Ishiguro, Y. Chujo, J. Am. Chem. Soc. 2010, 132, 17649.

[331] Manickam, S.; Cardiano, P.; Mineo, P. G.; Lo Schiavo, S. *Eur. J. Inorg. Chem.* **2014**, *16,* 2704.

[332] Liu, Y.; Leng, C.; Chisholm, B.; Stafslien, S.; Majumdar, P.; Chen, Z. *Langmuir* **2013**, *29*, 2897.

[333] Elumalai, V.; Dharmalingam, S. *Polym. Compos*. **2019,** *40*, 1536.

[334] Čolović, M.; Volavšek, J.; Stathatos, E.; Čelan Korošin, N.; Šobak, M.; Jerman, I. *Sol Energy* **2019,** *183*, 619.

[335] Li, W.; Wang, D.; Han, D.; Sun, R.; Zhang, J.; Feng, S. *Polymers* **2018**, *10*, 917.

[336] Li, W.; Feng, S. *J. Mol. Liq.* **2018**, *265*, 269.

[337] Matějka, L.; Dukh, O.; Brus, J.; Simonsick, W. J.; Meissner, B. *J. Non Cryst. Solids* **2000**, *270*, 34.

[338] Eisenberg, P.; Erra-Balsells, R.; Ishikawa, Y.; Lucas, J. C.; Mauri, A. N.; Nonami, H.; Riccardi, C. C.; Williams, R. J. J. *Macromolecules* **2000,** *33*, 1940.

[339] Ishii, T.; Mizumo, T.; Kaneko, Y. *Bull. Chem. Soc. Jpn.* **2014**, *87*, 155.

[340] Ishii, T.; Enoki, T.; Mizumo, T.; Ohshita, J.; Kaneko, Y. *RSC Adv.* **2015,** *5*, 15226.

[341] Harada, A.; Koge, S.; Ohshita, J.; Kaneko, Y. *Bull. Chem. Soc. Jpn.* **2016**, *89*. 1129.

[342] Pretsch, E.; Bühlmann, Ph.; Badertscher, M. Structure determination of organic compounds. Tables of spectral data. 4th, revised and enlaged edition, Springer-Verlag Berlin Heidelberg, Germany **2009**.

[343] Shevchenko, V. V.; Gumennaya, M. A.; Shevchuk, A. V.; Gomza, Yu. P.; Klimenko, N. S.; Boichuk, V. V. *Polym. Sci. Ser. B* **2009**, *51*, 46.

[344] Greaves, T. L.; Drummond, C. J. *Chem. Rev.* **2015**, *115*, 11379.

[345] Greaves, T. L.; Drummond, C. J. *Chem. Rev.* **2008**, *108*, 206.

[346] Maeda, D.; Ishii, T.; Kaneko, Y. *Bull. Chem. Soc. Jpn.* **2018,** *91*, 1112.

[347] Renyves, R.; Schmutz, M.; Horner, I. J.; Bright, F. V.; Rzayev. J. *J. Am. Chem. Soc.* **2014**, *136,* 7762.

[348] Li, C.; Li, Q.; Kaneti, Y. V.; Hou, D.; Yamauchi, Y.; Mai, Y. *Chem. Soc. Rev.* **2020**, *49,* 4681.

[349] Israelachvili, J. N.; Mitchell D. J.; Ninham, B. W. *J. Chem. Soc. Faraday Trans. II* **1976**, *172,* 1525.

[350] Thota, B. N. S.; Urner, L. H.; Haag, R. *Chem. Rev.* **2016**, *116, 4*, 2079.

[351] Vadillo-Rodriguez, V.; Busscher, H. J.; van der Mei, H. C.; de Vries, J. ; Norde. W. *Colloid. Surfaces B: Biointerface*s **2005**, *41*, 33.

[352] Kumar, A.; Dixit. C. K. Chapter 3. "Methods for characterization of nanoparticles" in book "Advances in nanomedicine for the delivery of therapeutic nucleic acids" **2017**.

[353] Rogers, R. D.; Seddon, K. R. *Science* **2003**, *302*, 792.

[354] Néouze, M. A.; Le Bideau, J.; Gaveau, P.; Bellaver, S.; Vioux, A. *Chem. Mater.* **2006**, *18*, 3931.

[355] Wasserscheid, P.; Welton, T. *Ionic Liquids in Synthesis,* Willey-VCH, Weinheim, Germany **2008.**

[356] Francis, C. F. J.; Kyratzis, I. L.; Best, A. S. *Adv. Mater.* **2020**, *32, 18*, 1904205.

[357] Noda, A.; Susan, M. A. B. H.; Kudo, K.; Mitsushima, S.; Hayamizu, K.; Watanabe, M. *J. Phys. Chem. B* **2003**, *107*, 4024.

[358] Wang, P.; Zakeeruddin, S. M.; Humphry-Baker, R.; Graetzel, M. *Chem. Mater.* **2004**, *16*, 2694.

[359] Lewandowski, A.; Świderska-Mocek, A. *J. Power Sources* **2009**, *194*, 601.

[360] Ye, Y. S.; Rick, J.; Hwang, B. J. *J. Mater. Chem. A* **2013**, *1,* 2719.

[361] Qian, W.; Texter, J.; Yan, F. *Chem. Soc. Rev.* **2017**, *46*, 1124.

[362] Ohno, H.; Ito, K. *Chem. Lett.* **1998**, *27*, 751.

[363] Hirao, M.; Ito, K.; Ohno, H. *Electrochim. Acta* **2000**, *45*, 1291.

[364] Döbbelin, M.; Azcune, I.; Bedu, M.; de Luzuriaga, A. R.; Genua, A.; Jovanovski, V.; Cabañero, G.; Odriozola, I. *Chem. Mater.* **2012**, *24, 9,* 1583.

[365] Chen, N.; Zhang, H.; Li, L.; Chen, R.; Guo, S. *Adv. Energy Mater.* **2018**, *8, 12,* 1702675.

[366] Wu, F.; Luo, L.; Tang, Z.; Liu, D.; Shen, Z.; Fan, X.-H. *ACS Appl. Energy Mater.* **2020**, *3*, 6536.

[367] Pelz, A.; Dörr, T. S.; Zhang, P.; de Oliveira, P. W.; Winter, M.; Wiemhöfer, H.-D.; Kraus, T. *Chem. Mater.* **2019**, *31*, 277.

[368] Tang, B.; White, S. P.; Frisbie, C. D.; Lodge, T. P. *Macromolecules* **2015**, *48*, 4942.

[369] Hashimoto, K.; Hirasawa, M.; Kokubo, H.; Tamate, R.; Li, X.; Shibayama, M.; Watanabe, M. *Macromolecules* **2019**, *52*, 8430.

[370] Lind, F.; Rebollar, L.; Bengani-Lutz, P.; Zsatekin, A.; Panzer, M. J. *Chem. Mater.* **2016**, *28*, 8480.

[371] Taylor, M. E.; Panzer, M. J. *J. Phys. Chem. B* **2018**, *122,* 8469.

[372] Fox, R. J.; Yu, D.; Hegde, M.; Kumbhar, A. S.; Madsen, L. A.; Dingemans, T. J. *ACS Appl. Mater. Interfaces* **2019**, *11*, 40551.

[373] Yu, D.; Pan, X.; Bostwick, J. E.; Zaenelotti, C. J.; Mu, L.; Colby, R. H.; Lin, F.; Madsen, L. A. *Adv. Energy Mater.* **2021**, 2003559.

[374] Song, H.; Niu, Y.; Wang, Z. Zhang, J. *Biomacromolecules* **2011**, *12*, 1087.

[375] Vidinha, P.; Lourenco Nuno, M. T.; Pinheiro, C.; Bras Ana, R.; Carvalho, T.; Santos-Silva, T.; Mukhopadhyay, A.; Romao Maria, J.; Parola, J.; Dionisio, M.; Cabral Joaquim, M. S.; Afonso Carlos, A. M.; Barreiros, S. *Chem. Commun.* **2008**, *44*, 5842.

[376] Singh, P. K.; Bhattacharya, B.; Nagarale, R. K.; Kim, K.-W.; Rhee, H.-W. *Synthetic Metals* **2010**, *160*, 139.

[377] Pohako-Esko, K.; Bahlmann, M.; Schulz, P. S.; Wasserscheid, P. *Ind. Eng. Chen. Res.* **2016**, *55*, 7052.

[378] Kato, R.; Lettow, J. H.; Patel, S. N.; Rowan, S. J. *ACS Appl. Mater. Interfaces* **2020**, *12*, 54083.

[379] Tanpichai, S.; Quero, F.; Nogi, M.; Yano, H.; Young, R. J.; Lindström, T.; Sampson, W. W.; Eichhorn, S. J. *Biomacromolecules* **2012**, *13,* 1340.

[380] Sehaqui, H.; Mushi, N. E.; Morimune, S.; Salajkova, S. M.; Nishino, T.; Berglund, L. A. *ACS Appl. Mater. Interfaces* **2012**, *4*, 1043.

[381] Lahiji, R. R.; Xu, X.; Reifenberger, R.; Raman, A.; Rudie, A.; Moon, R. J. *Langmuir* **2010**, *26, 6,* 4480.

[382] Shevchenko, V. V.; Stryutsky, A. V.; Klymenko, N. S.; Gumenna, M. A.; Fomenko, A. A.; Bliznyuk, V. N.; Trachevsky, V. V.; Davydenko, V. V.; Tsukruk, V. V. *Polymer* **2014**, *55,* 3349.

[383] Capadona, J. R.; van den Berg, O.; Capadona, L. A.; Schroeter, M.; Rowan, S. J.; Tyler, D. J.; Weder, C. A. *Nat. Nanotech.* **2007**, *2,* 765.

[384] Capadona, J. R.; Shanmuganathan, K.; Triftschuh, S.; Seidel, S.; Rowan, S. J.; Weder, C. *Biomacromolecules* **2009**, *10, 4,* 712.

[385] Haward, R. N.; Thackray, G. *Proc. Roy. Soc. A* **1968**, *302*, 453.

[386] Jasper, L. E.; Deramond, H.; Mathis, J. M.; Belkoff, S. M. *Bone* **1999,** *25, 2,* 27S.

[387] Ang, K. C.; Leong, K. F.; Chua, C. K.; Chandrasekaran, M. *J. Biomed. Mater. Res. A* **2007**, *80A, 3,* 655.

[388] Zein, I.; Hutmacher, D. W.; Tan, K. C.; Teoh, S. H. *Biomaterials* **2002**, *23, 4*, 1169.

[389] Hoque, M. E.; San, W. Y.; Wei, F.; Li, S.; Huang, M.-H.; Vert, M.; Hutmacher, D. W. *Tissue Eng. Part A* **2009**, *15,* 3013.

[390] Guidetti, G.; Atifi, S.; Vignolini, S.; Hamad, W. Y. *Adv. Mater.* **2016**, *28, 45*, 10042.

[391] Ranjbar, D.; Hatzikiriakos, S. G. *Langmuir* **2020**, *36*, 293.

[392] Viera, R. G. P.; Filho, G. R.; de Assuncao, R. M. N.; Meireles, C. S.; Vieira, J. G.; de Oliveira, G. S. *Carbohydr. Polym.* **2007**, *67*, 182.

[393] Lee, H.; Sundaram, J.; Zhu, L.; Zhao, Y.; Mani, S. *Carbohydr. Polym.* **2018**, *181*, 506.

[394] Adebajo, M. O.; Frost, R. L. *Spectrochimica Acta Part A* **2004,** *60*, 449.

[395] Wang, Z. M.; Li, L.; Zheng, B. S.; Normakhamatov, N.; Guo, S. Y. *Int. J. Biol. Macromol.* **2007,** *41,* 376.

[396] Hobza, P.; Špirko, V.; Selzle, H. L.; Schlag, E. *J. Phys. Chem. A* **1998**, *102, 15,* 2501.

[397] Hobza, P.; Špirko, V.; Havlas, Z.; Buchhold, K.; Reimann, B.; Barth, H.-D.; Brutschy, B. *Chem. Phys. Lett.* **1999**, *299, 2,* 180.

[398] Shirhatti, P.; Wategaonkar, S. *Phys. Chem. Chem. Phys.* **2010**, *12***,** 6650.

[399] Gopi, R.; Ramanathan, N.; Sundararajan, K. *Spectrochimica Acta A* **2017**, *181, 15*, 137.

[400] Xiong, R.; Grant, A. M.; Ma, R.; Zhang, S.; Tsukruk, V. V. *Mater. Sci. Eng. R Rep.* **2018**, *125*, 1.

[401] Lu, P.; Hsieh, Y.-L. *Carbohydr. Polym.* **2010**, *82, 2,* 329.

[402] Nan, F.; Nagarajan, S.; Chen, Y.; Liu, P.; Duan, Y.; Men, Y.; Zhang, J. *ACS Sustainable Chem. Eng.* **2017**, *5*, 8951.

[403] Yuan, C.; Zhu, X.; Su, L.; Yang, D.; Wang, Y.; Yang, K.; Cheng, X. *Colloid. Polym. Sci.* **2015**, *293*, 1945.

[404] Ikari, T.; Keppler, A.; Reinmöller, M.; Beenken, W. J. D.; Krischok, S.; Marschewski, M.; Maus-Friedrichs, W.; Höfft, O.; Endres, F. *e-J. Surf. Sci. Nanotechnol.* **2010,** *8*, 241.

[405] Verma, Y. L.; Sing, R. K. *J. Phys. Chem. C* **2015**, *119,* 24381.

[406] Wu, Q.; Xu, J.; Zhu, S.; Kuang, Y.; Wang, B.; Gao, W. *Carbohydr. Polym.* **2020**, *249*, 116827.
[407] Ben-Naim, A. *J. Chem. Phys.* **1985**, *82*, 4668.
[408] Koç, B.; Eren, I.; Ertekin, F. K. *J. Food Eng.* **2008**, *85, 3*, 340.
[409] Safa, M.; Hao, Y.; Chamaani, A.; Adelowo, E.; Chawla, N.; Wang, C.; El-Zahab, B. *Electrochim. Acta* **2017**, *258*, 1284.
[410] Cowan, M. G.; Lopez, A. M.; Masuda, M.; Kohno, Y.; McDanel, W. M.; Noble, R. D.; Gin, D. L. *Macromol. Rapid Commun.* **2016**, *37, 14*, 1150.
[411] Kerner, M.; Plylahan, N.; Scheers, J.; Johansson, P. *Phys. Chem. Chem. Phys.* **2015**, *17*, 19569.
[412] Asbani, B.; Bounor, B.; Robert, K.; Douard, C.; Athouel, L.; Lethien, C.; Le Bideau, J.; Brousse, T. *J. Electrochem. Soc.* **2020**, *167,* 100551.
[413] Singh, M. P.; Singh, R. K.; Chandra, S. *J. Phys. Chem. B* **2011,** *115*, 7505.
[414] Shen, B.; Lang, J.; Guo, R.; Zhang, X.; Yan, X. *ACS Appl. Mater. Interfaces* **2015**, *7*, 25378
[415] D. Deb, S. Bhattacharya, *J. Phys. Chem. C* **2017**, *121, 12,* 6962.
[416] Dri, F. L.; Hector Jr., L. G.; Moon, R. J.; Zavattieri, P. D. *Cellulose* **2013**, *20*, 2703.
[417] Samir, M. A. S. A.; Alloin, F.; Dufresne, A. *Biomacromol.* **2005**, *6, 2*, 612.
[418] Gibson, L. J.; Ashby, M F. *Cellular solids*, Cambridge University Press, Cambridge, United Kingdom, **1997**.
[419] Rajkhowa, R.; Gil, E. S.; Kluge, J.; Numata, K.; Wang, L.; Wang, X.; Kaplan, D. L. *Macromol. Biosci.* **2010,** *10*, 599.
[420] Alhassan, S. M.; Qutubuddin, S.; Schiraldi, D. *Langmuir* **2010**, *26, 14*, 12198.
[421] Murakawa, K.; King, D. R.; Sun, T.; Guo, H.; Kurokawa, T.; Gong, J. P. *J. Mater. Chem. B* **2019**, *7*, 5296.
[422] Huang, T.; Xu, H.; Jiao, K.; Zhu, L.; Brown, H. R.; Wang, H. *Adv. Mater.* **2007**, *19*, 1622.
[423] Dai, X.; Zhang, Y.; Gao, L.; Bai, T.; Wang, W.; Cui, Y.; Liu, W. *Adv. Mater.* **2015**, *27*, 3566.
[424] Li, J.; Liu, H.; Wang, C.; Haung, G. *RSC Adv.* **2017**, *7*, 35311.
[425] Visentin, A. F.; Panzer, M. J. *ACS Appl. Mater. Interfaces* **2012**, *4, 6,* 2836.
[426] Wang, Z.; Liu, J.; Zhang, J.; Hao, S.; Duan, X.; Song, H.; Zhang, J. *Cellulose* **2020**, *27,* 5121.
[427] Pittenger, B.; Osechinskiy, S.; Yablon, D.; Mueller, T. *JOM* **2019**, *71, 10*, 3390.
[428] Kavanagh, G. M.; Ross-Murphy, S. B. *Prog. Polym. Sci.* **1998,** *23*, 533.
[429] Hao, J.; Weiss, R. A. *Macromolecules* **2011**, *44,* 9390.
[430] Kitazawa, Y.; Iwata, K.; Kido, R.; Imaizumi, S.; Tsuzuki, S.; Shinoda, W.; Ueno, K.; Mandai, T.; Kokubo, H.; Dokko, K.; Watanabe, M. *Chem. Mater.* **2018**, *30, 1*, 252.
[431] Kitazawa, Y.; Iwata, K.; Imaizumi, S.; Ahn, H.; Kim, S. Y.; Ueno, K.; Park, M. J.; Watanabe, M. *Macromolecules* **2014**, *47, 17*, 6009.
[432] D'Angelo, A. J.; Panzer, M. J. *J. Phys. Chem. B* **2017**, *121, 4*, 890.
[433] Paluch, M.; Wojnarowska, Z.; Goodrich, P.; Jacquemin, J.; Pionteck, J.; Hensel-Bielowka, S. *Soft Matter* **2015**, *11,* 6520.
[434] Wojnarowska, Z.; Thoms, E.; Blanchard, B.; Tripathy, S. N.; Goodrich, P.; Jacquemin, J.; Knapik-Kowalczuk, J.; Paluch, M. *Phys. Chem. Chem. Phys.* **2017**, *18*, 14141.
[435] Horowitz, A. I.; Panzer, M. J. *J. Mater. Chem.* **2012**, *22*, 16534.
[436] Visentin, A. F.; Alimena, S.; Panzer, M. J. *ChemElectroChem* **2014**, *1,* 718.
[437] Kinsey, T.; Glynn, K.; Cosby, T.; Iacob, C.; Sangoro, J. *ACS Appl. Mater. Interfaces* **2020**, *12,*

44325.

[438] Iacob, C.; Sangoro, J. R.; Papadopoulos, P.; Schubert, T.; Naumov, S.; Valiullin, R.; Karger, J.; Kremer, F. *Phys. Chem. Chem. Phys*. **2010**, *12, 42*, 13798.

[439] Tripathi, A. K.; Singh, R. K. *RSC Adv.* **2016,** *6, 51*, 45147.

[440] Tarnacka, M.; Chrobok, A.; Matuszek, K.; Golba, S.; Maksym, P.; Kaminski, K.; Paluch, M. *ACS Appl. Mater. Interfaces* **2016**, *8*, 29779.

[441]Cui, J.; Nie, F.-M.; Yang, J.-X.; Ma, Z.; Li, Y.-S. *J. Mater. Chem. A* **2017,** *5*, 25220.

[442] Biwas, Y.; Maji, T.; Dule, M.; Mandal, T. K. *Polym. Chem.* **2016,** *7*, 867.

[443] Jana, S.; Biswas, Y.; Anas, Md.; Saha, A.; Mandal, T. K. *Langmuir* **2018**, *34,* 12653.

[444] Mao, J. X.; Nulwala, H. B.; Luebke, D. R.; Damodaran, K. *J. Mol. Liq.* **2012,** *175,* 141.

[445] Nonemacher, J. F.; Huter, C.; Zheng, H.; Malzbender, J.; Kruger, M.; Spatschek, R.; Finsterbusch, M. *Solid State Ionics* **2018**, *321*, 126.

[446] Zsila, F. Electronic Circular Dichroism Spectroscopy. In *Pharmaceutical Sciences Encyclopedia*, John Wiley & Sons, Hoboken, NJ, **2010**.

[447] Meinert, C.; Bredehöft, J. H.; Filippi, J.-J.; Baraud, Y.; Nahon, L.; Wien, F.; Jones, N. C.; Hoffmann, S. V.; Meierhenrich, U. J. *Angew. Chem. Int. Ed.* **2012**, *51*, 4484.

[448] Bredehöft, J. H.; Jones, N. C.; Meinert, C.; Evans, A. C.; Hoffmann, S. V.; Meierhenrich, U. J. *Chirality* **2014**, *26*, 373.

[449] Qu, D.; Zheng, H.; Jiang, H.; Xu, Y.; Tang, Z. *Adv. Opt. Mater.* **2019**, *7*, 1801395.

[450] Shen, Z.; Wang, T.; Shi, L.; Tang, Z.; Liu, M. *Chem. Sci.* **2015**, *6*, 4267.

[451] Dolamic, I.; Knoppe, S.; Dass, A.; Bürgi, T. *Nat. Commun.* **2012**, *3*, 798.

[452] Kehrer, M.; Duchoslav, J.; Hinterreiter, A.; Cobet, M.; Mehic, A.; Stehrer, T.; Stifter, D. *Plasma Proc. Polym.* **2019**, *16*, e1800160.

[453] Alanis, A.; Valdes, J. H.; Guadalupe, N.-V. M.; Lopez, R.; Mendoza, R.; Mathew, A. P.; de Leon, R. D.; Valencia, L. *RSC Adv.* **2019**, *9*, 17417.

[454] Smith, E. F.; Rutten, F. J. M.; Villar-Garcia, I. J.; Briggs, D.; Licence, P. *Langmuir* **2006**, *22*, 9386.

[455] Lovelock, K. R. J.; Smith, E. F.; Deyko, A.; Villar-Garcia, I. J.; Licence, P.; Jones, R. G. *Chem. Commun*. **2007**, *46*, 4866.

[456] Kiefer, J.; Fries, J.; Leipertz, A. *Appl. Spectroscopy* **2007**, *61*, 1306.

[457] Snyder, J. F.; Carter, R. H.; Wetzel, E. D. *Chem. Mater*. **2007**, *19*, 3793.

[458] Tang, W.; Tang, S.; Zhang, C.; Ma, Q.; Xiang, Q.; Yang, Y.-W.; Luo, J. *Adv. Energy Mater*. **2018**, *8*, 1800866.

[459]Klongkan, S.; Pumchusak, J. *Electrochimica Acta* **2015**, *161*, 171.

[460] Liu, C.; Wang, J.; Kou, W.; Yang, Z.; Zhai, P.; Liu, Y.; Wu, W.; Wang, J. *Chem. Eng. J.* **2021**, *404*, 126517.

[461] Lu, J.; Liu, Y.; Yao, P.; Ding, Z.; Tang, Q.; Wu, J.; Ye, Z.; Huang, K.; Liu, X. *Chem. Eng. J.* **2019**, *367*, 230.

[462] Tan, J.; Ao, X.; Dai, A.; Yuan, Y.; Zhuo, H.; Lu, H.; Zhuang, L.; Ke, Y.; Su, C.; Peng, X.; Tian, B.; Lu, J. *Energy Storage Mater.* **2020**, *33*, 173.

[463] Hu, J.; Wang, W.; Zhou, B.; Feng, Y.; Xie, X.; Xue, Z. *J. Membrane. Sci.* **2019**, *575*, 200.

[464] Zhang, M.; Zuo, Q.; Wang, L.; Yu, S.; Mai, Y.; Zhou, Y. *Chem. Commun.* **2020**, *56*, 7929.

[465] Zhong, Y.; Nguyen, G. T. M.; Plesse, C.; Vidal, F.; Jager, E. W. H. *J. Mater. Chem. C* **2019**, *7*, 256.

[466] Sun, Z.; Li, Y.; Zhang, S.; Shi, L.; Wu, H.; Bu, H.; Ding, S. *J. Mater. Chem. A* **2019**, *7*, 11069.

[467] Wen, J.; Zhang, R.; Zhao, Q.; Liu, W.; Lu, G.; Hu, X.; Sun, J.; Wang, R.; Jiang, X.; Hu, N.; Liu, J.; Liu, X.; Xu, C. *ACS Appl. Mater. Interfaces* **2020**, *12*, 54637.

[468] Zhai, H.; Xu, P.; Ning, M.; Cheng, Q.; Mandai, J.; Yang, Y. *Nano Lett*. **2017**, *17*, 3182.

[469] Kou, W.; Lv, R.; Zho, S.; Yang, Z.; Huang, J.; Wu, W.; Wang, J. *J. Membrane Sci*. **2021**, *618*, 118702.

[470] Zekoll, S.; Marriner-Edwards, C.; Ola Hekselman, A. K.; Kasemchainan, J.; Kuss, C.; Armstrong, D. E. J.; Cai, D.; Wallace, R. J.; Richter, F. H.; Thijssen, J. H. J.; Bruce, P. G. *Energy Environ. Sci.* **2018**, *11*, 185.

[471] Sakuda, A.; Hayashi, A.; Tatsumisago, M. *Sci. Reports* **2013**, *3*, 2261.

[472] Sakuda, A.; Hayashi, A.; Takigawa, Y.; Higashi, K.; Tatsumisago, M. *J. Ceram. Soc. Jpn.* **2013**, *121*, 946.

[473] Lim, J. Y.; Kang, D. A.; Kim, N. U.; Lee, J. M.; Kim, J. H. *J. Membrane Sci.* **2019**, *589*, 117250.

[474] Zhong, Y.; Nguyen, G. T. M.; Plesse, C.; Vidal, F.; Jager, E. W. H. *ACS Appl. Mater. Interfaces* **2018**, *10*, 21601.

[475] Hong, K.; Yuk, J.; Kim, H. J.; Lee, J. Y.; Kim, S.; Lee, J.-L.; Lee, K. H. *Composites, Part B* **2018**, *152*, 275.

[476] Guan, J.; Li, Y.; Li, J. *Ind. Eng. Chem. Res.* **2017**, *56*, 12456.

[477] Kim, Y. M.; Seo, D. G.; Oh, H.; Moon, H. C. *J. Mater. Chem. C* **2019**, *7*, 161.

[478] Seo, D. G.; Moon, H. C. *Adv. Funct. Mater*. **2018**, *28*, 1706948.

[479] Hwang, H.; Park, S. Y.; Kim, J. K.; Kim, Y. M.; Moon, H. C. *ACS Appl. Mater. Interfaces* **2019**, *11*, 4399.

[480] Visentin, A. F.; Dong, T.; Poli, J.; Panzer, M. J. *J. Mater. Chem. A* **2014**, *2*, 7723.

[481] Fujii, K.; Asai, H.; Ueki, T.; Sakai, T.; Imaizumi, S.; Chung, U.-I.; Watanabe, M.; Shibayama, M. *Soft Matter* **2012**, *8*, 1756.

[482] Sun, L.; Chen, S.; Guo, Y.; Song, J.; Zhang, L.; Xiao, L.; Guan, Q.; You, Z. *Nano Energy* **2019**, *63*, 103847.

[483] Horowitz, A. I.; Panzer, M. J. *Angew. Chem.* **2014**, *126*, 9938.

[484] D'Angelo, A. J.; Panzer, M. J. *Adv. Energy Mater*. **2018**, *8*, 1801646.

[485] Smith, D. M.; Pan, Q.; Cheng, S.; Wang, W.; Bunning, T. J.; Li, C. Y. *Adv. Mater. Interfaces* **2018**, *5*, 1700861.

[486] Yoshikawa, H. Y.; Rossetti, F. F.; Kaufmann, S.; Kaindl, T.; Madsen, J.; Engel, U.; Lewis, A. L.; Armes, S. P.; Tanaka, M. *J. Am. Chem. Soc.* **2011**, *133*, 1367.

[487] Mohammadi, E.; Zhao, C.; Meng, Y.; Qu, G.; Zhang, F.; Zhao, X.; Mei, J.; Zuo, J.-M.; Shukla, D.; Diao, Y. *Nat. Commun.* **2017**, *8*, 16070.

[488] Choi, W. S.; Koo, H. Y.; Park, J.-H.; Kim, D.-Y. *J. Am. Chem. Soc.* **2005**, *127, 46*, 161137.

[489] Schrinner, M.; Polzer, F.; Mei, Y.; Lu, Y.; Haupt, B.; Ballauff, M.; Göldel, A.; Drechsler, M.; Preussner, J.; Glatzel, U. *Macromol. Chem. Phys*. **2007**, *208,* 1542.

[490] Schrinner, M.; Ballaruff, M.; Talmon, Y>; Kauffmann, J.; Tun, M.; Möller, J. *Science* **2009**, *323*, 617.

[491] Zhu, Z.; Guo, X.; Wu, S.; Zhang, R.; Jie, Z.; Li, L. *Ind. Eng. Chem. Res.* **2011,** *50*, 13848.

[492] Binnemans, K. Ionic Liquid Crystals. Chem. Rev. 2005, 105, 4148−4204.

[493] Bhowmik, P. K.; Akhter, S.; Han, H. *J. Polym. Sci., Part A: Polym. Chem.* **1995,** *33*, 1927.

[494] Vuillaume, P. Y.; Galin, J. C.; Bazuin, C. G. *Macromolecules* **2001**, *34*, 859.

[495] Shchukin, D. G.; Sviridov, D. V. *J. Photochem. Photobio. C: Photochem. Rev.* **2006**, *7,* 1, 23.

[496] Manzano, M.; Vallent-Regi, M. *Adv. Funct. Mater.* **2020**, *30*, 2, 1902634.

[497] Hwang, H.; Ejsmont, A.; Freund, R.; Goscianska, J.; Schmidt, B. V. K. J.; Wuttke, S. *Chem. Soc. Rev.* **2020**, 49, 3348.

[498] Yu, J.; Xie, L. H.; Li, J. R.; Ma, Y.; Seminario, J. M.; Balbuena, P. B. *Chem. Rev.* **2017,** *117,* 9674.

[499] Zheng, H.; Zhang, Y.; Liu, L.; Wan, W.; Guo, P.; Nystrom, A. M.; Zou, X. *J. Am. Chem. Soc.* **2016,** *138*, 962.

[500] Lee, J.; Farha, O. K.; Roberts, J.; Scheidt, K. A.; Nguyen, S. T.; Hupp, J. T. *Chem. Soc. Rev.* **2009**, *38,* 1450.

[501] Zhu, H.; Zhang, Q.; Zhu, S. *ACS Appl. Mater. Interfaces* **2016**, *8*, 17395.

[502] Lim, J.; Lee, E. J.; Choi, J. S.; Jeong, N. C. *ACS Appl. Mater. Interfaces* **2018**, *10*, 3793**.**

[503] Park, K. S.; Ni, Z.; Cote, A. P.; Choi, J. Y.; Huang, R.; Uribe-Romo, F. J.; Chae, H. K.; O'Keeffe, M.; Yaghi, O. M. *Proc. Natl. Acad. Sci. U. S. A.* **2006**, *103*, 10186.

[504] Wu, K.; Song, Z.; Zhang, S.; Ni, Y.; Cai, S.; Gong, X.; He, L.; Yu, S.-H. *Proc. Natl. Acad. Sci. U. S. A.* **2020***, 117*, 15465.

[505] K. S. Park, Z. Ni, A. P. Côté, J. Y. Choi, R. Huang, F. J. Uribe-Romo, H. K. Chae, M. O'Keeffe and O. M. Yaghi, *Proc. Natl. Acad. Sci. U. S. A.* **2006**, *103, 27*, 10186.

[506] Y. Pan, Y. Liu, G. Zeng, L. Zhao and Z. La, Chem. Commun. **2011**, 47, 7, 2071.

[507] Zhang, Y.; Jia, Y.; Hou, L. *RSC, Adv.* **2018**, *8*, 31471.

[508] Debye, P.; Anderson, H. R., Jr.; Brumberger, H. *J. Appl. Phys.* **1957**, *28*, 679.

[509] Curtis, J. E.; McAuley, A.; Nanda, H.; Krueger, S. *Faraday Discuss.* **2012**, *158,* 285.

[510] Wang, H. *Polymer* **2006,** *4, 14*, 4897.

[511] Yu, L.; Yakubov, G. E.; Gilbert, E. P.; Sewell, K.; van de Meene, A. M. L.; Stokes, J. R. *Carbohydr. Polym.* **2019**, *297*, 333.